Uranium Isotope Variations Across Key Evolutionary Intervals in Geological History

by

Feifei Zhang

A Dissertation Presented in Partial Fulfillment
of the Requirements for the Degree
Doctor of Philosophy

Approved June 2018 by the
Graduate Supervisory Committee:

Ariel Anbar, Chair
Hilairy Hartnett
Meenakshi Wadhwa
Gwyneth Gordon
Steven Ruff

ARIZONA STATE UNIVERSITY

August 2018

ABSTRACT

There is a growing body of evidence that the evolving redox structure of the oceans has been an important influence on the evolutionary trajectory of animals. However, current understanding of connections between marine redox conditions and marine extinctions and recoveries is hampered by limited detailed knowledge of the timing, duration, and extent of marine redox changes.

The recent development of U isotopes ($\delta^{238}U$) in carbonates as a global ocean redox proxy has provided new insight into this problem. Reliable application and interpretation of the $\delta^{238}U$ paleoproxy in geological records requires a thorough understanding of the reliability of $\delta^{238}U$ recorded by bulk carbonate sediments. In this dissertation, I evaluate the robustness of $\delta^{238}U$ paleoproxy by examining $\delta^{238}U$ variations in marine carbonates across Permian-Triassic boundary (PTB) sections from different paleogeographic locations. Close agreement of $\delta^{238}U$ profiles from coeval carbonate sections thousands of kilometers apart, in different ocean basins, and with different diagenetic histories, strongly suggests that bulk carbonate sediments can reliably preserve primary marine $\delta^{238}U$ signals, validating the carbonate U-isotope proxy for global-ocean redox analysis.

To improve understanding of the role of marine redox in shaping the evolutionary trajectory of animals, high-resolution $\delta^{238}U$ records were generated across several key evolutionary periods, including the Ediacaran-to-Early Cambrian Explosion of complex life (635-541 Ma) and the delayed Early Triassic Earth system recovery from the PTB extinction (252-246 Ma). Based on U isotope variations in the Ediacaran-to-the Early Cambrian ocean, the initial diversification of the Ediacara biota immediately postdates an episode of pervasive ocean oxygenation across the Shuram event. The subsequent decline

and extinction of the Ediacara biota is coincident with an episode of extensive anoxic conditions during the latest Ediacaran Period. These findings suggest that global marine redox changes drove the rise and fall of the Ediacara biota. Based on U isotope variations, the Early Triassic ocean was characterized by multiple episodes of extensive marine anoxia. By comparing the high-resolution $\delta^{238}U$ record with the sub-stage ammonoid extinction rate curve, it appears that multiple oscillations in marine anoxia modulated the recovery of marine ecosystems following the latest Permian mass extinction.

ACKNOWLEDGMENTS

I've been fortunate to be surrounded these last years by an incredible group of people; this dissertation would not have been possible without their support. To those that I consider scientific and professional mentors that have kept me interested, grounded, and challenged – most notably Ariel Anbar, Stephen Romaniello, Shuhai Xiao, and Thomas Algeo – thank you for all that you do. There're so many thanks that I want to devote to my advisor, Ariel Anbar, who supported and funded all aspects of my work. "It's your Ph.D., you can do whatever you want", a simple phrase from my first conversation with Ariel deeply inspired me to look for ideas where I can do my own research throughout my graduate career.

I've also been very fortunate to be surrounded by a great group of people both in the Anbar lab and outside ASU. In the Anbar lab, I especially thank Gwyneth Gordon and Wang Zheng for the countless hours of analytical training and support they provided. Outside ASU, I thank Shuhai Xiao (Virginia Tech), Thomas Algeo (University of Cincinnati), Brian Kendall (University of Waterloo), Boris G. Pokrovsky (Geological Institute, Russian Academy of Sciences), Chao Li (China University of Geosciences, Wuhan), Dalton Hardisty (Woods Hole Oceanographic Institution), Geoffrey Gilleaudeau (Arizona State University), Genming Luo (China University of Geosciences, Wuhan), Huan Cui (University of Wisconsin–Madison), Kimberly Lau (University of California, Riverside), Laishi Zhao (China University of Geosciences, Wuhan), Magdalena Osburn (Northwestern University), Mike Meyer (Carnegie Institution of Washington), Tim Lenton (University of Exeter), Victor A. Melezhik (Geological Survey of Norway), Tais Dahl (University of Copenhagen), Zhong-Qiang Chen (China University of Geosciences,

Wuhan), Shuzhong Shen (Nanjing Institute of Geology and Palaeontology, Chinese Academy of Sciences), and Hua Zhang (Nanjing Institute of Geology and Palaeontology, Chinese Academy of Sciences) for providing samples and for helpful discussions. I thank the Chinese visiting students (Meng Cheng, Ziheng Li, and He Zhao) in the Anbar lab, who make my laboratory life colorful. I also want to take this opportunity to give a special thank you to the "*2015 GeoBiology Summer Course*" friends. I might be a challenging student at that time, but thank you for your patient and support.

Thanks also to my family for being a constant source of support, encouragement, and inspiration. I've always been encouraged to do what interests me, for as long as I can remember. Lastly (but not leastly), to my wife for her love, support, understanding, and companionship during the last two years of my graduate career. I couldn't have finished this dissertation without her support. She makes me want to be a better person in this world, she understands.

TABLE OF CONTENTS

Page

CHAPTER Page

Appendix Page

LIST OF TABLES

Table Page

LIST OF FIGURES

Figure Page

Figure Page

Figure Page

Figure Page

Figure Page

CHAPTER 1

INTRODUCTION

1.1 Overview

Profound changes in the abundance of molecular oxygen (O_2) in Earth's atmosphere and oceans shaped the course of biological evolution (e.g., Anbar and Knoll, 2002; Lyons et al., 2014). Understanding the "redox history" of the Earth's surface environment is therefore central to understanding the evolution of the Earth as a planet capable of hosting complex life.

The history of life on Earth is punctuated by numerous mass extinction events (Figure 1.1). There is a growing body of evidence that the evolving redox structure of the oceans has been an important influence on the evolutionary trajectory of animals, and ocean anoxia is widely cited as a direct cause of several major extinction events (e.g., Wignall and Twitchett, 1996; Sheehan et al., 2001; Bond et al., 2004; Brennecka et al., 2011; Hammarlund et al., 2012; Jost et al., 2017). The first known extinction event, the terminal Ediacaran extinction event, occurred at the close of the Precambrian Era (Laflamme et al., 2013). During the subsequent Phanerozoic Era, there are five major mass extinctions: the end-Ordovician mass extinction, the Late Devonian mass extinction, the end-Permian mass extinction, the end-Triassic mass extinction, and the end-Cretaceous mass extinction (e.g., Alroy, 2010; Bambach, 2006; Barnosky et al., 2011; Jablonski and Chaloner, 1994; Raup and Sepkoski, 1982; Figure 1.1). Among these six major extinction events, the first five (Figure 1.1) have been proposed to have been associated with periods of expanded marine anoxia (e.g., Amthor et al., 2003; Bartlett et al., 2018; Grice et al., 2005; Isozaki, 1997; Jost et al., 2017; Kimura and Watanabe, 2001; Laflamme et al., 2013;

Meyer et al., 2008; Schroder and Grotzinger, 2007; Wignall and Twitchett, 1996). However, our current understanding of connections between marine redox conditions and marine extinctions is hampered by poor constraints on the detailed timing and duration, extent, and degree of marine anoxia. For instance, during the end-Permian mass extinction (EPME), the timing of onset of marine anoxia was inferred to be several million years before the EPME in some studies (Isozaki, 1997; Wignall and Twitchett, 1996), but no more than ~100 kyr prior to the EPME in others (Algeo and Twitchett, 2010; Shen et al., 2012b; Winguth and Winguth, 2012). Different studies have also argued both for (Grice et al., 2005) and against (Loope et al., 2013) the presence of anoxia in shallow-marine facies. Recent work favors a more complex scenario, characterized by widespread expansion of anoxia at intermediate depths (~200-1000 m) prior to the EPME (Feng and Algeo, 2014; Winguth and Winguth, 2012) followed by episodic upward chemocline excursions into the ocean-surface layer commencing at the EPME (Algeo et al., 2008; Kump et al., 2005). These uncertainties make the significance of anoxia as a kill mechanism for the EPME range from a primary driver to, relatively unimportant.

For the most part, insights into marine redox history are derived from measurements of geochemical signatures sensitive to the abundance of O_2 – so-called "paleoredox proxies". In the past decade, a variety of new proxies have been developed, significantly changing our knowledge of Earth's redox history. Most of these proxies consist of measurements of metal abundances or isotope ratios in ancient black shales (see Anbar and Rouxel, 2007, Lyons et al., 2009 for reviews). Unfortunately, the distribution of black shales in the geologic record is sporadic. In contrast to black shales, marine carbonate sedimentary rocks are common in the geologic record, often continuous over long periods

of time, and geographically widespread in open ocean basins. Importantly, many major mass extinction events are largely represented by marine carbonate sedimentary rocks. Paleoredox proxies that can be characterized in carbonate rocks therefore offer great potential to broaden our knowledge of Earth's redox history.

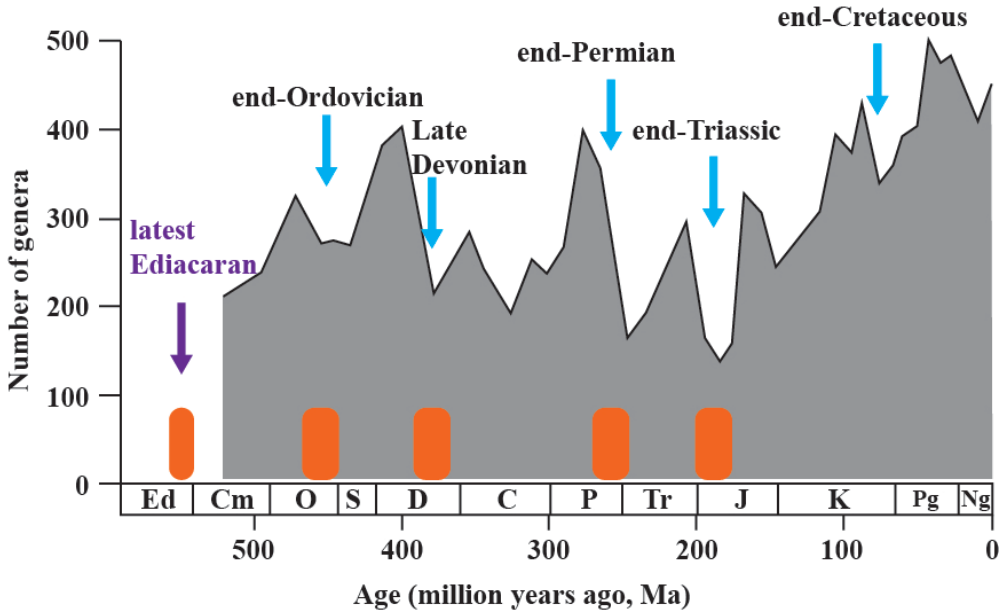

Figure 1.1 Major mass extinction events in geological history (modified after Alroy, 2010). Orange bars denote evidence for expanded marine anoxia. Ed, Ediacaran; Cm, Cambrian; O, Ordovician; S, Silurian; D, Devonian; C, Carboniferous; P, Permian; Tr, Triassic; J, Jurassic; K, Cretaceous; Pg, Paleogene; Ng, Neogene. Because the latest Ediacaran extinction is a recently identified extinction event, it is less well characterized than the Phanerozoic extinction events (e.g., Laflamme et al., 2013).

Existing paleoredox proxies in carbonates are inherently local or indirect tracers of oxygenation/anoxia. For example, Rare Earth Element (REE) patterns in carbonates have

been used to assess ocean redox for many years (German and Elderfield, 1990; Kakuwa and Matsumoto, 2006). However, the ocean residence times for the REE are short (50-130 yr; e.g., German and Elderfield, 1990) compared to the time scale of ocean mixing, making them local or regional redox indicators.

Iron speciation techniques have recently been applied to marine carbonate sediments (Clarkson et al., 2014; Clarkson et al., 2016; Wood et al., 2015), however, this proxy only provides redox information on a basin or regional scale.

The C and S isotope systems in marine carbonates do not appear to be direct measures of ocean redox conditions. Inorganic carbon isotopes respond to changes in the proportion of carbon buried as carbonate and inorganic carbon (Kump and Arthur, 1999), as well as the fraction of authigenic carbonates (Cui et al., 2016b; Schrag et al., 2013) and recycling of crustal organic matter (Daines et al., 2017). Sulfur isotopes respond to changes in the proportion of sulfur buried as pyrite, and to changes in factors that control the fractionation of S isotopes between sulfate and pyrite (e.g., primary production and availability of organic matter, marine sulfate concentration, cell-specific sulfate reduction rate, and oxidative recycling of sulfide; Algeo et al., 2015; Fike et al., 2015). However, C isotopes and S isotopes respond indirectly to changes in ocean redox conditions through these processes, providing qualitative information.

The recent development of U isotopes ($\delta^{238}U$) in marine carbonates as a globally-integrative paleoredox proxy provides a unique opportunity to quantitatively track global marine redox changes. Variations in the relative abundances of long-lived isotopes of uranium (U) – namely ^{238}U and ^{235}U – arising from redox-dependent isotope fractionation (Wang et al., 2015; Weyer et al., 2008). Variations in the isotope abundances of many

transition metals are now well known. In many instances, these variations arise from redox-dependent isotope fractionation. This is the basis for many promising new paleoredox proxies. All these proxies are based on the isotopic mass balance between inputs to the oceans, primarily via continental weathering, and a variety of sedimentary sinks, such as oxic, anoxic, and euxinic marine sediments, accumulating under different redox conditions. Because different sinks are characterized by different isotopic fractionation factors, the isotopic composition of the dissolved metal in seawater is a sensitive indicator of the proportion of each removal mechanism, and hence to the redox conditions at the seafloor.

As described further below, substantial $^{238}U/^{235}U$ variations in the environment associated with sedimentary redox environments are well documented (Andersen et al., 2014; Noordmann et al., 2016; Noordmann et al., 2015; Rolison et al., 2017; Romaniello et al., 2013; Stirling et al., 2007; Weyer et al., 2008). These observations are the basis of initial attempts to use U isotopes as a paleoredox proxy (Bartlett et al., 2018; Brennecka et al., 2011a; Elrick et al., 2017; Jost et al., 2017; Lau et al., 2017; Lau et al., 2016; Zhang et al., 2018a; Zhang et al., 2018b; Zhang et al., 2018c). U isotopes in carbonate rocks may be especially useful because this element is readily incorporated into carbonate minerals (Chung and Swart, 1990). Concentrations of U in natural marine carbonates can approach 4 ppm, in contrast to geochemically analogous elements, like Mo, which has concentrations of 0.02–0.06 ppm in natural carbonate sands (Voegelin et al., 2009). Additionally, U (along with Mo and Re) is one of a small group of redox-sensitive trace metals that have long oceanic residence times ($>10^5$ yr) relative to the time scale of ocean mixing ($\sim10^3$ yr). Hence, the $^{238}U/^{235}U$ in the oceans should be uniform. This means that the isotope composition of U in marine carbonates from a single site might be used to infer global

redox conditions. Therefore, the $^{238}U/^{235}U$ proxy may provide the potential for new insights into the mass extinction events.

However, the $^{238}U/^{235}U$ records in marine carbonates are likely influenced by both syn-depositional and post-depositional alterations. It is thus essential to investigate variations of $^{238}U/^{235}U$ in both modern and ancient marine carbonates to understand the degree to which U isotope proxy records are affected by depositional alteration and how we can account for this alteration when trying to assess ancient marine redox conditions. In modern marine carbonates, and in relevant experiments, a number of researches have examined variations of $^{238}U/^{235}U$ to understand alteration processes (e.g., Romaniello et al., 2013; Chen et al., 2016; Chen et al., 2018). This dissertation focuses on ancient marine carbonates, examining U isotope variations in ancient marine carbonates during periods of known change in ocean anoxia. The goal is to see if U isotopes vary as expected during these periods, especially when looking for consistent variations in multiple contemporaneous but geographically disparate sections, and to use the context provided by other proxies to improve our interpretations of U isotope variations.

This dissertation first presents a critical review of the uranium isotopes in marine carboantes (Chapter 1) and then focuses on validating the U isotope proxy using Permian-Triassic boundary marine carbonates (Chapters 2). Widespread changes in ocean redox in advance of the PTB extinction have been inferred for decades, based on a variety of existing proxies (Algeo and Twitchett, 2010; Grice et al., 2005; Isozaki, 1997; Shen et al., 2012b; Wignall and Twitchett, 1996; Winguth and Winguth, 2012). This may have been the most significant change in ocean redox, with respect extent and duration, in the last 500 Ma. Many continuous carbonate and other sedimentary sections that are available to this

dissertation span the PTB and cover a wide paleogeographic range. A number of these sections have been studied using other biogeochemical tracers. The PTB therefore provides an exceptional opportunity to validate if U isotopes in carbonates are a robust, global paleoredox proxy, as assumed, or if global signatures are overwhelmed by local effects and/or are overprinted by diagenesis.

This dissertation then moves to other key evolution periods, the Early Triassic delayed marine ecosystem recovery (252–246 Ma; Chapter 3 and 4) following the PTB mass extinction and the Ediacaran-to-Early Cambrian Explosion of complex life (635–541 Ma; Chapter 5 and 6). The goal of this dissertation is to explore the answer to a key question (Chapter 7): Do uranium isotopes of marine carbonates provide evidence for marine anoxia as a common driver for major mass extinctions? This is part of the author's long-term research goal of piecing together a clearer picture of how life on Earth and its planetary environments have co-evolved through geological history.

I conceived all these studies, obtained the samples from coauthors, carried out the analyses in the Anbar lab, led the effort to interpret the findings aided by key coauthors, and led the paper-writing with help from key coauthors. Samples used in chapter 2 are requested from Thomas Algeo, Laishi Zhao, and Zhong-Qiang Chen. Samples used in chapter 3 are requested from Tom Algeo. Samples used in chapter 4 are requested from Tom Algeo, Sylvain Richoz, and Micha Horacek. Samples used in chapter 5 are requested from Shuhai Xiao and Huan Cui. Samples used in chapter 6 are requested from Chao Li, Dalton Hardisty, Victor Melezhik, and Boris Pokrovsky.

1.2 Uranium isotope fractionation

It had long been thought that uranium was too heavy to undergo measurable isotopic fractionation in nature. Recent investigations show relatively large isotopic variations of the uranium isotopes in natural samples that is far beyond the analytical precision of the MC-ICP-MS measurements (e.g., Stirling et al., 2007; Weyer et al., 2008; Brennecka et al., 2011; Andersen et al., 2014; Tissot and Dauphas, 2015). This discovery was made possible by the development of an accurate ^{233}U:^{236}U double-spike to precisely correct for isotopic fractionation introduced during chemical purification and MC-ICP-MS measurements.

Uranium has five naturally occuring isotopes, ^{233}U, ^{234}U, ^{235}U, ^{236}U, and ^{238}U. Two of them, ^{235}U and ^{238}U are primordial, with half-lives of 4.468×10^9 yr and 0.7038×10^9 yr, respectively. Their natural abundances are 99.274 % and 0.720 %. ^{234}U occurs in nature as a decay product of ^{238}U with a natural abundance of 0.005 % and a half-life of 2.48×10^5 yr. The other two isotopes, ^{233}U and ^{236}U have half-lives of 1.59×10^5 yr and 2.34×10^7 yr, respectively and natural abundances of ^{233}U and ^{236}U isotopes are minute.

Uranium isotope fractionation is mostly driven by redox chemistry. Uranium occurs in two redox states in surface environments: soluble U(VI) under oxygenated conditions and insoluble U(IV) under anoxic conditions (e.g., Langmuir, 1978). Chemical species of U(VI) are generally soluble in oxic seawater and form the conservative form of uranyl ions that bind to carbonate ions, forming $UO_2(CO_3)_3^{4-}$ (e.g., Anderson et al., 1989; Tribovillard et al., 2006). Chemical species of U(IV) are generally insoluble in oxic seawater and form the dominant U oxides (e.g., UO_2, U_3O_7 or U_3O_8) that quickly remove from seawater (e.g., Klinkhammer and Palmer, 1991; Crusius et al., 1996; Zheng et al.,

2000; Morford et al., 2001; Chaillou et al., 2002; McManus et al., 2005; Tribovillard et al., 2006). Reduction of U (VI) to U(IV) occurs under conditions similar to those of Fe(III) to Fe(II) reduction (Klinkhammer and Palmer, 1991; Crusius et al., 1996; Zheng et al., 2000; Morford et al., 2001; Chaillou et al., 2002; McManus et al., 2005).

The reduction of U (VI) to U(IV) in surface environments is associated with a relatively large and detectable U isotope ($^{238}U/^{235}U$) fractionation (e.g., Weyer et al., 2008), expressed as $\delta^{238}U$ $\{\delta^{238}U=[(^{238}U/^{235}U)_{sample}/(^{238}U/^{235}U)_{standard}-1]\times1000\}$. Isotope fractionation between U(IV) and U(VI) is driven by the dominance of nuclear volume effects (Bigeleisen, 1996; Schauble, 2007). As a result, during reduction of U(VI) to U(IV), the reduced U(IV) is enriched in the heavier ^{238}U isotope, thus enriching the remaining dissolved U(VI) reservoir in the lighter ^{235}U isotope. This phenomenon is observed in the Black Sea (e.g., Andersen et al., 2014; Rolison et al., 2017). Microbially mediated reduction of U(VI) to U(IV) under anoxic conditions is associated with a large isotopic fractionation, $0.68\ ‰ < \delta^{238}U < 0.99\ ‰$ (Basu et al., 2014; Stirling et al., 2015; Stylo et al., 2015).

As a result, during periods of expanded marine anoxia, the enhanced U(VI) reduction to U(IV) and the subsequent U(IV) removal from seawater would shift the $\delta^{238}U$ of seawater towards lighter values. Such a shift in seawater $\delta^{238}U$ could potential be recorded by marine carboantes (discussed further below).

Because U has a long residence time in seawater (~500 kyr for the modern; Dunk et al., 2002), which is significantly longer than the time scale of ocean mixing (~1.6 kyr; Broecker and Peng, 1982), U is well-mixed in the modern ocean (e.g., Dunk et al., 2000;

Tissot and Dauphas, 2015). As a result, measurements in one location may provide information about paleoredox on a global scale.

1.3 U isotope analytical methods

1.3.1 Sample digestions

This section summarizes existing carbonate sample dissolution protocols from different research groups, which has been given in Table 1.1. There is no uniform sample digestion protocol, but the general principle is to use diluted hydrochloric acid and nitric acid (e.g., Stirling et al., 2007, 2015; Weyer et al., 2008; Brennecka et al., 2011; Romaniello et al., 2013; Andersen et al., 2014; Dhal et al., 2014, 2017; Lau et al., 2016, 2017; Elrick et al., 2017; Jost et al., 2017; Zhang-F. et al., 2018a, b; Wei et al., 2018), or less commonly, diluted acetic acid (e.g., Bartlett et al., 2018; Zhang-F. et al., 2018b).

I compared carbonate dissolution protocols using 1M hydrochloric acid, 1M acetic acid, and 3M nitric acid (ash at 750°C then dissolve in 3M nitric acid). Five Permian-Triassic age carbonate samples (DW330-345, DW435+450, DXK-11 base, DXK-2, and DXK-32) that were collected from South China were selected for this purpose. These dissolution methods yielded indistinguishable $\delta^{238}U$ results provided that excess acid is available to ensure complete carbonate dissolution (Table A.2).

In addition, to better understand the range and variability of $\delta^{238}U$ in bulk carbonate sediments, I conducted a leaching experiment using acetic acid with different molarities to sequentially extract carbonate components in Permian-Triassic carbonate sediments. In this experiment, I analyzed five samples, two from the Permian-Triassic Kamura section (KAMD-20 and KAMD-31) and three from the modern Bahamian carbonate platform

(including one modern coral sample and two sediment core samples: core 1 40-42 cm, and core 4 24-28 cm, which were previously studied by Romaniello et al. (2013)). I used a 16-step sequential extraction protocol following the Sr-leaching methods of Liu et al. (2013), as summarized in Table A.1.

Owing to low U concentrations for some samples, I combined Steps S1 and S2 (= Label 1), Steps S3 to S9 (= Label 2), Steps S10 to S12 (= Label 3), Steps S13 and S14 (= Label 4), and Steps S14 to S16 (= Label 5) for the purpose of U isotope analysis. U isotope results from this leaching experiment are given in Table A.5.

One of the key questions that I investigated is whether the measured isotopic variations in each sample were actually generated as an artefact of isotopic fractionation during the sequential leaching experiments. The modern coral sample showed no isotopic fractionation during the sequential leaching experiments, since the results for Labels 1 to 5 are statistically indistinguishable (Table A.5). I therefore tentatively suggest that differences in $\delta^{238}U$ among leaching steps for the other samples reflect true isotopic inhomogeneities within these samples.

For the two Permian-Triassic samples and two modern Bahamian carbonate sediments, the leaching experiments yielded large differences in $\delta^{238}U$ (to ~0.5 ‰) among different fractions. I infer that different carbonate components of these samples have different $\delta^{238}U$ compositions, and that partial carbonate leaching leads to expression of these isotopic differences. My leaching results thus agree with Hood et al. (2016) that $\delta^{238}U$ varies among different carbonate fractions. However, the weighted sums of $\delta^{238}U$ of all leaching steps are indistinguishable to those of the bulk analysis (Table A.5), indicating that the bulk U isotopes are not typically isotopically reset. I note that this sequential

leaching protocol is very simple; a more sophisticated analysis is essential to better understand variations of $\delta^{238}U$ in carbonates. For example, further investigations need to determine what carbonate minerals or what carbonate phases have been dissolved in each leaching step.

In summary, there's no single best sample dissolution procedure. Given results from my dissolution and leaching experiments, it appears that the most critical step is to ensure complete carbonate dissolution. In this dissertation, all samples were dissolved using 1M hydrochloric acid or 1 M nitric acid. I am currently working with colleagues to test samples digestion methods using 0.125M. 0.25 M, 0.5 M, 0.75 M, 1 M, 2 M, 3 M, and 4 M hydrochloric acid and nitric acid, respectively.

1.3.2 Chemical purification and isotope measurements of U using MC-ICP-MS

In all high precision metal isotope measurements in the MC-ICP-MS, it is essential to separate the element of interest from other matrix elements to reduce the "matrix effects" that can cause isobaric interferences and complicate instrumental mass bias. The commonly used method to separate U from other matrix elements is the "UTEVA method", using an ion exchange resin (Brennecka et al., 2011; Romaniello et al., 2013; Weyer et al., 2008), which is then followed by U isotope measurements using MC-ICP-MS.

U concentration measurements and chemical purification. Digests from section 1.3.1 were centrifuged and the supernatant was separated. Major, minor, and trace element concentrations were measured on splits from each supernatant. About 500 ng of U was taken out from each supernatant to pre-cleaned Teflon beakers. Prior to column chemistry, appropriate amounts of the ^{236}U:^{233}U (IRMM-3636) double spike were added to each sample based on the amount of uranium to make a spike:sample molar ratio of ~0.0363.

The spike-sample mixtures were treated with concentrate nitric acid for 3 times and evaporated to dryness and re-dissolved in 10–30 mL 3 M HNO_3. Uranium was purified for isotopic analysis using the UTEVA method (Table 1.2; Weyer et al., 2008; Brennecka et al., 2011; Romaniello et al., 2013; Zheng F. et al., 2018 a,b,c). Purified U was dissolved in 0.32 M HNO_3 and diluted to a U concentration of 50 ppb for MC-ICP-MS analysis. Although the details of the UTEVA methods vary slight from groups to groups, the general procedures are similar.

U isotope measurements using MC-ICP-MS. Uranium isotopes were measured on a multi-collector ICP-MS (MC-ICP-MS) at low mass resolution. During measurements, ^{232}Th, ^{234}U, and ^{235}U are putting on 10^{12} amplifiers, while ^{238}U, ^{236}U, and ^{233}U are putting on 10^{11} amplifiers. The U isotope measurements use a standard-sample-standard bracketing methods. Sample $\delta^{238}U$ values were normalized by the average of the bracketing CRM145 standard. CRM145 standard shares its U-isotopic composition with another common standard CRM112a, from which it was prepared. Intercalibration of standards SRM950a and CRM145 has shown no $\delta^{238}U$ offset between them (Condon et al., 2010). Detailed analytical methods for U isotopes and the data processing have been described in many prior studies (e.g., Weyer et al., 2008; Tissot and Dauphas, 2015), which will not be repeated here.

1.4 Isotope geochemistry and marine budget of uranium

Understanding the modern marine isotopic budget of U cycle is important for the application of $\delta^{238}U$ values of sedimentary records to reconstruct redox environmental changes in the past. To date, several studies have been focused on this topic with the

purpose of quantifying the marine U mass balance in the geological history (e.g., Barnes and Cochran, 1990; Morford and Emerson, 1999; Dunk et al., 2002; Henderson and Anderson, 2003).

1.4.1 The sources

The only major source of U to the ocean is oxidative mobilization of U from the upper continental crust and transport of dissolved U(VI) to the oceans via riverine inputs (80–100%) (Figure 1.2). The estimated global riverine U flux is 42×10^6 mol yr^{-1} (Dunk et al., 2002). The average $\delta^{238}U$ of the world's major rivers is ca. –0.26 ‰ (Andersen et al., 2017), which matches the estimated average $\delta^{238}U$ of the continental crust [-0.30 ± 0.04 ‰ (2σ) (Noordmann et al., 2016); -0.31 ± 0.05 ‰ (2σ) (Tissot and Dauphas, 2015)]. An exception not included in the riverine average is the Yangtze River of China, for which two analyses of $\delta^{238}U$ have averaged ca. −0.64‰ (Andersen et al., 2016). Although these data and their ability to represent the entire Yangtze catchment need to be confirmed, this "outlier" is interpreted to reflect local U contributions from Permian-Triassic carbonates with low $\delta^{238}U$ in the lower river basin or from evaporite minerals (halite) that are abundant near its headwaters (Andersen et al., 2016). If so, this is an unusual situation because carbonates and evaporites are not major sources of U to the oceans overall. Existing data suggest that the composition of upper continental crust has not changed much since the end of Archean (Gaschnig et al., 2016; Hawkesworth and Kemp, 2006). It is therefore reasonable to assume that riverine $\delta^{238}U$ through time has been similar to the $\delta^{238}U$ of modern rivers, unless the source lithology of rivers has changed significantly (Andersen et al., 2016).

The remaining U sources to the ocean are very uncertain. These sources include groundwater discharge and atmospheric dust. The $\delta^{238}U$ of groundwater discharge is not yet known, and the atmospheric dust input likely has the same isotopic composition as the upper continental crust (e.g., Tissot and Dauphas, 2015). Nevertheless, these U sources to the ocean are likely negligible.

1.4.2 The sinks

There are multiple sinks for U in the ocean (Figure 1.2). The major sinks are sediments deposited beneath anoxic/euxinic bottom waters, sediments deposited beneath weakly oxygenated bottom waters, and marine carbonates (Dunk et al., 2002; Morford and Emerson, 1999; Tissot and Dauphas, 2015). Minor sinks include ferromanganese oxides and hydrothermal alteration of oceanic crust (Dunk et al., 2002; Morford and Emerson, 1999; Tissot and Dauphas, 2015). The largest expression of U isotope fractionation (~0.4 ‰ to ~1.2 ‰) in the marine environment occurs during U burial in anoxic/euxinic sediments, like those of the Black Sea, the Saanich Inlet, and the Framvaren Fjord (Andersen et al., 2013; Holmden et al., 2015; Kaltenbach, 2013; Rolison et al., 2017; Weyer et al., 2008). By contrast, the fractionation of U isotopes during removal to suboxic sediments is only ~0.1 ‰ based on observations from the continental margins of Peru and Washington State, where sediments underlying weakly oxygenated waters have average $\delta^{238}U$ of -0.28 ± 0.19 ‰ (Weyer et al., 2008) and -0.23 ± 0.19‰ (Andersen et al., 2016), respectively. Both natural and laboratory observations suggest at most a small offset between the $\delta^{238}U$ of primary carbonate precipitates and seawater (Andersen et al., 2014; Chen et al., 2016; Romaniello et al., 2013; Stirling et al., 2007; Weyer et al., 2008). Sedimentary carbonates may

incorporate U(IV) from sulfidic pore waters, leading to values that are 0.2–0.4 ‰ higher compared with seawater (Romaniello et al., 2013; see below). The fractionation of U isotopes during removal to Mn nodules and metalliferous sediments (–0.24 ‰) is well constrained by both natural samples (Goto et al., 2014; Wang et al., 2016) and adsorption experiments (Brennecka et al., 2011b). Seafloor alteration at high temperatures is assumed to yield no isotopic fractionation, and seafloor alteration at low temperatures is estimated to have a fractionation factor of 0.25 ‰ (Tissot and Dauphas, 2015).

The contrasting isotopic behaviors among these sinks, particularly oxic vs. anoxic, give rise to the use of U isotopes as a paleoredox proxy (Weyer et al., 2008). Based on mass balance modeling of the marine U isotope budget, seawater is expected to have lower $\delta^{238}U$ at times of expanded ocean anoxia and higher $\delta^{238}U$ at times of extensive ocean oxygenation. Such variation in seawater $\delta^{238}U$ can potentially be recorded in the sedimentary record, specifically by marine carbonates.

1.5 Uranium isotopes in marine carbonates

Most existing paleoredox proxies are essentially developed for black shales. For example, the Fe speciation, and the Fe, Mo, V, and Tl isotopes. These proxies have greatly improved our understanding of the environmental conditions during some critical periods in Earth's history. However, the distribution of black shale in the geologic record is sporadic and not continuous, leaving significant gaps in our understanding of Earth's redox history. While marine carbonates are common and would complement the black shale record nicely, there are only a few paleoredox proxies (e.g., the Ce anomalies, the I/Ca ratio, the C and S isotopes, and the chromium isotopes) that can be applied to marine carbonates and none of

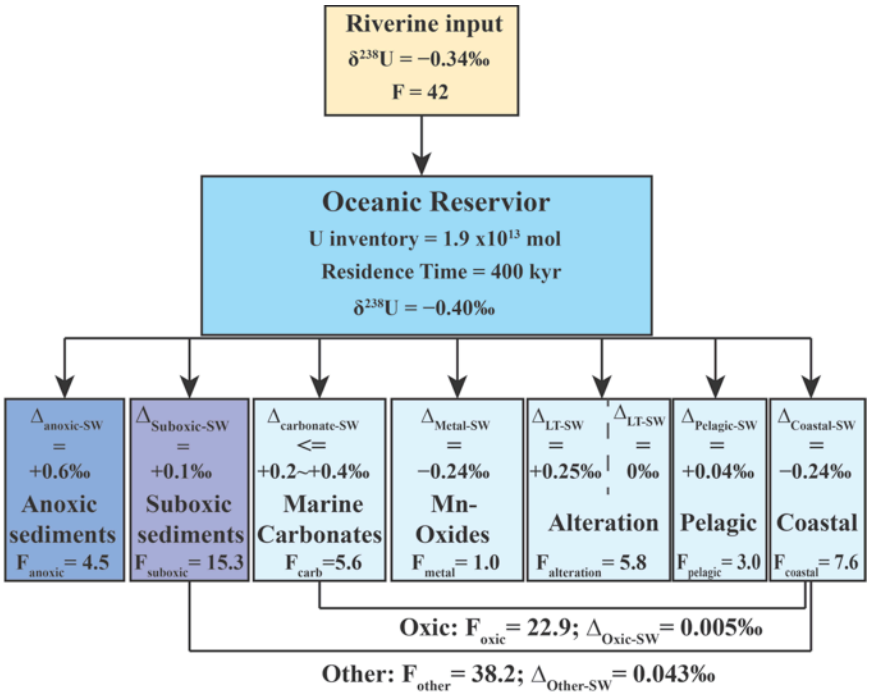

Figure 1.2 Simplified schematic representation of the major source and sinks of U in the modern ocean along with their isotopic compositions (sources) or associated isotopic fractionations (sinks) [modified after Tissot and Daup has (2015) and Wang et al. (2016)]. The $\delta^{238}U$ of riverine input was from Andersen et al. (2016). In the alteration box, LT denotes low temperature alteration, and HT denotes high temperature alteration. Sinks including suboxic, carbonates, Mn-oxides, oceanic crust alteration, pelagic clays, and coastal retention are treated as one single "other" sink, with the fractionation factors being the weighted average of these individual sinks. All flux data (F) have a unit of 10^6 mol/yr.

them could provide global marine redox information (Lu et al., 2010; Zhou et al., 2014, 2015; Frei et al., 2013; Ling et al., 2013; D'Arcy et al., 2017; Holmden et al., 2016; Gilleaudeau et al., 2016). Critically, changes in marine redox on a global scale is critical to explore the causes and consequences of major atmospheric, environmental, and

biogeochemical perturbations as well as major biological innovation and extinction events. This section presents a critical review of what we know and what don't know but need to know about the U isotope proxy in marine carbonates.

1.5.1 U isotope fractionation during incorporation into carbonates

The U isotope fractionation during incorporation into major marine carbonate minerals is relatively well constrained by laboratory abiotic precipitation experiments. Chen et al. (2006) conducted aragonite and calcite coprecipitation experiments at pH ~7.5 and ~8.5 to study possible U isotope fractionation during incorporation into these minerals. They found no resolvable U isotope fractionation in an aragonite experiment at pH ~7.5 or in calcite experiments at both pH. In contract, a small offset (< 0.13 ‰) was observed between aragonite precipitate and solution at pH ~8.5, which is likely due to isotopic fractionation among dissolved U complexes (Chen et al., 2016; Chen et al., 2017). Measurements of recent Bahamian shallow-marine carbonates (Romaniello et al., 2013) also demonstrate that primary precipitates (such as scleractinian corals, calcareous green and red algae, ooids, and mollusks) closely record seawater $\delta^{238}U$.

1.5.2 U isotope variation during dolomitization

Dolomitization is a common process throughout geological history, which is a potential concern to alter many geochemical proxies (e.g., Mn and Sr contents, $\delta^{13}C$, $\delta^{18}O$, and $^{87}Sr/^{86}Sr$) in marine carbonates, which is also a potential concern for U isotopes in marine carbonates. Stirling et al. (2007) reported low $\delta^{238}U$ values for three dolomite chimney samples. Similarly, Romaniello et al. (2013) also observed low $\delta^{238}U$ values

associated with dolomitization in one Bahamian tidal pond. There was a strong correlation with Mg/Ca ratio, suggesting that U-isotope change may have been associated with dolomitization. This seems to be a special, spatially restricted case, however, and Chen et al. (2018) revisited the dolomitization question with a larger sample set from several cores through the Bahamian carbonate platform. Their data show no statistically significant differences between calcite and dolomite, suggesting that early marine dolomitization does not have a strong effect on U-isotopes. Further confidence that dolomitization may not have been an issue for paleo-$\delta^{238}U$ records comes from a global compilation of $\delta^{238}U$ studies across the Permian-Triassic boundary. Both the dolomitized section (the Dawen section; Brennecka et al., 2011) and the non-dolomitized sections (the Kamura section, the Dajiang section, the Daxiakou section, and the Taskent section; Lau et al., 2016; Elrick et al., 2017; Zhang et al., 2018) show congruent $\delta^{238}U$ records.

These low $\delta^{238}U$ values in Bahamian dolomites might have caused by other processes rather than the dolomitization itself. For instance, in the Romaniello et al. (2013) paper, they provided an alternative that the low $\delta^{238}U$ values (−0.65 to −0.71‰) found in the dolomite-containing interval could also be explained by weathering of surrounding bedrock. The $\delta^{234}U$ values of these dolomites are characteristic of Eemian age carbonate sediments and were mostly likely deposited in a freshwater or evaporative pond well above sea level as a result of weathering that occurred during the last glacial cycle (Romaniello et al., 2013).

1.5.3 U isotope variation during diagenesis

Alteration of U isotope during diagenesis is not well known because the U isotope proxy is still a relatively young proxy and there are limited work focusing on this area. To date, the U isotope studies are looking at traditionally well-established diagenetic indictors, such as Mn and Sr contents, Mn/Sr ratios, U/Al ratios, $\delta^{18}O$, Sr/Ca ratios, Mo/U ratios, Mg/Ca molar ratios. Although the appropriability of applying these indictors to the U isotope proxy is questionable because the behavior of U might be different than that of better-studied carbonate isotope proxies during diagenesis, these proxies are still useful in that they provide information on how well are the studied carbonate rocks were preserved and what diagenesis processes might have been occurred for the studied carbonates. Some simple fluid-rock interaction models predict that bulk carbonate $\delta^{238}U$ should be less susceptible to diagenetic alteration than $\delta^{13}C$ and $\delta^{18}O$, or $^{87}Sr/^{86}Sr$ (Lau et al., 2017; Chen et al., 2018).

Romaniello et al. (2013) found that $\delta^{238}U$ in modern banktop carbonate sediments from the Bahamas are 0.2–0.4 ‰ heavier than seawater, raising concerns about diagenetic influences on the carbonate $\delta^{238}U$ records. These heavier $\delta^{238}U$ values likely reflect incorporation of ^{238}U-enriched U(IV) from anoxic porewaters during early diagenesis and/or variation in porewater U-speciation during carbonate recrystallization (Chen et al., 2016; Romaniello et al., 2013). Measurements of $\delta^{238}U$ in deep Bahamian drillcores (Clino, Unda, and IODP Core 1006) extending to the upper Miocene have yielded a similar normal distribution with a mean and standard deviation of 0.27±0.14 ‰ (Chen et al., 2018), which is close to the average for bank-top carbonates (Romaniello et al., 2013). The similarity between unconsolidated banktop and slope drill core samples suggests that diagenesis of

$\delta^{238}U$ in these carbonates is primarily syndepositional and is a rapid process occurring during early burial. Syndepositional diagenesis of carbonates occurs because shallow, relatively permeable carbonates can sequester dissolved U(VI) from the overlying oxic water via advective and diffusive transport. This semi-open system behavior provides for the exchange of U isotopes and allows the bulk carbonates to become slightly enriched in ^{238}U. However, this process does not operate at greater burial depths, as the mobility of U is severely restricted in anoxic porewaters, as shown by near-zero porewater U concentrations in deep Bahamian drillcores (Henderson et al., 1999).

Similarly, a recent study of Cryogenian carbonates by Hood et al. (2016) revealed considerable $\delta^{238}U$ variation among components in a single sample. They measured texture-specific $\delta^{238}U$ values from a Cryogenian (Balcanoona) reef complex in South Australia and found high variability in $\delta^{238}U$ values between different carbonate components, even within a single sample. Such variation likely reflects small-scale (mm-cm) redistribution of U isotopes during carbonate diagenesis and recrystallization, rather than large-scale resetting of bulk carbonate $\delta^{238}U$. To test this hypothesis, I conducted leaching experiments on both modern and PTB carbonates (Table A.5). In agreement with Hood et al. (2016), they reveal large variability in $\delta^{238}U$ (up to 0.5 ‰) for successive leaching steps, suggesting that $\delta^{238}U$ is inhomogeneous among different carbonate components. Despite this heterogeneity, bulk carbonate $\delta^{238}U$ measurements yield coherent stratigraphic trends that are reproducible in both modern bank-top carbonates and widely separated PTB sections, suggesting that such component-specific variation generally does not compromise primary bulk-carbonate $\delta^{238}U$ signals.

In summary, both modern and ancient $\delta^{238}U$ studies demonstrate that when using large, high-resolution stratigraphic data to average out diagenetically-induced noise and when properly considering the syndepositonal diagenetic offset and screening for diagenesis, U isotopes in marine carbonate provide a powerful way to reconstruct marine redox conditions on a global scale (e.g., Brennecka et al., 2011; Romaniello et al., 2013; Dahl et al., 2014; Lau et al., 2016, 2017; Chen et al., 2016, 2018; Elrick et al., 2016; Jost et al., 2017; Bartlett et al., 2018; Clarkson et al., 2018; Zhang F. et al., 2018 a,b,c).

1.6 U isotope mass balance modeling calculation

One of the key advantages of U isotopes over other paleoredox proxies is that the U isotope system can provide quantitative estimates of the extent of global marine redox changes. This is because variations in seawater $\delta^{238}U$ are sensitive to the proportion of U removal into different sedimentary sinks, which are redox controlled.

1.6.1 Basic mass and isotopic balance equations

The rate of change of seawater uranium inventory and its isotopic composition can be described by differential mass balance equations (following Lau et al. (2016), Wang et al. (2016), and Zhang F. et al. (2018)):

$$\frac{dN_{sw}}{dt} = J_{riv} - J_{oxic} - J_{anox} \qquad \text{Eq. 1}$$

$$\frac{d(N_{sw} \cdot \delta^{238}U_{sw})}{dt} = J_{riv} \cdot \delta^{238}U_{riv} - J_{oxic} \cdot \delta^{238}U_{oxic} - J_{anox} \cdot \delta^{238}U_{anox} \qquad \text{Eq. 2}$$

$$\delta^{238}U_{anox} = \delta^{238}U_{sw} + \Delta_{anox} \qquad \text{Eq. 3}$$

$$\delta^{238}U_{oxic} = \delta^{238}U_{sw} + \Delta_{oxic} \quad \text{Eq. 4}$$

where N_{sw} is the seawater uranium inventory in moles, $\delta^{238}U_{sw}$, $\delta^{238}U_{riv}$, and $\delta^{238}U_{anox}$ are the values of seawater, the riverine source, and the anoxic sedimentary sinks, respectively, and $\delta^{238}U_{oxic}$ is average U isotope composition of the remaining other sinks. Here, we simplify the inputs to J_{riv}, the riverine flux, whose modern value is ~4×10^7 moles U/yr. The outputs are assumed to consist of the anoxic sediment sink (J_{anox}) and the sum of the other sinks (J_{oxic}). In this model, we use the estimate of 0.6×10^7 moles U/yr for J_{anox} and calculate J_{oxic} by mass balance to an initial steady-state value of 3.4×10^7 moles U/yr. Δ_{anox} = +0.6 ‰ is the effective fractionation factor associated with anoxic sediment deposition, and Δ_{oxic} is the effective fractionation factor associated with the remaining other sinks (+0.005 ‰, calculated to maintain isotopic steady state in the modern ocean (e.g., Brennecka et al., 2011; Wang et al. 2016).

We define the oxic and anoxic sinks in Eqs. 1–4 assuming a first-order dependence on seawater U concentration:

$$J_{anox} = k_{anox} \cdot N_{sw} \cdot A_{anox} \quad \text{Eq. 5}$$

$$J_{oxic} = k_{oxic} \cdot N_{sw} \cdot A_{oxic} \quad \text{Eq. 6}$$

where A_{anox} and A_{oxic} are the total seafloor area overlain by anoxia waters and the total seafloor area overlain by non-anoxic waters, respectively, and k_{anox} and k_{other} are rate constants associated with anoxic sediment deposition and all other sediment deposition and are calculated for the modern uranium system.

1.6.1 Steady state solution

A steady state solution applies when dealing with a time window that is significantly longer than the residence time of U in the ocean.

At steady state, the sum of all inputs and outputs of U to seawater are equal, and thus the inventory and $\delta^{238}U$ of seawater through time is constant. In this case, rewriting equations 1 and 2, we have:

$$J_{riv} - J_{oxic} - J_{anox} = 0 \quad \text{Eq. 7}$$

$$J_{riv} \cdot \delta^{238}U_{riv} - J_{oxic} \cdot \delta^{238}U_{oxic} - J_{anox} \cdot \delta^{238}U_{anox} = 0 \quad \text{Eq. 8}$$

Rearrange Eqs. 7 and 8, we have

$$J_{riv} = J_{oxic} + J_{anox} \quad \text{Eq. 9}$$

$$J_{riv} \cdot \delta^{238}U_{riv} = J_{oxic} \cdot \delta^{238}U_{oxic} + J_{anox} \cdot \delta^{238}U_{anox} \quad \text{Eq. 10}$$

We define a term f_{anox}, the total fraction of U removal to anoxic sedimentary sinks:

$$f_{anox} = \frac{J_{anox}}{J_{riv}} \quad \text{Eq. 11}$$

Putting Eqs. 3–4 and Eqs. 11 to Eqs. 9–10 and solving Eqs. 9–10, we have

$$f_{anox} = \frac{\delta^{238}U_{riv} - \delta^{238}U_{sw} - \delta^{238}U_{oxic}}{\Delta_{anox} - \Delta_{oxic}} \quad \text{Eq. 12}$$

We also define a term $f_{AnoxArea}$, the total fraction of seafloor area overlain by anoxic waters:

$$f_{AnoxArea} = \frac{A_{anox}}{A_{ocean}} \quad \text{Eq. 13}$$

where A_{ocean} is the total seafloor area of the ocean. Putting Eqs. 3–6 and Eqs. 13–14 to Eqs. 9–10 and solving Eqs. 9–10, we have

$$f_{AnoxArea} = \frac{f_{anox} \cdot k_{oxic}}{(k_{anox} + f_{anox} \cdot k_{oxic} - f_{anox} \cdot k_{anox})} \quad \text{Eq. 14}$$

Eq. 14 can also be rewritten as:

$$\delta^{238}U_{sw} = \delta^{238}U_{input} - \frac{f_{AnoxArea} \cdot k_{anox} \cdot \Delta_{anox} + (1 - f_{AnoxArea}) \cdot k_{oxic} \cdot \Delta_{oxic}}{f_{AnoxArea} \cdot k_{anox} + (1 - f_{AnoxArea}) \cdot k_{oxic}} \quad \text{Eq. 15}$$

Eq. 15 will be useful to explore how $\delta^{238}U$ of seawater changes with expanding anoxic seafloor area. When looking at a specific sink, the lumped oxic sedimentary sink can be expanded to multiple other sinks, for instance, suboxic sinks and metal oxide sinks.

1.6.2 Non-steady (dynamic) state solution

A dynamic situation applies when dealing with a relatively short time window. For example, when exploring the detailed timing of onset, duration, and extent of marine anoxia during the Permian-Triassic mass extinction interval (Lau et al., 2016; Zhang F. et al., 2018a).

Eq. 2 can be simplified to give an expression for the changing isotope composition:

$$\frac{d(\delta^{238}U_{sw})}{dt} = \frac{J_{riv} \cdot (\delta^{238}U_{riv} - \delta^{238}U_{sw}) - J_{oxic} \cdot \Delta_{oxic} - J_{anox} \cdot \Delta_{anox}}{N_{sw}} \quad \text{Eq. 16}$$

Eq. 16 can be integrated using first-order Euler integration by giving some initial conditions. Before numerical integration, it is essential to smooth the data to eliminate the nosy associated with diagenetic influences.

1.6.3 Modeling uncertainties

The U isotope mass balance modeling outputs depend heavily on several parameters, some of which are not well constrained due to limited modern observations. Major uncertainties include:

(1) The diagenetic correction factors. Studies of modern Bahamian carbonate sediments suggest that carbonate sediments record $\delta^{238}U$ of seawater that are 0.2 to 0.4 ‰ higher than seawater with an average of 0.27±0.14 ‰ (1SD). This provides a range of correction when study carbonates in geological records. Given the relatively small natural range of variation of $\delta^{238}U$, this uncertainty of diagenetic correction factor will have large effects on U isotope mass balance modeling outputs.

(2) The U isotope fractionation factor between seawater and each sedimentary sink. The isotopic fractionation factor between seawater and anoxic sedimentary sinks is not well constrained because of limited observations from analogy modern environments. Current observations suggest that the Δ_{anox} values can vary from 0.4 ‰ to 1.3 ‰, although the relative open ocean environment might be characterized by 0.6 ‰ to 0.85 ‰. As shows in Eqs. 15 and 16, the Δ_{anox} has large influence on the modeling outputs.

(3) The age models. In the dynamic solution, the U isotope mass balance model depends strongly on the rate of $\delta^{238}U$ change. Although there are often good ages for a study section, from geochronology or biostratigraphy, getting the relative timing of samples along a setion–key to get the rate of change of $\delta^{238}U$–is difficult because it is necessary to extrapolate from the horizon that is precisely dated by making assumptions about sedimention rate. Most studies use a relatively simple approach that assumes constant sedimentation rates to estimate ages of individual samples, this is a potential source of

uncertainties during U isotope mass balance modeling, which may result in large differences in modeling outputs.

(4) The removal rate constants of U into different sedimentary sinks. These rate constants are typically calculated based on sediment trap experiments. However, there are only a few U sediment trap experiments in the modern marine environments.

(5) The data smoothing. When calculating $f_{AnoxArea}$ in a dynamic situation, the smoothing methods have large influence on the rate of $\delta^{238}U$ change. The most widely used sedimentary geochemical data smoothing method is the LOWESS function. It is always a challenge to determine what span should be used when smoothing the geochemical data.

Minor uncertainties include:

(1) Analytical uncertainties. The current uncertainties of U isotope measurements using MC-ICP-MS is between 0.02‰ and 0.1 ‰.

(2) The U isotope compositions of riverine inputs. The only major source of U to the ocean is oxidative mobilization of U from the upper continental crust and transport of dissolved U(VI) to the oceans via riverine inputs. Existing data suggest that the U-isotopic composition of upper continental crust has not changed much since the end of Archean (Hawkesworth and Kemp, 2006; Gaschnig et al., 2016; Tang et al., 2016). It is therefore reasonable to assume that riverine $\delta^{238}U$ through time has been similar to the $\delta^{238}U$ of modern rivers. However, in a short time scale, the riverine input may have shifted in association with some extremely climatic events, which may have temporarily shifted the dominant weathering lithology from the modern distribution.

In summary, the exact mechanisms controlling U isotopic shifts in different marine environments need to be clearly addressed in order to advance our estimation of marine redox changes using the U isotope proxy. These include:

(1) The isotopic fractionation during U removal into euxinic sinks. It is interesting that laboratory experiments suggest that the U isotope fractionation factor during U(VI) can be as large as 1.0–1.2‰. However, in modern anoxic basins, such as the Black Sea and the Saanich Inlet, the U observed U isotope fractionation factor is between 0.4‰ and 0.8‰. These fractionation factors are interpreted to reflect diffusion-limited U reduction below the sediment-water interface, which reduces the magnitude of the apparent isotopic fractionation factor by ~50%. However, the exact cause needs to be clear in future studies.

(2) The U isotopic fractionation during removal into suboxic sinks. Limited observations from the continental margins of Peru and Washington State suggest the U removal into anoxic sinks is only associated with a small isotopic fractionation factor (~0.1‰), the reason which remains unknown and needs to be further investigated.

(3) The U isotope fractionation under ferruginous conditions is poorly constrained. Ferruginous conditions might have been a common feature in geological history. A prior study argues that U isotope fractionation may be similar in euxinic and ferruginous settings (Yang et al., 2017). While another study argues that the fractionation factor associated with U removal to ferruginous sediments is close to 0 ‰ (Hood et al., 2016). Further studies are needed to confirm the fractionation factor for ferruginous environments.

1.7 U concentrations and Th/U ratios in marine carbonates

The U concentrations and the Th/U ratios, in addition to the $\delta^{238}U$ proxy, in marine carboantes have widely been used as an indictor for marine redox conditions (e.g., Wignall and Twitchett, 1996; Chun et al., 2010; Brennecka, et al., 2011; Lau et al., 2016, 2017). In unaltered marine carbonates, U concentrations and Th/U ratios may reflect changes to the extent of global seafloor oxygenation and the rate of U removal to the sediment (Brennecka et al., 2011a; Elrick et al., 2017; Lau et al., 2016). Under ideal conditions, stratigraphic variations in U concentrations can record meaningful seawater redox variations, but this relationship can be easily masked by other sources of variation. The U concentration of sedimentary carbonates strongly depends on the mineral phases present and the diagenetic history of the sediment. For example, the distribution coefficient of U into aragonite is significant larger than for calcite. An experimental study showed that the partition coefficient for U in aragonite ranges from 1.8 to 9.8 whereas that for U in calcite is <0.2 and may be as low as 0.046 (Meece and Benninger, 1993). Thus, environmental and ecological changes that drive variations in the abundance of primary aragonite and calcite will have a large effect on sediment U concentrations, resulting in much higher U concentrations in aragonitic sediments (up to tens of ppm) than in calcitic sediments (Kelly et al., 2003; Kelly et al., 2006; Reeder et al., 2000). Th/U ratios are potentially influenced by environmental factors other than redox conditions or by the presence of high-Th minerals.

In contrast to their effects on U concentrations and Th/U ratios, carbonate mineralogy and carbonate ion concentrations have only limited effects on sediment $\delta^{238}U$. Uranium isotope measurements of aragonite and high-Mg calcite primary precipitates

exhibit no offset from seawater (Romaniello et al., 2013), and experimentally precipitated calcite and aragonite showed only minor fractionation (<0.13 ‰) between the liquid medium and the solid (Chen et al., 2016). Thus, variations in carbonate mineralogy can result in large differences in U concentrations but only small changes in U-isotopic composition. This has well been demonstrated by carbonates from Permian-Triassic boundary sections, as shown by a compilation of data for Kamura (Japan), Dawen and Dajiang (South China), Taskent (Turkey), and Zal (Iran) (Elrick et al., 2017; Lau et al., 2016; Zhang et al., 2018a; Zhang et al., 2018b). All of these sections show an obvious negative shift in $\delta^{238}U$ at the Permian-Triassic boundary, even though they yield rather variable U concentrations and Th/U ratios.

In view of these considerations, we focus in this dissertation on analysis of paleoredox patterns based on $\delta^{238}U$ data, not Th/U. We recommend that future studies make use primarily of U isotopes rather than U concentrations and Th/U ratios in carbonates for the purpose of paleo-redox interpretations. If such data (i.e., U concentrations and Th/U ratios) are used for paleo-redox analysis, then it is essential that changes in carbonate mineralogy are examined in order to preclude potential misinterpretations of paleo-redox patterns.

Table 1.1 A summary of digestion methods for carbonate U isotope analysis.

Authors/Research groups	Acid and molarity
Stirling et al., (2007, 2015)	diluted nitric acid
Weyer et al., (2008)	2% hydrochloric acid
Brennecka et al., (2011)	Diluted (~1M) hydrochloric acid
Romaniello et al., (2013)	3M nitric acid
Andersen et al., (2014)	diluted nitric acid
Dhal et al., (2014, 2017)	>1M hydrochloric acid
Lau et al., (2016,2017)	1M hydrochloric acid, 0.25M hydrochloric acid
Song et al., (2017)	1M nitric acid
Elrick et al., (2017)	2M hydrochloric acid
Jost et al., (2017)	0.25M hydrochloric acid
Zhang-F et al., (2018a)	1M hydrochloric acid, 1 M acetic acid, 3 M nitric acid
Zhang-F et al., (2018b)	1M hydrochloric acid
Wei et al., (2018)	1M hydrochloric acid
Bartlett et al., (2018)	1M acetic acid

Table 1.2 A summary of U purification method using UTEVA resin.

Steps	details
1	set 1.0–1.2 mL of UTEVA resin in BioRad columns and wash 6 × 2.5 mL of 0.05 M HCl
2	condition column with 3 × 2.5 ml of 3 M HNO_3
3	load samples on column dissolved in 10–30 mL of 3 M HNO_3
4	rinse with 5 × 3 mL 3M HNO_3 to get rid of everything but U and Th
5	add 3 × 2 mL 10M HCl to convert the column to chloride form
6	rinse column with 3 × 2 mL mix of 5M HCl and 0.05M oxalic acid to remove Th
7	rinse with 3 × 2 mL 5M HCl to remove oxalic acid
8	elute U with 2 + 2 +2 + 3 + 4 ml of 0.05 M HCl

CHAPTER 2

CONGRUENT PERMIAN-TRIASSIC $\delta^{238}U$ RECORDS AT PANTHALASSIC AND TETHYAN SITES: CONFIRMATION OF GLOBAL-OCEAN ANOXIA AND VALIDATION OF THE U-ISOTOPE PALEOREDOX PROXY

This chapter has been published in *Geology*:

Zhang F., Algeo T.J., Romaniello S.J., Zhao L., Chen Z.-Q., Cui Y., Anbar A.D., 2018. Congruent Permian-Triassic $\delta^{238}U$ records at Panthalassic and Tethyan sites: confirmation of global-oceanic anoxia and validation of the U-isotope paleoredox proxy. Geology 46 (4): 327-330, doi: https://doi.org/10.1130/G39695.1.

This chapter includes a supplementary material that is presented in *APPENDIX A*.

2.1 Introduction

The existence of oceanic anoxia during the Permian-Triassic Boundary (PTB) crisis, the most severe biotic crisis in Earth history due to its ~90 % species-level mortality rate, was inferred by previous studies on the basis of petrographic, geochemical, and biomarker data (Grice et al., 2005; Isozaki, 1997; Meyer et al., 2008; Wignall and Twitchett, 1996). However, reliance on local redox proxies has resulted in divergent views regarding the timing, extent, and intensity of oceanic anoxia that remain unresolved to date. For example, the onset of anoxia was inferred to be several million years before the EPME in some studies (Isozaki, 1997; Wignall and Twitchett, 1996) but no more than ~100 kyr prior to

the EPME in others (Algeo et al., 2012; Shen et al., 2012), and different studies have argued both for (Grice et al., 2005) and against (Loope et al., 2013) the presence of anoxia in shallow-marine facies. Recent work favors a more complex scenario, characterized by widespread expansion of anoxia at intermediate depths (~200-1000 m) prior to the EPME (Winguth and Winguth, 2012; Feng and Algeo, 2014) followed by episodic upward chemocline excursions into the ocean-surface layer commencing at the EPME (Algeo et al., 2008).

The recent development of U isotopes ($\delta^{238}U$) in marine carbonates as a globally-integrative paleoredox proxy has provided new insights into this problem. Three recent studies of Permian-Triassic boundary (PTB) sections document a large (0.4–0.5 ‰) negative $\delta^{238}U$ excursion, suggesting a close relationship between ocean-redox changes and the EPME (Brennecka et al., 2011; Elrick et al., 2017; Lau et al., 2016). However, the reliability and global significance of these records have been challenged on the basis of two issues: (1) potential influences of diagenetic alteration on bulk carbonate $\delta^{238}U$ records (Hood et al., 2016; Romaniello et al., 2013), and (2) geographic limitation of existing U-isotope studies of the PTB to the Tethys Ocean, which represented only ~10–15 % of contemporaneous global-ocean area. Thus, despite the congruency of previously published Tethyan $\delta^{238}U$ records, an independent test of U-isotopes from a Panthalassic section with a dissimilar diagenetic history is needed to verify oceanic redox changes during the Permian-Triassic transition. Here, we report the first Permian-Triassic carbonate $\delta^{238}U$ record from an open Panthalassic Ocean site (Kamura, Japan), evaluate its redox implications relative to existing Tethyan $\delta^{238}U$ records, and address concerns about preservation of marine $\delta^{238}U$ signals by bulk carbonate sediments.

2.2 Uranium isotope system

The power of U isotopes as a global-ocean redox proxy derives from the long residence time (~500 kyr for the modern; Dunk et al., 2002) and well-mixed character of U in seawater. Seawater $\delta^{238}U$ responds to redox changes because reduction of dissolved U(VI) to U(IV), which is rapidly removed to anoxic sediments, results in a detectable fractionation of U isotopes (Stylo et al., 2015), sequestering heavy isotopes in the reduced species (Andersen et al., 2014). Thus, the $\delta^{238}U$ of U(VI) dissolved in seawater decreases as the areal extent of bottom-water anoxia increases (Brennecka et al., 2011), providing a direct proxy of global-ocean redox changes. Marine carbonate sediments have been demonstrated to record the $\delta^{238}U$ of seawater, subject to a 0.2–0.4 ‰ (average ~0.3 ‰) offset during early diagenesis (Romaniello et al., 2013). After correction for this diagenetic effect, variations of $\delta^{238}U$ in ancient marine carbonates can be used to reconstruct secular variation in global-ocean redox conditions (Brennecka et al., 2011; Dahl et al., 2017; Elrick et al., 2017; Lau et al., 2016; Romaniello et al., 2013).

2.3 Geological background

The Kamura section (32.7552 ºN, 131.3386 ºE), located in the Chichibu Belt of Kyushu Island in southern Japan, is a carbonate succession deposited on a shallow atoll in the mid-Panthalassic Ocean at peri-equatorial latitudes during the Late Permian to Late Triassic (Figure 2.1A). The Upper Permian Mitai Formation and uppermost Permian-Lower Triassic Kamura Formation consist of light-gray limestone and dolomitic limestone (Figure 2.1B). The lack of terrigenous clastics in these limestones is consistent with a mid-oceanic setting remote from continental areas (Musashi et al., 2001). This section is

important because it is one of very few surviving shallow-marine deposits from the Panthalassic Ocean and provides an important window into open ocean environmental conditions in the largest Permian-Triassic ocean basin. The carbon isotope stratigraphy and conodont biostratigraphy of Kamura were recently updated by Zhang et al. (2017b), providing a high-resolution temporal framework that allows precise correlation to the Meishan GSSP and to previously published Tethyan $\delta^{238}U$ records. The EPME and PTB at Kamura are defined by a negative $\delta^{13}C$ excursion and by the first appearance of the conodont *Hindeodus parvus*, respectively (Zhang et al., 2017b). Sixteen samples from the Kamura section were analyzed for $\delta^{238}U$ and major and trace elements in this study. Expanded discussions of the geological background and analytical methods are given in the *APPENDIX A*.

2.4 Results and evaluation of carbonate diagenesis

The analytical results have been summarized in Table 2.1. The EPME at Kamura is characterized by a negative carbon isotope excursion (from +1.31 ‰ to −0.21 ‰; Figure 2.1B) that is recognized globally in almost all PTB sections. Our $\delta^{238}U$ record shows relatively higher $\delta^{238}U$ values in the pre-EPME Upper Permian, with two samples yielding values of −0.32 ‰ and −0.41 ‰. $\delta^{238}U$ shifts rapidly across the EPME toward values as low as −0.78 ‰, with a minimum ~0.5 m above the PTB. The negative shifts of $\delta^{238}U$ and $\delta^{13}C$ are positively correlated (Table 2.2; $R^2 = 0.50$, $p < 0.01$). The trace element

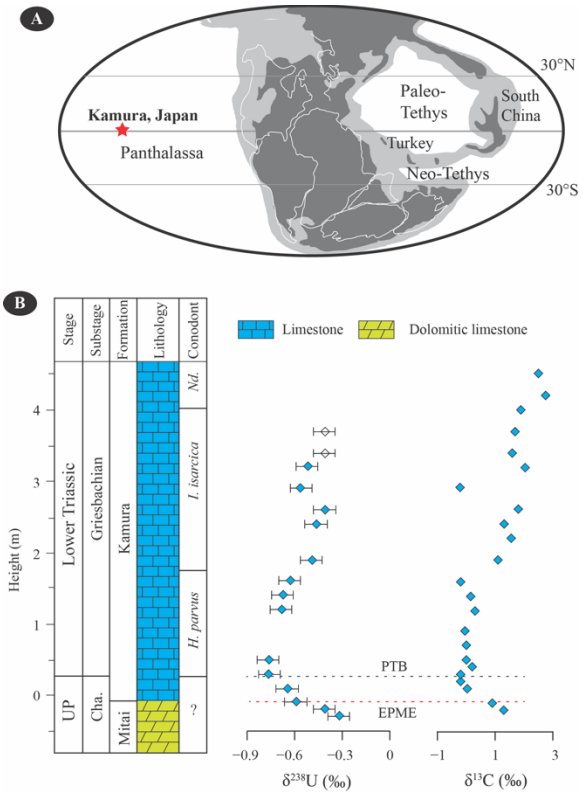

Figure 2.1 (A) Latest Permian paleogeography with location of Kamura section (Japan). (B) $\delta^{238}U$ profile and $\delta^{13}C$ profile for the Kamura section. $\delta^{13}C$ profile and conodont data are from Zhang et al. (2017b). The two open diamonds at the top of the record denote sample with Mn/Sr ratios > 1 and have been excluded the discussions of the main text. SC: South China; UP: Upper Permian; Cha.: Changhsingian; *Nd.*: *Ns. Dieneri*.

compositions (Al, Mn, Sr) and elemental ratios (Mn/Sr, Rb/Sr, U/Al) of most of the study samples are consistent with well-preserved marine carbonate with little influence from detrital siliciclastics (see *APPENDIX A*). Fourteen of 16 study samples exhibit Mn/Sr < 1, a conservative threshold for diagenetic alteration (cf. Lau et al., 2016). It is worth noting that the two samples with elevated Mn/Sr ratios (7.6, 4.4) show no deviation from the

overall $\delta^{238}U$ trend, suggesting that the U-isotope system may be robust even in moderately altered carbonate samples (Figure 2.1B).

2.5 Comparison of Permian-Triassic $\delta^{238}U$ records at Panthalassic and Tethyan sites

The Kamura $\delta^{238}U$ record exhibits a negative excursion through the EPME interval that is essentially identical both in timing and magnitude to those reported for the coeval Dawen, Dajiang, and Daxiakou sections in South China and the Taşkent section in Turkey (Brennecka et al., 2011a; Elrick et al., 2017; Lau et al., 2016) (Figure 2.2). The correlated sections show excellent agreement with clear evidence for elevated $\delta^{238}U$ (−0.2 to +0.1 ‰) prior to the EPME (251.94 Ma) and a sharp drop to low $\delta^{238}U$ (−0.6 to −0.8 ‰) in the earliest Triassic (Figure 2.2A-B). The nearly identical $\delta^{238}U$ trends among these five sections are especially significant in view of their vastly different burial histories. The Kamura section was obducted as part of an accretionary complex in the Middle Jurassic to Early Cretaceous, undergoing greenschist-grade metamorphism at that time (Isozaki, 2009). In contrast, the four Tethyan sections accumulated in stable cratonic settings and mostly experienced milder burial effects. The fact that five sections with dissimilar diagenetic histories (Table 2.2) from two ocean basins yield the same $\delta^{238}U$ trend argues strongly against any explanation other than a primary signal (see *APPENDIX A*). The present study represents, to the best of our knowledge, the first empirical test of the coherence of a non-traditional isotope paleoredox proxy across multiple, globally distributed sections in the ancient geologic record. The Kamura record thus confirms that the previously reported $\delta^{238}U$ trends represent a global signal, and that the end-Permian oceanic anoxic event was not just a Tethyan but a global event.

The negative shift in $\delta^{238}U$ of 0.4–0.5 ‰ across the EPME horizon is most readily interpreted as an increase in the global flux of isotopically heavy U into anoxic facies, suggesting an expanded area of seafloor anoxia in conjunction with the EPME event. We used a U-isotope mass balance model similar to that of Brennecka et al. (2011a) to assess the implications of this U isotope shift for global-ocean redox conditions. Modeling results indicate that 0–26 % of seawater U was removed to anoxic facies prior to the EPME (Figure 2.2C), which is similar to the estimate of 12–25 % for the modern ocean (Dunk et al., 2002).

Following the EPME, modeling suggests that anoxic sinks were responsible for nearly 100% of the U removal to sediments. A LOWESS smoothing of the combined $\delta^{238}U$ dataset suggests that the negative shift in $\delta^{238}U$ began $\leq$70 kyr before the EPME (see *APPENDIX A*). This estimate is similar to those of other studies identifying a pre-EPME disturbance (Algeo and Twitchett, 2010; Shen et al., 2012b; Winguth and Winguth, 2012). The LOWESS curve also shows that the shift toward more negative $\delta^{238}U$ values was most rapid almost exactly at the EPME horizon. This temporal correspondence of rapid expansion of oceanic anoxia with the EPME strongly suggests that anoxia was a significant cause of mass mortality. Potentially, widespread expansion of anoxia enhanced global sulfate reduction rates, allowing buildup of H_2S in the oceanic thermocline region, setting the stage for upward chemocline excursions into the ocean-surface layer (Algeo and Twitchett, 2010; Shen et al., 2012b; Winguth and Winguth, 2012). Evidence of sulfidic conditions in latest Permian oceans is present in both Panthalassic (Zhang et al., 2017a) and Tethyan sections (Grice et al., 2005; Schobben et al., 2015).

Oceanic anoxia may have increased due to elevated atmospheric pCO_2 and associated extreme global warming triggered by greenhouse gas emissions of the Siberian

Traps Large Igneous Province (Joachimski et al., 2012). Warming, in turn, diminished thermohaline circulation and oxygen solubility (Bond and Wignall, 2014; Joachimski et al., 2012). Climatic warming also enhanced continental weathering rates (e.g., a ~4× to 16× increase across the EPME; Schobben et al., 2015) and riverine nutrient fluxes that may have locally stimulated marine productivity. Diminished thermohaline circulation and elevated seawater nutrient levels were primary factors in the development of widespread oceanic anoxia (Meyer et al., 2008; Schobben et al., 2015).

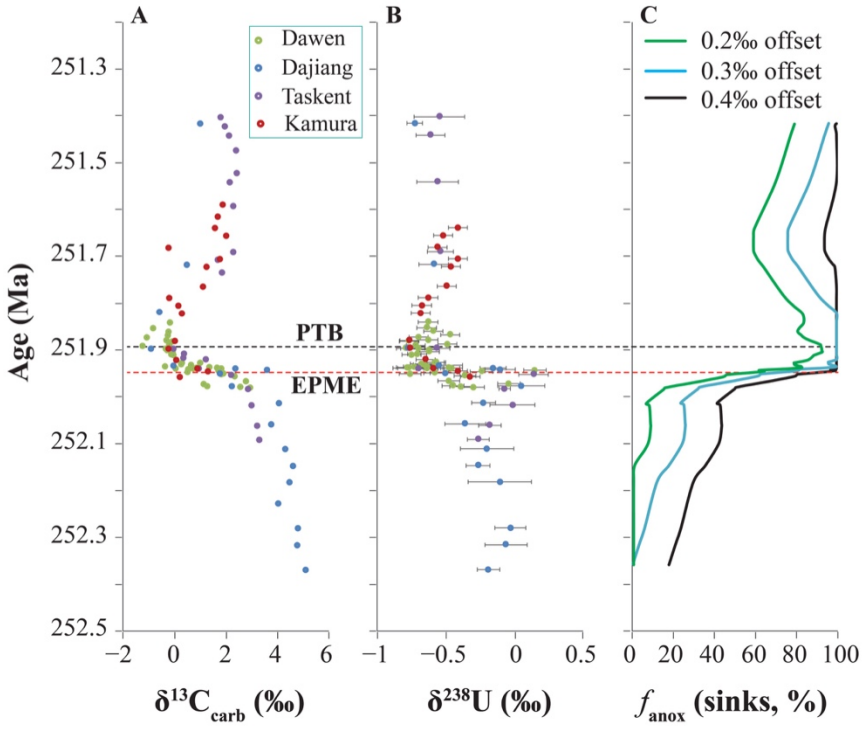

Figure 2.2 (A): A global compilation of $\delta^{13}C$ data across the Permian-Triassic boundary. (B): A global compilation of $\delta^{238}U$ data from measurements across the Permian-Triassic boundary. (C) Mass balance calculation of the fraction of U removal into anoxic sinks associated with diagenetic offsets ranging from 0.1 ‰ to 0.3 ‰. $\delta^{238}U$ and $\delta^{13}C$ data of the Dawen section are from Brennecka et al. (2011a), and $\delta^{238}U$ and $\delta^{13}C$ data of the Dajiang

section and the Taşkent Section are from Lau et al. (2016). The age model used in the compilation is from Burgess et al. (2014). Temporal correlations among sections are based on carbon isotopes, the PTB horizon, and the EPME horizon.

2.6 Robustness of primary $\delta^{238}U$ signal in bulk carbonates

Strong agreement of U isotope trends between multiple, widely separated sections provides a critical demonstration of the reliability of U isotopes in carbonates as a recorder of global-ocean redox conditions. Below we reconcile these observations and conclusions with recent work that raised concerns about the influence of diagenetic alteration on the reliability of $\delta^{238}U$ records in carbonate sediments (Romaniello et al., 2013; Hood et al., 2016).

Romaniello et al. (2013) observed a $\delta^{238}U$ offset of 0.2–0.4 ‰ between modern seawater and Bahamian bank-top carbonates, first raising concerns about burial diagenesis. In the modern Bahamas, all bank-top carbonate sediments have a $\delta^{238}U$ composition that is 0.2–0.4 ‰ heavier than that of modern seawater (Romaniello et al., 2013), which likely reflects incorporation of ^{238}U-enriched U(IV) from anoxic porewaters during early diagenesis and/or variation in porewater U-speciation during carbonate recrystallization (Chen et al., 2016). However, this process is likely to be self-limiting: sediments just below the sediment-water interface can sequester dissolved U(VI) from overlying oxic waters via advective and diffusive transport, leading to limited ^{238}U enrichment, but this process does not operate at depth owing to the restricted mobility of U in anoxic porewaters, as shown by near-zero porewater U concentrations in deep Bahamian drillcores (Henderson et al., 1999). Closure of sediment porewaters to U isotope exchange with increasing burial locks

in the early diagenetic offset of 0.2–0.4 ‰ in bulk-carbonate $\delta^{238}U$, with no subsequent effects linked to burial diagenesis. The similarity of $\delta^{238}U$ values in multiple PTB sections (Brennecka et al., 2011a; Elrick et al., 2017; Lau et al., 2016) is consistent with a nearly uniform diagenetic offset.

Dolomitization is another possible influence on bulk-carbonate U-isotope compositions. Extensive dolomitization of carbonate sediments perturbs many isotopic systems (e.g., C, O, Ca, and Sr; and empirical data shows $\delta^{238}U$ changes linked to supratidal dolomitization in a Bahamian tidal pond; Romaniello et al., 2013). On this basis, Romaniello et al. (2013) raised concerns that strong (30-50 %) dolomitization might have compromised the $\delta^{238}U$ record of the Dawen PTB section (Brennecka et al., 2011a). However, subsequent work, as well as results from this study, documented nearly identical $\delta^{238}U$ shifts in non-dolomitized marine carbonate sections (Elrick et al., 2017; Lau et al., 2016), suggesting that the primary $\delta^{238}U$ records at Dawen and Kamura were preserved despite extensive dolomitization. Bulk resetting of $\delta^{238}U$ in carbonates may be restricted to relatively oxidizing subaerial and supratidal environments and/or late-stage diagenetic settings in which basinal fluids carry sufficient dissolved U(VI) to influence bulk carbonate compositions.

One further concern is that burial diagenesis may lead to alteration of primary $\delta^{238}U$ signals through redistribution of U during dissolution-reprecipitation reactions. A recent study of Cryogenian carbonates revealed considerable $\delta^{238}U$ variation among components in a single sample (Hood et al., 2016). Such variation likely reflects small-scale (mm-cm) redistribution of U isotopes during carbonate diagenesis and recrystallization, rather than large-scale resetting of bulk carbonate $\delta^{238}U$. To test this hypothesis, we conducted

leaching experiments on both modern and PTB carbonates (see *APPENDIX A*). In agreement with Hood et al. (2016), our results reveal large variability in $\delta^{238}U$ (up to 0.5 ‰) for successive leaching steps, suggesting that $\delta^{238}U$ is inhomogeneous among different carbonate components. Despite this heterogeneity, bulk carbonate $\delta^{238}U$ measurements yield coherent stratigraphic trends that are reproducible in both modern bank-top carbonates and widely separated PTB sections, suggesting that such component-specific variation generally does not compromise primary bulk-carbonate $\delta^{238}U$ signals. Thus, our experimental results also support the robustness of the carbonate U-isotope proxy for paleoredox analysis.

2.7 Conclusions

Our new $\delta^{238}U$ profile from Kamura, Japan confirms that $\delta^{238}U$ records in sections from the Tethys and Panthalassic oceans are essentially identical, and hence that the end-Permian oceanic anoxic event was of global significance. The temporal correspondence of rapid expansion of seafloor anoxia and the end-Permian biocrisis suggests that redox changes played an important proximate role in mass mortality. Close agreement of $\delta^{238}U$ profiles from coeval carbonate sections thousands of kilometers apart, in different ocean basins, and with different diagenetic histories strongly suggests that bulk carbonate sediments can reliably preserve primary marine $\delta^{238}U$ signals, validating the carbonate U-isotope proxy for global-ocean redox analysis.

CHAPTER 3

GLOBAL-OCEAN REDOX VARIATION ACROSS THE SMITHIAN-SPATHIAN BOUNDARY LINKED TO CONCURRET CLIMATIC AND BIOTIC CHANGES

GLOBAL-OCEAN REDOX VARIATION ACROSS THE SMITHIAN-SPATHIAN BOUNDARY LINKED TO CONCURRET CLIMATIC AND BIOTIC CHANGES

This chapter is currently in revision in *Earth-Science Reviews*:

Zhang F., Algeo T.J., Ying Cui, Shen, J., Sano, H., Rowe, H.D., Anbar A.D., Global-ocean redox variation across the Smithian-Spathian boundary linked to concurrent climatic and biotic changes. Earth-Science Reviews: in revision.

3.1 Introduction

The ~5-Myr-long Early Triassic represents an extended interval of environmentally disturbed conditions following the ~252-Ma end-Permian mass extinction, the largest biocrisis of the Phanerozoic (Erwin et al., 2002; Knoll et al., 2007; Payne and Clapham, 2012). It was characterized by large marine carbon cycle perturbations (Payne et al., 2004; Tong et al., 2007), high sea-surface temperatures (Romano et al., 2012; Sun et al., 2012), recurrent episodes of ocean-redox and environmental perturbations (Grasby et al., 2012; Lau et al., 2016; Zhang et al., 2018b), and the most protracted marine ecosystem recovery following any Phanerozoic extinction event (Chen and Benton, 2012; Wei et al., 2015).

Within the Early Triassic, the Smithian-Spathian boundary (SSB) transition is a particularly interesting interval because it coincided with the largest and most rapid

climatic cooling episode following the end-Permian biocrisis as well as further biotic turnover. Paleotemperature reconstructions based on conodont oxygen isotopes suggest that tropical SSTs peaked at >38 °C during the late Smithian and then cooled rapidly to ~30-32 °C in the early Spathian (Galfetti et al., 2007; Romano et al., 2012; Sun et al., 2012). Although overshadowed by the end-Permian mass extinction, the SSB transition was recently identified as a major marine biocrisis (Brayard et al., 2009; Chen and Benton, 2012; Orchard, 2007; Stanley, 2009). Following the end-Permian mass extinction event, many marine clades (including conodonts, ammonoids, *Claraia* bivalves, and bellerophontid gastropods) showed a rapid partial recovery of diversity during the early Early Triassic (Chen and Benton, 2012) but then experienced further biodiversity losses in the late Smithian and at the SSB (Brayard et al., 2009; Orchard, 2007; Stanley, 2009). For instance, in Utah, the SSB is marked by the extinction of 10 out of 11 Smithian conodont species (Solien, 1979). The SSB transition was also marked by a major perturbation of the global carbon cycle, with a shift of >5 ‰ from the late Smithian minimum (N3) to the early Spathian maximum (P3) (Grasby et al., 2012; Payne et al., 2004; Tong et al., 2007); note: numbering system of Song-HY et al. (Song et al., 2013)).

The SSB transition coincided with major changes in marine redox conditions. For example, Song-HJ et al. (2012) inferred oceanic anoxia from the late Smithian to the earliest Spathian based on Ce-anomalies and Th/U ratios in conodont apatite from three sections in South China. Grasby et al. (2012) inferred oceanic anoxia during the same interval based on Mo concentration, Mo/Al ratio, Fe_{pyrite} concentration, and pyrite framboid data from the Sverdrup Basin, Canada. Sun et al. (2015) inferred oceanic anoxia during the SSB transition followed by a sharp shift to highly oxygenated conditions in the early-

middle Spathian based on analysis of pyrite framboids and trace metal enrichments in shallow- and deep-water sections from South China. Wei et al. (2015) used redox sensitive trace metal enrichments to infer variably suboxic to anoxic conditions during the SSB transition in three Lower Triassic sections from South China and one section from India. Zhang et al. (2015) used C-S isotopes, Ce anomalies, and redox sensitive trace metal enrichments to infer anoxic conditions just prior to the SSB and suboxic conditions following it in a deep-water section from South China. These studies thus document a largely consistent pattern of intensified oceanic anoxia during the SSB transition, subject to minor local variations.

Although these earlier studies have likely provided insight into marine redox changes across the SSB, key aspects of redox variation remain unresolved. For instance, the timing of onset and the duration of anoxia, the global extent of anoxia, and the triggering mechanisms of anoxia are not well established. Furthermore, all of the redox proxies used to date are inherently local proxies and, thus, possibly not representative of global-scale redox changes. The C and S isotope systems are not direct measures of ocean redox conditions. Carbon isotopes respond to changes in the proportion of carbon buried as carbonate and inorganic carbon (Fike et al., 2006; Kump and Arthur, 1999), as well as the fraction of authigenic carbonates (Cui et al., 2016b; Schrag et al., 2013) and recycling of crustal organic matter (Daines et al., 2017). Sulfur isotopes respond to changes in the proportion of sulfur buried as pyrite, and to changes in factors that control the fractionation of S isotopes between sulfate and pyrite (e.g., primary production and availability of organic matter, marine sulfate concentration, cell-specific sulfate reduction rate, and oxidative recycling of sulfide) (Algeo et al., 2015; Fike et al., 2006). However, C isotopes

and S isotopes respond indirectly to changes in ocean redox conditions through these processes, providing qualitative information.

In this study, we address this gap in knowledge regarding SSB oceanic redox variation through analysis of a geochemical proxy, carbonate U-isotopic compositions ($^{238}U/^{235}U$, denoted as $\delta^{238}U$), that can be used to quantitatively track changes in global-ocean paleoredox conditions. In the past decade, carbonate $\delta^{238}U$ has been developed as a new proxy for global-ocean anoxia and has been increasingly used to quantitatively estimate global-ocean redox changes during key geological periods (Bartlett et al., 2018; Brennecka et al., 2011a; Clarkson et al., 2018; Dahl et al., 2014; Dahl et al., 2017; Elrick et al., 2017; Jost et al., 2017; Lau et al., 2017; Lau et al., 2016; Zhang et al., 2018a; Zhang et al., 2018b; Zhang et al., 2018c). Here, we apply this proxy to two widely spaced carbonate sections (Figure 3.1) to place quantitative constraints on the timing and extent of ocean anoxia during the SSB transition, and to explore possible connections between ocean redox variation and the contemporaneous marine biocrisis, $\delta^{13}C_{carb}$ excursion, and climatic changes.

3.2 Geological background

3.2.1 Jesmond section, British Columbia, Canada

The Jesmond section of the Cache Creek Terrane, located in the Marble Range of southern British Columbia, western Canada, is a carbonate succession deposited on a mid-Panthalassic Ocean seamount (or an oceanic plateau) during the Late Permian to Late Triassic. The geological background of the Jesmond section was detailed by Sano et al. (2011). Briefly, the uppermost Smithian to mid-Spathian at Jesmond is ~91 m in thickness

and can be divided lithologically into three units. The lower unit (0-16 m) is dominated by thick-bedded, light-gray lime-mudstone facies. The middle unit (16-62 m) is primarily composed of thick-bedded, light gray, fine-grained dolostone (dolomicrite) with intermittent skeletal limestones. The upper unit (62-91 m) comprises mainly thick-bedded peloidal facies with subordinate skeletal limestones and flat-pebble conglomerates.

The Jesmond section has moderately good conodont biostratigraphic control. The conodonts *Pachycladina obliqua*, *Parapachycladina peculiaris*, and *Pachycladina* sp. were found in the lower unit, suggesting an uppermost Smithian to earliest Spathian age (e.g., Chen et al., 2015; Chen et al., 2016). The middle and upper units contain *Triassospathodus homeri*, *T. symmetricus*, and *Neospathodus* sp., which are characteristic of the *T. homeri* Zone that overlies the lowermost Spathian *Novispathodus pingdingshanensis* and *Icriospathodus collinsoni* zones (Kozur, 2003; Chen et al., 2015), and which suggest a broadly mid-Spathian age for these units (Sano et al., 2011). Absence of the *Novispathodus pingdingshanensis* and *Icriospathodus collinsoni* zones may be due to the presence of a disconformity (subaerial exposure horizon) between about +12 and +14 m in the section (Sano et al., 2011). Based on these conodont data, Sano et al. (2011) tentatively placed the SSB at 12-14 m in the Jesmond section.

C-isotope stratigraphy supports these general age assignments but allows more accurate placement of the SSB. Globally, the SSB can be placed at the midpoint of the positive carbon isotope excursion (CIE) from the late Smithian minimum (N3) to the earliest Spathian maximum (P3) (Zhang-L et al., 2018a). The Jesmond $\delta^{13}C_{carb}$ profile exhibits several key features: (1) a minimum of –0.3 ‰ to +0.3 ‰ at the base of the section (0-3 m) that is thought to be close to the N3 minimum of late Smithian age; (2) an abrupt

shift from +0.2 ‰ to +3.5 ‰ between 6.4 and 7.8 m that represents the N3-P3 shift at the SSB and that may indicate a condensed or disconformable substage contact; and (3) a slow and nearly continuous decline to a value of +0.4 ‰ at 87.7 m near the top of the section that is probably at or slightly below the mid-Spathian N4 minimum (cf. Song et al. (2013). These features unambiguously show that the SSB should be placed at ~7.0±0.5 m, or 5 to 7 m lower than inferred by Sano et al. (2011).

We developed an age model for the Jesmond section based on three age tie-points: (1) N3, which is close to or at the base of the section and has an age of ~250.75 Ma, (2) the SSB, which is at ~7.0 m and has an age of 250.6 Ma, and (3) N4, which is close to or at the top of the section and has an age of ~248.5 Ma (ages based on the timescale of Algeo et al., 2013; Shen et al., 2015; Zhang-L et al., 2018a). Individual sample ages were calculated by linear interpolation between age tie-points. Based on this age model, we calculated average sedimentation rates of 46.7 m Myr^{-1} for the Smithian and 40.3 m Myr^{-1} for the Spathian at Jesmond. These sedimentation rate estimates are reasonable for carbonate platforms, and the slightly higher rates for the Smithian versus the Spathian are consistent with earlier sedimentation rate calculations (e.g., Shen et al., 2015).

3.2.2 Zuodeng section, South China

The Zuodeng section is located in Zuodeng County, Tiandong city, in Guangxi Province, South China. During the Early Triassic, this section was located on the Debao Platform within the Nanpanjiang Basin, a deep-marine embayment on the southwestern (paleo-southeastern) margin of the South China Block that existed from the Late Paleozoic to the Late Triassic (Enos et al., 1997; Tong et al., 2007; Wei et al., 2015). The Debao

Platform was one of many isolated, shallow carbonate platforms within this basin, the largest being the Great Bank of Guizhou (Lehrmann et al., 2007). The Nanpanjiang Basin was adjacent to a subduction-zone volcanic arc along the South China–Indochina plate margin), where volcanism was more intense than on the northern margin of the South China Block (e.g., Xie et al., 2010).

The full Zuodeng section is >100 m in thickness and spans the interval from the basal Changhsingian to the upper Spathian. In this study, we focused on a 70-m-thick window (from 20 to 90 m above the base of the section) that ranges from the Dienerian-Smithian boundary to the middle or lower-upper Spathian. This interval consists of thin- to thick-bedded lime mudstone. Estimated depositional water depths in the Zuodeng area were ~30–50 m based on energy levels consistent with the subtidal character of Lower Triassic limestones on the Debao Platform (Lehrmann et al., 2007).

The Zuodeng section has a well-established conodont biostratigraphy (Tong et al., 2007; Zhang et al., 2015). The Smithian and Spathian substages of the Lower Triassic are represented by the *Novispathodus waageni* Zone of Smithian age at ~29–44 m, the *Nv. pingdingshanensis* Zone of early Spathian age at ~44–60 m, and the *Tr. homeri* Zone of mid to late Spathian age at ~60–102 m (above which the Anisian *Chiosella timorensis* Zone is present) (Tong et al., 2007; Zhang et al., 2015).

The Zuodeng section has yielded high-resolution $\delta^{13}C_{carb}$ profiles (Tong et al., 2007; this study) that exhibit all of the main excursions of the Early Triassic (Payne et al., 2004) and that support the conodont-based age assignments. The $\delta^{13}C_{carb}$ profile shows high values (ca. +4 ‰) in the lowermost Smithian (P2), a decrease to ~0 ‰ in the mid- to upper Smithian (N3) at 42.2 m, and a rebound to ca. +3 ‰ in the lower Spathian (P3; close to

base of the *Nv. pingdingshanensis* Zone) at 45.3 m (Tong et al., 2007). Zhang-L et al. (2018a) showed that the midpoint of the positive $\delta^{13}C$ excursion from the late Smithian minimum (N3) to the earliest Spathian maximum (P3) is a robust proxy for the base of the *Nv. pingdingshanensis* Zone and, thus, the SSB itself. At Zuodeng, the SSB can be constrained on the basis of carbon-isotope chemostratigraphy only to 44 ± 1 m because of a large negative anomaly (to –5.0 ‰) of probable diagenetic origin at 43-44 m that interrupts what would normally be a smooth transition between N3 (0 ‰) and P3 (+3 ‰). We speculate that this negative $\delta^{13}C_{carb}$ anomaly represents a meteoric alteration event associated with cooling and sea-level fall at the SSB (cf. Zhang-L et al., 2015, 2018b).

We developed an age model for the full Zuodeng section using the same timescale as for Jesmond. The portion of the Zuodeng section of relevance to the present study includes three age tie-points: (1) P2, which is at 20.2 m and has an age of ~250.95 Ma (note: P2 is just above the Dienerian-Smithian boundary, which is dated to 251.0 Ma), (2) N3, which is at 42.2 m and has an age of 250.75 Ma, and (3) P3, which is at 45.3 m and has an age of ~250.55 Ma. Individual sample ages were calculated by linear interpolation between age tie-points. Based on this age model, we calculated average sedimentation rates of 110.2 m Myr^{-1} for the early to early late Smithian (P2 to N3) and 15.5 m Myr^{-1} for the SSB transition (N3 to P3). The sedimentation rate estimates for the Smithian are high, but neither pre-Smithian rates (15-44 m Myr^{-1}) nor post-SSB rates (25-30 m Myr^{-1}) at Zuodeng are exceptional, and the same Early Triassic time scale has yielded lower sedimentation rate estimates for many other Smithian sections (cf. Shen et al., 2015) including Jesmond. Therefore, the high sedimentation rate estimates for the Smithian at Zuodeng are

considered accurate and are thought to reflect accelerated carbonate platform accretion during this substage of the Early Triassic.

3.3 Analytical methods

3.3.1 Sample digestion methods

Approximately 2-3 g of each sample were dissolved in 1-M HCl using a 50 mL trace-metal-clean centrifuge tube using the following protocol: 6×5 mL of 1-M HCl was slowly added in the tube with a time gap of 10 minutes between steps. In order to continue the reaction, 1 mL of 10-M HCl was slowly added every 25 minutes (producing 0.3-M HCl) for a total of 5 times. Finally, 1-M HCl was added to make a final volume 45 mL. After sitting at room temperature for 24 hours, the samples were centrifuged to separate the supernatant and undissolved residues. This dissolution protocol employs a 1.5× excess of HCl in order to ensure complete dissolution of the carbonate, thus avoiding U isotope fractionation from selective leaching of various carbonate phases.

3.3.2 Major and trace element analyses

Major, minor, and trace element concentrations were measured on a Thermo iCAP™ quadrupole inductively coupled plasma mass spectrometer (Q-ICP-MS) at the W. M. Keck Laboratory for Environmental Biogeochemistry at Arizona State University (ASU) on splits from each supernatant. Typical precision was better than 3 % and 5 % for major and trace elements, respectively, based on repeated analysis of in-run check standards.

3.3.3 Uranium isotope analysis

Prior to U-isotope column chemistry, appropriate amounts of the ^{236}U:^{233}U double spike (Brennecka et al., 2011a; Romaniello et al., 2013; Weyer et al., 2008) were added to each sample based on measured uranium concentrations (the U_{spike}/U_{sample} ratio was ~0.0363 for each sample). The spike-sample mixtures were evaporated to dryness and dissolved in 3-N HNO_3. Uranium was purified for isotopic analysis using the UTEVA method (Brennecka et al., 2011a; Romaniello et al., 2013; Weyer et al., 2008). A volume of 1.0–1.2 mL UTEVA resin was loaded on a column. The resin was then washed with 5 × 2.5 mL 0.05-M HCl to remove impurities. The resin was then converted to the nitric form by loading 4 × 2.5 mL 3-M HNO_3. The double-spiked U sample (dissolved in 3-M HNO_3) was loaded on the column and rinsed with 10 × 2.5 mL 3-M HNO_3 to remove all matrix ions except U and Th. Then 10-M HCl (3 × 2 mL) was added to the column to convert the UTEVA resin to chloride form. Th was removed from the resin using a mixture of 5-M HCl and 0.05-M oxalic acid (3 × 2 mL). The oxalic acid left on the resin was rinsed with 3 × 2 mL 5-M HCl. The U adsorbed on the resin was eluted with 13 mL (2+2+2+3+4) of 0.05-M HCl. The U cuts were dried down and heated with concentrated HNO_3 + 30 % H_2O_2 (1.5 mL + 0.3 mL) to remove any organic residue eluted from the UTEVA resin. The last step was repeated three times in order to remove all organic residue. All samples have been put through U-isotope column chemistry twice in order to completely remove matrix ions. The final purified U was dissolved in 0.32-M HNO_3 and diluted to a U concentration of 50 ppb.

Uranium isotopes were measured at ASU on a Themo-Finnigan Neptune multi-collector ICP-MS at low mass resolution through 50 cycles with 4.194 s integration time.

Rinsing time was typically 210 s or more. When using a 100 µl nebulizer, a 50 ppb sample solution yielded 30-36 V of ^{238}U signal on a 10^{11} Ω amplifier. The standard solution CRM145 (50 ppb U) was analyzed every two samples. Two secondary standards (CRM129a and an in-house Ricca ICP solution) were measured after every 15 measurements. Sample $\delta^{238}U$ values were normalized by the average of the bracketing CRM145 standard. CRM145 standard shares its U-isotopic composition with another common standard CRM112a, from which it was prepared. Intercalibration of standards SRM950a and CRM145 has shown no $\delta^{238}U$ offset between them (Condon et al., 2010). The measured $\delta^{238}U$ compositions of standards CRM145, CRM129a, and Ricca are −0.00±0.07 ‰ (2σ, n = 61), −1.74±0.06 ‰ (2σ, n = 9), and −0.28±0.08 ‰ (2σ, n = 7), respectively.

3.3.4 Carbon isotope analysis

The carbon and oxygen isotopic compositions of the Jesmond samples were measured at the University of Kentucky Environmental Research Training Laboratory using a GasBench—II peripheral coupled to a DeltaPlusXP isotope ratio mass spectrometer. Samples (450±50 µg) were equilibrated at 40 °C for 24 h before analysis. Average precisions (1σ) were 0.05 ‰ for $\delta^{13}C$ and 0.05 ‰ for $\delta^{18}O$ of the NBS-19 standard ($\delta^{13}C$ = +1.95 ‰, $\delta^{18}O$ = –2.20 ‰), and 0.02 ‰ for $\delta^{13}C$ and 0.05 ‰ for $\delta^{18}O$ of unknowns. The carbon and oxygen isotopic compositions of the Zuodeng samples were measured at the State Key Laboratory of Biogeology and Environmental Geology of the China University of Geosciences (Wuhan). For each rock sample, ~150-400 µg of powder was weighed in a 10 mL Na-glass vial, sealed with a butyl rubber septum, and reacted with 100% phosphoric

acid at 72 °C after flushing with helium. The evolved CO_2 gas was analyzed for $\delta^{13}C$ and $\delta^{18}O$ using a MAT 253 mass-spectrometer coupled directly to a Finnigan Gasbench II interface (Thermo Scientific). Analytical precision was better than ±0.1 for $\delta^{13}C$ and ±0.1 for $\delta^{18}O$ based on replicate analyses of two laboratory standards (GBW 04416 and GBW 04417). All $\delta^{13}C$ and $\delta^{18}O$ values are reported as per mille variation relative to the Vienna Pee Dee belemnite (VPDB) standard.

3.4 Results

All geochemical data ($\delta^{238}U$, $\delta^{13}C$, and elemental concentrations) for this study are given in Tables 3.1-3.4 and key results are shown in Figure 3.2.

3.4.1 The Jesmond section

At Jesmond, the $\delta^{13}C_{carb}$ profile exhibits relatively light values to ca. –0.2 ‰ in the uppermost Smithian (below 7 m; N3). There is a positive excursion to ca. +3.5 ‰ in the lowermost Spathian (immediately above 7 m; P3). Except six samples within the 13.5-14.5 m and 84.2-87.6 m intervals (Figure 3.2), $\delta^{13}C_{carb}$ exhibits positive and relatively invariant values that range between +1.2 ‰ and +3.7 ‰ in the lower to middle Spathian.

$\delta^{238}U$ shifts toward higher values across the SSB, concurrently with a positive shift in $\delta^{13}C_{carb}$ (Figure 3.2). The two uppermost Smithian samples (below 7 m) yield $\delta^{238}U$ values of −0.48 ‰ and −0.38 ‰. The $\delta^{238}U$ values of the lowermost Spathian samples (7.8-13.2 m) range between −0.05 ‰ and −0.30 ‰ with a mean of −0.18 ‰. This positive shift in $\delta^{238}U$ at the SSB is followed by large fluctuations between low (−0.60 ‰) and high (+0.04 ‰) values in the lower Spathian (13.2-40 m). The mid-Spathian samples (40-90 m)

show intermediate and relatively invariant $\delta^{238}U$ values ranging between −0.26 ‰ and −0.45 ‰ with a mean of −0.33 ‰. Compared to the $\delta^{238}U$, uranium concentrations exhibit large stratigraphic variations, fluctuating between low (0.12 ppm) and high (4.0 ppm) values, without any clear temporal trends (Figure 3.3).

3.4.2 The Zuodeng section

At Zuodeng, the $\delta^{13}C_{carb}$ profile exhibits a gradual decrease from +4.4 ‰ in the lowermost Smithian to ca. –1.2 ‰ in the uppermost Smithian (N3), followed by a positive excursion to ca. +2.0 ‰ (P3) across the SSB. Except for three outliers (marked in Figure 3.2), our $\delta^{13}C_{carb}$ profile agrees with the $\delta^{13}C_{carb}$ profile for Zuodeng generated by Tong et al. (2007).

The $\delta^{238}U$ profile also exhibits large stratigraphic variations (Figure 3.2). $\delta^{238}U$ shows a small positive shift from −0.46 ‰ to −0.17 ‰ in the lower Smithian at 20-31 m, followed by a gradual decrease to a minimum of −0.67 ‰ at 38.5 m in the uppermost Smithian. The $\delta^{238}U$ profile then shows a rapid shift toward higher values across the SSB, concurrently with a positive shift in $\delta^{13}C_{carb}$. The $\delta^{238}U$ of the lowermost Spathian samples (44-50.6 m) ranges between −0.23 ‰ and −0.39 ‰ with a mean of −0.32 ‰. This positive shift in $\delta^{238}U$ across the SSB is consistent with a recent study from the Zal section in Iran (Zhang-F. et al., 2018a), suggesting that this shift is of global significance. Above 50.6 m, the $\delta^{238}U$ profile shows another major negative shift towards lower values, although this shift is interrupted by a small and short-lived positive shift at 62.5-64.5 m. In contrast to the Jesmond section, the uranium concentration profile at Zuodeng shows a clear decline below the SSB, concurrently with the negative shift in $\delta^{238}U$ (Figure 3.4). U concentrations

increase, ranging between 0.9 and 1.9 ppm with a mean of 1.4±0.8 ppm (standard deviations are reported as 2σ) in the lower Smithian at 20-31 m. U concentrations then decrease rapidly above 31 m and show an intermediate and relatively invariant range between 0.2 and 1.3 ppm with a mean of 0.6±0.5 ppm.

3.5 Evidence of primary oceanographic $\delta^{238}U$ signal

3.5.1 Diagenetic alteration by meteoric or burial fluids

To assess diagenesis, we used previously established geochemical criteria. Specifically, we compared our $\delta^{238}U$ data to standard carbonate diagenetic indicators such as O isotope composition, Mn content, Sr content, and Mn/Sr ratios to evaluate the influence of meteoric or burial fluids on preserved U isotope signatures (Table 3.5).

The isotopic composition of oxygen in carbonates can be altered easily during diagenesis owing to the high concentration of oxygen in diagenetic fluids (Banner and Hanson, 1990; Gilleaudeau et al., 2018; Jacobsen and Kaufman, 1999). Prior studies have suggested that carbonate sedimentary rocks with $\delta^{18}O$ values > −9 ‰ (e.g., Kah et al., 2012; Kah et al., 1999). or > −5 ‰ (e.g., Kaufman and Knoll, 1995). may be relatively reliable indicators of limited alteration by meteoric or burial fluids. A simple open-system model of the diagenetic evolution of carbonates during burial predicts that the $\delta^{238}U$ signal is more robust than the $\delta^{18}O$ (and $^{87}Sr/^{86}Sr$) signal (Lau et al., 2017). $\delta^{18}O$ values of the Zuodeng section range between −4.52 ‰ and −7.94 ‰ with a mean of −5.79 ‰ (Table 3.1), and those of the Jesmond section range between −2.29 ‰ and −4.91 ‰ with a mean of −3.60 ‰ (Table 3.2), which are indicative of moderate and weak alteration, respectively (cf. Algeo et al., 1992; Gilleaudeau et al., 2018). In addition, there is no statistically significant

correlation between $\delta^{18}O$ and $\delta^{238}U$ in either section (Table 3.5), indicating that the study samples are likely well-preserved with limited influence by meteoric or burial diagenetic alteration.

Trace elements (e.g., Sr and Mn) substituted into the lattice of carbonate minerals can also be used as diagenetic indicators. Primary carbonate precipitates and early diagenetic carbonate phases formed in the presence of oxic seawater are generally enriched in Sr relative to Mn (Veizer, 1983; Banner and Hanson, 1990). Meteoric and burial fluids, by contrast, tend to be depleted in Sr relative to seawater (Banner and Hanson, 1990). As a result, meteoric or burial diagenetic carbonate phases are often depleted in Sr relative to precursor marine phases, and burial fluids and secondary carbonate precipitates can be enriched in Mn, particularly under reducing conditions (Veizer, 1983). Prior studies have suggested that both limestone and dolostone with Mn/Sr ratios < 10 can be expected to retain their primary marine isotopic signatures, such as carbon isotopes (Kaufman and Knoll, 1995; Gilleaudeau and Kah, 2013). In this study, we used a conservative Mn/Sr ratio of 2.5 as an initial benchmark for assessing diagenesis (e.g., Zhang-F. et al., 2018a,c).

The Jesmond samples are characterized by low Mn contents (< 50 ppm with the exception of two samples containing 113 and 86 ppm, respectively) and relatively low Sr concentrations (from 106 to 179 ppm) (Figure 3.3). Sr is easily expelled from the crystal lattice during recrystallization, and dolomite has a generally lower preference for Sr than calcite, such that early fabric-retentive dolomite formed in the presence of seawater is often depleted in Sr (Veizer, 1983; Vahrenkamp and Swart, 1990). The enrichments in Sr relative to Mn and the low Mn/Sr ratios of these samples (< 1 for all samples, and < 0.3 for 24 out of 26 samples), together with a lack of statistically significant correlations between $\delta^{238}U$

and Mn content, Sr content, or Mn/Sr ratio (Table 3.5), suggest a high degree of preservation of original carbonate mineralogy.

At Zuodeng, most samples are characterized by relatively low Mn contents (< 400 ppm with the exception of four samples). The Sr shows relative large stratigraphic variations with samples below 51.5 m have relatively high Sr concentrations (> 200 ppm with the exception of only one sample) and samples above 51.5 m have lower Sr concentrations range between 113 and 223 ppm (Figure 3.3). With the exception of five samples from 68.7–76.3 m interval, all samples have Mn/Sr < 2.5. These five "outliers" with Mn/Sr ratio > 2.5 have been marked in yellow in Figure 3.4 and have been excluded from the discussions below. Additionally, no statistically significant correlations between $\delta^{238}U$ and Mn contents, Sr contents, and Mn/Sr ratios are observed for samples with Mn/Sr <2.5 (Table 3.5), suggest a high degree of preservation of original carbonate mineralogy.

3.5.2 Contamination by detrital components

Changes in the extent of detrital U inputs might also cause a $\delta^{238}U$ shift. We examined this possibility by looking at U/Al ratios and elements tied mostly to the terrigenous detrital fraction (e.g., Al; Ling et al., 2013; Wallace et al., 2017). For most sedimentary deposits, aluminum can be considered as an indicator of the detrital fraction of the sediment, with very little ability to move during diagenesis (Tribovillard et al., 2006). Thus, an easy means to check whether the content of a given element is dominantly controlled by the detrital flux is to crossplot the trace element versus aluminum. If a good correlation is observed and if the trace element exhibits concentrations that do not deviate

too greatly from average upper continental crust concentrations, it can be inferred that the trace element is mainly of detrital provenance (Tribovillard et al., 2006).

Our samples were dissolved in 1 M hydrochloric acid (HCl) prior to extraction of U, which will minimize dissolution of any non-carbonate minerals (e.g., silicates) and organic matter (Brennecka et al., 2011a; Zhang-F et al., 2018a,b). This expectation is supported by the overall high U/Al ratios in our analyses. The U/Al ratio (ppm/wt.%) of the upper continental crust is 0.33 ppm/wt.% (Rudnick and Gao, 2003). The U/Al ratios in the Zuodeng samples range between 0.8 and 349 with a mean of 27 (Figure 3.3), and those in the Jesmond samples range between 4.2 and 153 with a mean of 35 (Figure 3.4). The U/Al ratios in all samples of both sections are thus enriched above average crustal values by approximately two orders of magnitude. Additionally, we found no correlations between $\delta^{238}U$ and Al contents, U concentrations, U/Al ratios, Al contents, U/(Ca+Mg) ratios, and Al/(Ca+Mg) ratios (Table 3.5), indicating that the observed $\delta^{238}U$ trends were not related to detrital U inputs.

3.5.3 Changes in carbonate mineralogy

The Zuodeng section is primarily composed of limestones with only three dolomitic limestone samples (at 36.6-37.5 m), whereas the Jesmond section is composed mainly of dolostones. Prior studies have shown that dolomite can have low $\delta^{238}U$ values (Stirling et al., 2007; Romaniello et al., 2013). In particular, Romaniello et al. (2013) observed $\delta^{238}U$ changes associated with dolomitization in a Bahamian tidal pond, as indicated by a strong correlation with Mg/Ca molar ratios. On this basis, Romaniello et al. (2013) raised concerns that strong (>30–50 %) dolomitization might have compromised the $\delta^{238}U$ record

across the end-Permian mass extinction (EPME) horizon in the Dawen section in South China (Brennecka et al., 2011a). However, there are now $\delta^{238}U$ data from seven carbonate sections spanning the EPME: the Dajiang (Lau et al., 2016), Guandao (Lau et al., 2016), Dawen (Brennecka et al., 2011a), and Daxiakou sections (Elrick et al., 2017) in South China, the Taşkent sections in Turkey (Lau et al., 2016), the Kamura section in Japan (Zhang et al., 2018a), and the Zal section in Iran (Zhang et al., 2018b). All of these sections show strikingly similar trends in $\delta^{238}U$ across the EPME horizon, which is remarkable because they span 1000s of km—even different ocean basins—and have experienced very different diagenetic histories, including dolomitization. These studies strongly suggest that dolomitization is not a major influence on paleo-$\delta^{238}U$ records (Zhang-F et al., 2018b). In addition, there are no statistically significant correlations between $\delta^{238}U$ and Mg/Ca molar ratios in our samples (Table 3.5).

In general, aragonite has higher Sr concentrations compared to calcite and dolomite because of the high distribution coefficient of Sr into aragonite compared to other carbonate minerals (Veizer, 1983). In past studies, Sr/Ca ratios have been adopted as an indicator of variation in carbonate mineralogy (i.e., aragonite vs. calcite) (Lau et al., 2016, 2017; Dahl et al., 2017). We plotted $\delta^{238}U$ versus Sr/Ca ratios for the two study sections and found no correlations (Table 3.5), suggesting little influence from variations in carbonate minerology.

3.5.4 Changes in riverine uranium isotopic compositions

Changes in riverine $\delta^{238}U$ values may also cause variations in seawater uranium isotopic compositions because riverine inputs serve as the dominant source of uranium to

the ocean. In this study, we observed a 0.4–0.6 ‰ positive shift in $\delta^{238}U$ from the late Smithian to the SSB, and a 0.3–0.4 ‰ positive shift in $\delta^{238}U$ from the SSB to the early-middle Spathian (Figure 3.5). Changes in riverine U-isotopic composition of these magnitudes would require the dominant weathering lithology to shift rapidly from that of average upper continental crust to one dominated by ^{238}U-enriched materials (e.g., euxinic shales; Weyer et al., 2008) or ^{238}U-enriched materials (e.g., manganese oxides, or carbonates deposited under reducing conditions; Brennecka et al., 2011a; Tissot and Dauphas, 2015; Lau et al., 2016). Such rapid shifts are inherently improbable and are not supported by reconstructions of subaerially exposed lithologies during the Permo-Triassic (Bluth and Kump, 1991). In addition, the average composition of upper continental crust has not changed much since the end of the Archean (Gaschnig et al., 2016; Tang et al., 2016). Thus, changes in riverine $\delta^{238}U$ values cannot explain the rapid shifts in $\delta^{238}U$ observed in this study.

We acknowledge the limitations of existing diagenetic proxies for evaluating the diagenesis of carbonate $\delta^{238}U$. Existing indicators of carbonate diagenesis have been primarily developed for carbon, oxygen, and strontium isotopes studies, and further work is required to develop specific diagenetic indicators for uranium isotopes. Although local diagenetic processes undoubtedly account for some of the variation (or scatter) in our $\delta^{238}U$ dataset, the analysis presented above strongly suggests that the observed signal is mainly a primary marine signature reflecting the U isotopic composition of contemporaneous seawater. The $\delta^{238}U$ records of the two study sections can therefore be used to evaluate secular variations in mean global-ocean redox states during the Smithian-Spathian substages of the Early Triassic. We also note that the quantitative assessment of redox

variations across the SSB presented below is built on a combination of $\delta^{238}U$ data from the two study sections. Samples above 61.1 m at Zuodeng have been excluded in the marine U-cycle mass balance model calculation because of the relatively low resolution of the $\delta^{238}U$ data. We encourage high-resolution $\delta^{238}U$ studies to test the secular trends observed above 61.1 m at Zuodeng and to build a solid U-cycle mass balance model in the future.

3.6 Quantitative assessment of redox variations across the SSB

The high-resolution $\delta^{238}U$ data across the SSB from this study demonstrate that (1) the late Smithian was characterized by an episode of extensive oceanic anoxia, (2) the extent of oceanic anoxia was reduced substantially at the SSB, and (3) the early-middle Spathian was characterized by a second episode of expanded oceanic anoxia. Quantitative assessment of redox variation across the SSB requires compensation for early diagenetic effects on carbonate $\delta^{238}U$. We adopted a mean diagenetic offset of 0.3 ‰, an average based on observations from modern Bahamian carbonates (Romaniello et al., 2013). In order to quantitatively estimate the extent of marine redox variation, we used a dynamic U isotope mass balance model to calculate the fraction of U removal into anoxic sedimentary sinks (F_{anox}) and the total seafloor areas overlain by anoxic waters (f_{anox}).

The implied changes to the extent of bottom water anoxia can be described by differential mass balance equations for the seawater uranium inventory and its isotopic composition (following Lau et al., 2016 and Zhang et al., 2018a):

$$\frac{dN_{sw}}{dt} = J_{riv}^{U} - J_{oxic} - J_{anox} \qquad \text{Eq.17}$$

$$\frac{d(N_{sw}\cdot\delta^{238}U_{sw})}{dt}=J_{riv}^{U}\cdot\delta^{238}U_{riv}-J_{oxic}\cdot\delta^{238}U_{oxic}-J_{anox}\cdot\delta^{238}U_{anox} \quad \text{Eq.18}$$

$$\delta^{238}U_{anox}=\delta^{238}U_{sw}+\Delta_{anox} \quad \text{Eq.19}$$

$$\delta^{238}U_{oxic}=\delta^{238}U_{sw}+\Delta_{oxic} \quad \text{Eq.20}$$

Eq. 18 can be simplified to give an expression for the changing isotope composition:

$$\frac{d(\delta^{238}U_{sw})}{dt}=\frac{J_{riv}^{U}\cdot(\delta^{238}U_{riv}-\delta^{238}U_{sw})-J_{oxic}\cdot\Delta_{oxic}-J_{anox}\cdot\Delta_{anox}}{N_{sw}} \quad \text{Eq.21}$$

where N_{sw} is the oceanic uranium inventory in moles, $\delta^{238}U_{sw}$, $\delta^{238}U_{riv}$, $\delta^{238}U_{anox}$, and $\delta^{238}U_{oxic}$ are the U isotope composition of seawater, the U isotope composition of the riverine source, the U isotope composition of anoxic sedimentary sinks, and the average U isotope compositions of the remaining other sinks, respectively. In this model, we simplify the inputs to $J_{\mathrm{riv}}{}^{\mathrm{U}}$, the riverine flux, whose modern value is ~4 × 10^7 mol U/yr (Morford and Emerson, 1999). The outputs are assumed to consist of the anoxic sediment sink (J_{anox}) and the sum of the other sinks (J_{oxic}). In this model, we used an estimate of 0.6 × 10^7 mol U/yr (Morford and Emerson, 1999) for J_{anox} and calculated J_{oxic} by mass balance to an initial steady-state value of 3.4 × 10^7 mol U/yr. Δ_{anox} = +0.6 ‰ is the effective fractionation factor associated with anoxic sediment deposition (Andersen et al., 2014), and Δ_{oxic} is the effective fractionation factor associated with the remaining other sinks (+0.0043 ‰, calculated to maintain isotopic steady state in the modern ocean (e.g., Montoya-Pino et al., 2010; Brennecka et al., 2011a; Wang et al., 2016).

We defined the oxic and anoxic sinks in Eqs. 17-21, assuming a first-order dependence on seawater U concentration (e.g., Partin et al., 2013; Reinhard et al., 2013; Lau et al., 2016; Wang et al., 2016; Zhang-F., et al., 2017a):

$$J_{anox} = k_{anox} \cdot N_{sw} \cdot A_{anox} \quad \text{Eq.22}$$

$$J_{oxic} = k_{oxic} \cdot N_{sw} \cdot A_{oxic} \quad \text{Eq.23}$$

where A_{anox} and A_{oxic} are the total seafloor areas overlain by anoxic waters and non-anoxic waters, respectively. k_{anox} and k_{other} are rate constants associated with anoxic sediment deposition and all other sediment deposition and are calculated for the modern uranium system (e.g., Lau et al., 2016; Wang et al., 2016).

We defined the fraction of seafloor area overlain by anoxic waters as:

$$f_{anox} = \frac{A_{anox}}{A_{ocean}} \quad \text{Eq.24}$$

where f_{anox} is the total seafloor area overlain by anoxic waters, and A_{ocean} is the total seafloor area of the modern ocean.

We defined the fraction of seawater U removal into anoxic sedimentary sinks as:

$$F_{anox} = 1 - \frac{N_{sw,t}}{N_{sw,0}} \quad \text{Eq.25}$$

where F_{anox} is the total fraction of seawater U removal into anoxic sedimentary sinks, $N_{sw,t}$ and $N_{sw,0}$ are the seawater U inventory at time t and the U inventory in the modern ocean.

Before making U-model calculations, we first interpolated and smoothed the measured $\delta^{238}U$ data (black solid circles in Figure 3.5A) using a LOWESS (LOcally WEighted Scatterplot Smoothing) fit method (black curve in Figure 3.5A). The LOWESS fit was performed in the program R using function "loess" with span parameter equal to 0.2. The ~0.3 ‰ adjustment for an early diagenetic offset is given by the green curve in Figure 3.5A. An initial N_{sw} of 9.36×10^{12} moles U was calculated assuming that the late

Smithian ocean was at steady state. In order to calculate the fraction of anoxic seafloor area (f_{anox}), we solved Eq. 21 such that:

$$f_{\text{anox}} = \frac{\dfrac{J_{riv}(\delta^{238}U_{riv} - \delta^{238}U_{sw})}{N_{sw}} - \dfrac{d\delta^{238}U_{sw}}{dt} + k_{oxic}\Delta_{oxic}A_{seafloor}}{k_{anox}\Delta_{anox}A_{seafloor} - k_{oxic}\Delta_{oxic}A_{seafloor}} \qquad \text{Eq.26}$$

where model input parameters are determined based on studies of the modern U cycle and summarized in Table 3.6. The derivative of $\delta^{238}U$ was calculated using the interpolated and smoothed LOWESS curve shown in Figure 3.5A. As U is removed to anoxic sediments, the total inventory of U in the ocean should decline--therefore, we can solve for Equation 1 using equations 6 and 7 such that:

$$N_{\text{sw},\,t+1} = N_{\text{sw},\,t} + [J_{riv} - k_{oxic}N_{sw,\,t}(1 - f_{anox,\,t})A_{seafloor} - k_{anox}N_{sw,\,t}f_{anox,\,t}A_{seafloor}]\times dt \qquad \text{Eq.27}$$

where $N_{sw,\,t+1}$ is the total U left in the ocean at time t+1 after U is removed to anoxic sediments at time t. The time step between time t and t+1 is denoted as dt, which was set to 10,000 years. We solved for $N_{sw,\,t+1}$ and f_{anox} iteratively, and the modeling outputs for F_{anox} and f_{anox} are shown in Figure 3.5B and 3.5C.

This U-isotope model suggests that, during the late Smithian, ~65 % of seawater U was removed to anoxic facies, a flux that corresponds to an anoxic seafloor area equal to ~11 % of total seafloor area. This situation changed markedly at the SSB, when the fraction of seawater U that was removed to anoxic facies decreased to ~48 % and anoxic seafloor area was reduced to just ~2 %. During the early-middle Spathian, the fraction of seawater U removed to anoxic facies increased again, to ~70 %, and anoxic seafloor area expanded to 10–13 % of total seafloor area. Expansion of anoxic facies during the late Smithian is

also supported by the uranium concentration data from Zuodeng: [U] declines sharply when $\delta^{238}U$ goes more negative in the late Smithian, consistent with drawdown of the seawater uranium inventory because of enhanced uranium removal. The paucity of pre-SSB samples at Jesmond make evaluation of its [U] trend across the SSB uncertain. However, our inference of widespread oceanic anoxia during the late Smithian is consistent with evidence from other Lower Triassic sections in the Nanpanjiang Basin, South China (Song-HJ et al., 2012; Sun et al., 2015; Wei et al., 2015; Zhang et al., 2015), and in British Columbia, Canada (Grasby et al., 2012).

3.7 Ocean-redox variation associated with late Smithian hyperwarming

The marine redox changes documented by our $\delta^{238}U$ data show a good first-order correlation with the sea-surface temperature (SST) records that have been generated from conodont oxygen isotopes (Figure 3.6A-B). Calculation of SSTs from $\delta^{18}O$ values revealed a temperature rise from ~30 °C in the early Smithian to ~38-40 °C in the late Smithian, followed by a rapid temperature fall to 31-33 °C immediately after the SSB (Sun et al., 2012; Romano et al., 2013). Thus, the expansion of oceanic anoxia in the late Smithian coincided with the Late Smithian Thermal Maximum (LSTM; Zhang-L et al., 2018a), and the subsequent reduction of oceanic anoxia at the SSB coincided with a climatic cooling event (cf. Song-HY et al., 2018; Stebbins et al., 2018a,b).

The mechanism that we hypothesize to have linked oceanic redox conditions to climate in the late Smithian involves interconnected changes in temperature, seawater O_2 solubility, thermal stratification, and vertical mixing (Keeling et al., 2010; Danise et al., 2013; Shepherd et al., 2017). Tropical SST reconstructions suggest a 6-10 °C increase from

the early Smithian to the late Smithian (Sun et al., 2012; Romano et al., 2013). This warming led to reduced O_2 solubility, intensified stratification, and suppressed vertical mixing, all of which contributed to expansion of oceanic anoxia, as shown by sensitivity studies conducted using climate system and oceanic biogeochemical models (Matear and Hirst, 2003; Long et al., 2016b). This, together with O_2 consumption by remineralization of sinking particulate organic matter, would most likely have led to expansion of anoxia in the thermocline region of the ocean (Matear and Hirst, 2003; Long et al., 2016b).

We note that climatic warming would have also enhanced continental weathering, riverine nutrient fluxes, and marine primary productivity, further contributing to the expansion of oceanic anoxia (cf. Zhang-F et al., 2018a). Prior studies of seawater Sr isotopes have inferred a 5× increase in riverine Sr flux to the ocean during the late Smithian, followed by a rapid decrease at the SSB (Sedlacek et al., 2014). Assuming a P/Sr molar ratio of 0.6 to 0.9 (Froelich, 1988; Richter and Turekian, 1993; Tyrrell, 1999; Paytan and McLaughlin, 2007; Reinhard et al., 2017; Zhang-F et al., 2018a), we estimate a 3-4.5× increase in riverine PO_4^{3-} flux to the late Smithian ocean. Sensitivity studies conducted using spatially resolved GCM models of Early Triassic climate and ocean circulation indicate that seawater PO_4^{3-} increases of this magnitude would have led to expansion of anoxic watermasses due to increased marine productivity and organic carbon input to the deep ocean (Winguth and Winguth, 2012; Meyer et al., 2016). However, further work will be required using intermediate-complexity Earth system models to evaluate the relative importance of intensified oceanic stratification versus enhanced marine productivity in the development of oceanic anoxia during the late Smithian. Subsequent climatic cooling at the SSB increased O_2 solubility, reduced thermal stratification, increased oceanic

ventilation, and reduced weathering nutrient fluxes (cf. Zhang-L et al., 2015; Song-HY et al., 2018; Stebbins et al., 2018a,b; Zhang-F et al., 2018a). Some combination of these factors led to reduced oceanic anoxia during the SSB transition.

3. 8 Oceanic-redox variation and $\delta^{13}C_{carb}$ excursions at the SSB

3.8.1 Empirical observations

The temporal relationship between marine anoxia and Early Triassic $\delta^{13}C_{carb}$ excursions is a subject of debate (Payne et al., 2004; Galfetti et al., 2007; Horacek et al., 2007; Meyer et al., 2011; Song-HJ et al., 2012; Song-HY et al., 2013; Sun et al., 2015; Thomazo et al., 2016; Zhang-F et al., 2018a, b). The late Smithian negative $\delta^{13}C_{carb}$ excursion (N3 of Song-HY et al., 2013) has been attributed to massive release of ^{12}C-enriched CO_2 from volcanogenic or thermogenic sources associated with the Siberian Traps Large Igneous Province (Payne et al., 2004; Payne and Kump, 2007). In this scenario, the release of CO_2 triggered climatic warming and expansion of oceanic anoxia, and the latter process contributed to enhanced burial of isotopically light organic C in anoxic sediments, generating the ensuing positive $\delta^{13}C_{carb}$ excursion (P3) at the SSB (Galfetti et al., 2007; Sun et al., 2015). This hypothesis predicts that ocean anoxia peaked as $\delta^{13}C_{carb}$ approached or reached maximum values in the earliest Spathian (i.e., P3). This prediction, however, is not to be supported by our U-isotope dataset, which demonstrates that global-ocean anoxia peaked in the late Smithian, i.e., coevally with the $\delta^{13}C_{carb}$ N3 minimum (Figure 3.5D), and that the earliest Spathian $\delta^{13}C_{carb}$ P3 maximum was associated with reduced global-ocean anoxia (Figure 3.2).

Another mechanism was proposed by Horacek et al. (2007), who argued that the late Smithian negative $\delta^{13}C_{carb}$ excursion was driven by the overturn of a previously stratified ocean, leading to release of isotopically light dissolved inorganic carbon, derived from remineralized organic matter, into the ocean surface layer. This model predicts development of peak anoxia just prior to the $\delta^{13}C_{carb}$ N3 minimum, which is broadly consistent with our U-isotope record. However, the overturn event should have led to rapid ventilation of the deep ocean, effectively concurrently with the N3 minimum, rather than during the subsequent P3 maximum, as actually recorded in our U-isotope profile (Figure 3.2). More fundamentally, this model is inconsistent with conodont $\delta^{18}O$ records showing peak warming during the Late Smithian Thermal Maximum (Sun et al., 2012; Romano et al., 2013), as strong warming flattens equator-to-pole temperature gradients, thus reducing oceanic overturning circulation (cf. Barron and Washington, 1982; Huber et al., 1995).

Shallow-to-deep gradients in $\delta^{13}C_{carb}$ ($\Delta^{13}C$) show large values (~3-8 ‰) during the Griesbachian to Smithian substages of the Early Triassic, but a sharp decline in the Spathian (Meyer et al., 2011; Song-HY et al., 2013). Meyer et al. (2011) attributed the large pre-SSB $\Delta^{13}C$ values to increased ocean-surface productivity and export of isotopically light organic carbon to the thermocline, and the decline in $\Delta^{13}C$ at the SSB to sharply diminished productivity, and they linked these patterns to strong ocean anoxia in the pre-SSB interval and reduced anoxia at the SSB. In contrast, Song-HY et al. (2013) argued that only intense oceanic stratification was likely to yield $\delta^{13}C$ gradients as large as 8 ‰, and that the negative $\Delta^{13}C$ values observed in the earliest Spathian (to –2 ‰) were a consequence of localized upwelling of ^{13}C-depleted thermocline waters. The redox-C-isotope relationship inferred by Meyer et al. (2011) is broadly consistent with the U-based

redox results of the present study, although the predictions of Song-HY et al. (2013) regarding enhanced upwelling at the SSB appear to be supported by evidence based on biomarkers (Saito et al., 2013) and C-S isotopic studies (Zhang et al., 2015, 2018c; Stebbins et al., 2018).

Our U-isotope results appear to be consistent with the oceanographic model proposed by Song-HY et al. (2013) and Zhang et al. (2015). That model invoked intensified stratification linked to late Smithian hyperwarming as the immediate driver of the large shallow-to-deep $\Delta^{13}C$ at N3, which reduced upwelling of ^{12}C-enriched DIC to the ocean-surface layer. Intensified stratification also caused a concurrent shift toward lower $\delta^{13}C_{carb}$ owing to reduced productivity rates in the absence of nutrient resupply through upwelling (Song-HY et al., 2013). Climatic cooling had the opposite effect, invigorating thermohaline overturning circulation in the global ocean and breaking down oceanic stratification (cf. Clark et al., 2002; Stouffer et al., 2006). More vigorous circulation led to upwelling of nutrients from the thermocline, stimulating marine productivity (cf. Sarmiento et al., 2003; Whitney et al., 2005), an effect recorded by the large positive N3-to-P3 $\delta^{13}C$ excursion straddling the SSB (Song-HY et al., 2013). This model predicts development of peak ocean anoxia around the $\delta^{13}C_{carb}$ N3 minimum and a sharp reduction in anoxia during the N3-to-P3 shift associated with the SSB, which closely mirrors our U-isotope redox record (Figure 3.2).

3.8.2 Modeling implications

In order to evaluate the role of increased riverine phosphate versus the decrease in ocean overturning circulation triggered by the LSTM on $\delta^{13}C$ variation during the SSB

transition, we employed a simple carbon cycle box model similar to that used in Kump and Arthur (1999) to simulate the surface-ocean carbon isotope evolution. The assumed oceanic-atmospheric CO_2 reservoir size during the Early Triassic was 4.9×10^{18} mol (Cui et al., 2013) significantly higher than the canonical value of 3.8×10^{18} mol due to the higher DIC concentration in the Early Triassic Neritan ocean (Ridgwell, 2005). The steady-state $\delta^{13}C$ value is +0.8 ‰, which closely matches the $\delta^{13}C$ value from shallow-marine carbonates at Zuodeng (Figure 3.2B). The steady-state model was initially perturbed by a 50 % decrease in thermohaline circulation strength and then by a two-fold increase in riverine phosphate flux, each of which was sustained for 220 kyr from 250.8 Ma to 250.58 Ma (Figure 3.7).

A decrease in ocean circulation strength is a likely consequence of elevated global temperatures, as demonstrated in many studies (e.g. Liu et al., 2017; Stouffer et al., 2006). In the model simulation reducing ocean circulation strength by 50 %, we noticed that the organic carbon burial rate decreased by 50 % immediately following the perturbation, and then overshot the steady-state value by 70 % (Figures 3.7A and B). The immediate response of carbon isotopes to decreased ocean turnover rate (and therefore reduced organic carbon burial, or $F_{b,org}$) was a decrease in $\delta^{13}C$, followed by a 3 ‰ increase in $\delta^{13}C$ in response to an increase in $F_{b,org}$ during relaxation of the perturbation. At the end of the simulation, the $\delta^{13}C$ value remained elevated by 0.2 ‰. During the decreasing phase of $F_{b,org}$, pCO_2 increased by 28 % due to the effect of slower overturning circulation alone. However, there was no net change in $F_{b,org}$ and pCO_2 after the perturbation was removed, which is inconsistent with the subsequent decrease in SSTs based on the conodont oxygen isotope record (Sun et al., 2012). Extreme warming occurred when $\delta^{13}C$ values reached

their minimum values immediately before the SSB, whereas the cooling occurred immediately after the SSB (Figs. 3.2 and 3.6). The size of the positive $\delta^{13}C$ excursion following the recovery of thermohaline circulation in the model simulation (Figure 3.7B) appears to be slightly smaller (~4‰) than that observed in actual $\delta^{13}C$ records, suggesting additional contributions from other sources.

An increase in riverine phosphate flux is a likely consequence of climatic warming and enhanced chemical weathering (Bluth and Kump, 1994; Hartmann et al., 2014; Zhang et al., 2018a). In the model simulation doubling the riverine delivery of phosphate, we included the pCO_2-dependent silicate weathering feedback, in which as pCO_2 increases, silicate weathering rate goes up proportionally, similar to that implemented in Kump and Arthur (1999). We also imposed a 100% increase in carbonate weathering rate in order to connect riverine phosphate input with the riverine carbon input. The model results show an initial 1 ‰ negative excursion in marine carbonate $\delta^{13}C$, followed by a ~3.5 ‰ positive excursion, as a direct result of the increased $F_{b,org}$ due to elevated phosphate levels in the surface ocean, promoting primary productivity (Figure 3.7C, D). Because the model included a realistic pCO_2-dependent silicate weathering feedback, as the perturbation is removed, pCO_2 first increases to 3500 ppm, followed by a decrease to 2600 ppm, and finally a gradual stabilization at 2800 ppm (i.e., the pre-perturbation level). This drop in pCO_2 would have led a further decrease in global temperatures into the early Spathian, consistent with the oxygen isotope evidence suggesting a gradual cooling following the SSB.

The modeling results are thus consistent with both a decrease in ocean overturning circulation and an increase in riverine phosphate flux. Both developments were ultimately

driven by the extreme global warming of the Late Smithian Thermal Maximum, which played a fundamental role in driving global-ocean redox variation and carbon cycle changes during the SSB transition.

3.9 Oceanic anoxia and the SSB marine biotic crisis

Following the end-Permian mass extinction event, the recovery of marine ecosystems during the Early Triassic was a fitful process (Chen and Benton, 2012). Some marine clades, such as conodonts and ammonoids, rebounded rapidly from the end-Permian mass extinction (Orchard, 2007; Brayard et al., 2009; Stanley, 2009; Chen and Benton, 2012). However, the diversity levels of these clades underwent another major decline in late Smithian (Brayard et al., 2009; Stanley, 2009) before a more sustained recovery during the Spathian (Chen et al., 2011; Payne et al., 2011; Song-HJ et al., 2011; Chen and Benton, 2012).

Ocean acidification and high SSTs are commonly cited causes of the SSB marine biotic crisis (Galfetti et al., 2008; Sun et al., 2012; Saito et al., 2013). Here, our study highlights that, apart from any changes in seawater pH or sea-surface temperatures, the expansion of oceanic anoxia during the late Smithian is likely to have been another significant stress on contemporaneous marine organisms and communities (Figure 3.6). The expansion of anoxic/hypoxic zones in the modern ocean is at the top of the list of emerging environmental challenges for marine organisms (Diaz and Rosenberg, 2008). Anoxia/hypoxia affects organisms through reduced growth and reproduction, physiologic stress, forced migration, reduction of suitable habitat, increased vulnerability to predation, and disruption of life cycles, and ultimately leads to death if sustained for too long

(Rabalais et al., 2002; Vaquer-Sunyer and Duarte, 2008). Our modeling results suggest that anoxic seafloor areas expanded to ~15 % during the late Smithian, an intensification sufficient to have driven the contemporaneous marine biocrisis. Concurrent warming during the late Smithian (Sun et al., 2012; Romano et al., 2013) would have compounded the harmful effects of anoxia because marine organisms tend to have higher O_2 requirements at higher temperatures (Portner and Knust, 2007).

In addition to physiological stresses on marine organisms, expansion of oceanic anoxia would have had major consequences for the biogeochemical cycling of bioessential elements such as C, N, S, P, Fe, and Mo (Keeling et al., 2010). For instance, at near-zero O_2 levels, sulfate-reducing microbes reduce large quantities of sulfate, leading to production of highly toxic H_2S (e.g., Kump et al., 2005; Algeo et al., 2008; Shen et al., 2011; Zhang et al., 2017). Additionally, some redox-sensitive trace metals (e.g., Fe and Mo) are essential micronutrients that can influence the growth and structure of phytoplankton communities (e.g., Behrenfeld and Kolber, 1999; Glass et al., 2012; Twining and Baines, 2013). During periods of expanded ocean anoxia, concentrations of bioessential redox-sensitive trace metals in seawater can decrease significantly (e.g., Anbar and Knoll, 2002; Grasby et al., 2012; Reinhard et al., 2013; Takahashi et al., 2014). The depletion of bioessential trace metals in the ocean would have influenced marine N and C fixation, potentially leading to instability of marine ecosystems or even mass mortality (e.g., Stüeken et al., 2015; Long et al., 2016a).

3.10 Conclusions

We studied $\delta^{238}U$ variations in carbonates from the middle Smithian to the middle Spathian in two paleogeographically widely separated sections: the Zuodeng section in South China, which was located on the eastern side of the paleo-Tethys, and the Jesmond section in British Columbia, which was located on the western side of the Panthalassic Ocean. These two sections allowed us to test the robustness of carbonate $\delta^{238}U$ as a global-ocean redox proxy through the SSB transition. The $\delta^{238}U$ profiles of these sections show large, synchronous secular variations, with negative values in the late Smithian (mean: −0.52 ‰), a positive shift at the SSB (mean: −0.32 ‰), and a second negative shift in the early-middle Spathian (mean: −0.37 ‰).

We used a simple U isotope mass balance model to quantify global-ocean redox variation through the Smithian-Spathian. During the late Smithian, ~65 % of seawater U was removed to anoxic facies, corresponding to an anoxic seafloor area equal to ~11 % of total seafloor area. Across the SSB, the fraction of seawater U removed to anoxic facies decreased to ~48 %, and anoxic seafloor area was reduced to just ~2 %. During the early-middle Spathian, the fraction of seawater U removed to anoxic facies increased again, to ~70 %, and anoxic seafloor area expanded to 10–13 % of total seafloor area.

Global-ocean redox variation through the SSB transition shows a good first-order correspondence to previously published topical sea surface temperature records, which record a hyperthermal event (the Late Smithian Thermal Maximum) prior to the SSB and a strong cooling event at the SSB. Our U-isotope results suggest that the late Smithian hyperthermal event was the immediate causes of expansion of oceanic anoxia prior to the SSB, and that the subsequent cooling event was responsible for the reduction of oceanic

anoxia at the SSB. Expanded oceanic anoxia during the late Smithian coincided with a renewed biocrisis among some marine invertebrate clades, including conodonts and ammonoids, suggesting that redox changes played an important role in the SSB extinctions.

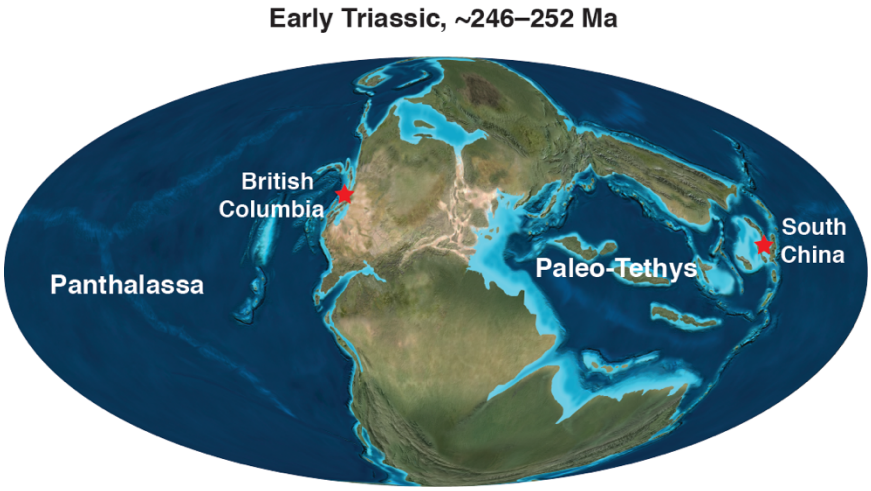

Figure 3.1 Palaeogeography illustrating the position of the Jesmond Second (British Columbia) and the Zuodeng Section (South China) during the Early Triassic (Colorado Plateau Geosystems image, updated by Ron Blakey, 2018).

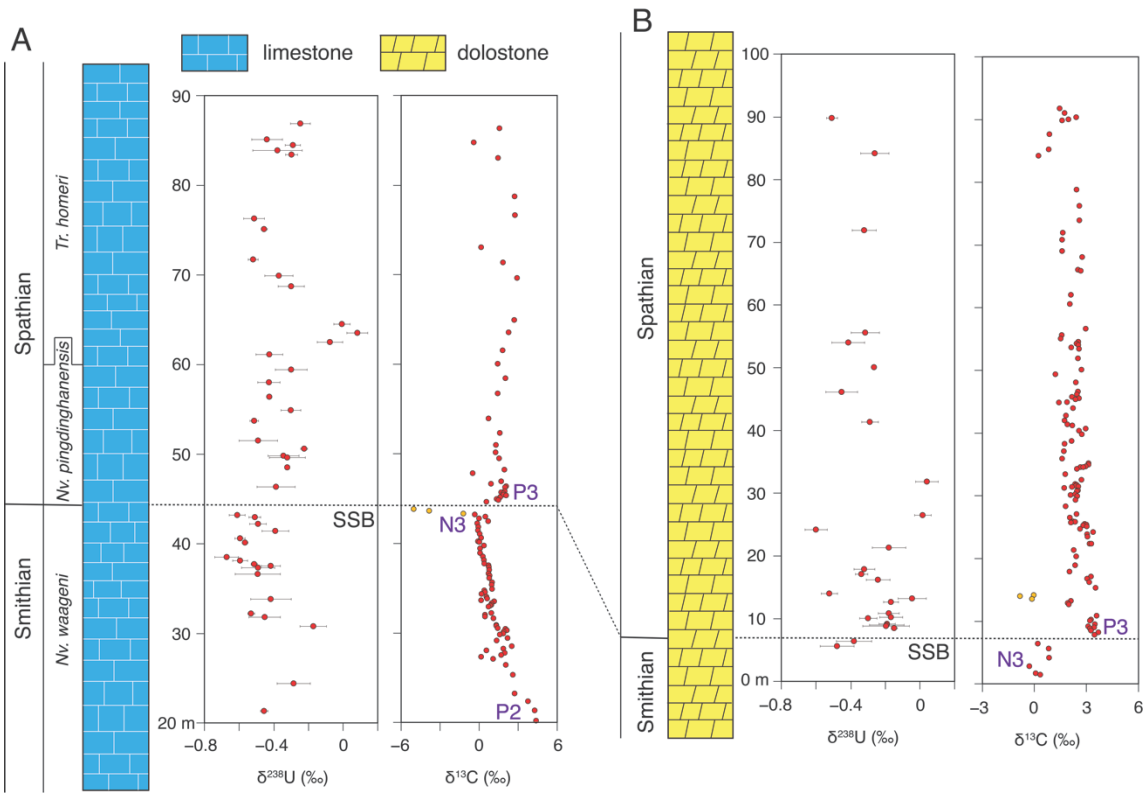

Figure 3.2 A. $\delta^{238}U$ and $\delta^{13}C$ profiles for the Zuodeng section, South China. B. $\delta^{238}U$ and $\delta^{13}C$ profiles for the Jesmond section, British Columbia. The $^{238}U/^{235}U$ ratios are reported in per mille using standard δ-notation, where $\delta^{238}U = [(^{238}U/^{235}U)_{sample} / (^{238}U/^{235}U)_{standard(CRM145)} - 1] \times 1000$.

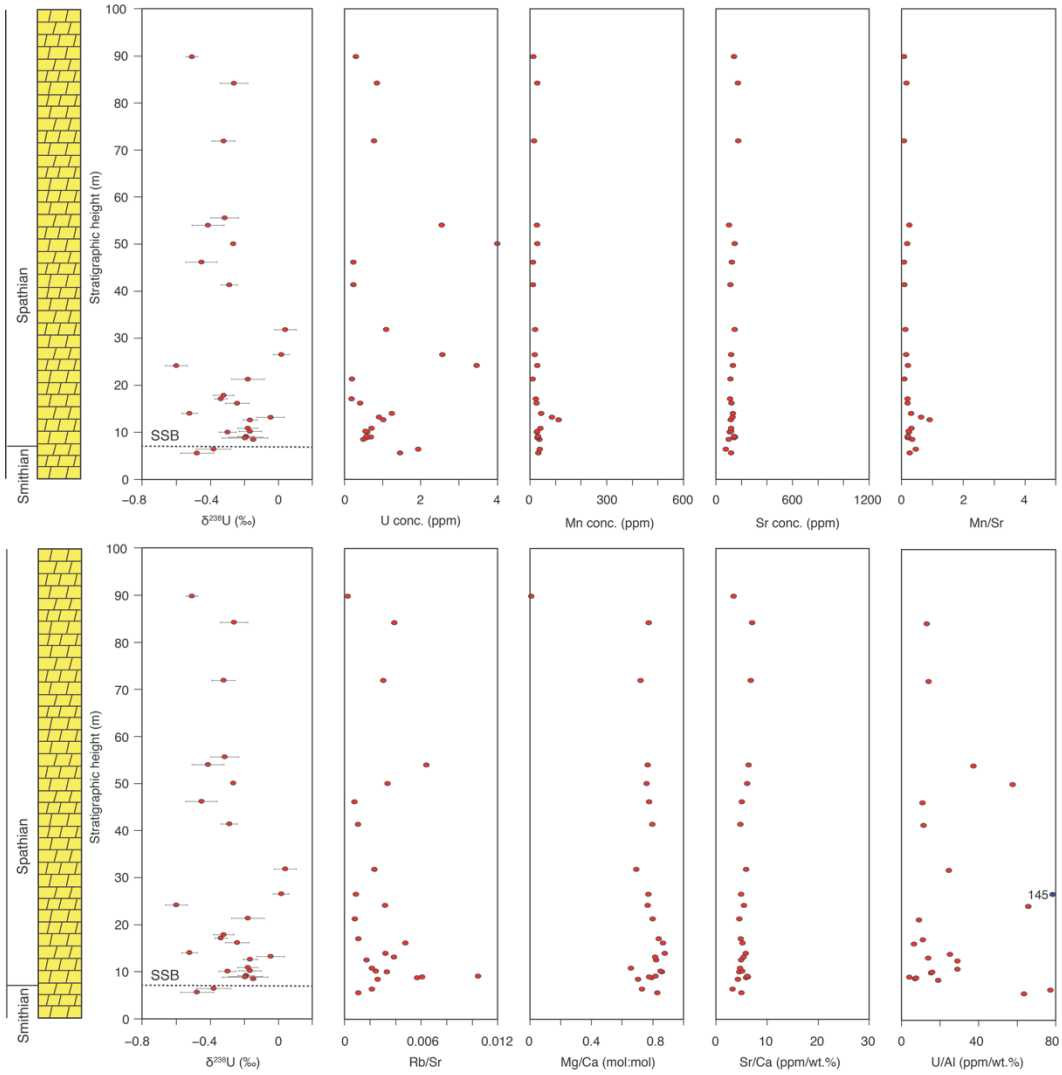

Figure 3.3 Geochemical profiles for the Jesmond section, British Columbia.

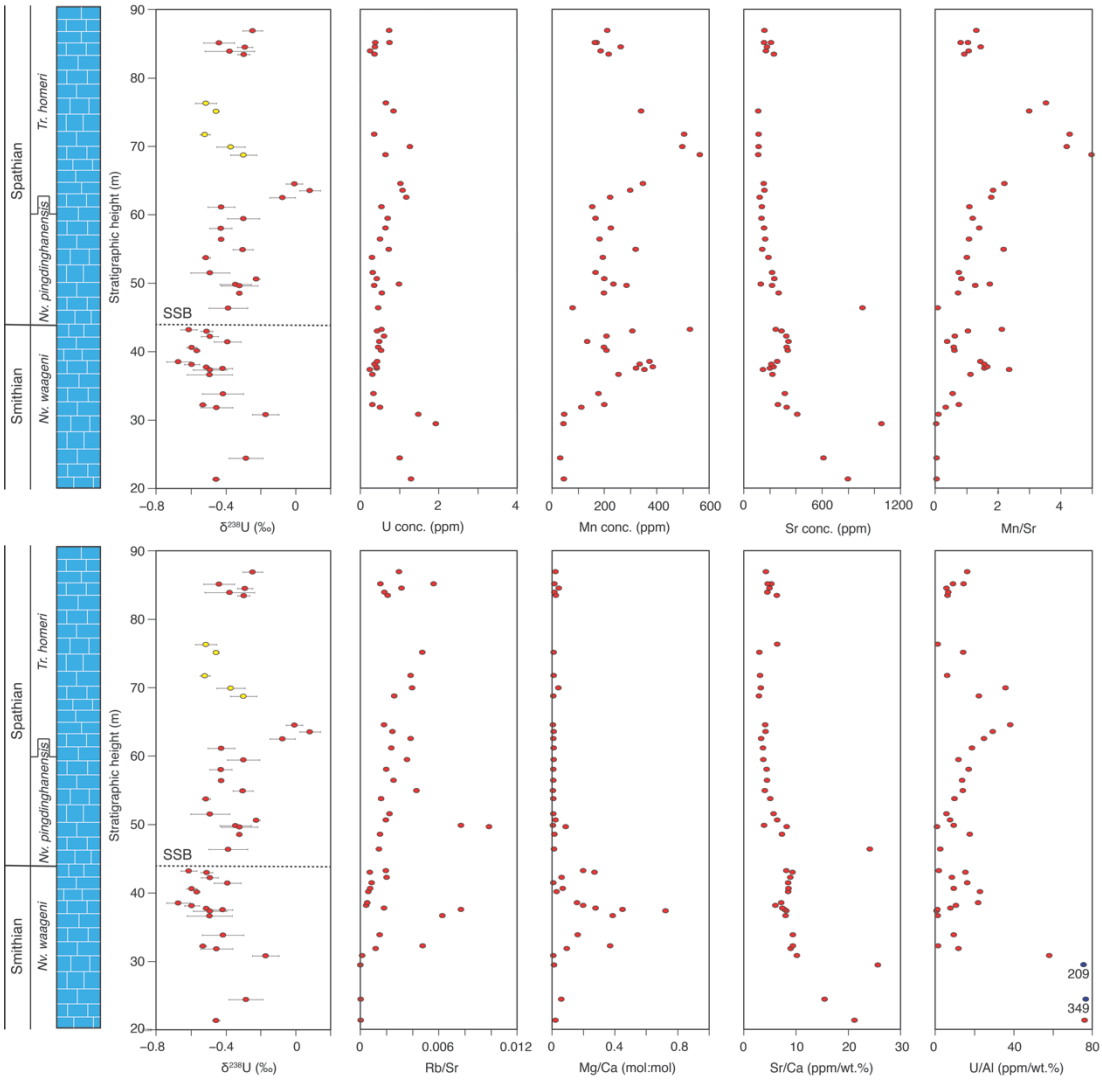

Figure 3.4 Geochemical profiles for the Zuodeng section, South China. δ^{238}U of samples with Mn/Sr ratio > 2.5 have been marked in yellow. We note that samples above 61.1 m have been excluded in the marine U-cycle mass balance model calculation because of relative low δ^{238}U data resolution when excluding the five "outlier" with Mn/Sr ratio > 2.5.

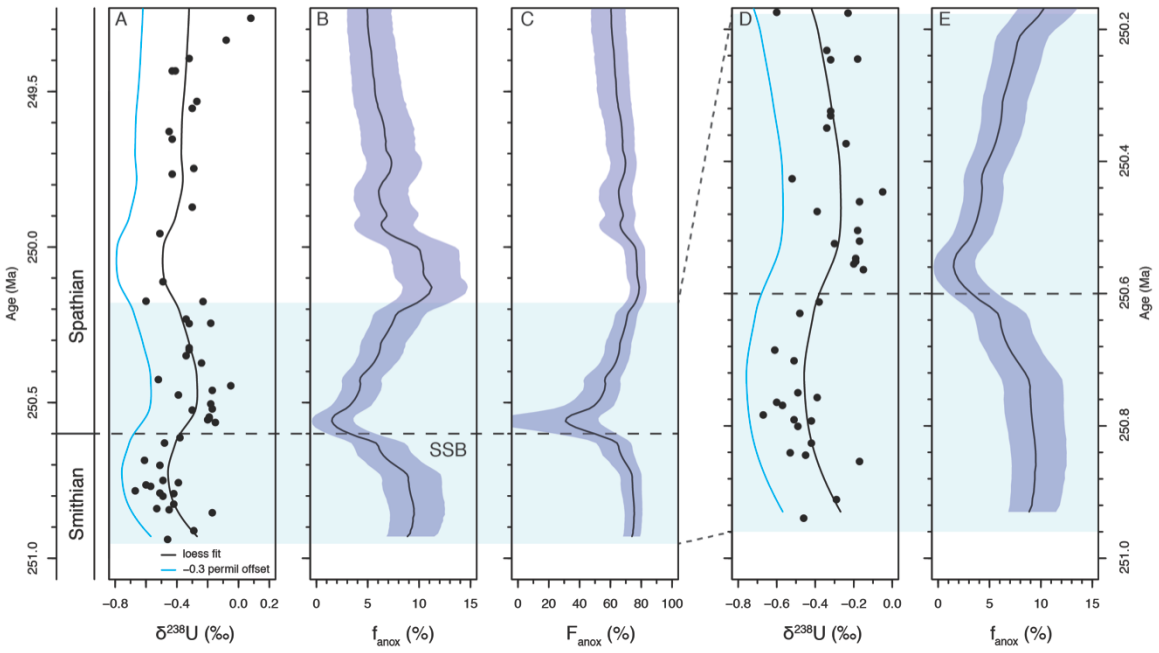

Figure 3.5 Marine U-cycle mass balance model**.** δ^{238}U data used in the model are a combination of data from the Zuodeng section (South China) and the Jesmond section (British Columbia). A. δ^{238}U data with LOWESS smoothing fit. The black curve denotes LOWESS smoothing fit of the original data, the green curve denotes the LOWESS smoothing fit curve minus a 0.3‰ early diagenesis offset. B. Calculated anoxic seafloor area (f_{anoxic}) using inverse modeling approach. C. Model estimates of U removal into anoxic sedimentary sinks (F_{anoxic}). D. Close-up view of δ^{238}U from 251 to 250.2 Ma (loess curve colors are the same as in A). E. Close-up view of modeled anoxic seafloor area (f_{anoxic}) from 251 to 250.2 Ma. Because δ^{238}U data resolution < 249.4 Ma is relative low, our U-cycle mass balance model is primarily focused on 251 to 249.4 Ma. We note that the δ^{238}U data < 249.4 Ma also show some interesting trends, and we encourage high-resolution δ^{238}U studies to confirm these trends and to build a more solid U mass balance model in the future.

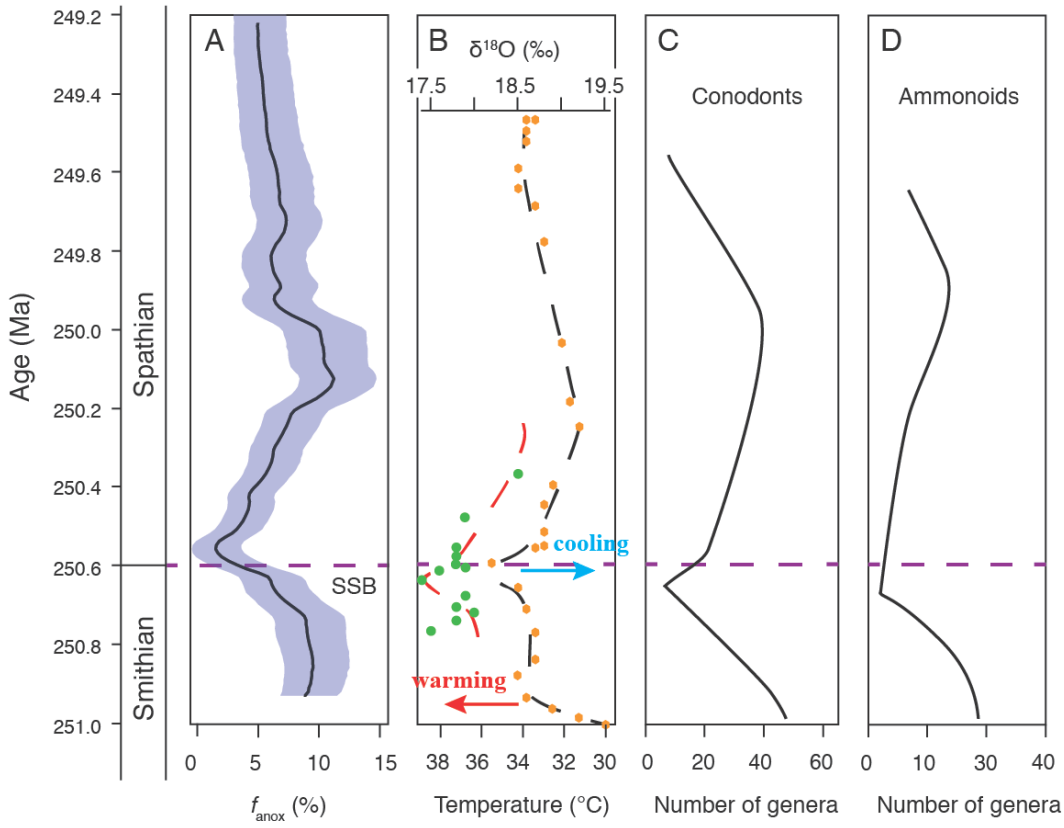

Figure 3.6 Marine redox, climatic change, and the number of genera of selected marine species (conodonts and ammonoids) relationships. A. Model estimates of anoxic seafloor area (f_{anoxic}). B. Previously published $\delta^{18}O$ data and estimated temperature curve across the SSB (according to Sun et al. (2012)). C. Changes in numbers of conodonts species across the SSB (according to Stanley (2009)). D. Changes in numbers of ammonoids species across the SSB (according to Stanley (2009).

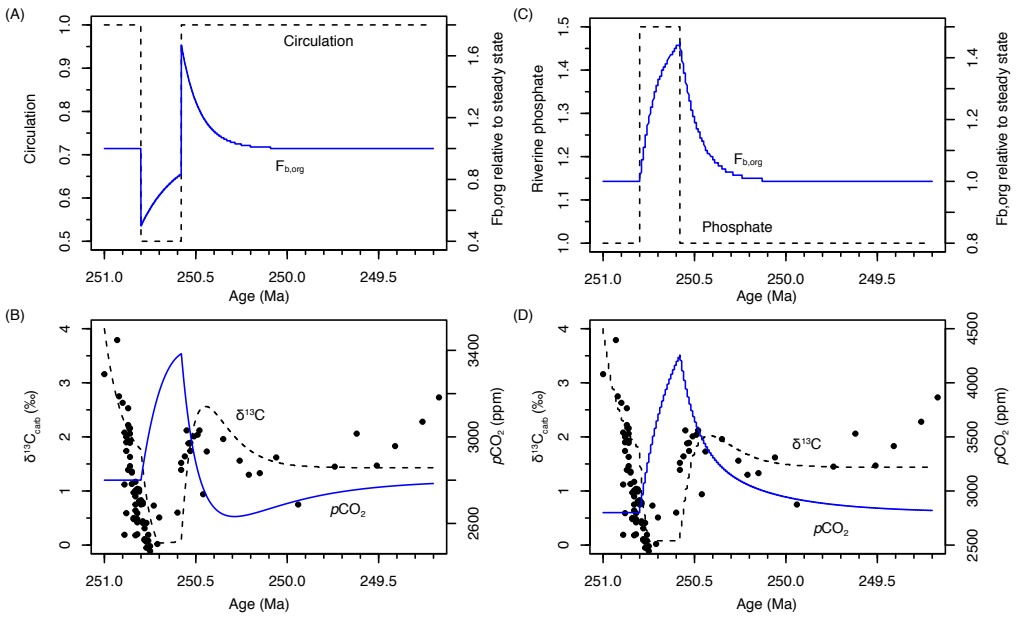

Figure 3.7 (A) Modeled response of global organic carbon burial rate ($F_{b,org}$; solid blue line) from 251.0 to 249.2 Ma due to 50% decrease in thermohaline circulation (dashed line) which persists for 200 kyr; (B) Modeled response of carbon isotopic composition of marine carbonate and atmospheric pCO_2 from the same forcing as A. (C) 100% increase in riverine phosphate flux which lasts 200 kyr (dashed line) and the resulting changes in $F_{b,org}$ (solid blue line); and (D) Modeled response of carbon isotopic composition of marine carbonate and atmospheric pCO_2 from the same forcing as C.

Table 3.1 Carbonate U isotope data ($\delta^{238}U$), C isotope data ($\delta^{13}C$), and O isotope data ($\delta^{18}O$) from the Smithian-Spathian boundary interval at the Zuodeng section, South China.

Sample number	Height	$\delta^{13}C_{carb}$	$\delta^{18}O_{carb}$	$\delta^{238}U_{carb}$	2SD	$\delta^{238}U_{carb}$ 2SD
	cm	‰	‰	‰	‰	Replicates (‰)
ZD BR B+390	8690			-0.25	0.06	
ZD BR B+330	8630	1.60	-9.10			
ZD BR B+210	8510			-0.44	0.09	
ZD BR B+170	8470	-0.38	-12.50			
ZD BR B+150	8450			-0.29	0.04	
ZD BR B+90	8390			-0.38	0.14	
ZD BR B+40	8340			-0.30	0.03	
ZD BR BASE	8300	1.49	-6.81			
ZD 21 B+3200	7870	2.77	-6.88			
ZD 21 B+2990	7660	2.78	-7.70			
ZD 21 B+2960	7630			-0.51	0.06	
ZD 21 B+2840	7510			-0.46	0.02	
ZD 21 B+2630	7300	0.19	-6.32			
ZD 21 B+2500	7170			-0.52	0.03	
ZD 21 B+2460	7130	1.87	-7.31			
ZD 21 B+2320	6990			-0.37	0.08	
ZD 21 B+2290	6960	2.94	-6.84			
ZD 21 B+2200	6870			-0.30	0.08	
ZD 21 B+1820	6490	2.73	-6.97			
ZD 21 B+1780	6450			-0.01	0.05	
ZD 21 B+1680	6350	2.28	-5.94	0.08	0.06	
ZD 21 B+1580	6250			-0.08	0.07	
ZD 21 B+1480	6150	1.83	-6.75			
ZD 21 B+1440	6110			-0.43	0.08	
ZD 21 B+1330	6000	1.47	-6.00			
ZD 21 B+1270	5940			-0.30	0.09	
ZD 21 B+1170	5840	2.06	-6.10			
ZD 21 B+1130	5800			-0.43	0.06	
ZD 21 B+1000	5670	1.45	-5.41			
ZD 21 B+970	5640			-0.43	0.01	
ZD 21 B+820	5490			-0.30	0.06	

ZD 21 B+720	5390	0.75	-6.28				
ZD 21 B+700	5370			-0.51	0.02		
ZD 21 B+560	5230	1.62	-5.83				
ZD 21 B+470	5150			-0.49	0.11		
ZD 21 B+415	5095	1.33	-6.16				
ZD 21 B+380	5060			-0.23	0.02		
ZD 21 B+330	5010	1.30	-6.79				
ZD 21 B+300	4980			-0.34	0.09		
ZD 21 B+280	4960			-0.32	0.10		
ZD 21 B+265	4945	1.56	-6.15				
ZD 21 B+170	4850			-0.32	0.01		
ZD 21 B+140	4820	1.96	-6.04				
ZD 21 B+100	4780	-0.46	0.10				
ZD 21 B+10	4690	1.73	-6.14				
ZD 20 B+230	4660	0.94	-6.51				
ZD 20 B+205	4635	2.12	-6.04	-0.39	0.11	-0.37	0.10
ZD 20 B+190	4620	2.04	-5.06				
ZD 20 B+150	4580	2.01	-5.69				
ZD 20 B+135	4565	1.74	-5.78				
ZD 20 B+125	4555	1.89	-4.48				
ZD 20 B+110	4540	1.88	-6.23				
ZD 20 B+100	4530	2.12	-5.94				
ZD 20 B+80	4510	1.64	-6.12				
ZD 20 B+60	4490	1.39	-5.44				
ZD 20 B+50	4480	1.52	-6.19				
ZD 20 B+30	4460	0.60	-7.05				
ZD 19 B+50	4380	-5.02	-11.16				
ZD 19 B+30	4360	-3.83	-11.47				
ZD 19 BASE	4330	-1.19	-12.01				
ZD 18 T	4320	-0.31	-6.42	-0.61	0.05		
ZD 18 T-25	4295	0.51	-5.60	-0.51	0.03		
ZD 18 T-45	4275	0.02	-6.97				
ZD 18 T-75	4245	0.73	-7.25				
ZD 18 T-100	4220	-0.11	-6.36	-0.49	0.05		
ZD 18 T-140	4180	-0.02	-6.52				
ZD 18 T-180	4140	-0.06	-6.04	-0.39	0.08		

ZD 18 T-220	4100	0.08	-5.66				
ZD 18 T-260	4060	0.19	-5.87	-0.60	0.03		
ZD 18 T-300	4020	-0.05	-5.80				
ZD 17 T	4010	0.06	-5.71	-0.57	0.02		
ZD 17 T-40	3970	0.41	-5.23				
ZD 17 T-70	3940	0.11	-5.44				
ZD 17 T-120	3890	0.09	-6.61				
ZD 17 T-160	3850	0.31	-5.58	-0.67	0.07		
ZD 17 T-200	3810	0.41	-5.76	-0.59	0.04		
ZD 17 T-240	3770	0.44	-5.77	-0.51	0.02		
ZD 16 T-10	3750	0.76	-5.34	-0.42	0.06		
ZD 16 T-30	3730	0.79	-4.52	-0.49	0.10		
ZD 16 middle	3700	0.80	-5.00				
ZD 15 B+300	3660	0.75	-5.35	-0.49	0.13		
ZD 15 B+275	3635	0.83	-5.08				
ZD 15 B+250	3610	0.81	-5.28				
ZD 15 B+200	3560	1.03	-5.05				
ZD 15 B+175	3535	0.99	-5.18				
ZD 15 B+125	3485	1.04	-5.31				
ZD 15 B+110	3470	0.42	-5.53				
ZD 15 B+90	3450	0.48	-5.35				
ZD 15 B+70	3430	0.20	-5.70				
ZD 15 B+40	3400	0.59	-5.09				
ZD 15 B+20	3380	0.64	-5.86	-0.42	0.12		
ZD 15 BASE	3360	0.18	-5.91				
ZD 14 B+240	3350	1.17	-4.70				
ZD 14 B+220	3330	1.01	-5.02				
ZD 14 B+200	3310	0.97	-4.63				
ZD 14 B+190	3300	0.90	-5.15				
ZD 14 B+180	3290	0.75	-5.18				
ZD 14 B+110	3220	0.97	-5.07	-0.53	0.02	-0.53	0.07
ZD 14 B+90	3200	0.48	-5.60				
ZD 14 B+70	3180	0.50	-5.73	-0.45	0.09		
ZD 14 B+50	3160	1.13	-4.29				
ZD 13 B+85	3085	1.36	-8.45				
ZD 13 B+75	3075	1.34	-7.81	-0.17	0.08		

ZD 13 B+50	3050	1.46	-7.37				
ZD 13 B+35 to +40	3040	2.06	-6.44				
ZD 13 B+20 to +25	3025	2.16	-6.97				
ZD 13 B+10	3010	1.93	-8.17				
ZD 12 T-10	2990	1.89	-6.98				
ZD 12 T-20	2980	1.63	-6.81				
ZD 12 T-60	2940	2.22	-6.68	0.41	0.06		
ZD 12 T-90	2910	1.39	-6.30				
ZD 12 T-150	2850	2.53	-6.89				
ZD 12 T-180	2820	1.90	-6.67				
ZD 12 T-200	2800	0.59	-7.04				
ZD 10 T-0 to T-12	2775	2.00	-9.92				
ZD 10 T-30	2750	1.74	-6.82				
ZD 10 T-50	2730	0.19	-6.35				
ZD 10 BASE	2705	1.12	-6.55				
ZD 9 B+440	2640	2.08	-7.39				
ZD 9 B+330	2530	2.63	-6.57				
ZD 9 B+240	2440			-0.29	0.10		
ZD 9 B+120	2320	2.75	-7.75				
ZD 9 B+35	2235	3.79	-6.05				
ZD 7 T-10	2130	4.30	-7.94	-0.46	0.02	-0.44	0.04
ZD 7 T-125	2015	4.41	-6.87				

Table 3.2 Carbonate U isotope data ($\delta^{238}U$), C isotope data ($\delta^{13}C$), and O isotope data ($\delta^{18}O$) from the Smithian-Spathian boundary interval at the Jesmond section, British Columbia.

Sample number	Height	$\delta^{13}C_{carb}$	$\delta^{18}O_{carb}$	$\delta^{238}U_{carb}$	2SD	$\delta^{238}U_{carb}$	2SD
	m	‰	‰	‰	‰	Replicate (‰)	
JE16-10	91.7	1.48	-4.6				
JE14-7	91	1.77	-2.8				
JE16-9	90.3	2.43	-3.67				
JE14-6	90	1.99	-2.64				
JE16-8	89.8	1.62	-4.4	-0.51	0.03		
JE14-5	87.6	0.88	-4.15				
JE14-4	85.2	0.84	-4.23				
JE14-3	84.2	0.25	-4.2	-0.26	0.08		
JE14-2	78.8	2.45	-2.74				
JE14-1	76.2	2.61	-1.58				
JE13-7	73.9	2.62	-2.11				
JE13-6	71.9	1.66	-3.41	-0.32	0.07		
JE13-5	70.8	1.61	-3.57				
JE13-4	69	1.61	-4.27				
JE13-3	68	2.77	-0.92				
JE13-2	66	2.54	-1.81				
JE13-1	65.8	2.7	-1.61				
JE12-6	62	2.12	-3.79				
JE12-5	60.55	2.06	-4.05				
JE12-2	56.6	2.97	-0.98				
JE12-1	55.6	1.6	-3.38	-0.32	0.08		
JE11-5	55	1.53	-3.51				
JE11-4	54.5	2.56	-2.39				
JE11-3	54.25	2.46	-1.83				
JE11-2	54	2.55	-2.44	-0.41	0.09	-0.35	0.02
JE11-1	53.6	2.15	-3.13				
JE10-8	53.4	2.6	-2.2				
JE10-6	51.85	2.53	-4.73				
JE10-4	50.05	2.74	-2.29	-0.27	0.01		
JE10-3	49.35	1.23	-5.15				
JE10-2	48.05	2.41	-4.82				

JE9-13	46.55	2.53	-3.91				
JE9-12	46.15	2.48	-3.73	-0.45	0.09		
JE9-11	45.75	2.18	-4.02				
JE9-10	45.5	2.59	-2.49				
JE9-9	45.35	2.4	-3.35				
JE9-8B	44.9	1.9	-3.89				
JE9-8A	44.8	1.44	-4.86				
JE9-7	43.95	2.24	-3.97				
JE9-6A	42.75	1.84	-3.89				
JE9-5	41.95	1.77	-5.11				
JE9-4	41.35	1.92	-3.93	-0.29	0.05	-0.31	0.06
JE9-3	41.15	2.2	-3.44				
JE9-2	40.65	2.97	-2.76				
JE9-1A	40.35	2.59	-4.21				
JE8-10	39.75	2.75	-3.23				
JE8-9	38.7	2.17	-4.19				
JE8-8	38.25	1.77	-4.08				
JE8-7	37.05	1.73	-3.58				
JE8-6	35.9	1.62	-4.3				
JE8-4	35.15	3.14	-3.49				
JE8-3	34.9	3.15	-3.59				
JE8-2	34.65	2.98	-3.41				
JE8-1	34.5	2.68	-3.33				
JE7-4	34.5	2.83	-3.65				
JE7-3B	34.25	2.47	-3.46				
JE7-2	33.4	1.81	-4.78				
JE6-10	32.5	2.74	-2.92				
JE7-1	31.85	2.38	-4.29				
JE6-8E	31.8			0.04	0.06		
JE6-8D	31.7	2.45	-3.79				
JE6-8C	31.55	2.42	-4.12				
JE6-8B	31.45	2.56	-3.63				
JE6-8A	31.35	2.18	-3.96				
JE6-7	31.2	1.74	-3.3				
JE6-6	30.8	2.54	-3.84				
JE6-5	30.7	2.47	-3.52				

JE6-4B	30.2	2.38	-3.45				
JE6-4A	30.1	2.1	-4.41				
JE6-3	29.9	2.5	-3.94				
JE6-2	29.3	2.4	-3.84				
JE5-8	28.3	1.83	-4.4				
JE5-7	27.05	2.45	-3.97				
JE5-6	26.5	2.07	-4.46	0.02	0.05		
JE5-5	25.85	2.25	-4.28				
JE5-4	25.8	2.36	-4.63				
JE5-3	25.7	2.13	-4.07				
JE5-2B	25.45	2.92	-2.41				
JE5-2A	25.35	3.01	-2.52				
JE5-1	25.25	2.84	-2.69				
JE4-10	25.05	3.05	-2.75				
JE4-9	24.65	2.66	-3.48				
JE4-8	24.15	3.41	-3.07	-0.60	0.06		
JE4-7	23.85	3.07	-2.87				
JE4-6	23.45	3.08	-2.72				
JE4-5A	22.3	3.21	-2.92				
JE4-5	22.3	3.31	-2.02				
JE4-4	21.3	2.29	-4.91	-0.18	0.10		
JE4-3	20.3	2.43	-4.17				
JE4-2	18.85	2.38	-4.45				
JE4-1	17.85	2.04	-4.77	-0.32	0.06	-0.25	0.05
JE3-4	17.1	3.28	-3.91	-0.34	0.04		
JE3-3	16.75	3.06	-2.94				
JE3-2	16.15	3.19	-3.13	-0.24	0.07	-0.24	0.06
JE3-1	15.25	3.54	-3.39				
JE2-6	14.15	-0.02	-4.46				
JE2-5	14	-0.82	-4.46	-0.52	0.05	-0.60	0.06
JE2-4	13.55	-0.13	-4.19				
JE2-3	13.2	2.12	-2.98	-0.05	0.08		
JE2-1A	12.85	1.94	-4.49				
JE2-1	12.6	2	-4.18	-0.17	0.04		
JE1-9	10.85	3.61	-2.78	-0.18	0.06	-0.20	0.06
JE1-8	10.2	3.28	-3.13	-0.17	0.07		

JE1-7	10.05	3.23	-2.84	-0.30	0.05
JE1-6	9.5	3.51	-2.48		
JE1-5	9.15	3.12	-2.97	-0.19	0.05
JE1-4	8.95	3.47	-3.1	-0.19	0.10
JE1-3	8.8	3.23	-3.57	-0.20	0.13
JE1-2	8.45	3.29	-2.75	-0.15	0.02
JE1-1	8.2	3.7	-2.13		
JE1-0	7.8	3.48	-2.07		
JE17-6	6.4	0.22	-4.56	-0.38	0.10
JE17-5	5.6	0.84	-4.22	-0.48	0.10
JE17-4	4.1	0.87	-3.54		
JE17-3	2.8	-0.28	-4.2		
JE17-2	1.65	0.09	-4.49		
JE17-1	1.45	0.35	-4.34		

Table 3.3 Selected major and trace elemental results of carbonates for the Zuodeng section, South China.

Sample No.	Height m	Mg ppm	Al ppm	Ca ppm	Mn ppm	Sr ppm	Th ppm	U ppm
ZD 7T-10	2130	5083.98	170.64	377129.75	45.85	802.19	0.50	1.30
ZD 9B+240	2440	14442.47	28.97	394833.72	32.55	613.73	0.18	1.01
ZD 12T-60	2940	3702.11	92.56	409965.01	44.94	1056.93	0.28	1.94
ZD 13B+75	3075	2609.08	255.45	400545.73	47.45	412.25	0.19	1.49
ZD 14B+70	3180	20963.05	421.23	366262.79	113.57	331.28	0.41	0.51
ZD 14B+110	3220	62108.94	2000.77	279351.28	200.61	265.70	0.85	0.31
ZD 15B+20	3380	33543.77	354.30	336222.23	177.83	318.27	0.65	0.34
ZD 15B +300	3660	64852.91	2249.85	277860.83	254.89	224.20	0.77	0.31
ZD 16T-30	3730	78738.00	2890.94	181372.65	353.20	149.62	0.44	0.24
ZD 16T-10	3750	70014.90	3710.52	258994.52	321.40	204.18	1.06	0.43
ZD 17T-240	3770	51911.79	521.26	310769.40	386.42	232.78	0.38	0.41
ZD 17T-200	3810	41849.15	345.36	347300.27	335.58	213.72	0.20	0.37
ZD 17T-160	3850	34660.78	196.83	357288.63	373.50	259.08	0.26	0.43
ZD 17T	4010	7156.95	233.24	394616.65	209.30	339.97	0.19	0.53
ZD 18T-260	4060	16146.39	478.73	384972.78	198.89	331.95	0.30	0.46
ZD 18T-180	4140	2303.77	299.81	403497.95	135.12	345.76	0.21	0.49
ZD 18T-100	4220	14057.19	708.17	365567.85	208.50	330.19	0.62	0.61
ZD 18T-25	4295	50852.11	281.09	312172.48	307.85	293.60	0.42	0.44
ZD 18T	4320	36448.98	2846.05	302590.39	528.60	248.43	0.69	0.55
ZD 20B+205	4635	3094.76	1659.41	377853.65	79.19	914.13	0.46	0.46
ZD 21B+170	4850	3758.42	311.56	363819.63	200.01	269.65	0.47	0.55
ZD 21B+280	4960	14200.05	3860.18	266814.81	285.36	221.70	1.62	0.36
ZD 21B+300	4980	1550.38	1041.28	340328.42	236.15	134.99	0.97	0.99
ZD 21B+380	5060	5397.73	558.80	364700.49	200.56	237.02	0.50	0.43
ZD 21B+470	5150	2253.10	552.98	378611.66	166.86	219.95	0.45	0.33
ZD 21B+700	5370	2024.47	305.72	373659.97	195.07	191.86	0.49	0.30
ZD 21B+820	5490	1752.31	518.87	353415.87	320.28	146.20	0.62	0.74
ZD 21B+970	5640	1977.89	365.21	368569.65	182.83	168.33	0.47	0.51
ZD 21B+1130	5800	2265.96	377.38	360871.50	225.96	160.41	0.58	0.65
ZD 21B+1270	5940	2585.35	590.41	364380.49	166.98	139.14	0.59	0.71
ZD 21B+1440	6110	2556.63	289.89	374830.21	154.98	141.82	0.41	0.55

ZD 21B+1580	6250	2270.05	472.67	365989.31	222.90	124.69	0.49	1.18
ZD 21B+1680	6350	2548.93	370.01	383210.85	300.26	162.57	0.39	1.09
ZD 21B+1780	6450	1897.10	267.84	379641.65	347.86	157.73	0.29	1.03
ZD 21B+2200	6870	2142.97	292.29	380246.58	565.37	113.44	0.31	0.65
ZD 21B+2320	6990	9079.78	353.93	352871.56	498.28	118.67	0.62	1.27
ZD 21B+2500	7170	2396.40	577.05	366569.95	505.19	117.98	0.74	0.36
ZD 21B+2840	7510	2874.51	590.84	371784.83	341.47	113.68	0.62	0.85
ZD 21B+2960	7630	1666.54	4626.81	2512.47	5.77	1.63	10.79	0.65
ZD BR B+40	8340	5911.61	584.99	363753.04	216.86	233.16	0.56	0.37
ZD BR-B+90	8390	3857.38	374.56	374908.45	187.39	173.74	0.28	0.26
ZD BR-B+150	8450	9702.54	659.81	361360.65	263.83	181.84	0.53	0.38
ZD BR B+210	8510	3869.00	269.06	394302.10	172.05	211.64	0.32	0.39
ZD BR-B210	8510	3373.11	819.89	337086.65	165.02	157.91	0.74	0.75
ZD BR-B+390	8690	5427.26	447.76	372462.80	212.06	161.32	0.47	0.74

Table 3.4 Selected major and trace elemental results of carbonates for the Jesmond section, British Columbia.

Sample No.	Height	Mg	Al	Ca	Mn	Sr	Th	U
	m	ppm	ppm	ppm	ppm	ppm	ppm	ppm
JE 17-5	5.6	120641.29	230.58	242209.55	33.95	123.61	0.16	1.47
JE-17-6	6.4	107743.33	251.33	245358.24	38.77	81.56	0.20	1.94
JE-1-2	8.45	99654.29	259.35	235675.84	38.01	104.40	0.45	0.50
JE 1-3	8.8	115516.22	817.01	242713.13	31.56	145.21	0.35	0.58
JE 1-4	8.95	111675.68	904.59	239619.62	32.49	152.47	0.42	0.69
JE 1-5	9.15	115418.29	1382.42	234443.94	31.77	145.74	0.29	0.59
JE 1-7	10.05	122530.54	387.66	237330.59	28.14	110.79	0.03	0.60
JE 1-8	10.2	119595.03	347.31	233995.90	29.13	121.74	0.11	0.56
JE-1-9	10.85	100778.31	247.13	254607.90	41.47	122.84	0.47	0.72
JE 2-1	12.6	119999.20	349.54	242360.07	112.64	121.48	0.11	1.02
JE 2-3	13.2	117767.81	654.18	240472.71	85.98	133.10	0.18	0.92
JE 2-5	14	121903.77	496.43	230931.51	44.43	136.61	0.18	1.25
JE 3-2	16.15	122839.84	624.88	235562.55	26.72	125.64	0.03	0.42
JE 3-4	17.1	118557.97	170.62	234906.03	24.29	115.68	0.14	0.19
JE 4-4	21.3	118351.03	223.90	246507.46	11.80	116.01	0.07	0.20
JE 4-8	24.15	112447.51	526.27	243940.33	29.32	135.52	0.17	3.47
JE 5-6	26.5	114049.89	177.28	245552.71	19.76	122.80	0.02	2.58
JE 6-8E	31.8	105729.58	445.89	253641.58	21.57	151.79	0.22	1.10
JE 9-4	41.35	116933.81	205.98	243773.45	12.47	118.28	0.07	0.24
JE 9-12	46.15	115760.51	218.90	248185.15	12.29	128.24	0.08	0.24
JE 10-4	50.05	111717.93	694.49	244181.83	29.96	151.45	0.17	4.01
JE 11-2	54	75530.15	682.11	163802.68	28.35	106.02	0.05	2.56
JE 13-6	71.9	112165.05	550.34	258675.19	17.02	178.67	0.24	0.79
JE 14-3	84.2	114090.41	638.07	244879.08	29.93	175.29	0.13	0.85
JE 16-8	89.8	2552.02	19.83	411574.99	13.65	145.55	0.01	0.30

Table 3.5 Cross-correlation coefficients (*r*) and *significance F* calculated to test the level for significance (confidence interval = 95%). Samples with Mn/Sr > 2.5 from the Zuodeng section have been excluded in the cross-correlation analysis.

The Zuodeng section, South China	*r*	*Significance F*
$\delta^{13}C$ vs. $\delta^{18}O$	0.51	<0.01
$\delta^{13}C$ vs. Mn/Sr	0.35	0.13
$\delta^{238}U$ vs. $\delta^{13}C$	0.50	<0.01
$\delta^{238}U$ vs. Mg/Ca (mol:mol)	0.36	0.02
$\delta^{238}U$ vs. $\delta^{18}O$	0.19	0.22
$\delta^{238}U$ vs. Sr concentration	0.29	0.07
$\delta^{238}U$ vs. Mn concentration	0.30	0.06
$\delta^{238}U$ vs. Mn/Sr	0.04	0.82
$\delta^{238}U$ vs. Rb/Sr	0.05	0.74
$\delta^{238}U$ vs. Sr/Ca (ppm/wt.%)	0.21	0.20
$\delta^{238}U$ vs. U concentration	0.74	<0.01
$\delta^{238}U$ vs. Al content	0.20	0.22
$\delta^{238}U$ vs. U/Al (ppm/wt.%)	0.42	<0.01
$\delta^{238}U$ vs. U/(Ca+Mg) (ppm/wt.%)	0.74	<0.01
$\delta^{238}U$ vs. Al/(Ca+Mg)	0.16	0.26
$\delta^{238}U$ vs. Th/U	0.27	0.10
$\delta^{238}U$ vs. TOC (wt.%)	n/a	n/a

The Jesmond section, British Columbia	*r*	*Significance F*
$\delta^{13}C$ vs. $\delta^{18}O$	0.50	0.01
$\delta^{13}C$ vs. Mn/Sr	0.10	0.64
$\delta^{238}U$ vs. $\delta^{13}C$	0.31	0.13
$\delta^{238}U$ vs. Mg/Ca (mol:mol)	0.23	0.25
$\delta^{238}U$ vs. $\delta^{18}O$	0.09	0.66
$\delta^{238}U$ vs. Sr concentration	0.07	0.74
$\delta^{238}U$ vs. Mn concentration	0.22	0.27
$\delta^{238}U$ vs. Mn/Sr	0.20	0.32
$\delta^{238}U$ vs. Rb/Sr	0.14	0.49
$\delta^{238}U$ vs. Sr/Ca (ppm/w.t.%)	0.13	0.53
$\delta^{238}U$ vs. U concentration	0.13	0.54
$\delta^{238}U$ vs. Al content	0.20	0.33
$\delta^{238}U$ vs. U/Al (ppm/w.t.%)	0.15	0.47
$\delta^{238}U$ vs. U/(Ca+Mg) (ppm/wt.%)	0.15	0.48
$\delta^{238}U$ vs. Al/(Ca+Mg) (ppm/wt.%)	0.15	0.46
$\delta^{238}U$ vs. Th/U	0.15	0.45
$\delta^{238}U$ vs. TOC (w.t.%)	0.13	0.54

Table 3.6 Uranium box model parameterization.

Parameter	Value	Reference
$N_{sw,0}$	1.96×10^{13} mol U	Ku et al. (1977)
J_{riv}	4×10^{7} mol U/yr	Morford and Emerson (1999)
J_{anox}	0.6×10^{7} mol U/yr	Morford and Emerson (1999)
J_{oxic}	3.4×10^{7} mol U/yr	Calculated at steady state conditions
$\delta^{238}U_{river}$	–0.26 ‰	Andersen et al. (2017)
$\delta^{238}U_{seawater}$	–0.39 ‰	Tissot and Dauphas (2015)
Δ_{anox}	+0.6 ‰	Andersen et al. (2014)
Δ_{oxic}	+0.043 ‰	Calculated at steady state conditions
k_{anox}	1.41×10^{-19}	Calculated at steady state conditions using equation 6
k_{oxic}	4.82×10^{-21}	Calculated at steady state conditions using equation 7
A_{ocean}	3.62×10^{14} m^2	Lutgens, Frederick. Essentials of Geology. New York: MacMillan, 1992: 269.
V_{ocean}	1.34×10^{21} L	"The World Ocean." The Columbia Encyclopedia. CD-ROM. 2007, 6th Ed. New York: Columbia University Press.
Diag. corr. factor	0.3 ‰	Romaniello et al. (2013)

CHAPTER 4

MULTIPLE EPISODES OF EXTENSIVE MARINE ANOXIA LINKED TO GLOBAL WARMING AND CONTINENTAL WEATHERING FOLLOWING THE LATEST PERMIAN MA

This chapter has been published in *Science Advances*:

Zhang F., Romaniello S.J., Algeo T.J., Lau K.V., Clapham M.E., Richoz S., Herrmann A.D., Smith H., Horacek M., Anbar A.D. Multiple episodes of extensive oceanic anoxia linked to global warming and continental weathering following the latest Permian mass extinction. Science Advances 4: e1602921, doi: 10.1126/sciadv.1602921.

This chapter includes a supplementary material that is presented in *APPENDIX B*.

4.1 Introduction

The ~252-Ma Permian–Triassic boundary (PTB) mass extinction represents the largest biotic crisis in Earth's history (Chen and Benton, 2012), during which ~90 % of marine and ~75 % of terrestrial species went extinct over ~61(±48) kyr (Burgess et al., 2014; Chen and Benton, 2012). The Early Triassic was an interval of protracted marine biotic recovery (Chen and Benton, 2012; Payne et al., 2004; Wei et al., 2015). An initial, aborted recovery occurred soon after the LPME crisis, during the Induan stage of the Early Triassic (Brayard et al., 2009; Chen and Benton, 2012; Stanley, 2009), and a more sustained recovery took place during the late Olenekian stage (Spathian substage) (Chen

and Benton, 2012; Chen et al., 2011; Payne et al., 2011; Song et al., 2011), but full marine ecosystem recovery did not occur until the Middle Triassic, 4–8 million years after the LPME (Chen and Benton, 2012). This delay has been attributed to various causes, including the intensity of the PTB extinction event (Sole et al., 2002), persistently high temperatures (Sun et al., 2012), productivity crises (Grasby et al., 2016), and/or episodically recurring environmental perturbations (Horacek et al., 2007; Retallack et al., 2011; Song et al., 2013; Zhang et al., 2017a).

Although the mechanisms for the long duration of the post–LPME recovery are debated, marine anoxia has been invoked in many studies (Clarkson et al., 2016; Grasby et al., 2012; Isozaki, 1997; Lau et al., 2016; Payne et al., 2004; Song et al., 2012; Wei et al., 2015). Ce-anomalies and Th/U ratios in conodont apatite were used to reconstruct a 20-Myr redox history from the latest Permian to Late Triassic, revealing anoxic events during the late Changhsingian-Griesbachian, Smithian-Spathian transition, and the mid-Spathian (Song et al., 2012). Mo/Al ratios and the pyrite content of mudstones on the continental slope of the eastern Panthalassic margin were used to infer euxinic conditions during the late Changhsingian to mid-Dienerian and mid-Smithian to mid-Spathian intervals (Grasby et al., 2012). Fe-speciation was used to demonstrate a dynamic redox history along the Oman margin, with an expanded oxygen-minimum zone during the late Changhsingian to earliest Griesbachian, the Dienerian-Smithian transition, and the Smithian-Spathian transition (Clarkson et al., 2016). However, these proxies are inherently local in terms of their paleoredox implications, and high-resolution changes in mean global-ocean redox conditions during the Early Triassic remain poorly constrained despite their likely

importance for understanding links between oceanic conditions and the delayed marine biotic recovery.

The present study addresses this gap in knowledge regarding Early Triassic oceanic redox conditions through analysis of a global-ocean redox proxy, the U isotopes in marine carbonates ($^{238}U/^{235}U$, denoted as $\delta^{238}U$; Brennecka et al., 2011a; Elrick et al., 2017; Lau et al., 2016; Romaniello et al., 2013; Zhang et al., 2018a). Because of the long residence time of U in the ocean (~500 kyr; Dunk et al., 2002), seawater U is well-mixed and exhibits globally uniform concentrations (3.14–3.59 μg/L; Ku et al., 1977) and isotopic compositions (ca. –0.39 ‰; Stirling et al., 2007; Tissot and Dauphas, 2015; Weyer et al., 2008). Seawater $\delta^{238}U$ will tend to remain well-mixed even when the extent of oceanic oxygenation is significantly lower than today (Zhang et al., 2018a). Variations in the U isotope compositions of primary carbonate precipitates (such as scleractinian corals, calcareous green and red algae, ooids, and mollusks) are thought to track the $\delta^{238}U$ of contemporaneous seawater (Romaniello et al., 2013).

The U-isotope composition of seawater depends on redox conditions of the global ocean because U isotopes undergo different amounts of isotopic fractionation during incorporation into oxic and anoxic depositional facies. The largest source of U to the ocean is weathering from the upper continental crust and transport of dissolved U(VI) to the oceans via rivers. The $\delta^{238}U$ of rivers ranges between –0.18 ‰ and –0.38 ‰ with a mean of –0.26 ‰ (Andersen et al., 2017), which is slightly higher than the $\delta^{238}U$ of seawater (–0.39 ‰; Tissot and Dauphas, 2015). There are multiple sinks for seawater U, of which biogenic carbonates, sediments in anoxic facies, and sediments in weakly oxygenated facies represent the bulk of U removal from the ocean, while adsorption to Fe- and Mn-

oxides and hydrothermal alteration of oceanic crust represent smaller sinks (Morford and Emerson, 1999; Tissot and Dauphas, 2015). Removal of U(IV) to anoxic sediments favors the ^{238}U isotope and is associated with an average fractionation ($\Delta^{238}U$) of +0.6 ‰ based on observations from the modern Black Sea, Kyllaren Fjord, and Saanich Inlet (Holmden et al., 2015; Noordmann et al., 2015; Rolison et al., 2017; Weyer et al., 2008). Removal of U under suboxic conditions (i.e., corresponding to the integrated NO_3-Fe-Mn reduction zones) favors ^{238}U with a fractionation factor of ca. +0.1 ‰ based on observations from the Peru Margin, where sediments underlying weakly oxygenated waters have an average $\delta^{238}U$ of −0.28 (±0.19) ‰ (Weyer et al., 2008). Therefore, seawater is expected to have lower $\delta^{238}U$ at times of expanded oceanic anoxia and higher $\delta^{238}U$ at times of enhanced oceanic oxygenation (Brennecka et al., 2011a; Lau et al., 2017; Lau et al., 2016; Weyer et al., 2008).

The $\delta^{238}U$ of primary marine carbonate precipitates reflects that of the seawater from which they precipitate (Romaniello et al., 2013; Stirling et al., 2007; Weyer et al., 2008). These natural observations are supported by laboratory experiments that suggest a negligible to small offset (<0.13 ‰) between primary carbonate and seawater $\delta^{238}U$ (Chen et al., 2016). However, sedimentary carbonates may incorporate U(IV) from sulfidic porewaters, leading to $\delta^{238}U$ values that are 0.2–0.4 ‰ higher than that of seawater (discussed further below and in the supplementary information) (Romaniello et al., 2013). Thus, provided care is taken to correct for possible diagenetic alteration, U isotopes in ancient marine carbonates can serve as a global-ocean paleoredox proxy.

To date, four published studies have examined U–isotope variation during the Permian–Triassic transition and its aftermath (Brennecka et al., 2011a; Elrick et al., 2017;

2016; Zhang et al., 2018a). Brennecka et al. (Brennecka et al., 2011a) analyzed the narrow PTB interval at Dawen, South China, and documented a rapid expansion of oceanic anoxia across the LPME. This pattern was subsequently confirmed by Lau et al. (2016) and Elrick et al. (Elrick et al., 2017) in Tethys sections, and by Zhang et al. (Zhang et al., 2018a) who confirmed the same trend for a Panthalassic section, confirming the global nature of this event and the overall reliability of contemporaneous carbonate $\delta^{238}U$ records from widely-spaced sections. Lau et al. (2016) provided evidence for widespread oceanic anoxia from the latest Permian until the early Middle Triassic. However, although Lau et al. (2016) provided evidence supporting the role of oceanic anoxia in the delayed recovery of marine ecosystems following the LPME, the resolution of this study was insufficient for recognition of high-frequency redox fluctuations during the first ~2 Myr of the Early Triassic, an interval characterized by large $\delta^{13}C$ excursions ranging from –3 to +8 ‰ (Payne et al., 2004). Here, we provide a high-resolution U-isotope record spanning the uppermost Permian to lowermost Middle Triassic at Zal, Iran, in order to investigate secular variation in global-ocean redox conditions and its connection to the delayed recovery of marine ecosystems during the Early Triassic.

4.2 Materials and methods

We measured U isotopes ($\delta^{238}U$) in well-preserved Permian-Triassic marine carbonates from Zal, Iran, which were deposited on a peri-equatorial carbonate ramp at the margin of a microcontinent in the west-central Tethys Ocean (Figure 4.1A). This site accumulated mainly limestones until the late Early Triassic and mainly dolostones thereafter (Figure 4.1B). The Zal section accumulated in a well-aerated deep shelf

environment below wave base (Horacek et al., 2007; Richoz et al., 2010), at estimated water depths of 100–200 m during the late Permian and 50–100 m during the Griesbachian. Further shallowing yielded a high-energy shelf environment characterized by oolitic and oncoidal facies by the late Early Triassic (Horacek et al., 2007). The Zal study section has a well-developed lithostratigraphic, biostratigraphic, $\delta^{13}C_{carb}$, and $^{87}Sr/^{86}Sr$ chemostratigraphic framework (Horacek et al., 2007; Richoz et al., 2010; Sedlacek et al., 2014).

We analyzed a total of 155 carbonate samples for U isotopes. For each sample, ~3 g of powder was dissolved in 1 M hydrochloric acid (HCl). The resulting supernatant was spiked using a double spike containing ^{236}U and ^{233}U, and the spiked U was purified using chromatography methods as described by Zhang et al. (2018a). The $^{238}U/^{235}U$ values were determined with a ThermoFinnigan Neptune MC-ICP-MS instrument at Arizona State University (W.M. Keck Laboratory for Environmental Biogeochemistry). The U isotopic compositions of samples are reported relative to that of CRM145 standard (whose $\delta^{238}U$ value is identical to those of CRM 112a and SRM 950a, other commonly used standards). The analytical precision of this method is better than ±0.08 ‰ (all uncertainties reported in this chapter are 2SD). The analytical results have been summarized in Table 4.1.

4.3 Multiple episodes of expanded oceanic anoxia during the Early Triassic

Marine carbonate sediments can faithfully record chemical signatures of seawater provided that post-depositional processes and detrital contamination do not cause significant alteration. These processes likely did not confound the U isotope pattern across the LPME observed in the Zal section because this pattern agrees with those at Dawen,

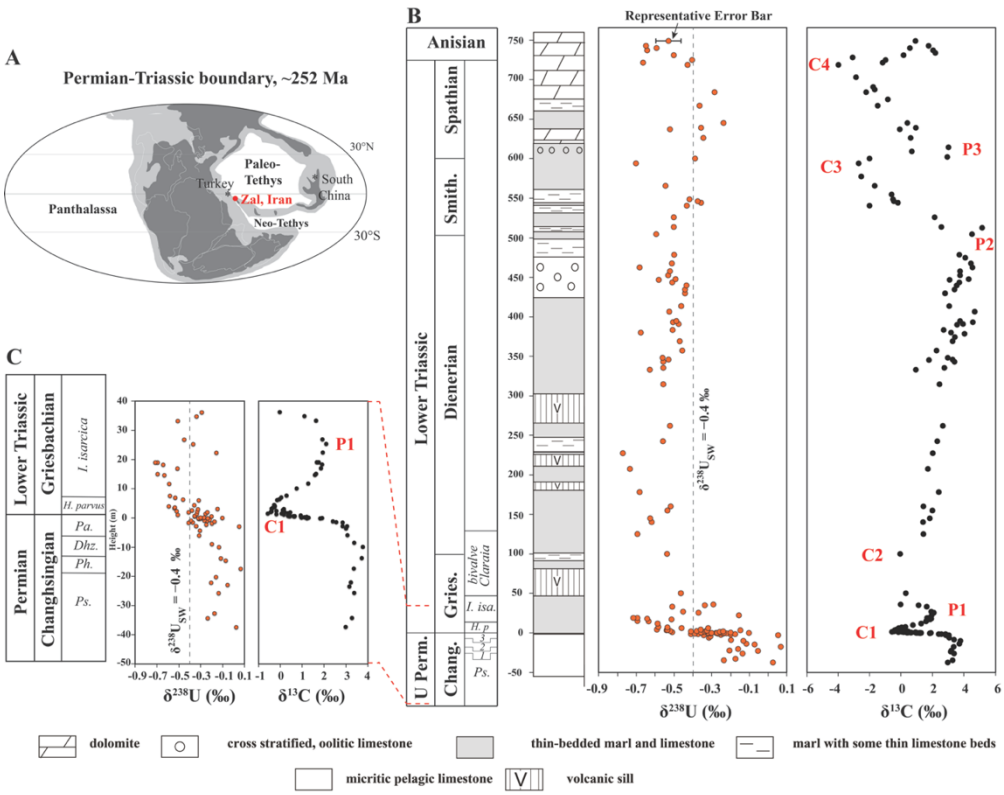

Figure 4.1 Paleogeographic location of Iran at ~252 Ma (A, modified after ref. Payne et al., 2007) and geochemical profiles for Zal, Iran (B and C). The $^{238}U/^{235}U$ ratios are reported in per mille using standard δ-notation, where $\delta^{238}U = [(^{238}U/^{235}U)_{sample} / (^{238}U/^{235}U)_{standard(CRM145)} - 1] \times 1000$. $\delta^{13}C$ data and stratigraphic column are from Horacek et al. (2007) and Richoz et al. (2010). With respect to the $\delta^{13}C$ profile, C1 to C4 are equivalent to the N1 to N4 negative excursions of Song et al. (2013). $\delta^{238}U_{SW}$ in B and C denotes $\delta^{238}U$ of modern seawater. A representative uncertainty range of two standard deviations (2SD) is shown for the uppermost $\delta^{238}U$ data point in B. C is an expanded view of the −40 m to 40 m interval. Only samples with Mn/Sr < 2.5 are shown. Chang.: Changhsingian; Gries.: Griesbachian; Smith.: Smithian. *I. isa.*: *I. isarcica*; *H. p.*: *H. parvus*; Ammonoid Zone 3, Pa.: *Paratirolites*; Ammonoid Zone 2, Dhz.: *Dhzulfites*; Ammonoid Zone 1, Ph.: *Phisonites*; *Ps.*: *Pseudotoceras*.

Dajiang, and Daxiakou, China, which were located on the eastern side of the Paleo-Tethys Ocean (Brennecka et al., 2011a; Elrick et al., 2017; Lau et al., 2016), Kamura which was deposited in the open Panthalassic Ocean (Zhang et al., 2018a), and at Taşkent, Turkey, which was located northwest of Zal on the western margin of the Paleo-Tethys Ocean (Lau et al., 2016). The fact that these six paleogeographically widely-separated PTB sections exhibit a similar negative shift of $\delta^{238}U$ at the LPME supports the use of carbonate U isotopes as a paleoredox proxy for the Early Triassic global ocean (Brennecka et al., 2011a; Elrick et al., 2017; Lau et al., 2016).

Confidence in this conclusion is enhanced by examining trace element compositions (Al, Mn, Sr) and elemental ratios (Mn/Sr, Rb/Sr) as indicators of sedimentary diagenesis. In most of the study samples, these elemental tracers are consistent with well-preserved marine carbonate with little influence from detrital components, and cross plots of $\delta^{238}U$ vs. these tracers shows no evidence for diagenetic alteration. Carbonate diagenesis models predict that the $\delta^{238}U$ signal is more robust than the $^{87}Sr/^{86}Sr$ signal with respect to secondary alteration (Lau et al., 2017). $^{87}Sr/^{86}Sr$ values from Zal carbonates show good agreement with other records of Early Triassic seawater $^{87}Sr/^{86}Sr$ (Sedlacek et al., 2014; Song et al., 2015), which suggests that the primary seawater $\delta^{238}U$ signal may also be well-preserved. We adopted Mn/Sr < 2.5 as a diagenetic alteration threshold (after Kaufman and Knoll, 1995), with 127 out of the 155 study samples meeting this criterion. Only those samples with Mn/Sr < 2.5 are plotted in Figure 4.1 and utilized in the discussion below.

The $\delta^{238}U$ profile for Zal shows scatter of 0.2–0.4 ‰ through the Permian-Triassic transition interval, similar to that seen in sub-Recent Bahamian carbonates. Although Bahamian primary carbonate precipitates appear to directly record seawater $\delta^{238}U$, all

shallowly buried sediments have $\delta^{238}U$ that is isotopically heavier by 0.2–0.4 ‰ (mean 0.3 ‰) than $\delta^{238}U$ of modern seawater (Romaniello et al., 2013). This is thought to reflect differential incorporation of ^{238}U-enriched U(IV) from anoxic porewaters during early diagenesis, or variation in porewater U-speciation during carbonate recrystallization (Chen et al., 2016). Porewater data from deep Bahamian drill cores suggest that the potential for alteration following burial may be limited because porewater anoxia renders U essentially immobile (Henderson et al., 1999). On this basis, we have applied a diagenetic correction factor of 0.3 ‰ to measured $\delta^{238}U$ values prior to U isotope mass balance calculations.

The PTB interval at Zal is characterized by a large (3.5 ‰) and globally recognized negative $\delta^{13}C$ excursion commencing immediately before the LPME horizon (Figure 4.1C, labeled "C1") (Richoz et al., 2010). A negative shift in $\delta^{238}U$ of ~0.4 ‰ commenced shortly below the LPME horizon. The shift toward lower carbonate $\delta^{238}U$ values in association with the extinction event is most readily interpreted as an increase in the flux of isotopically heavy U into anoxic facies, suggesting a rapid increase in the global area of anoxic seafloor in conjunction with the LPME event (Brennecka et al., 2011a; Elrick et al., 2017; Lau et al., 2016).

The high-resolution $\delta^{238}U$ dataset presented here demonstrates that the Early Triassic ocean was characterized by multiple episodes of expanded anoxia. The negative $\delta^{238}U$ shift commencing shortly prior to the LPME reached a minimum of −0.62±0.15 ‰ about 15 m above the PTB (Figure 4.1B). Low $\delta^{238}U$ values persisted through the Griesbachian substage, reaching a second, larger negative peak (−0.73±0.09 ‰) about 220–230 m above the PTB. This late Griesbachian to early Dienerian $\delta^{238}U$ minimum suggests that the most reducing conditions in the global ocean may have developed

following the LPME crisis. The $\delta^{238}U$ values then gradually shift toward higher values from ~230 to 550 m, recording a reduction in anoxic conditions during the mid-Dienerian to mid-Smithian. A third negative peak may be present at ~600 m, based on a sample close to the Smithian-Spathian boundary with a $\delta^{238}U$ of −0.70 ‰, although more data are needed to confirm the existence of this feature. These values suggest widely reducing oceanic conditions throughout the Griesbachian to Smithian with periodic fluctuations in areal extent. The top of the Zal section (700–752 m) shows a fourth negative $\delta^{238}U$ shift (−0.57±0.19 ‰), recording a major anoxic event during the latest Spathian to Early/Middle Triassic transition that is poorly known to date. Earlier U-isotope studies of Lower Triassic sections (Brennecka et al., 2011a; Elrick et al., 2017; Lau et al., 2016) did not clearly delineate these multiple negative $\delta^{238}U$ shifts because of either insufficient stratigraphic coverage or insufficient temporal resolution. We predict that they will be observed in other coeval sections, and we encourage high-resolution $\delta^{238}U$ studies to reproduce these excursions.

4.4 Oceanic anoxia linked to climatic warming and marine nutrient levels

The U-isotope dataset of the present study was generated using the same set of samples reported in earlier studies of $\delta^{13}C$ and $^{87}Sr/^{86}Sr$ at Zal (Horacek et al., 2007; Sedlacek et al., 2014) (Figure 4.2A-C), allowing for direct comparisons among these records. All three isotopic records exhibit a series of four correlatable excursions, during each of which negative excursions in $\delta^{238}U$ and $\delta^{13}C$ were accompanied by an accelerated rate of increase in $^{87}Sr/^{86}Sr$. The C1 event, which is latest Changhsingian to earliest Griesbachian in age, represents the well-documented marine environmental response to the

LPME (Brennecka et al., 2011a; Burgess and Bowring, 2015; Shen et al., 2012a; Sun et al., 2012; Zhang et al., 2018a). The C2 event, which is latest Griesbachian to earliest Dienerian in age, exhibits U- and C-isotope minima that are similar to those of the C1 event, although the magnitudes of the excursions are smaller owing to more negative initial values (Figure 4.2). The C3 event, which is mid- to late Smithian in age, is well-defined in the C- and Sr-isotope records, but more data are needed to fully test the duration and magnitude of a coeval U-isotope shift. The C4 event, which is latest Spathian to earliest Anisian in age, is characterized by smaller and more protracted $\delta^{238}U$ and $\delta^{13}C$ excursions than for the earlier events and by no apparent change in $^{87}Sr/^{86}Sr$ (although the existing Sr-isotope dataset is too limited to adequately test for the C4 event) (Figure 4.2A-C). Although the patterns of excursions (e.g., amplitude and duration) in the $\delta^{238}U$, $\delta^{13}C$ and $^{87}Sr/^{86}Sr$ profiles vary from one event to the next, the episodic nature of these events points to repeated global-scale perturbations that must have had significant impacts on global climate, weathering, and ocean-redox dynamics.

The relationships between the $\delta^{238}U$, $\delta^{13}C$, and $^{87}Sr/^{86}Sr$ profiles for the Zal section were investigated through cross-correlation analysis of LOWESS-smoothed curves for each record (Figure 4.2A-C). This analysis indicates that the negative shifts in $\delta^{238}U$ lagged behind the negative $\delta^{13}C$ excursions and the stepwise increases in the $^{87}Sr/^{86}Sr$ profile by 125–150 kyr and 175–200 kyr, respectively, and that the negative shifts in $\delta^{13}C$ lagged behind the stepwise increases in the $^{87}Sr/^{86}Sr$ profile by 0–50 kyr. These lags are presumed to reflect differences in the residence times (and thus the relative response times) of seawater U, dissolved inorganic carbon (DIC), and Sr in Early Triassic oceans. Although each transient stepwise increase in the $^{87}Sr/^{86}Sr$ profile was significantly shorter than the

residence time of ~3 Myr for Sr in the modern ocean, the observed pattern could have been generated by rapid pulsed injection of old radiogenic (i.e., ^{87}Sr-enriched) Sr into the ocean system on time scales much shorter than the residence time of Sr. Similar effects have been reported from glacial-interglacial (~100-kyr) cycles of the Quaternary (e.g., Martin et al., 2000; Tütken et al., 2002).

We hypothesize that these isotopic records were linked via a combination of enhanced volcanism and climatic warming, leading to increased crustal weathering and seawater PO_4^{3-} concentrations. Concurrent rapid warming and increases in seawater nutrient inventories would have led to oceanic anoxia as a result of increased marine primary productivity, reduced oxygen solubility, and reduced vertical mixing due to steeper thermal gradients in the oceanic thermocline.

Sr isotope paleoweathering and O isotope paleotemperature records suggest a general causal connection between climate warming and elevated weathering rates during the Early Triassic (Sedlacek et al., 2014; Sun et al., 2012). The increase in seawater $^{87}Sr/^{86}Sr$ from the latest Permian to the Early/Middle Triassic boundary occurred in a series of steps. Because each step is short, these events must represent large transient increases in the delivery of ^{87}Sr-rich weathering products to the ocean (Sedlacek et al., 2014). Rising seawater $^{87}Sr/^{86}Sr$ could not have resulted from weathering of fresh basalts from the Siberian Traps (Burgess and Bowring, 2015) but, rather, must have included a large contribution from weathering of old continental rocks with high $^{87}Sr/^{86}Sr$ ratios. $^{87}Sr/^{86}Sr$ records and sedimentary flux investigations suggest 3–7×, 2–5×, 5–6×, and 1–2× increases in weathering fluxes across the C1, C2, C3, and C4 events, respectively (Algeo and Twitchett, 2010; Sedlacek et al., 2014; Song et al., 2015). Intensified continental

weathering would have flushed large amounts of PO_4^{3-} and other nutrients into the ocean, leading to higher marine productivity, higher organic carbon export from the euphotic zone, increased respiratory oxygen demand at depth, and a decrease in oceanic dissolved oxygen levels.

We propose that perturbations in marine redox chemistry were closely linked to changes in continental weathering fluxes and increased marine PO_4^{3-} levels. Phosphorus is commonly considered to be the ultimate biolimiting nutrient on marine productivity at geological timescales, and it plays a significant role in controlling the amount and spatial distribution of dissolved O_2 in the oceans (Lenton et al., 2014; Meyer et al., 2016; Van Cappellen and Ingall, 1994; Winguth and Winguth, 2012). Increased phosphorus input to the ocean would have led to rapid (10^3–10^4 kyr) increases in new production, higher O_2 demand, a larger vertical $\delta^{13}C$ gradient, and deep-water anoxia (Lenton et al., 2014; Meyer et al., 2016; Meyer et al., 2011). We constructed a box model to estimate average seawater $[PO_4^{3-}]$ during the study interval. We calculated riverine phosphorus inputs from $^{87}Sr/^{86}Sr$-derived estimates of the continental weathering flux (Sedlacek et al., 2014; Song et al., 2015) assuming a P:Sr ratio of 0.61–0.91 mol:mol. This ratio may have been locally amplified by preferential recycling of PO_4^{3-} through an anoxic and non-ferruginous water column (Van Cappellen and Ingall, 1994). Our calculations suggest that seawater PO_4^{3-} concentrations increased to ~12×$[PO_4^{3-}]_0$, ~10×$[PO_4^{3-}]_0$, ~12×$[PO_4^{3-}]_0$, and ~9×$[PO_4^{3-}]_0$ during the C1, C2, C3, and C4 events, where $[PO_4^{3-}]_0$ is the initial PO_4^{3-} concentration in the pre-LPME Late Permian ocean (Figure 4.3C). Sensitivity studies conducted using spatially-resolved GCM models of early Triassic climate and ocean circulation indicate that $[PO_4^{3-}]$ increases of this magnitude would have led to a significant expansion of anoxic

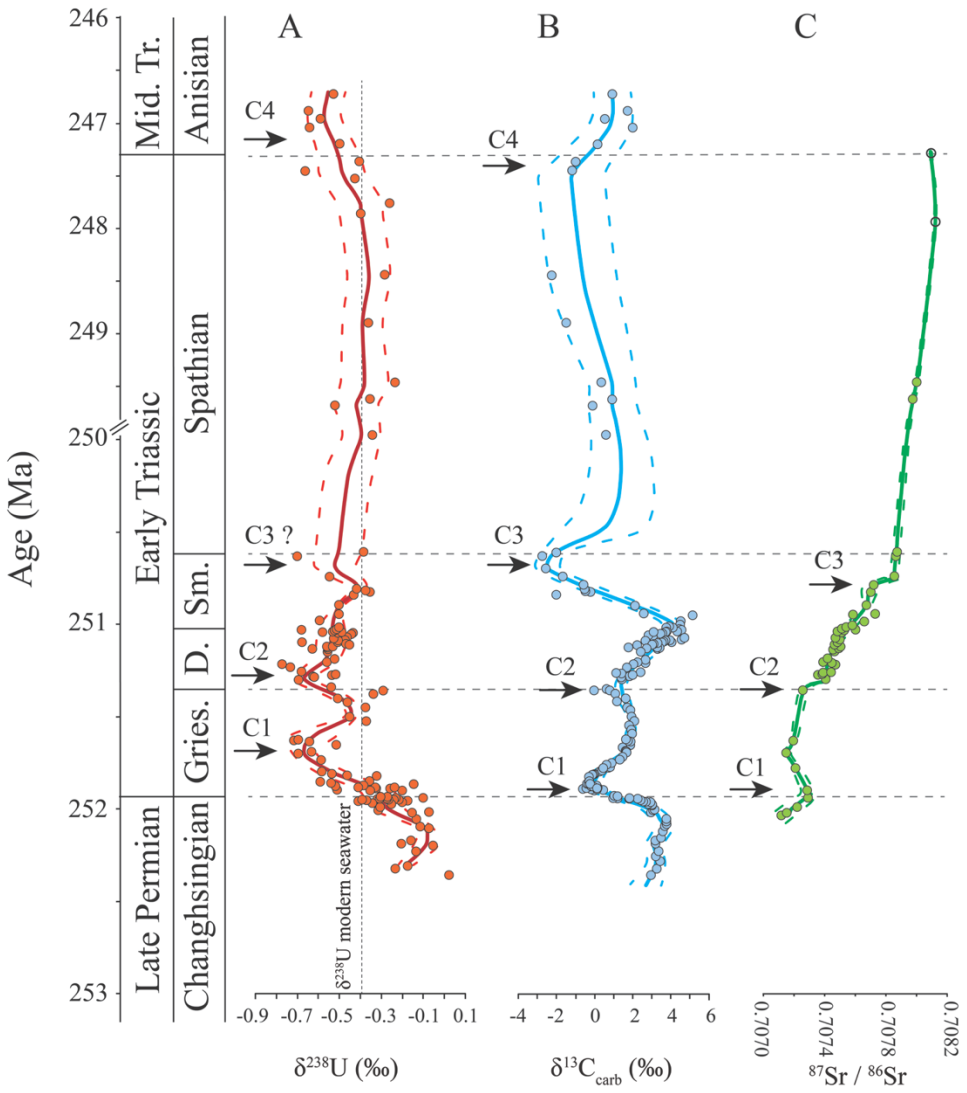

Figure 4.2 LOWESS curves for $\delta^{238}U$, $\delta^{13}C$, and $^{87}Sr/^{86}Sr$ profiles of Zal, Iran. A: Uranium isotope ($\delta^{238}U$) profile. B: Carbon isotope ($\delta^{13}C$) profile (Horacek et al., 2007; Richoz et al., 2010). $\delta^{13}C$ of samples without paired $\delta^{238}U$ data are now shown in this figure. C. Strontium isotope ($^{87}Sr/^{86}Sr$) profile (Sedlacek et al., 2014). U-C-Sr isotopes were measured from the same suite of samples. Samples with Mn/Sr > 2.5 have been removed from A and B, and samples with Mn/Sr > 2.5 are indicated with open circles in C. U. Perm.: Upper Permian; Mid. Tr.: Middle Triassic; Gries.: Griesbachian; Di.: Dienerian; Sm.: Smithian. Note change in time scale at 250 Ma.

water masses (Meyer et al., 2016; Winguth and Winguth, 2012). We therefore hypothesize that elevated seawater PO_4^{3-} levels associated with enhanced weathering fluxes played a key role in driving expansion of anoxia in the Early Triassic ocean.

In addition to enhanced nutrient inputs, intensified thermal stratification and reduced vertical mixing associated with rapid climatic warming may have further contributed to the expansion of oceanic anoxia (Sun et al., 2012). A previous study (Song et al., 2013) argued that large $\delta^{13}C$ gradients in the Early Triassic ocean point to evidence of enhanced vertical stratification, yielding $\delta^{13}C$ gradients from the ocean surface to the mid-thermocline of ~8.5 ‰, ~3.5 ‰, ~7.8 ‰, and ~2.2 ‰ during the C1 to C4 intervals, respectively, for sections from the northern Yangtze Platform and Nanpanjiang Basin in South China (Figure 4.2D).

4.5 Relationship of oceanic anoxia and Early Triassic negative $\delta^{13}C$ excursions

The relationship between Early Triassic $\delta^{13}C$ excursions and marine redox changes has been the subject of lengthy debate (e.g., Meyer et al., 2011; Payne and Kump, 2007; Payne et al., 2004; Sephton et al., 2005; Song et al., 2013). The negative $\delta^{13}C$ excursions have been linked to both higher marine productivity (Meyer et al., 2011) and lower marine productivity (Grasby et al., 2016; Song et al., 2013). In the present study, relationships among the $^{87}Sr/^{86}Sr$, $\delta^{238}U$ and $\delta^{13}C$ profiles support a relationship of negative $\delta^{13}C$ excursions to higher marine productivity and expanded oceanic anoxia. This interpretation, however, runs counter to the paradigmatic view of the marine carbon cycle, in which higher productivity and expanded anoxia increase the export flux of organic matter and, thus,

stimulate a positive $\delta^{13}C$ excursion. A modeling study (Payne and Kump, 2007) suggested that the C1 to C4 negative $\delta^{13}C$ excursions might have been triggered by injection of light carbon associated with eruption of the Siberian Traps, or by methane release via contact metamorphism of West Siberian Coal Field deposits. Variations in the proportions of different carbon sources may account for differences in the shape and magnitude of Early Triassic carbon isotope excursions (Payne and Kump, 2007), but determining secular variation in these influences (including volcanic carbon sources (Payne and Kump, 2007), marine productivity (Meyer et al., 2011), and soil organic matter (Sephton et al., 2005)) will require further study.

4.6 Relationship of oceanic anoxia to the PTB extinction and the protracted recovery of marine ecosystems

There is a growing body of evidence that the evolving redox structure of the oceans has been an important influence on the evolutionary trajectory of animals, including extinctions such as the LPME (Brennecka et al., 2011a; Feng and Algeo, 2014; Zhang et al., 2018a). Given their physiological requirements, oceanic anoxia can rapidly kill animals and potentially trigger a restructuring of marine ecosystems. In the modern ocean, continental shelves comprise <7 % of the seafloor area but host the majority of marine animal diversity, biomass, and organic carbon and phosphorus burial. A simple U isotope mass balance model predicts that anoxic seafloor area expanded from an initial value of 0.2 % (assuming that pre-crisis redox conditions were similar to the modern ocean) to ~17–60 %, ~23–65 %, ~12–21 %, and ~17–37 % in the latest Changhsingian-earliest Griesbachian, the latest Griesbachian to earliest Dienerian, the mid- to late Smithian, and

the latest Spathian-earliest Anisian (i.e., during C1 to C4), respectively (Figure 4.3; modeling description has been summarized in Chapter 3). Each expansion of anoxic waters likely covered a large proportion of continental shelves and upper slopes since numerous sections worldwide from such settings show evidence of anoxia (e.g., Bond and Wignall, 2010; Clarkson et al., 2016; Grasby et al., 2012; Grice et al., 2005; Lau et al., 2016; Song et al., 2012).

The patterns of redox variation documented by the U-isotope record show a good first-order correspondence to ammonoid extinction rates during the Early Triassic (Brayard et al., 2009; Chen and Benton, 2012; Stanley, 2009) (Figure 4.3D). Intervals of expanded oceanic anoxia approximately coincided with extinction rate peaks in the end-Permian (251.94 Ma), possibly the mid-Griesbachian (251.7 Ma), the mid-Dienerian (251.2 Ma), the late Smithian (250.5 Ma), and the end-Spathian (247.2 Ma) (Figure 4.3D). Ammonoid extinctions appear to be synchronous in multiple regions (e.g., the Indian margin of the Neo-Tethys Ocean, the western Laurentian margin of the Panthalassic Ocean, and the Boreal ocean; Figure 4.3D), suggesting that the crises were global in extent. Global diversity and extinction data for other invertebrate clades (e.g., foraminifers, gastropods, bivalves, brachiopods and ostracods) lack the high (biozone-level) resolution of the ammonoid data but suffice to show that biodiversity levels were generally low until the early Middle Triassic, when a rapid recovery ensued (Payne et al., 2011; Wei et al., 2015). Although benthic invertebrate communities may have undergone restructuring during the late Dienerian and late Smithian (Foster et al., 2017; Hofmann et al., 2014), active swimming organisms such as ammonoids, as well as vertebrates (Scheyer et al., 2014), were more dramatically affected because of their active physiology and higher metabolic

oxygen demand. Therefore, our results imply that the delayed Early Triassic marine recovery was a function of repeated environmental perturbations rather than the severity of the LPME event itself (Grasby et al., 2012; Lau et al., 2016).

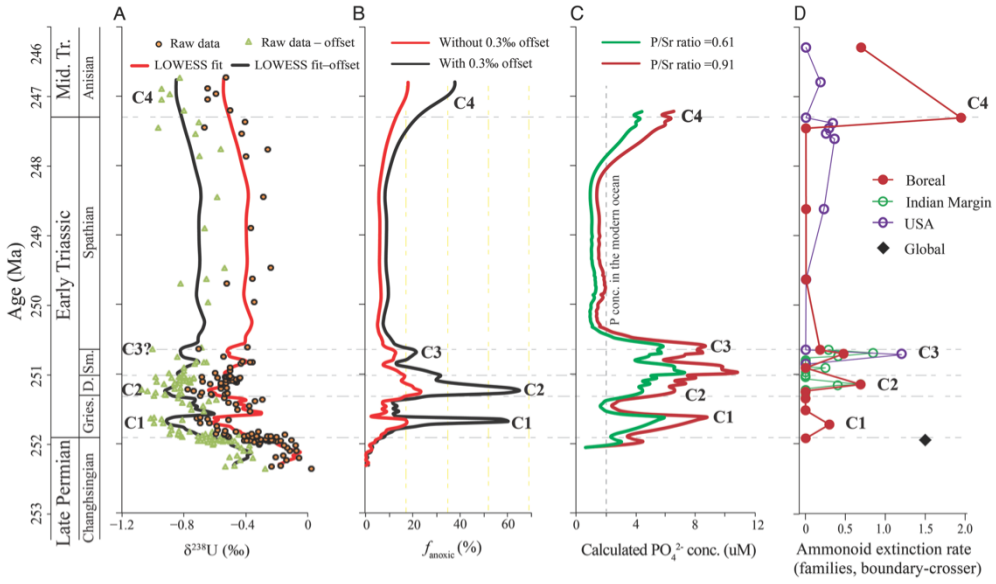

Figure 4.3 Marine U-cycle mass balance model, calculated PO_4^{3-} concentrations, and ammonoid extinction rate curve. A. $\delta^{238}U$ data with LOWESS smoothing fit; see the top of figure for legend. B. Model estimates of anoxic seafloor area (f_{anoxic}) during Late Permian through Early/Middle Triassic time. The red and black lines denote modeling output without and with a diagenetic offset of 0.3 ‰, respectively. We note that the low $\delta^{238}U$ data resolution at the C3 event makes its model estimated timing and extent of oceanic anoxia with larger uncertainties compared to the other events. C. Calculated PO_4^{3-} concentrations in the Early Triassic ocean. The red and black lines denote modeling output assuming a P:Sr ratio of 0.61 and 0.91, respectively. D. Ammonoid extinction rate curve. See Figure 4.1 for stage and substage abbreviations.

CHAPTER 5

EXTENSIVE MARINE ANOXIA DURING THE TERMINAL EDIACARAN PERIOD

This chapter has been published in *Science Advances*:

Zhang F., Xiao S., Kendall B., Romaniello S. J., Cui H., Meyer M., Gilleaudeau G. J., Kaufman A. J., Anbar A. D., 2018. Extensive marine anoxia during the terminal Ediacaran Period. Science Advances 4, eaan8983.

This chapter includes a supplementary material that is presented in APPENDIX C.

5.1 Introduction

Macroscopic and morphologically complex multicellular eukaryotes, including stem-groups animals, diversified in the second half of the Ediacaran Period starting ~570 Ma (Pu et al., 2016). The fossil record of these eukaryotes is sometimes referred to as the Ediacara biota (Xiao and Laflamme, 2009). The Ediacara biota reached their maximum taxonomic diversity and morphological disparity about 560 Ma, then subsequently declined in the terminal Ediacaran Period (~550–541 Ma), and almost completely disappeared at the Ediacaran-Cambrian transition about 541 Ma (Laflamme et al., 2013; Shen et al., 2008; Xiao and Laflamme, 2009). The causes of the decline and eventual disappearance of the Ediacara biota remain a subject of intensive debate (Darroch et al., 2015; Laflamme et al., 2013; Tostevin et al., 2016).

Changes in ocean redox conditions are often implicated as a driver of the decline of the Ediacara biota (Amthor et al., 2003; Kimura and Watanabe, 2001; Laflamme et al., 2013; Schroder and Grotzinger, 2007). Given the physiological requirements of Ediacara organisms, particularly macroscopic diffusion-dependent stem-group animals (Catling et al., 2005), O_2 availability is expected to have an impact on the distribution of the Ediacara biota, both locally and globally (Canfield et al., 2007; Planavsky et al., 2014; Sahoo et al., 2016; Wood et al., 2015). Indeed, it has been shown that Ediacaran organisms were locally restricted to oxygenated environments under highly dynamic redox conditions (Wood et al., 2015). Planavsky et al. (2014) suggested that generally low global O_2 availability until ~750 Ma was a key factor delaying the rise of multicellular animals. Canfield et al. (2007) specifically linked the initial diversification of the Ediacara biota at ~570 Ma with a deep ocean oxygenation event (Fike et al., 2006; McFadden et al., 2008). However, the possible relationship between ocean redox evolution and the decline of the Ediacara biota has not been clearly demonstrated.

Previous studies reported geochemical evidence for oceanic anoxia at the Ediacaran-Cambrian boundary (Kimura and Watanabe, 2001; Schroder and Grotzinger, 2007). However, current fossil evidence points to a significant decline in biodiversity in the terminal Ediacaran Period, up to 10 Myr before the Ediacaran-Cambrian boundary (Darroch et al., 2015; Laflamme et al., 2013). This temporal mismatch and a protracted decline of the biota have prompted some to favor a biotic replacement model as an explanation for the decline of the Ediacara biota (Darroch et al., 2015; Laflamme et al., 2013). This model suggests that Ediacaran organisms were progressively outcompeted by

newly evolved bilaterian animals, which may have directly or indirectly modulated the availability of resources including both substrates and nutrients (Laflamme et al., 2013). Resolving this debate requires the integration of paleontological and geochemical data. At a global scale, this integration is challenging because precise stratigraphic correlation of Ediacaran strata is difficult (Xiao et al., 2016) and proxies for global oceanic redox conditions are few. Sperling et al. (2015) assembled a global compilation of Fe speciation data, but the temporal resolution of this compilation is dependent on inter-regional correlation and is insufficient for the reconstruction of short-term oceanic redox dynamics in the terminal Ediacaran Period. In contrast, other studies have focused on local redox proxies from fossiliferous successions so that geochemical and paleontological data were collected from the same successions, avoiding the challenges of inter-regional correlation. For example, Darroch et al. (2015), Wood et al. (2015), and Tostevin et al. (Tostevin et al., 2016) applied Fe speciation and Ce anomalies to carbonates and siliciclastic rocks of the Nama Group to understand factors controlling the distribution and decline of the Ediacara biota in the terminal Ediacaran Period. Darroch et al. (2015) presented Fe speciation data from a single terminal Ediacaran section that records lower genus richness than older Ediacaran assemblages. Their data show that these sediments that record declining diversity of the Ediacara biota were deposited in oxic environments, from which they concluded that oxygen stress probably did not play a role in the decline of the Ediacaran biota. However, their data are also consistent with the possibility that terminal Ediacaran organisms were challenged by a global expansion of anoxia and were restricted to oxic refugia in oceans with highly heterogeneous redox conditions. Indeed, Wood et al. (2015) and Tostevin et al. (Tostevin et al., 2016) have shown that terminal Ediacaran organisms

are not found in anoxic environments and their distribution is strongly controlled by oxygen availability. Terminal Ediacaran organisms may have been globally challenged by an expansion of oceanic anoxia and locally relegated to oxic refugia.

Uranium isotopes ($^{238}U/^{235}U$, denoted as $\delta^{238}U$) in carbonates may be uniquely suited to differentiate global from local perturbations in ocean redox chemistry (Brennecka et al., 2011a; Lau et al., 2017; Zhang et al., 2018a), and therefore to test the degree to which changing global ocean redox conditions may have shaped the evolutionary trajectory of the Ediacara biota. To meet this challenge and to specifically address the question of whether the decline of the Ediacara biota was driven by an episode of expanded marine anoxia, we analyzed $\delta^{238}U$ in carbonates from the ca. 551–541 Ma Dengying Formation (South China) that also contains terminal Ediacaran macrofossils characteristic of the Nama assemblage. The integration of $\delta^{238}U$ data and paleontological data from the same suite of rocks allows us to reconstruct global ocean redox conditions at a time when the Ediacara biota began to decline.

5.2 Geological background

The Ediacaran System in South China is represented by the Doushantuo Formation (~635–551 Ma) and the Dengying Formation (551–541 Ma), which are overlain by the lower Cambrian Yanjiahe Formation and its equivalents. We sampled the terminal Ediacaran Dengying Formation at the Wuhe section in the Yangtze Gorges area and at the Gaojiashan section in southern Shaanxi Province (Figure 5.1). The age constraints of the Dengying Formation come from a 551 Ma U-Pb zircon date in the underlying Doushantuo Formation (Condon et al., 2005), and an estimated 541 Ma age for the Ediacaran–Cambrian

boundary (Amthor et al., 2003). Paleogeographically, these two sections were located on carbonate platforms on the southeastern and northwestern margins of the Yangtze Block (Cai et al., 2010; Cui et al., 2016a; Meyer et al., 2014). At Wuhe, the Dengying Formation includes the basal Hamajing Member (peritidal dolostone), the middle Shibantan Member (subtidal limestone), and the upper Baimatuo Member (peritidal dolostone). These three members are lithostratigraphically similar to, and traditionally correlated with, the Algal Dolomite, Gaojiashan, and Beiwan members at Gaojiashan (Cai et al., 2010). The Shibantan and Gaojiashan members in South China may be partially correlated with the upper Nafun Group – lower Ara Group in Oman, the upper Zaris Formation – Urusis Formation of the Nama Group in Namibia, and the Khatyspyt Formation in Arctic Siberia, on the basis of chemostratigraphic data and the occurrence of the earliest skeletal animal fossils such as *Cloudina* (Xiao et al., 2016).

Twenty-seven samples from the Gaojiashan Member at the Gaojiashan section, 56 samples from the Dengying Formation at the Wuhe section, and 6 samples of the early Cambrian Yanjiahe Formation at the Wuhe section were analyzed in this study. Detailed geological background of the study sites and analytical methods have been summarized in the supplementary information.

5.3 Resuts

The Analytical results have been summarized in Table 5.1 and Table 5.2. Large stratigraphic variations in $\delta^{238}U$ are observed in the studied sections (Figure 5.2). At Wuhe, the $\delta^{238}U$ of the Hamajing Member declines upsection from −0.45 ‰ to −1.19 ‰. The Shibantan Member has a relatively narrow variation in $\delta^{238}U$ from −0.81 ‰ to −1.20 ‰,

with an average of –0.97 ± 0.18 ‰. In the Baimatuo Member, a positive excursion in $\delta^{238}U$ from –0.95 ‰ to –0.50 ‰ occurs at the Precambrian-Cambrian boundary. This positive shift in $\delta^{238}U$ is followed by a negative excursion in $\delta^{238}U$ from −0.52 ‰ to −0.82 ‰ in the overlying Yanjiahe Formation.

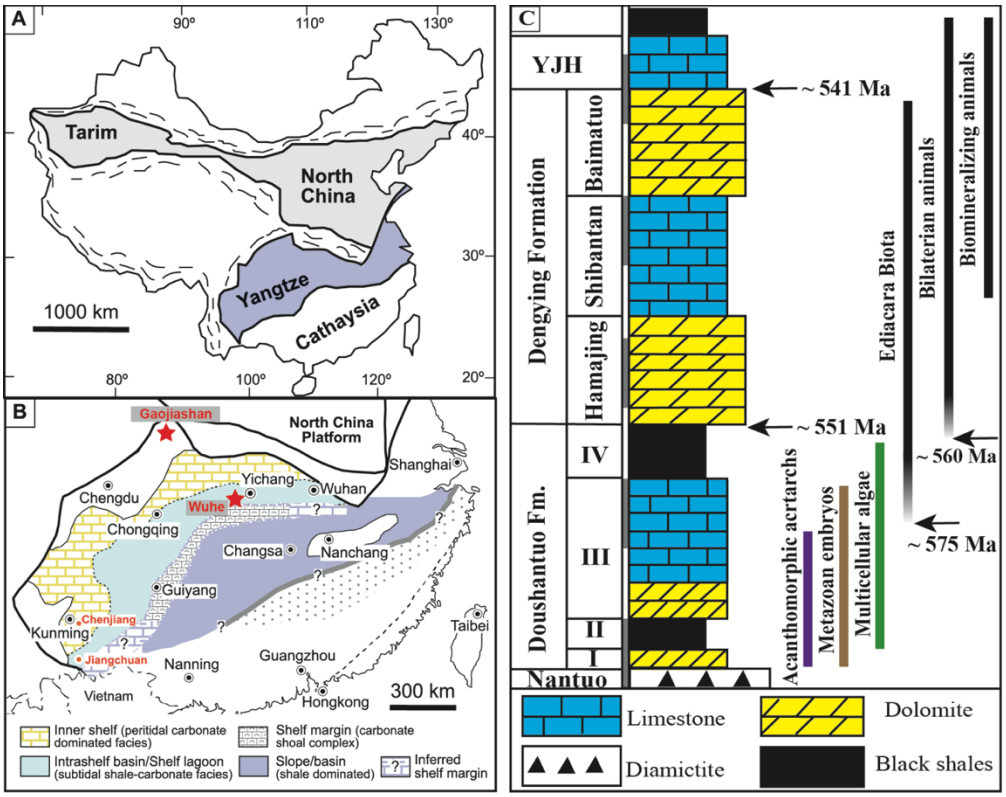

Figure 5.1 (A) Simplified map showing the location of the Yangtze Block (Cui et al., 2016a; Meyer et al., 2014). (B) Paleogeographic map of the Yangtze Block showing the location of the Wuhe section and the Gaojiashan section. (C) Simplified stratigraphic column of the Ediacaran Doushantuo and Dengying formations, and the Early Cambrian Yanjiahe Formation (YJH), as well as the chronology for the evolution of major Ediacaran animal groups (McFadden et al., 2008).

At Gaojiashan, $\delta^{238}U$ in the lower Gaojiashan Member varies between −0.18 ‰ and −0.76 ‰ (only data that passed the diagenetic evaluation described below is shown in Figure 5.2). The $\delta^{238}U$ of the middle-upper Gaojiashan Member shows relative narrow variations in $\delta^{238}U$ from −0.80 ‰ to −1.17 ‰, with an average of –0.94 ± 0.20 ‰; these values are indistinguishable from those of the stratigraphically equivalent Shibantan Member.

5.4 Evidence for primary oceanographic signals

Previous studies cited low Sr content, high Mn content, high Mn/Sr ratio, and ^{18}O-depletion as characteristics of diagenetic alteration by meteoric or burial fluids (Jacobsen and Kaufman, 1999; Sawaki et al., 2010). In this study, we adopted a conservative Mn/Sr ratio of ≤ 2.5 as an initial diagenetic alteration threshold. The majority of limestone and dolostone samples from the Hamajing, Gaojiashan, Shibantan, Baimatuo, and Yanjiahe members have Mn/Sr ratios less than 2.5 and are thus regarded as least-altered samples with the potential to preserve primary geochemical signatures. Additionally, we also investigated the correlations of $\delta^{238}U$–Mn content, $\delta^{238}U$–Sr content, $\delta^{238}U$–Mn/Sr, $\delta^{238}U$–Sr/(Mg+Ca), $\delta^{238}U$–Mn/(Mg+Ca), and $\delta^{238}U$–$\delta^{18}O$ for samples with Mn/Sr ratios less than 2.5 (Table 5.3). No systematic trends are apparent, suggesting that interaction with meteoric or burial fluids did not significantly alter $\delta^{238}U$.

In carbonates that underwent extensive recrystallization, $\delta^{238}U$ may be diagenetically altered, and therefore petrographic studies and comparison of data from multiple coeval sections are necessary to confirm that carbonate $\delta^{238}U$ captures depositional conditions (Hood et al., 2016). The Gaojiashan, Shibantan, and Yanjiahe

members typically preserve pristine sedimentary fabrics such as microbially laminated micrites and $\delta^{13}C$ signatures consistent with marine carbonates of similar age (Cai et al., 2010; Cui et al., 2016a; Sawaki et al., 2010), suggesting that their geochemistry was not strongly altered by diagenesis. These petrographic observations and similar $\delta^{238}U$ signatures in two widely separated limestone sections together strongly suggest that $\delta^{238}U$ was not significantly altered by diagenesis. The Hamajing Member and Beiwan Member are characterized by micritic to microsparitic fabric-retentive dolomite, with no apparent evidence for fabric-destructive dolomitization (Sawaki et al., 2010). The majority of dolostone samples (27 out of 30) from the Hamajing and Beiwan members have $\delta^{18}O$ values greater than −6‰, and $^{87}Sr/^{86}Sr$ values from both the Hamajing (0.7085–0.7088) and Baimatuo (0.7087–0.7102) members are well within the range of typical latest Ediacaran seawater (0.7085–0.7100) (Jacobsen and Kaufman, 1999; Sawaki et al., 2010; Shields and Veizer, 2002). A simple model of carbonate diagenesis predicts that U is more robust than $\delta^{18}O$ and $^{87}Sr/^{86}Sr$ with respect to diagenetic alteration (Lau et al., 2017). Therefore, these latest Ediacaran carbonates appear capable of preserving the $\delta^{238}U$ of contemporaneous seawater.

Changes in lithology—such as dolomitization—could also potentially impact $\delta^{238}U$, but this is unlikely to be a major factor in the sections studied here. Romaniello et al. (Romaniello et al., 2013) reported a sharp decrease in $\delta^{238}U$ below −0.6‰ corresponding to the appearance of dolomite in a tidal pond in the Bahamian carbonate platform. Although the cause for these negative values is not yet fully understood, $\delta^{238}U$ is strongly correlated with the Mg/Ca molar ratio (R^2=0.96), a proxy that indicates the extent of dolomitization. By contrast, although the Shibantan Member and the Yanjiahe Formation are comprised of

limestone and the Hamajing Member and the Baimatuo Member are comprised of dolostone, no statistically significant correlations are observed between $\delta^{238}U$ and Mg/Ca molar ratio for these carbonates at Wuhe (R^2=0.22). Furthermore, a recent global compilation of $\delta^{238}U$ variation across the Permian-Triassic boundary indicates that both the dolomitized sections and the non-dolomitized sections show congruent $\delta^{238}U$ records, indicating that dolomitization alone may not significantly alter paleo-$\delta^{238}U$ records (Zhang et al., 2018a). These observations suggest that dolomitization has not systematically altered the primary U isotopic record in the Wuhe section.

The effect of other changes in mineralogy—such as transformation of aragonite to calcite—on $\delta^{238}U$ are also likely to be small or negligible. The Shibantan and Gaojiashan limestone (low-Mg calcite) was likely originally aragonite and/or high-Mg calcite. Prior studies have shown that the distribution coefficient of U into aragonite is higher than for calcite (Meece and Benninger, 1993). In contrast, the effect of mineralogy and carbonate ion concentration on $\delta^{238}U$ is more limited. Uranium isotope measurements of aragonite and high-Mg calcite primary precipitates exhibit no offset from seawater (Romaniello et al., 2013). Laboratory-precipitated calcite and aragonite at pH ~ 8.5 showed only minor (<0.13‰) U isotope fractionation between the liquid medium and the solid (Chen et al., 2016). In contrast, at pH ~ 7.5, the precipitates of both polymorphs exhibit no U isotope fractionation (Chen et al., 2016). Therefore, changing carbonate mineralogy can result in large differences in uranium concentrations but only small changes in the isotopic composition (Lau et al., 2017).

Detrital U contamination could also cause a $\delta^{238}U$ offset. Our samples were dissolved in 1 M hydrochloric acid (HCl) prior to extraction of U, which will minimize

dissolution of any non-carbonate minerals (e.g., silicates) and organic matter. This expectation is supported by the high U/Al ratios in our analyses. The U/Al ratios of our dissolved samples are two orders of magnitude higher than the upper continental crust ratio (~0.331 ppm/wt.%). Assuming all the measured Al comes from detrital material, and using a U/Al ratio of 0.331 (ppm/wt.%) for the upper continental crust, we estimate that detrital U accounts for <2 % of total U in the dissolved samples from Wuhe, and < 10 % of total U for the majority of Gaojiashan samples. Although the estimated amount of U derived from detrital material is different between the Shibantan Member at Wuhe and its equivalent Gaojiashan Member at Gaojiashan, the $\delta^{238}U$ signals of these two members are essentially identical. Furthermore, there is no correlations between $\delta^{238}U$ and Al contents (R^2=0.19, p=0.38 for Shibantan carbonates, and R^2=0.11, p=0.67 for Gaojiashan carbonates). Therefore, we are confident that our observed $\delta^{238}U$ trends are not related to detrital contamination.

Changes in redox conditions of the local water column might affect the ability of carbonate sediments to passively incorporate U(VI), which is essential for capturing the $\delta^{238}U$ value of seawater (Romaniello et al., 2013). Specifically, it is essential that carbonates act as an oxic sink for U, with no change in redox state (and thus a potential isotopic fractionation) of U in the local water column. We examined water column redox conditions by looking at the Ce anomaly (Ce/Ce*) in our carbonates. The Ce anomalies at Wuhe and at Gaojiashan range between 0.29 and 0.79 (mean of 0.50) and between 0.70 and 0.98 (mean of 0.74), respectively, suggesting that local water column redox conditions at Wuhe and at Gaojiashan were oxic (Ling et al., 2013). This confirms that our carbonates

can be considered an oxic sink for U, and thus can passively capture the $\delta^{238}U$ signal of seawater.

In addition to the water column, it is also important to consider pore water redox conditions because they can also affect the ability of carbonate sediments to preserve the $\delta^{238}U$ value of seawater. For example, under sulfidic pore water conditions, bulk carbonate sediments may incorporate ^{238}U-enriched U(IV), leading to a $\delta^{238}U$ value that is 0.2–0.4 ‰ heavier than seawater. We examined this possibility using Mo concentrations and correlations between $\delta^{238}U$ and U/(Mg+Ca) ratios and Mo/(Mg+Ca) ratios. Under sulfidic pore water conditions, U and Mo become authigenically enriched in carbonate (Romaniello et al., 2013), thus increasing U/(Mg+Ca) and Mo/(Mg+Ca) values. In our samples, Mo concentrations are significantly lower than in modern Bahamas box core sediments by approximately two orders of magnitude, and there is no systematic stratigraphic variation in U/(Mg+Ca) or Mo/(Mg+Ca) ratios, indicating that pore water euxinia during early diagenesis was less prevalent than on the modern Bahamian carbonate platform (Romaniello et al., 2013). Furthermore, there are no statistically significant correlations between $\delta^{238}U$ and U/(Mg+Ca) and Mo/(Mg+Ca) in our carbonates (Table 5.3). Thus, the $\delta^{238}U$ record in these latest Ediacaran carbonates was likely not significantly altered by pore water anoxia. We also note that if our carbonates were influenced by pore water anoxia, then our estimation of terminal Ediacaran seawater $\delta^{238}U$ can be considered conservative, such that we would underestimate the extent of ocean anoxia in the terminal Ediacaran ocean.

After consideration of each of these factors, we conclude that the Dengying carbonates likely reflect the $\delta^{238}U$ of late Ediacaran seawater. Samples that pass our diagenetic and detrital quality control checks are plotted in Figure 5.2.

The Shibantan Member and the stratigraphically-correlated Gaojiashan Member yield the most negative carbonate $\delta^{238}U$ values ever reported from the geological record. The average $\delta^{238}U$ values of the Shibantan Member and the Gaojiashan Member are –0.97 ± 0.18‰ and –0.95 ± 0.21‰, respectively. The Hamajing Member, Baimatuo Member and Yanjiahe Formation yield higher $\delta^{238}U$ values of –0.74 ± 0.54‰, –0.72 ± 0.25‰ and –0.71 ± 0.16‰, respectively (Figure 5.2). The extremely negative $\delta^{238}U$ values in the Gaojiashan and Shibantan members are associated with positive carbonate carbon isotope excursions in both sections (Figure 5.2). A positive shift in $\delta^{238}U$, starting in the Baimatuo Member and peaking at the Dengying-Yanjiahe boundary (maximum values of –0.6‰ to –0.5‰), occurs coevally with a negative carbonate carbon isotope excursion (Figure 5.2) that has been observed globally near the Ediacaran-Cambrian boundary (Amthor et al., 2003; Kimura and Watanabe, 2001; Xiao et al., 2016). This positive $\delta^{238}U$ excursion is followed by another shift back to relatively negative $\delta^{238}U$ values (minimum values of –0.7‰ to –0.8‰) above the Ediacaran-Cambrian boundary, although more data from Cambrian age sediments are required to confirm this pattern.

5.5 Extensive ocean anoxia in the latest Ediacaran ocean

Since diagenesis cannot easily explain the very negative $\delta^{238}U$ values observed in the Shibantan/Gaojiashan members, the data likely indicate an episode of extensive

expansion in marine anoxia. We evaluate the extent and the possible causes for those extremely negative values below.

First, we evaluate the extent of ocean anoxia based on U isotope mass balance equations 12 – 15 for the terminal Ediacaran oceans:

$$\delta^{238}U_{input} = (f_{anoxic} \times \delta^{238}U_{anoxic}) + (f_{other} \times \delta^{238}U_{other}) \quad \text{Eq. 28}$$

$$\delta^{238}U_{anoxic} = \delta^{238}U_{seawater} + \Delta_{anoxic} \quad \text{Eq.29}$$

$$\delta^{238}U_{other} = \delta^{238}U_{seawater} + \Delta_{other} \quad \text{Eq.30}$$

where the subscripts *seawater*, *input*, *anoxic*, and *other* denote the seawater, riverine input, anoxic/euxinic sink, and all other sedimentary sinks, respectively. f_{anoxic} and f_{other} represent the fraction of total U removed to each sediment type, and Δ_{anoxic} and Δ_{other} represent the isotope fractionation factor between seawater and each sediment type. In this simplified calculation, all types of sinks other than anoxic/euxinic sinks are lumped into a single "other" sink (see Figure 1.2). Because the fraction of U removed into anoxic/euxinic sedimentary sinks is intimately coupled to the proportion of anoxic/euxinic versus oxic bottom waters, $\delta^{238}U_{seawater}$ can be used to calculate the area of anoxic/euxinic seafloor using the equation below, derived from the U isotope mass balance and assuming a first-order relationship between U burial rate into each sink and the global seawater U reservoir:

$$\delta^{238}U_{seawater} = \delta^{238}U_{input} - \frac{A_{anoxic} \cdot k_{anoxic} \cdot \Delta_{anoxic} + A_{suboxic} \cdot k_{suboxic} \cdot \Delta_{suboxic} + A_{oxic} \cdot k_{oxic} \cdot \Delta_{oxic}}{A_{anoxic} \cdot k_{anoxic} + A_{suboxic} \cdot k_{suboxic} + A_{oxic} \cdot k_{oxic}}$$

Eq.31

where A_{anoxic}, $A_{suboxic}$, and A_{oxic} denote anoxic/euxinic seafloor area, suboxic seafloor area, and oxic seafloor area ($A_{anoxic} + A_{suboxic} + A_{oxic} = A_{ocean}$, where A_{ocean} is the seafloor area of

the whole ocean), respectively, and k_{anoxic}, $k_{suboxic}$, and k_{oxic} represent removal rate constants for each sink type.

We use the following values for terminal Ediacaran seawater: $\delta^{238}U_{seawater} = -0.95‰$ (average isotopic composition of the Shibantan and Gaojiashan members), $\delta^{238}U_{input} = -0.34‰$, $\delta^{238}U_{anoxic} = -0.95‰+\Delta_{anoxic}$, and $\delta^{238}U_{other} = -0.91‰$ (*i.e.,* $-0.95‰+\Delta_{other}$, assuming a constant Δ_{other} of 0.04‰). Using a Δ_{anoxic} of 0.6‰ that is a representative average observed in the modern Saanich Inlet (Holmden et al., 2015), we calculate that $f_{anoxic} \approx 1$, meaning that anoxic/euxinic sinks were responsible for nearly 100% of the U removal to sediments when the Shibantan/Gaojiashan members were deposited (Figure 5.3A). A simple mass balance seafloor area calculation [equation (4)] predicts that nearly ~100% of the seafloor area was covered by anoxic/euxinic sediments (Figure 5.3B). Hence, the data suggest that an episode of extensive ocean anoxia occurred during the terminal Ediacaran Period. However, this extreme scenario is inconsistent with the presence of benthic oxygen-breathing organisms in the terminal Ediacaran Period, necessitating a sensitivity test of the mass balance calculation to assess the impact of Δ_{anoxic} values on the model estimates.

The inferred extent of ocean anoxia calculated from the mass balance model depends on the average fractionation factor between seawater and anoxic/euxinic sediments. This parameter is not tightly constrained because data exists for only a small number of modern anoxic environments. Considering this uncertainty, we explored the effect of a large range of Δ_{anoxic} values (0.4‰ to 1.3‰) on the marine U isotope mass balance. The results are summarized in Figure 5.3B. Large U isotope fractionations of between 0.68‰ and 0.99‰ have been reported during reduction of U(VI) to U(IV) by

different species of metal-reducing bacteria (Basu et al., 2014; Stylo et al., 2015). While studies of U reduction in modern anoxic marine basins commonly find apparent fractionation factors of $\Delta_{anoxic} = 0.6 \pm 0.1$‰ (Andersen et al., 2014; Holmden et al., 2015; Rolison et al., 2017), these fractionation factors are interpreted to reflect diffusion-limited U reduction below the sediment-water interface, which reduces the magnitude of the apparent isotopic fractionation factor by ~50% (Andersen et al., 2014). Studies of U reduction in most modern anoxic basins have shown that little, if any, U reduction occurs directly in the water column (Holmden et al., 2015; Rolison et al., 2017). Nevertheless, there is some evidence that microbial U reduction can occur at significant rates directly in the water column of strongly reducing marine basins, such as Framvaren Fjord (McKee and Todd, 1993). Under these conditions, U reduction appears to be accompanied by a larger isotopic fractionation factor of 1.0−1.3 ‰, similar to that predicted by laboratory experiments and theoretical calculations (Bigeleisen, 1996; Wang et al., 2015). Taken together, existing observations imply that reductive removal of U from seawater could result in effective isotopic fractionation factors of 0.4−1.3 ‰ between euxinic sediments and the overlying water column. In contrast, the isotopic fractionation of U isotopes under ferruginous conditions remain poorly known. A recent study suggested that U isotope fractionation may be similar in euxinic and ferruginous settings (Yang et al., 2017), however, another study has suggested that the fractionation of U isotopes under ferruginous conditions may be close to 0 ‰ (Hood et al., 2016). Further studies are needed to confirm the fractionation factor for ferruginous environments. We explore the implications of these uncertainties below.

Although the fraction of U removal into anoxic/euxinic sediments (Figure 5.3A) and the calculated anoxic/euxinic seafloor areas (Figure 5.3B) are very sensitive to Δ_{anoxic} values, extensive ocean anoxia is implicated for all plausible Δ_{anoxic} in order to drive terminal Ediacaran seawater $\delta^{238}U$ values as low as –0.95‰. For instance, when applying Δ_{anoxic} of 0.6 ‰, 0.8 ‰, 1.0 ‰, and 1.2 ‰, the calculated percent of U removal into anoxic/euxinic sediments are 100%, 75%, 60%, and 50 %, respectively, and the estimated anoxic/euxinic seafloor areas are ~100%, ~27%, ~10% and ~6%, respectively. If we assume that the maximum value of Δ_{anoxic} likely to represent Neoproterozoic oceans is similar to the maximum Δ_{anoxic} values observed both in the modern Saanich Inlet (0.79‰) (Holmden et al., 2015) and in the Black Sea (0.83‰) (Rolison et al., 2017; Weyer et al., 2008), then we calculate that $f_{anoxic} = 0.7$. This means that a minimum of 70% of the global riverine U input was removed into anoxic/euxinic organic-rich sediments when the Shibantan/Gaojiashan members were deposited. Based this estimate and Eq. 31, our best estimate for the minimum global anoxic/euxinic seafloor area during the terminal Ediacaran is ~21%. Hence, a significant portion of the seafloor area (21−100 %) overlain by anoxic/euxinic sediments during the terminal Ediacaran Period is indicated for all plausible fractionation factors between anoxic/euxinic sediments and seawater.

Our study highlights that marine anoxia may have been a global phenomenon from ca. 551 to 541 Ma, though there were likely redox fluctuations within local continental margin basins. For example, Fe−S−C systematics and redox-sensitive metal enrichments from latest Ediacaran sediments in South China suggest predominance of anoxia in deep water settings (Li et al., 2010; Sahoo et al., 2016; Xiang et al., 2017), with oxic water masses only present in very shallow settings (Cui et al., 2016a; Ling et al., 2013). The Fe

speciation and Ce anomaly data from the Nama Group in Namibia suggest locally dynamic redox conditions with frequent anoxia in deep water settings (Schroder and Grotzinger, 2007; Tostevin et al., 2016; Wood et al., 2015).

A gradual recovery to heavier U isotope values occurs in the stratigraphically overlying Baimatuo Member, with the highest $\delta^{238}U$ values (–0.6‰ to –0.5‰) occurring at the Ediacaran−Cambrian boundary (Figure 5.2). Above the boundary, $\delta^{238}U$ data hint at a return to low values (–0.7‰ to –0.8‰), although more data are needed to confirm this pattern. These observations suggest a temporary transition to more oxygenated conditions at the Ediacaran−Cambrian boundary (Sahoo et al., 2016; Wen et al., 2011), followed by a return to extensive oceanic anoxia in the earliest Cambrian (Sahoo et al., 2016; Xiang et al., 2017).

Because the U isotope fractionation under ferruginous conditions is poorly constrained, it is possible that the fluctuating $\delta^{238}U$ values in the Dengying Formation represent global redox oscillation between ferruginous vs. euxinic conditions, rather than oscillation between oxic vs. anoxic conditions. For example, if the fractionation factor associated with U removal to ferruginous sediments is close to 0 ‰ (as has been suggested by Hood et al., 2016), then the positive $\delta^{238}U$ shift observed in the upper Wuhe section could be explained by a shift from dominantly euxinic to ferruginous conditions. However, it is more likely that the variations reflect a shift between anoxic and oxic conditions because higher $\delta^{238}U$ values in the lowest Hamajing and upper Baimatuo members and in lowest Yanjiahe Formation (Figure 5.2) are consistent with existing evidence for widespread ocean oxygenation immediately preceding the Hamajing stage (Kendall et al., 2015) and at the Ediacaran-Cambrian boundary (Sahoo et al., 2016; Wen et al., 2011).

Regardless, the main conclusion still holds that the terminal Ediacaran Period experienced extensive ocean anoxia (euxinic or ferruginous), although the detailed redox history of this time period will not be resolved until the U isotope fractionation in ferruginous settings is better understood.

The cause(s) of rapid (million-year timescale) variations in global marine redox chemistry during the terminal Ediacaran Period are unclear and merit further study. However, variations between oxic and anoxic conditions may have been linked to changes in continental weathering fluxes and increased marine PO_4^{3-} levels. Phosphorus is commonly considered to be the ultimate biolimiting nutrient on geological timescales, and it plays a role in controlling the amount and spatial distribution of dissolved O_2 in the oceans (Lenton et al., 2014). The terminal Ediacaran Period was associated with high continental weathering as indicated by the significant rise in seawater $^{87}Sr/^{86}Sr$ (Jacobsen and Kaufman, 1999; Sawaki et al., 2010; Shields and Veizer, 2002). High continental weathering rates could have increased marine phosphorus levels, thus stimulating marine productivity. On a short timescale (10^4-year), increased phosphorus input to the ocean would have led to rapid increases in primary production, higher O_2 demand, and deep-water anoxia and lower seawater $\delta^{238}U$ values (e.g., the Shibantan/Gaojiashan stage, and the early Baimatuo Stage) (Lenton et al., 2014). On a long timescale (10^6-year), it would have tended to increase organic carbon burial and atmospheric oxygen (Lenton et al., 2014), and elevated marine sulphate concentrations (Cui et al., 2016a; Fike et al., 2006), ocean oxygenation, extensive phosphorite formation (Wen et al., 2011), and higher seawater $\delta^{238}U$ values in the latest Ediacaran and earliest Cambrian ocean (e.g., the late Baimatuo and the earliest Yanjiahe Stage).

5.6 Oscillatory ocean redox conditions at the Ediacaran-Cambrian transition

The geochemical data from this study combined with previous Ediacaran and Early Cambrian paleoredox studies yield a complex picture of oscillatory ocean redox conditions at the Ediacaran−Cambrian transition (Figure 5.4). Fe−S−C systematics and redox-sensitive metal enrichments in organic-rich mudrocks (~635–~551 Ma) revealed three distinctive Ediacaran ocean oxygenation events at ca. 635, ca. 580, and ca. 560 Ma, with oceanic anoxia possibly dominating the intervals between these oxygenation events (Sahoo et al., 2016; Scott et al., 2008). Studies focusing on the Shuram/Wonoka negative carbon isotope excursion (~580–~553 Ma, although the time and duration of this event are still uncertain) provided evidence of profound deep ocean oxygenation (Fike et al., 2006; McFadden et al., 2008), although other studies argued that the global response of ocean redox chemistry at this time was likely complex (Li et al., 2010; Sahoo et al., 2016; Sperling et al., 2015). Organic-rich mudrocks deposited near the end of the Shuram/Wonoka excursion have high Mo enrichments and isotopically heavy U isotope compositions that point to an episode of extensive ocean oxygenation ca. 560 to 551 Myr ago (Kendall et al., 2015; Sahoo et al., 2016; Scott et al., 2008). In this study, we provide strong evidence for an episode of extensive oceanic anoxia that follows this episode of oxygenation. Geochemical studies focusing on the Ediacaran−Cambrian boundary (~541 Ma) and the earliest Cambrian also present a complex picture of ocean redox chemistry, with apparently conflicting views of both oxygenation (Sahoo et al., 2016; Wen et al., 2011) and anoxia (Kimura and Watanabe, 2001; Schroder and Grotzinger, 2007). However, our new $\delta^{238}U$ data provide evidence of an increase in global ocean oxygenation at the Ediacaran−Cambrian boundary, consistent with prior redox-sensitive trace metal

enrichment and Mo isotope evidence of ocean oxygenation at the Ediacaran−Cambrian boundary (Sahoo et al., 2016; Wen et al., 2011). Therefore, the overall picture emerging from this study and prior studies is that global marine redox evolution across the Ediacaran−Cambrian transition was not a simple unidirectional march toward oxygenation, but a dynamic and more complicated history than expected, with rapid oscillations between anoxic and oxic conditions.

5.7 Ocean anoxia and the decline of the Ediacaran biota

Although the geochronological constraints on Ediacaran successions are generally poor, available data seem to suggest that the Ediacara biota consists of three taxonomically distinct assemblages that at least partially represent evolutionary successions (Xiao and Laflamme, 2009): the Avalon (~570-560 Ma), White Sea (~560–550 Ma), and Nama assemblages (~550–540 Ma). The Shibantan Member of the Dengying Formation (~551–541 Ma) studied in this paper contains *Cloudina* that is only found in the Nama assemblage (Cai et al., 2010) as well as taxa (e.g., *Rangea*, *Pteridinium*) that are commonly present in the Nama Group (Chen et al., 2014), but does not yield any fossils (e.g., *Dickinsonia* and *Yorgia*) that are characteristic of the White Sea assemblage (Chen et al., 2014). Thus, in both taxonomic composition and depositional age, the Shibantan Member represents an example of the Nama assemblage, contrary to Laflamme et al. (2013) who assigned the Dengying Formation to the White Sea assemblage.

In the context of the oscillatory redox model presented in this paper (Figure 5.4), it is tempting to consider the potential correlation between ocean redox history and the evolution of the Ediacara biota. It seems that the Ediacara biota diversified and thrived as

oxygenated conditions prevailed at 570–550 Ma, but started to decline as oceanic anoxia began to expand globally around 550 Ma. Among the three assemblages of the Ediacara biota, the White Sea assemblage shows the peak diversity, and there is a significant decline in both global and local taxonomic diversity from the White Sea to the Nama assemblage (Darroch et al., 2015; Laflamme et al., 2013; Shen et al., 2008; Xiao and Laflamme, 2009). This decline in the terminal Ediacaran Period seems to be a robust pattern that has been supported by rarefaction analyses of both global and local taxonomic data (Darroch et al., 2015; Shen et al., 2008). The U isotope data presented here suggest that oxic water masses began to contract around 550 Ma, raising the intriguing possibility that the decline of the Ediacara biota is correlated with the expansion of oceanic anoxia.

Acknowledging correlation is not necessarily causation, we offer some speculative thoughts about the potential mechanisms through which marine anoxia may have driven the decline of the Ediacara biota. These mechanisms can be inferred from an examination of the extinction vs. survival selectivity during the decline of the Ediacara biota. Most Ediacara-type organisms were sessile benthic macroorganisms (Erwin et al., 2011) with little motility, although exceptions exist in some dickinsoniomorphs [e.g., *Yorgia* (Ivantsov and Malakhovskaya, 2002) and *Dickinsonia* (Gehling et al., 2005)], bilateralomorphs [e.g., *Parvacorina* (Darroch et al., 2017)], and kimberellomorphs [e.g., *Kimberella (Gehling et al., 2015)]*, which may have developed facultative or limited mobility. It remains unknown whether all members of dickinsoniomorphs, bilateralomorphs, and kimberellomorphs are facultatively mobile. However, it is interesting to note that these facultatively mobile and centimeter-sized macroorganisms (and indeed all dickinsoniomorphs, bilateralomorphs, and kimberellomorphs) are exclusively found in the White Sea assemblage but did not

survive into the Nama assemblage (Laflamme et al., 2013). One intriguing possibility is that their facultative mobility may have increased their oxygen demand, yet their relatively large body size (and hence low surface area to volume ratios) may have hampered their capability to acquire oxygen through diffusion across body surface. This effect could have exacerbated if the combination of their large body size and limited mobility prevented them from exploiting localized oxygen oases such as those associated with cyanobacterial mats. As a result, these taxa may have been particularly vulnerable when oceanic anoxia began to expand in the terminal Ediacaran Period. In contrast, sessile Ediacara organisms (including erniettomorphs, rangeomorphs, and arboreomorphs), particularly rangeomorphs that have a repeatedly branching system and large surface area to volume ratios (Laflamme et al., 2009), may have been able to survive the terminal Ediacaran anoxia event because of their relatively low oxygen demand and, for rangeomorphs, their improved capability to supply oxygen through diffusion. Millimeter-sized bilaterian animals may have been even better-equipped to survive the terminal Ediacaran anoxia event, because their agility and small body size allowed them to explore localized oxygen oases in cyanobacterial mats. Indeed, millimeter-sized bilaterian animal traces in the Shibantan Member are only found in association with microbial mats, indicating these animals may have dynamically searched for oxygen oases in cyanobacterial mats (Meyer et al., 2014). Terminal Ediacaran biomineralizing animals such as *Cloudina* and Namacalathus are preferentially associated with stromatolites and thrombolites (Penny et al., 2014), perhaps to take advantage of a localized oxygen source in these environments. In addition, there is evidence that at least some of these biomineralizing animals may have developed the capability for ecological dispersal (Cortijo et al., 2015), allowing them to track localized oxic environments (Wood

et al., 2015) during the terminal Ediacaran anoxia event. Therefore, it appears that body size, surface area to volume ratio, mobility, and ecological dispersal may have been the factors that determined the metazoan survivors during the terminal Ediacaran anoxia event. The picture seems to be more complex than a simple relationship between a terminal Ediacaran decline in biodiversity and expansion in oceanic anoxia; instead, as oceanic anoxia expanded, spatial redox pattern may have become increasingly heterogeneous, and the ability to explore localized oxygen oases or refugia became a critical survival skill. We emphasize that the possible role of anoxia in driving the decline of the Ediacara biota does not necessarily rule out the importance of ecological factors (Darroch et al., 2015), because the environmental perturbation and biotic replacement models do not need to be mutually exclusive. Instead, we argue that the decline of the Ediacara biota did not happen in the absence of environmental change.

This study provides the first direct geochemical evidence supporting an episode of extensive oceanic anoxia in the terminal Ediacaran Period, coincident with the decline of the Ediacara biota as recorded in the Nama assemblage. Hence, the Ediacara biota likely capitalized on a geologically brief oxygenated window about 570–550 Ma, but subsequent oceanic anoxia along with other environmental and ecological factors may have contributed to its decline in the terminal Ediacaran Period. This hypothesis offers new research opportunities to investigate other Ediacaran successions using more redox proxies and more precise age models.

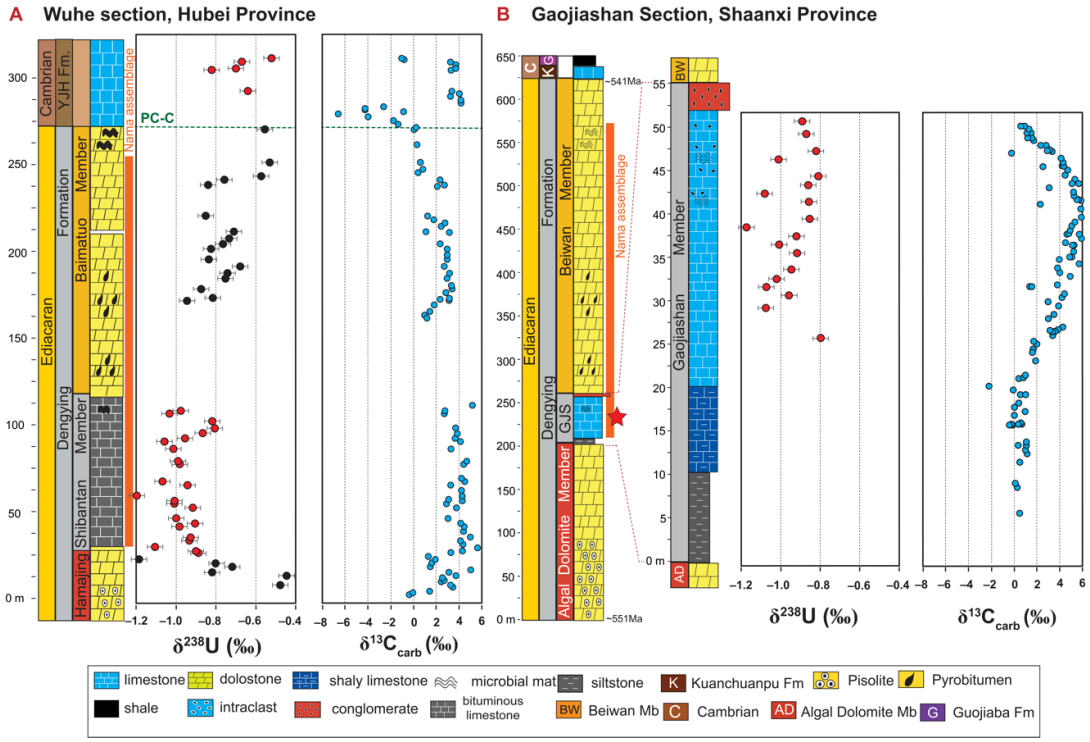

Figure 5.2 (A) Geochemical profiles of the terminal Ediacaran Dengying Formation at the Wuhe and Gaojiashan sections. Stratigraphic columns and $\delta^{13}C$ data of Gaojiashan are from Cui et al. (Cui et al., 2016a). $\delta^{238}U$ data from the Hamajing Member and samples with Mn/Sr > 2.5, Rb/Sr > 0.02, and Al > 0.35% are excluded in this plot.

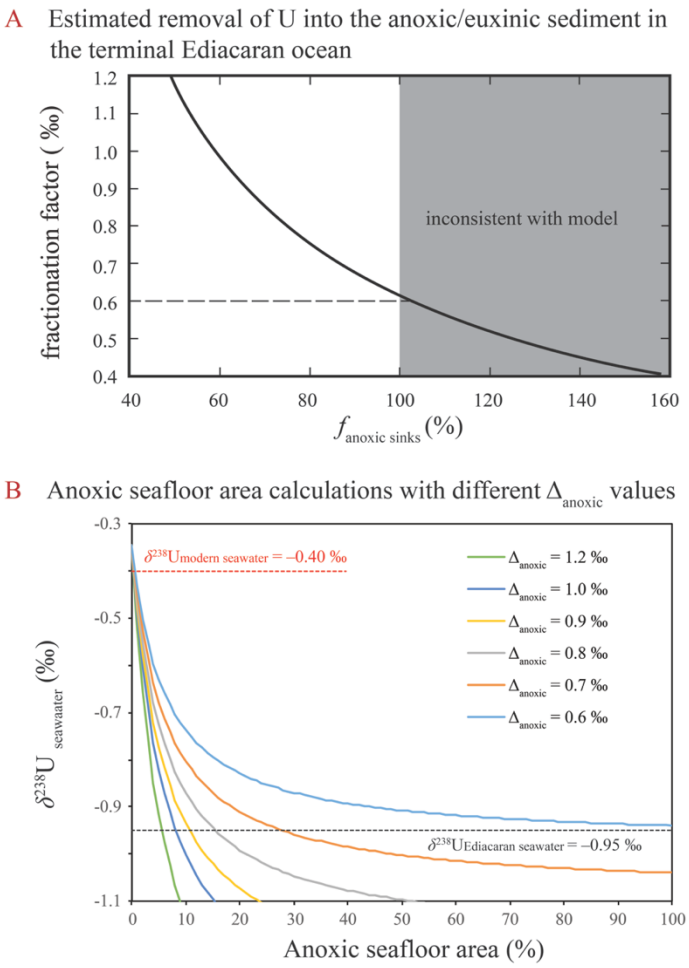

Figure 5.3 Model results. (A) The fraction of oceanic U inputs removed into anoxic/euxinic sediments (horizontal axis) varies as a function of the fractionation factor (Δ_{anoxic}; vertical axis) between seawater and anoxic/euxinic sediments. The estimates are based on calculations using the average carbonate $\delta^{238}U$ of the Shibantan/Gaojiashan members ($\delta^{238}U = -0.95$ ‰). (B) Mass balance calculations show variations of seawater $\delta^{238}U$ values as a function of anoxic seafloor area, keeping suboxic seafloor area fixed at 0 % of total seafloor area and testing the sensitivity to possible Δ_{anoxic} values. In reality, suboxic seafloor area would co-vary with anoxic/euxinic seafloor area; thus, this modeling exercise gives us the lowest estimation of anoxic/euxinic seafloor area.

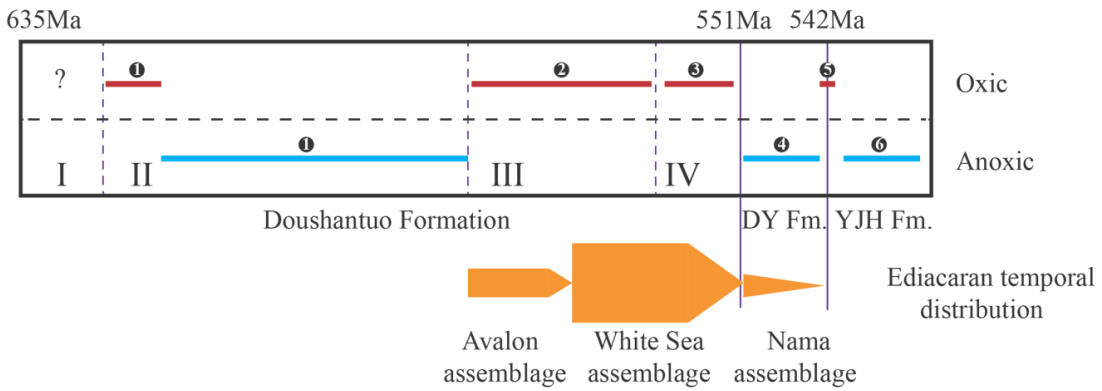

Figure 5.4 Summary of global ocean redox chemistry in the Ediacaran and Early Cambrian periods. Data sources: 1, Fe-S-C systematics and redox sensitive metal enrichments in euxinic shales from South China (Sahoo et al., 2016); 2, S and C isotopes in carbonates and siliciclastic rocks from Oman (Fike et al., 2006) and South China (McFadden et al., 2008); 3, Redox sensitive metal enrichments and Mo-U isotopes in organic rich shales from South China (Kendall et al., 2015; Sahoo et al., 2016; Scott et al., 2008); 4, U isotopes in carbonates from South China (this study); 5, U isotopes in carbonates (this study), Mo isotopes in phosphorites (Wen et al., 2011), and redox sensitive trace metal enrichments in euxinic shales from South China (Sahoo et al., 2016); 6, U isotopes in carbonates (this study). I–IV: Member I–IV of the Doushantuo Formation. The Ediacaran temporal distribution is modified after Laflamme et al. (2013).

CHAPTER 6

NEAR-MODERN LEVELS OF OCEAN OXYGENATION CONTRIBUTED TO THE EDIACARAN EVOLUTION OF EARLY ANIMALS

This chapter is currently under in preparation for resubmission:

Zhang F., Romaniello S.J., Xiao, S., Hardisty D., Lenton, T., Li C., Daines S., Melezhik V.A, Pokrovsky B.G., Shi W., Cheng M., Anbar A.D., Near-modern levels of ocean oxygenation contributed to the initial diversification of animals. In preparation.

6.1 Introduction

After life first emerged more than 3 billion years ago, single-celled organisms dominated the planet for most of its history. It is not until the Ediacaran Period (635–541 Ma) when large and morphologically complex multicellular eukaryotes became abundant and diverse. Mobile animals, including both cnidarians and bilaterians, appeared in the middle Ediacaran Period (Gehling et al., 2015; Liu et al., 2010; Xiao and Laflamme, 2009). The cause of this evolutionary innovation remains a subject of debate. A temporal correlation with evidence for a major redox transition suggests that a profound ocean oxygenation event may have sparked this evolutionary event (Canfield et al., 2007; Fike et al., 2006; McFadden et al., 2008). However, others have argued that the diversification of bilaterians may have been enabled by the evolution of key developmental toolkits (Erwin, 2009) or that the rise of eumetazoans was driven by positive ecological feedbacks (Butterfield, 2007).

The oxygenation hypothesis is attractive because aerobic metabolic pathways provide much more energy than anaerobic ones, and so the presence of free O_2 is often regarded as a prerequisite for the evolution of macroscopic animals, particularly those involved in energetically expensive lifestyles such as mobility, burrowing, and predation (Sperling et al., 2013). Given the importance of O_2 for animal physiology, researchers have combed Neoproterozoic successions to determine when there were significant changes in the proportion of oxic to anoxic waters in the deep ocean (Canfield et al., 2008; Canfield et al., 2007; Fike et al., 2006; Johnston et al., 2013; McFadden et al., 2008; Sperling et al., 2015).

Carbonate sedimentary rocks from the Middle Ediacaran Period have attracted special attention (Fike et al., 2006; Grotzinger et al., 2011; McFadden et al., 2008). Middle Ediacaran carbonates from all over the globe (including South China, Siberia, western United States, Oman, and South Australia) record the largest negative $\delta^{13}C_{carb}$ excursion (<-12 ‰) in Earth history, termed the "Shuram Excursion" (SE) after its initial discovery in the Shuram Formation of Oman (Grotzinger et al., 2011). According to a scheme of Ediacaran stratigraphic correlation (i.e., correlation 2 of ref. 8), rapid diversification of the Ediacara biota, including the appearance of large, mobile, and morphologically complex animals and their traces, immediately followed the onset of the SE (Canfield et al., 2007; McFadden et al., 2008; Xiao et al., 2016). It has been proposed that the SE represents an unprecedented change in deep ocean oxygenation, and that this change sparked the diversification of complex animals (Canfield et al., 2007; Fike et al., 2006; McFadden et al., 2008). However, the extent of global ocean redox change across this critical interval is poorly constrained. For instance, proxies for tracking local or regional Fe-S-C systematics

and iodine chemistry have been used to infer oxygenation of the deep ocean in some locations during or after the SE (Canfield et al., 2007; Fike et al., 2006; Hardisty et al., 2017; McFadden et al., 2008). However, similar data from other localities have been used to argue for a persistence of redox-stratified and ferruginous marine environments during or across this critical interval (Canfield et al., 2008; Johnston et al., 2013; Li et al., 2010; Sahoo et al., 2016; Sperling et al., 2015). These contrasting views likely arise because these paleoredox proxies are inherently local or indirect tracers of oxygenation.

Compared to these other proxies, the U isotope system ($^{238}U/^{235}U$, denoted as $\delta^{238}U$) measured in carbonate sedimentary rocks is a more direct probe of global ocean redox conditions and can be used to place quantitative constraints on the extent of global redox changes. The power of U isotopes as a global proxy derives from the fact that U has a long residence time in the ocean (e.g., ~500 kyr in the modern ocean; Dunk et al., 2002), and hence $\delta^{238}U$ is uniform in the modern ocean and will tend to be well-mixed even when the extent of ocean oxygenation is significantly lower than today (Zhang et al., 2018a). Seawater $\delta^{238}U$ varies with redox conditions because the reduction of dissolved U(VI) to U(IV), which is immobilized in anoxic sediments, results in a large and detectable change in $\delta^{238}U$, favoring heavy isotopes in the reduced species (Andersen et al., 2014). Thus, $\delta^{238}U$ of U(VI) dissolved in seawater decreases as the global areal extent of bottom water anoxia increases (Brennecka et al., 2011a). Marine carbonate sediments have been demonstrated to record the $\delta^{238}U$ of seawater, subject to a 0.2–0.4 ‰ offset, which likely reflects incorporation of U(IV) into shallow sediments from anoxic porewaters (Romaniello et al., 2013). Consistent with these modern observations, similar trends and

absolute values of $\delta^{238}U$ have been identified in synchronous but spatially disparate ancient marine carbonates (Zhang et al., 2018a).

6.2 Geological background

To obtain new constraints on the extent of global redox change across the SE event, we applied the U isotope proxy and associated major and trace elements to carbonates across the SE from three widely separated and well-studied sections (Grotzinger et al., 2011) (Figure 6.1): the Jiulongwan section in South China (n = 46); the Bol'shoy Patom section in Siberia (n = 45); and the Death Valley section (the Johnnie Formation; n = 15) in the western United States.

The SE at the Jiulongwan section (GPS: N 30°48'15.05", W 111°3'18.61") is represented by the Doushantuo Member III (Li et al., 2016; McFadden et al., 2008), which is ≈70 m thick and is composed of dolostone and bedded chert in the lower part that passes up-section into limestone and dolostone. Sedimentological evidence suggests that the entire Doushantuo Formation at Jiulongwan was deposited below or near wave base (McFadden et al., 2008).

The SE at the Bol'shoy Patom section is represented by the Kholychskaya Formation, the Alyanchskaya Formation, and the Nikol'skaya Formation, which are ≈200 m, ≈530 m, and ≈390 m thick, respectively, and are composed of well-preserved high Sr limestone (Melezhik et al., 2009). The sedimentary facies associations suggest deposition on a shallow carbonate platform that was well connected to the open ocean with neither basin isolation nor chemical or physical stratification (Melezhik et al., 2009).

The SE in the Death Valley region, California comes from Saddle Peak Hills (GPS: N 35°45.439', W 116°20.936') and is represented by the Rainstorm Member of the Johnnie Formation, which is >100 m thick in the study section and is composed of interbedded siltstone, sandstone, and conglomerate, with locally abundant dolostone. Sedimentary features suggest deposition under distal-fluvial and shallow-marine (above storm wave base) conditions (Verdel et al., 2011). The Shuram $\delta^{13}C_{carb}$ excursion occurs primarily in dolomitic siltstone, but begins in an ~2 m thick dolomitic oolite member known as the Johnnie Oolite. The Johnnie Oolite is pervasive marker bed across the Death Valley region and has been characterized and discussed in many previous studies (Bergmann et al., 2011; Corsetti and J. Kaufman, 2003; Kaufman et al., 2007; Verdel et al., 2011).

The extreme negative $\delta^{13}C_{carb}$ excursion that characterizes the SE is observed in all three sections (Figure 6.2). The precise stratigraphic/temporal correlation between different Shuram sections is difficult because of the lack of a radiometric date to constrain the beginning of the Shuram excursion. Recent paleomagnetic, rock magnetic, and cyclostratigraphic studies suggest that the Shuram Excursion from different locations occurred synchronously (Gong et al., 2017; Minguez and Kodama, 2017; Minguez et al., 2015). For example, rock magnetic studies from globally separated sites—the Doushantuo Member III (EN3) in South China, the Wonoka Formation from the Flinders Ranges in South Australia, and the Johnnie Formation from the Death Valley, California, USA—suggest that the Shuram Excursion at each location occurred synchronously (Gong et al., 2017; Minguez and Kodama, 2017; Minguez et al., 2015) over a duration of 8–10 Ma. In the absence of absolute age constraints and rock magnetic studies from the Bol'shoy Patom section in Siberia, the largest $\delta^{13}C_{carb}$ excursion found in Siberia is assumed and accepted

to be correlated to the Shuram Excursion found in other localities (Grotzinger et al., 2011; Melezhik et al., 2005; Melezhik et al., 2009).

6.3 Analytical methods

Fresh rock samples were collected in the field. The rock samples have been crushed into small pieces in the core lab. We have carefully picked fresh pieces that without veins and cleaned using 18.2 MΩ Milli-Q water. The cleaned pieces were then dried and powdered to ~200 mesh using agate ball mill. Approximately 5 g of each sample was dissolved in 1 M hydrochloric acid (HCl) for 24 hours at room temperature. This method minimizes dissolution of non-carbonate minerals (e.g., silicates and sulfides) and organic matter. Digests were centrifuged and the supernatant was separated. Major, minor, and trace element concentrations were measured on a Thermo iCAP™ quadrupole inductively coupled plasma mass spectrometer (Q-ICP-MS) at the W. M. Keck Laboratory for Environmental Biogeochemistry at Arizona State University (ASU) on splits from each supernatant. Typical precision was better than 3 % and 5 % for major and trace elements, respectively, based on repeated analysis of in-run check standards.

Prior to U isotopes column chemistry, appropriate amounts of the ^{236}U:^{233}U double spike (Brennecka et al., 2011a; Romaniello et al., 2013; Weyer et al., 2008; Zhang et al., 2018a; Zhang et al., 2018b; Zhang et al., 2018c) were added to each sample to obtain molar spike/sample ratio of 0.0342. The spike-sample mixtures were evaporated to dryness and taken up in 3N HNO_3. Uranium was purified using the UTEVA method (Brennecka et al., 2011a; Romaniello et al., 2013; Weyer et al., 2008; Zhang et al., 2018a; Zhang et al., 2018b; Zhang et al., 2018c) for isotopic analysis. A volume of 1.0–1.2 mL UTEVA resin was

loaded on a column. The resin was then washed with 5 × 2.5 mL 0.05 M HCl to remove impurities. The resin was then converted to the nitric form by loading 4 × 2.5 mL 3 M HNO_3. The double-spiked U sample (dissolved in 3 M HNO_3) was loaded on the column and rinsed with 10 × 2.5 mL 3 M HNO_3 to remove all matrix ions except U and Th. Then 10 M HCl (3 × 2 mL) was added to the column to convert the UTEVA resin to chloride form. Th was removed from the resin using a mixture of 5 M HCl and 0.05 M oxalic acid (3 × 2 mL). The oxalic acid left on the resin was rinsed with 3 × 2 mL 5 M HCl. The U adsorbed on the resin was eluted with 13 mL (2+2+2+3+4) 0.05 M HCl. The U cuts were dried down and heated with concentrated HNO_3 + 30 % H_2O_2 (1.5 mL + 0.3 mL) to remove any organic residue eluted from the UTEVA resin. The last step was repeated for three times in order to remove all organic residue. All samples have been put through U isotopes column chemistry twice in order to completely remove matrix ions. The final purified U was dissolved in 0.32 M HNO_3 and diluted to a U concentration of 50 ppb.

Uranium isotopes were measured at ASU on a Themo-Finnigan Neptune multi-collector ICP-MS at low mass resolution and consisted of 50 cycles of 4.194 s integration time. Rinsing time was typically 210 s or more. When using a 100 μl nebulizer, a 50 ppb sample solution yielded 42−45 V of ^{238}U signal on a 10^{11} Ω amplifier. The standard solution CRM145 (50 ppb U) was analyzed every two samples. Two secondary standards CRM129a and Ricca ICP solution were measured after every fifteen measurements. Sample $\delta^{238}U$ values were normalized by the average of the bracketing standards. The isotopic compositions of standards CRM145, CRM129a, and Ricca are 0.00±0.07 ‰(2SD), −1.74±0.06 ‰(2SD), and −0.28±0.08 ‰(2SD), respectively. The $\delta^{238}U$ results are summarized in Figure 6.2 in the main text and in the Table 6.1-6.3.

6.4 Results

In each section, $\delta^{238}U$ shifts toward heavier values across the SE, in correlation with the negative shifts in $\delta^{13}C_{carb}$ (Figure 6.2). Samples immediately preceding the SE (pre-SE) at Jiulongwan, at Bol'shoy Patom, and at Death Valley have remarkably consistent $\delta^{238}U$ values of −0.74 ± 0.20 ‰ (2SD, and hereafter), −0.75 ± 0.15 ‰, and −0.73 ± 0.14 ‰, respectively (Figure 6.2). Samples deposited during the SE at Jiulongwan, at Bol'shoy Patom, and at Death Valley again are consistent, with $\delta^{238}U$ values of −0.23 ± 0.38 ‰, −0.28 ± 0.20 ‰, and −0.31 ± 0.31 ‰, respectively (Figure 6.2). Averaged over all three sections, $\delta^{238}U$ values of the SE carbonates (−0.26 ± 0.29 ‰) are significantly higher than those of pre-SE carbonates (−0.74 ± 0.17 ‰, $p < 0.0001$) but are only slightly lower than modern Bahamian carbonates (−0.13 ± 0.21 ‰, 2sd) (Romaniello et al., 2013). This shift of ~ 0.5 ‰ is the largest $\delta^{238}U$ shift ever reported in the geologic record.

6.5 Evidence of primary oceanographic signals

We evaluated potential diagenetic alteration of $\delta^{238}U$ by examining established diagenetic indicators (Table 6.4). The samples displayed no systematic correlations between the $\delta^{238}U$ excursions and indicators of local redox conditions (Mo/U ratios), dolomitization (Mg/Ca molar ratios), diagenetic alteration (Mn and Sr concentrations, Mn/Sr ratios, and $\delta^{18}O$), detrital input (U concentrations and U/Al ratios) or primary carbonate mineralogy (Sr/Ca) that might produce such a positive $\delta^{238}U$ excursion or an offset from contemporaneous seawater. These geochemical observations, together with the fact that the same $\delta^{238}U$ signatures are present in three widely separated sections that

experienced completely different diagenetic histories, strongly argue that the SE $\delta^{238}U$ shift is a primary oceanographic signature recording an episode of extensive global marine redox change.

Modern carbonate sediments have a $\delta^{238}U$ composition that is 0.2–0.4 ‰ heavier than that of the contemporaneous seawater (Romaniello et al., 2013), which likely reflects incorporation of ^{238}U-enriched U(IV) from anoxic porewaters during early diagenesis or variation in porewater U-speciation during carbonate recrystallization (Chen et al., 2016). Syndepositional diagenesis of carbonates occurs because shallow, relatively permeable carbonates can sequester dissolved U(VI) from the overlying oxic water via advective and diffusive transport. This semi-open system behavior provides for the exchange of U isotopes and allows the bulk carbonates to become slightly enriched in ^{238}U. However, this process does not operate at greater burial depths as the mobility of U is severely restricted in anoxic porewaters, as shown by near-zero porewater U concentrations in deep Bahamian drillcores (Henderson et al., 1999). On this basis, we have applied a diagenetic correction factor of 0.2–0.4 ‰ to the measured $\delta^{238}U$ values prior to U isotope mass balance calculations. Considering this range of diagenetic offset, our best estimates of $\delta^{238}U$ for the pre-SE seawater and the SE seawater are −0.94 ‰ to −1.14 ‰ and −0.46 ‰ to −0.66 ‰, respectively.

6.6 Quantify global marine redox changes across the Shuran Excursion

We use an isotopic mass balance model combined with our measured data to assess changes in the size of the anoxic U sink, and the implications for the areal extent of anoxic bottom waters:

$$\delta^{238}U_{input} = (f_{anoxic} \times \delta^{238}U_{anoxic}) + (f_{other} \times \delta^{238}U_{other}) \quad \text{Eq.32}$$

$$\delta^{238}U_{seawater} = \delta^{238}U_{input} - \frac{A_{anoxic} * k_{anoxic} * \Delta_{anoxic} + (A_{ocean} - A_{anoxic}) * k_{other} * \Delta_{other}}{A_{anoxic} * k_{anoxic} + (A_{ocean} - A_{anoxic}) * k_{other}} \quad \text{Eq.33}$$

where the subscripts input, anoxic, and other denote the riverine input, anoxic sink, and all other sedimentary sinks. Variables f_{anoxic} and f_{other} represent the fraction of total U removed to the respective sinks, Δ_{anoxic} and Δ_{other} represent the isotope fractionation factor between seawater and the respective sinks, A_{anoxic} and A_{ocean} denote anoxic seafloor area and seafloor area of the world ocean, and k_{anoxic} and k_{other} represent the area-weighted first-order removal rate constants for each of the respective sinks.

This model indicates that in order to account for pre-SE seawater $\delta^{238}U$ as low as −0.94 ‰ to −1.14 ‰, large areas of seafloor must have been overlain by anoxic waters. The precise extent of ocean anoxia calculated from the mass balance model (equation 17) is sensitive to Δ_{anoxic} values. Assuming Δ_{anoxic} = 0.6 ‰—an average value that is representative of modern anoxic basins like the Saanich Inlet (Holmden et al., 2015) and the Black Sea (Andersen et al., 2014)—implies that 100 % of the total U ocean sink in the pre-Shuram ocean was accounted for by removal into anoxic sediments. If we consider a range of plausible fractionation factors between 0.6–0.85 ‰, representing the range of estimates inferred from modern analogs and microbial U reduction experiments, the estimated area of anoxic seafloor in the pre-SE ocean ranges from 17–100 %. Thus, compared to the modern ocean which has ~ 0.6 % anoxic seafloor, widespread anoxia in the pre-SE ocean is implicated for all plausible values of Δ_{anoxic}.

During the SE, the marked shift of $\delta^{238}U_{seawater}$ to −0.46 ‰ to −0.66 ‰ corresponds to a dramatic expansion of seafloor oxygenation. The extent of ocean anoxia inferred from

these values is also sensitive to Δ_{anoxic} values. However, the majority of seafloor needed to be oxic to drive SE seawater $\delta^{238}U$ to higher values between −0.46 ‰ and −0.66 ‰. Under all circumstances, the calculated anoxic seafloor area in the SE ocean is < 6 %. Thus, the SE represents a significant ocean oxygenation event (Figure 6.3).

Our new evidence for global ocean oxygenation during the SE decisively reinforces prior indications of ocean oxygenation during the SE (Canfield et al., 2007; Fike et al., 2006; Hardisty et al., 2017; McFadden et al., 2008). Furthermore, seemingly conflicting results from Fe-S-C proxies for local oxygenation and local sustained anoxia (Canfield et al., 2008; Johnston et al., 2013; Li et al., 2010; Sahoo et al., 2016; Sperling et al., 2015) can be reconciled if the ocean redox regime during the SE was similar or slightly more reducing than the present day. Specifically, this would imply generally oxic global ocean conditions coexisting with anoxia in some local shelf settings (such as oxygen minimum zones) and some semi-enclosed basins (such as the modern Cariaco Basin). The combined use of Fe-S-C-I-U proxies ultimately provides a more detailed illustration of the redox state of the ocean on global and local scales.

Importantly, our data need not imply permanent oxygenation of the ocean during the Ediacaran Period. The present study specifically targets the Shuram Excursion, but other studies provide evidence for a background of widespread anoxic conditions and periodic fluctuations in the ocean redox conditions during the terminal Ediacaran Period (Tostevin et al., 2016; Zhang et al., 2018c) and Paleozoic (Gill et al., 2011; Sahoo et al., 2016; Sperling et al., 2015). The data presented in this and other studies reveal that the oceanic redox transition from the Neoproterozoic to the Paleozoic was not a simple,

unidirectional oxygenation, but one with rapid oscillations between anoxic and oxic conditions.

6.7 Implication to the origin of the Shuram Excursion and the diversification of the early animals

This hypothesis could also help explain the $\delta^{13}C$ excursion that defines the SE. Our mechanism is consistent with a scenario of localised incorporation of isotopically-light carbon from anaerobic sedimentary remineralisation processes into authigenic carbonate in some shelf sea settings (Cui et al., 2016b). Specifically, a globally-coherent water column oxygenation would set up a sharp redox gradient within the most organic-rich, shelf-sea sediments (especially when bioturbation intensity was low). The resulting sharp sedimentary redox gradient would allow isotopically-light carbon produced by methanogenesis deeper in the sediment column to be oxidised and trapped into authigenic carbonates in the sulphate-methane transition zone or the sulphate-reduction zone higher up the sediment column (Peter S. Mozley, 1993). The newly created sharp sedimentary redox gradient could also support authigenic phosphorite formation as observed on the Yangtze Platform (Cui et al., 2016c). Weaker negative carbon isotope excursions would be expected in deeper water settings due to weaker input of organic matter (Li et al., 2016). We note that although a sharp sedimentary redox gradient might also lead to the preferential incorporation of isotopically-heavy U(IV) in sediments, this would require that free O_2 and soluble U(VI) were available in the deep water column in the first place, supporting our qualitative conclusion that the deep oceans became oxygenated during the SE.

If our hypothesis is correct, then we argue that the large-scale oxygenation of the oceans during the SE was likely a consequence, rather than a direct cause, of early animal evolution. Molecular clock estimates and sponge biomarkers suggest that early animals diverged in the Cryogenian Period (~720-635 Myr ago) (Love et al., 2009), although Cryogenian animals were morphological simple and likely required little oxygen (Mills et al., 2014; Sperling et al., 2013). Macroscopic and morphologically complex animals that engaged in energetically expensive lifestyles such as mobility first appeared about 570 Ma (Xiao and Laflamme, 2009) as indicated by trace fossils (Liu et al., 2010) and the Ediacara biota (Xiao and Laflamme, 2009). With rare exceptions that warrant further investigation (Macdonald et al., 2013), elements of the Ediacara biota appeared during or shortly after the coupled excursion of C, S and U isotopes in Ediacaran Shuram-age sediments, and reached their maximum taxonomic diversity and morphological disparity about 560–550 Ma (Xiao and Laflamme, 2009). We therefore suggest that the evolution of more complex animal body plans and lifestyles during the Ediacaran was the result of rapid biogeochemical positive feedbacks, through which rising export efficiency, declining gross productivity, and increasing O_2 availability enable the development of animal mobility and increasingly sophisticated feeding strategies.

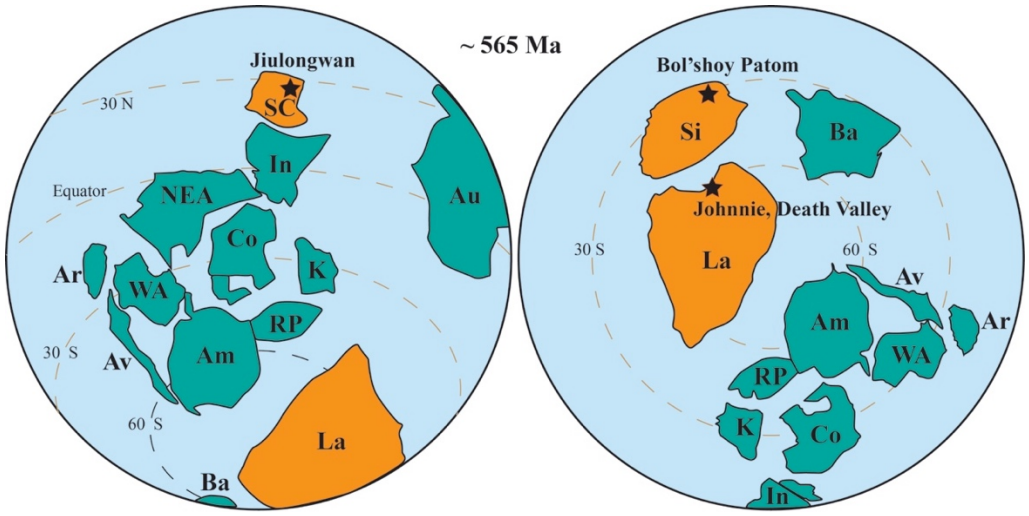

Figure 6.1 Paleogeography at 565 Ma, modified after Meert and Lieberman (2008). The black stars in the maps show the locations of study sections. Am, Amazonia; Au, Australia; Av, Avalonia; Ar, Armorica; Ba, Baltica; Co, Congo; I, India; K, Kalahari; La, Laurentia; NEA, NE Africa; S, Sahara; Si, Siberia; SC, South China; WA, Western Africa; RP, Rio Plata.

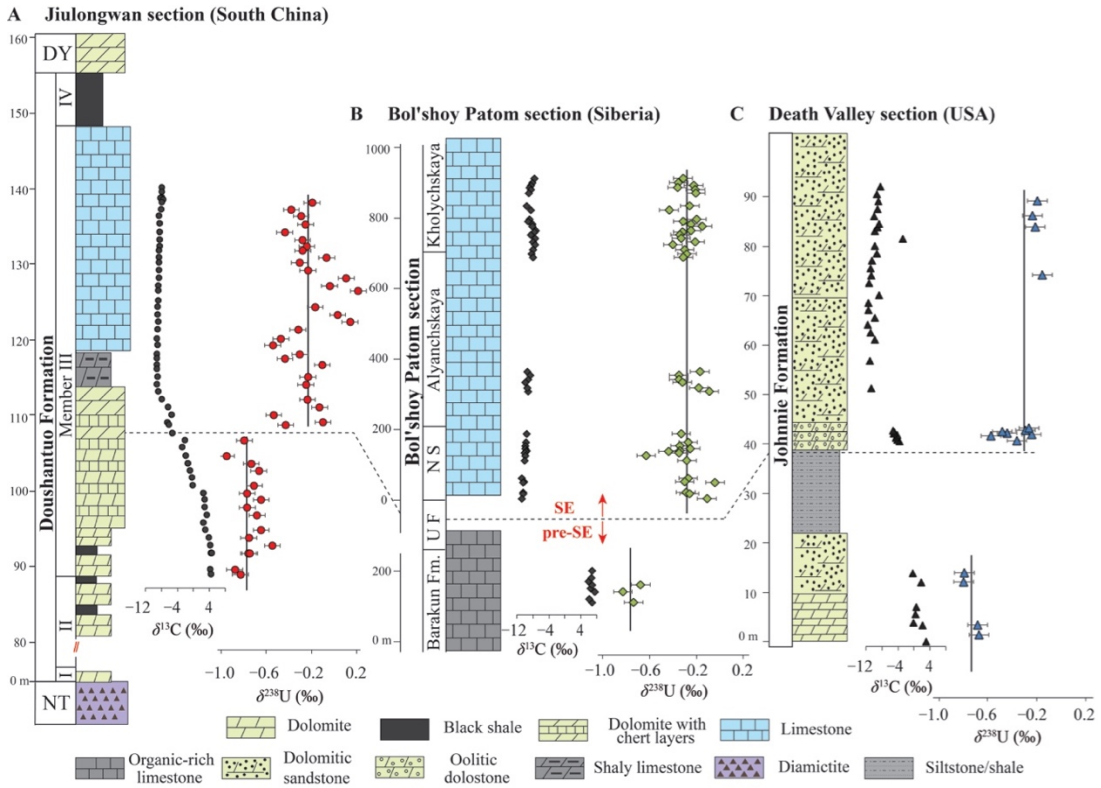

Figure 6.2 $\delta^{238}U$ and $\delta^{13}C_{carb}$ profiles of the three study sections. (A): Jiulongwan section in the Yangtze Platform, South China. (B): Bol'shoy Patom section, Siberia. (C): Death Valley section (the Johnnie Formation), western USA. Error bars of $\delta^{238}U$ denote 2 standard derivations. DY, Dengying Formation; NT, Nantuo Formation; UF, Urinskaya Formation; NS, Nikol'skaya Formation.

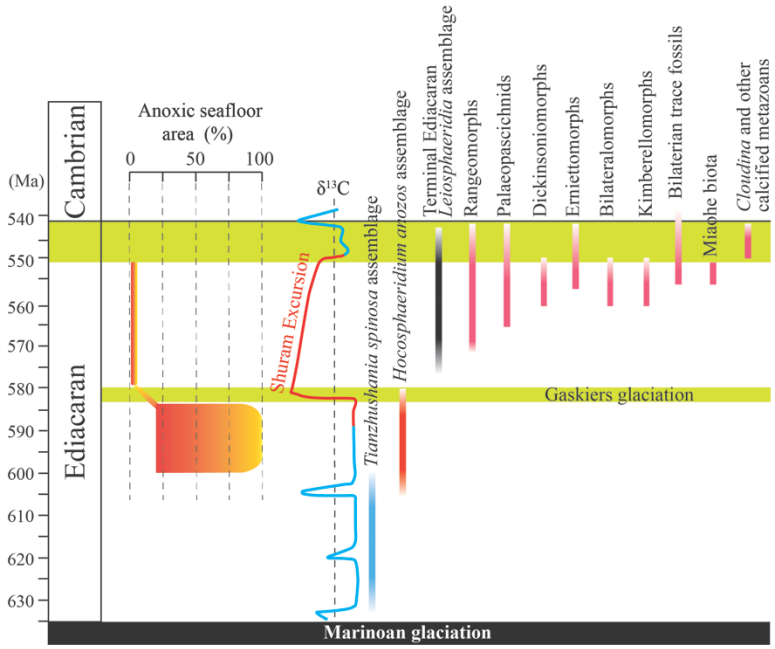

Figure 6.3 Correlation of marine redox evolution and the temporal distribution of macroscopic Ediacaran fossils. Wide-spread ocean oxygenation coincides with or slightly precedes the evolution of the main groups of Ediacara fauna (modified from Correlation 2 of Xiao et al., 2016).

Table 6.1 $\delta^{238}U$ and associated geochemical data for the Jiulongwan Section, South China.

Sample No.	$\delta^{238}U$	$\delta^{13}C$	heights	Mg	Al	Ca	Mn	U
	‰	‰	m	ppm	ppm	ppm	ppm	ppm
JLW-01		-7.8	139.9					
JLW-02		-7.7	139.3					
JLW-03		-7.7	138.6					
HN-07		-8.2	138.5					
JLW-04		-7.5	138.3					
JLW-05	-0.20	-7.9	137.9	83526.65	536.83	212946.47	158.31	0.90
JLW-06	-0.38	-8.0	137	61834.03	761.48	289067.70	125.44	0.49
JLW-07	-0.29	-8.5	136.2	8183.10	438.26	360744.62	72.33	0.46
JLW-08	-0.25	-8.4	135.1	4366.28	537.07	358636.05	51.95	0.37
JLW-09	-0.44	-8.3	134	3344.22	461.66	378589.01	50.00	0.35
JLW-10	-0.28	-8.4	133	4195.56	424.46	371009.54	51.23	0.41
JLW-11	-0.24	-8.4	132.2	24163.21	343.18	322399.07	105.44	0.66
JLW-12	-0.28	-8.4	131.6	12054.03	460.83	346437.07	82.12	0.66
JLW-13	-0.07	-8.5	130.7	5790.66	339.53	361710.68	70.31	1.17
JLW-14	-0.31	-8.5	130	3523.62	582.04	367318.68	50.34	0.41
JLW-15	-0.23	-8.5	129	4619.08	334.29	359829.99	53.03	0.41
JLW-16	0.11	-8.6	128	6993.29	719.58	372813.81	84.90	0.24
JLW-17	-0.04	-8.7	127	3730.37	445.82	375350.34	66.90	0.21
JLW-18	0.21	-8.8	126.3	3659.00	270.29	365815.32	61.13	0.29
JLW-19		-8.8	125	8424.51	265.60	317020.45	71.78	0.18
JLW-20	-0.17	-8.9	124.2	4081.42	341.18	371316.17	66.68	0.14
JLW-21	0.03	-8.9	123.2	13320.91	278.33	340640.90	97.00	0.22
JLW-22	0.14	-8.7	122.2	15612.93	398.72	340552.28	107.10	0.52
JLW-23	-0.32	-9.0	121.2	5170.67	342.21	355231.33	78.58	0.11
JLW-24	-0.47	-9.0	120	5979.17	258.16	353380.91	86.75	0.09
JLW-25	-0.54	-9.0	119.2	5141.32	292.64	351866.47	93.24	0.12
JLW-26	-0.30	-9.1	118	7132.58	440.25	304690.24	84.07	0.09
JLW-27	-0.44	-9.1	117.4	17148.17	391.90	328310.43	109.37	0.15
JLW-28	-0.11	-9.1	116.6	22401.44	663.60	303240.08	110.84	0.23
JLW-29		-9.0	116					
JLW-30	-0.23	-8.9	115	110823.39	893.54	183453.81	244.78	0.12
JLW-31	-0.25	-9.1	114	113624.23	661.91	208219.54	226.96	0.10

JLW-32		-8.7	113	112685.71	950.77	195234.90	233.65	0.17
JLW-33	-0.24	-7.8	112	106886.17	1333.80	180725.95	170.93	0.18
JLW-34	-0.13	-6.3	111	114322.16	1049.70	186423.40	204.42	0.32
JLW-35	-0.53	-5.4	110	124380.39	703.95	199847.28	156.28	0.39
JLW-36	-0.10	-6.4	109	111425.46	936.94	189914.73	228.55	0.25
JLW-37	-0.43	-6.1	108.7	103525.42	1320.24	171811.61	370.39	0.18
JLW-38		-5.1	107.6					
JLW-39	-0.79	-2.0	106.6	31224.13	61.12	72259.59	113.35	0.77
JLW-40		-2.7	105.7					
JLW-41	-0.95	-1.8	104.6	130540.65	382.31	210600.66	170.86	0.16
JLW-42	-0.73	-1.3	103.6	128955.87	376.83	213604.75	177.10	0.12
JLW-43	-0.67	-0.8	102.6	132259.83	352.10	213517.75	185.21	0.07
JLW-44		-0.2	101.7	120177.77	756.07	201578.59	177.25	0.12
JLW-45	-0.71	-0.1	100.7	129445.73	195.68	209469.50	189.68	0.09
JLW-46	-0.77	2.7	99.7	109845.63	493.96	182882.25	191.11	0.10
JLW-47	-0.65	2.9	98.8	120267.54	305.04	203221.60	208.75	0.10
JLW-48	-0.77	2.9	97.8	124654.04	240.36	216615.52	193.73	0.12
JLW-49	-0.68	3.5	96.8	104308.62	1962.69	194992.65	149.46	0.13
JLW-50		2.6	95.8	72073.23	2920.98	291143.03	135.42	0.13
JLW-51	-0.65	3.2	94.8	73908.26	1552.07	263193.46	125.94	0.06
JLW-52	-0.75	4.0	93.8	99137.59	1612.20	186357.60	114.40	0.08
JLW-53	-0.55	4.3	92.8	74283.48	2566.86	276413.15	102.91	0.14
JLW-54	-0.76	4.5	91.8	35294.87	200.60	262388.76	67.62	0.16
JLW-55	-0.74	4.8	91.8	7083.47	294.12	378471.11	66.68	0.10
JLW-56	-0.88	4.4	89.6	105834.26	98.60	185474.79	75.34	0.06
JLW-57	-0.83	4.5	89					

Table 6.2 $\delta^{238}U$ and associated geochemical data for the Bol'shoy Patom section, Siberia.

Sample No.	$\delta^{238}U$	$\delta^{13}C$	heights	Mg	Al	Ca	Mn	U
	‰	‰	m	ppm	ppm	ppm	ppm	ppm
'62-05'	-0.31	-7.5	912	5529.40	701.78	357226.39	155.03	0.45
'65-05'	-0.35	-8	899	13758.80	742.23	296676.67	191.92	1.16
'66-05'	-0.22	-8.3	892	7070.39	901.78	321939.34	228.89	2.99
'67-05'	-0.36	-8.8	885	4465.99	126.91	371484.09	210.29	1.45
'68-05'	-0.21	-8.3	880	36751.65	135.28	281649.80	229.19	3.16
'69-05'	-0.20	-8.9	869	20747.78	305.39	264348.04	170.35	2.25
'72-05'	-0.26	-9.4	833	7472.81	340.95	357280.17	251.87	1.99
'74-05'	-0.43	-8.3	821	4211.27	438.81	367442.48	175.41	3.12
'76-05'	-0.20	-8.7	796	8378.50	189.35	378855.59	346.35	2.81
'77-05'	-0.31	-9.1	789	4544.55	205.20	360931.86	399.76	3.10
'78-05'	-0.25	-8	781	4666.32	412.96	323904.10	155.72	2.59
'79-05'	-0.15	-8.1	775	4245.35	174.63	324023.04	118.53	3.65
'80-05'	-0.24	-7.2	763	3447.45	31.21	283782.70	162.18	0.84
'81-05'	-0.32	-7.5	760	12329.64	1011.45	288972.78	144.75	1.00
'82-05'	-0.34	-8.3	752	7390.58	892.71	282938.26	167.58	4.99
'83-05'	-0.33	-7.3	741	6174.67	162.22	356155.94	86.66	6.47
'85-05'	-0.21	-7.9	731	6638.20	897.32	321256.20	181.56	2.81
'86-05'	-0.4	-7.4	723	5202.18	627.50	328135.32	161.04	1.47
'87-05'	-0.3	-7.9	710	7724.35	663.59	326661.08	131.00	4.34
'88-05'	-0.28	-8.2	698	7391.47	260.56	355833.08	109.46	2.57
'89-05'	-0.31	-7.8	688	5485.54	153.09	381882.74	75.21	2.30
'99a-05'	-0.17	-9.2	363	6085.00	392.44	372935.89	76.64	1.22
'105-05'	-0.09	-9	308	3582.30	100.16	404336.85	71.83	4.30
101-05'	-0.35	-8.6	353	1934.43	144.52	416484.59	35.68	11.98
'102-05'	-0.35	-9.1	342	9655.69	397.59	349411.96	84.46	0.70
'103-05'	-0.32	-9.8	333	5350.55	113.26	388356.08	80.08	4.11
'104-05'	-0.18	-9.3	318	4454.39	127.83	389249.67	54.40	5.35
'126-05'	-0.33	-9.5	188	3561.55	336.37	397338.26	84.79	8.92
'125-05'	-0.27	-9.6	163	5181.92	176.97	368818.73	91.98	2.85
'124-05'	-0.34	-9.7	153	5746.98	159.52	384086.39	127.54	4.97
'123-05'	-0.25	-9.7	146	2640.67	326.91	402501.37	51.72	8.41
'122-05'	-0.34	-9.5	139	5549.86	397.00	370369.42	109.25	6.58

'121-05'	-0.44	-9.6	138	4848.63	254.53	372639.54	70.78	1.09
'120-05'	-0.35	-9.9	133	5346.24	408.94	383582.80	94.69	5.73
'119-05'	-0.63	-9.7	126	5460.21	147.84	381712.78	57.97	2.05
'117-05'	-0.28	-10	111	4376.85	230.65	386171.51	91.93	13.33
'113-05'	-0.27	-10.6	61	5092.29	251.18	344387.28	195.45	0.65
'112-05'	-0.3	-10.2	52	6881.14	940.31	303480.29	194.87	4.01
'111-05'	-0.04	-10.4	49	5491.18	241.16	357466.62	201.73	5.57
'110-05'	-0.29	-10.4	22	4340.97	370.08	382102.72	237.70	5.44
'109-05'	-0.26	-10.3	18	6666.99	1420.04	313245.43	203.31	2.64
'107-05'	-0.11	-10.7	4	6125.78	1451.77	286575.31	199.19	1.46

Table 6.3 $\delta^{238}U$ and associated geochemical data for the Death Valley section, Western United States.

Sample No.	$\delta^{238}U$	$\delta^{13}C$	heights	Mg	Al	Ca	Mn	Sr	U
	‰	‰	m	ppm	ppm	ppm	ppm	ppm	ppm
J2 1		3.12	0	91599.63	170.84	196383.61	623.88	223.56	1.04
J2 2	-0.67		1.2	97035.42	100.58	204512.53	597.81	205.56	0.40
J2 3	-0.68	2.24	3.2	90711.72	49.79	202745.59	588.27	79.54	0.67
J2 4		0.09	3.9						
J2 5		0.48	5.6						
J2 6		0.62	7						
J2 7			8.8						
J2 8	-0.795	1.86	12	90972.65	65.26	205541.53	1284.52	76.76	0.36
J2 9	-0.79	-0.16	13.8	91312.69	106.03	217515.52	2931.90	87.89	1.06
J2 10	-0.36	-3.58	40.6	84581.70	951.84	228143.53	2631.79	106.96	0.53
J2 11		-3.96	40.9	77172.35	445.85	227618.96	1558.55	203.87	0.51
J2 12		-4.41	41.2	99156.91	141.76	220641.07	1761.43	78.24	0.57
J2 13	-0.57	-4.20	41.5	96016.46	43.71	215862.68	1605.08	82.41	0.76
J2 14	-0.24	-4.04	41.8	94310.34	908.86	234363.13	2369.64	161.98	1.05
J2 15	-0.44	-4.95	42.1	96663.52	227.19	221289.35	1466.06	81.90	0.76
J2 16	-0.48	-4.65	42.4	89263.49	239.29	210201.57	1272.97	79.93	0.66
J2 17	-0.29	-5.06	42.7	95344.39	136.70	221477.63	1064.25	111.53	0.62
J2 18	-0.26		43.1	98543.64	338.31	227897.17	1313.28	73.52	0.60
JSH 1		-10.47	51.2	66573.14	226.92	158210.35	2313.01	65.23	0.19
JSH 2		-10.89	56.9						
JSH 3			57.3						
JSH 4			59.6						
JHS 5		-9.55	61.1						
JHS 6		-10.76	62.6						
JSH-7		-11.47	64.1						
JSH 8		-9.64	65.6						
JSH 9		-11.23	67.1						
JSH 10		-11.19	68.6						
JSH 11		-8.65	70.1						
JHS 12		-10.96	72.6						
JSH 13	-0.15	-10.56	74.1	77188.76	335.76	164012.75	1425.54	54.51	0.71

JSH 14		-10.60	75.6						
JHS 15		-10.28	77.1						
JHS 16		-9.11	78.6						
JSH 17		-9.63	80.1						
JSH 18		-2.70	81.6						
JSH 18.5		-9.63	83.1						
JSH 19	-0.21	-8.94	83.85	65385.24	821.93	161145.76	1258.66	105.59	0.82
JSH 20		-8.50	84.6						
JSH 21	-0.23	-9.74	86.1	79468.51	205.50	177232.37	1212.37	66.63	0.73
JSH 22		-8.90	87.6	57888.42	185.59	155021.53	954.78	89.51	0.46
JSH 23	-0.19	-8.69	89.1	79788.53	399.26	170062.46	1530.90	57.73	0.78
JSH 24		-9.12	90.6	84499.82	196.67	182305.12	833.05	49.09	0.64
JSH 25		-8.16	92.1						

Table 6.4 Cross-correlation coefficients (R^2) and *p*-values calculated to test the influence of diagenetic indicators on $\delta^{238}U$.

South China section	R^2	*p*-value
$\delta^{238}U$ vs. $\delta^{13}C$	**0.623**	0.000
$\delta^{238}U$ vs. Mg/Ca (mol:mol)	0.258	0.000
$\delta^{238}U$ vs. Sr/Ca (ppm/w.t.%)	0.084	0.053
$\delta^{238}U$ vs. $\delta^{18}O$	0.191	0.003
U concentration vs. $\delta^{18}O$	0.005	0.636
$\delta^{238}U$ vs. Sr concentration	0.244	0.001
$\delta^{238}U$ vs. Mn concentration	0.041	0.182
$\delta^{238}U$ vs. Mn/Sr	0.076	0.066
$\delta^{238}U$ vs. Fe concentration	0.433	0.000
$\delta^{238}U$ vs. Rb/Sr	0.003	0.740
$\delta^{238}U$ vs. U concentration	0.138	0.012
$\delta^{238}U$ vs. Th/U	0.095	0.039
$\delta^{238}U$ vs. U/Al (ppm/w.t.%)	0.006	0.620
$\delta^{238}U$ vs. Mo/U ratios	0.000	0.951

Siberia section	R^2	*p*-value
$\delta^{238}U$ vs. $\delta^{13}C$	**0.572**	0.000
$\delta^{238}U$ vs. Mg/Ca (mol:mol)	0.055	0.122
$\delta^{238}U$ vs. Sr/Ca (ppm/w.t.%)	0.146	0.009
$\delta^{238}U$ vs. $\delta^{18}O$	0.108	0.028
U concentration vs. $\delta^{18}O$	0.136	0.013
$\delta^{238}U$ vs. Sr concentration	0.191	0.003
$\delta^{238}U$ vs. Mn concentration	0.196	0.002
$\delta^{238}U$ vs. Mn/Sr	0.161	0.006
$\delta^{238}U$ vs. Fe concentration	0.193	0.003
$\delta^{238}U$ vs. Rb/Sr	0.071	0.076
$\delta^{238}U$ vs. U concentration	0.043	0.170
$\delta^{238}U$ vs. Th/U	0.013	0.423
$\delta^{238}U$ vs. U/Al (ppm/w.t.%)	0.032	0.236
$\delta^{238}U$ vs. Mo/U ratios	0.014	0.440
$\delta^{238}U$ vs. Pr-based Ce/Ce*	0.049	0.145
$\delta^{238}U$ vs. Nd-based Ce/Ce*	0.007	0.590

Death Valley section	R^2	*p*-value
$\delta^{238}U$ vs. $\delta^{13}C$	**0.799**	0.000
$\delta^{238}U$ vs. Mg/Ca (mol:mol)	0.008	0.747
$\delta^{238}U$ vs. Sr/Ca (ppm/w.t.%)	0.010	0.726
$\delta^{238}U$ vs. $\delta^{18}O$	0.410	0.018
U concentration vs. $\delta^{18}O$	0.029	0.575
$\delta^{238}U$ vs. Sr concentration	0.030	0.535
$\delta^{238}U$ vs. Mn concentration	0.000	0.957
$\delta^{238}U$ vs. Mn/Sr	0.012	0.694
$\delta^{238}U$ vs. Fe concentration	0.839	0.000

$\delta^{238}U$ vs. Rb/Sr	0.369	0.016
$\delta^{238}U$ vs. U concentration	0.058	0.388
$\delta^{238}U$ vs. Th/U	0.243	0.062
$\delta^{238}U$ vs. U/Al (ppm/w.t.%)	0.393	0.012
$\delta^{238}U$ vs. Mo/U ratios	0.019	0.625

CHAPTER 7

SUMMARY

7.1 Overview

It is telling that all but one of the extinction events listed in figure 1.1 (i.e., the end-Cretaceous mass extinction) are associated with periods of expanded marine anoxia. It is not surprising, then, that the expansion of anoxic zones in the modern ocean is at the top of the list of emerging environmental challenges for multi-cellular marine organisms (Diaz and Rosenberg, 2008). Anoxia affects multi-cellular organisms through reduced growth and reproduction, physiologic stress, forced migration, reduction of suitable habitat, increased vulnerability to predation, and disruption of life cycles (Rabalais et al., 2002; Vaquer-Sunyer and Duarte, 2008). This ultimately leads to death if sustained for too long (Rabalais et al., 2002; Vaquer-Sunyer and Duarte, 2008). Anoxia can also dramatically alter marine biogeochemical cycles of carbon, nitrogen, and sulfur, as well as many redox-sensitive trace metals. For example, at near-zero O_2 levels, sulfate-reducing microbes reduce large quantities of sulfate, leading to production and accumulation of highly toxic H_2S (Algeo et al., 2008; Kump et al., 2005; Shen et al., 2011; Zhang et al., 2017a).

In part motivated by concerns about the future, in the past several decades numerous studies have focused on constraining spatiotemporal variations in marine redox conditions through mass extinction intervals (e.g., Hallam, 1990; Joachimski and Buggisch, 1993, 2002; Wignall and Twitchett, 1996; Isozaki, 1997; Joachimski et al., 2001; Racki et al., 2002; Yudina et al., 2002; Tribovillard et al., 2004; Grice et al., 2005; van de Schootbrugge et al., 2008; Joachimski et al., 2009; Zhang et al., 2009; Algeo and Twitchett, 2010; John et al., 2010; Hammarlund et al., 2012; Shen et al., 2012b; Winguth and Winguth,

2012; Yan et al., 2012; Jones and Fike, 2013; van de Schootbrugge et al., 2013; George et al., 2014; Liu et al., 2016). However, evidence for anoxia as a significant extinction driver has been inferred primarily based on lithologic, biologic, or geochemical tracers that only record local or regional redox conditions. Key aspects, such as the detailed timing, duration, and extent, of marine anoxia remain largely unresolved, leaving the links between oceanic conditions and the mass extinctions ambiguous.

The recent development of U isotopes ($\delta^{238}U$) as a globally-integrative paleoredox proxy provides new insights into this problem. In this chapter, to test the hypothesis that global marine anoxia coincided with mass extinction events, I combine our new $\delta^{238}U$ measurements from this dissertation with published $\delta^{238}U$ data from the end-Ordovician mass extinction, the Late Devonian mass extinction, and the end-Triassic mass extinction. My comparison shows that $\delta^{238}U$ trends from all these extinctions show rapid negative shifts (which imply rapid expansion of marine anoxia) coincident with the onset of the mass extinction pulses, suggesting that extensive marine anoxia may have been a common factor for major mass extinction events in Earth's history.

7.2 Uranium isotope evidence for marine anoxia as a common driver for major mass extinction event in geological history

7.2.1 The terminal Ediacaran extinction

The concept of the Ediacaran evolution of the early animals—as represented by the Ediacara biota— was discussed in chapter 5 and chapter 6.

Macroscopic and morphologically complex multicellular eukaryotes, including stem-groups animals, diversified in the second half of the Ediacaran Period starting ~570

Ma. The fossil record of these eukaryotes is sometimes referred to as the Ediacara biota. The Ediacara biota reached their maximum taxonomic diversity and morphological disparity about 560 Ma, then subsequently declined in the terminal Ediacaran Period (~550–541 Ma) and almost completely disappeared at the Ediacaran-Cambrian transition about 541 Ma

The role of O_2 in the evolution of the Ediacara biota has been heavily debated (e.g., Fike et al., 2006; Butterfield et al., 2007; Canfield et al., 20007; McFadden et al., 2008; Canfield et al., 2008; Erwin et al., 2009; Johnston et al., 2013; Sperling et al., 2013; Sperling et al., 2015). Current geochemical evidence paints a conflicting picture regarding global marine O_2 levels during the Ediacaran Period with evidence for both profound oxygenation and persistent anoxic conditions. These contrasting views likely arise because many paleoredox proxies are inherently local (e.g., Fe speciation, Ce anomalies, I/Ca ratio) or indirect tracers (e.g., C and S isotopes) of oxygenation. Here I apply the U isotope paleoredox proxy in Ediacaran carbonates to quantify the extent of global ocean oxygenation/anoxia during the rise and fall of the Ediacara biota in an effort to help resolve this debate. Specifically, in order to test whether O_2 played a role in the diversification of early animals, I measured $\delta^{238}U$ in carbonates from three well-studied Shuram Excursion (SE) sections in South China, Siberia, and the USA. To explore whether the decline of the early animals was associated with the expansion of marine anoxia, I measured $\delta^{238}U$ in carbonates from two latest Ediacaran carbonate sections from the Dengying Formation (551—541 Ma) in South China.

The new data presented in chapter 5 and chapter 6 reveal the largest positive shift in $\delta^{238}U$ ever reported in the geologic record (from ~ −0.74 ‰ to ~ −0.26 ‰) across the

SE event. Subsequently, the latest Ediacaran carbonates (551–541 Ma) record the most negative carbonate $\delta^{238}U$ values yet reported (averaging −0.95 ‰). U isotope mass-balance modeling suggests that prior to the SE at least 40 % of the seafloor was overlain by anoxic waters and that global ocean oxygenation rose to near-modern levels during the SE. This episode of oxygenation was followed by an episode of extensive ocean anoxia—covering nearly 100 % of the seafloor—during the latest Ediacaran Period.

This episode of pervasive ocean oxygenation across the SE immediately predates the initial diversification of the Ediacara biota. The subsequent shift to extensive anoxic conditions during the latest Ediacaran Period coincides with the decline and extinction of the Ediacara biota. These findings suggest that global marine redox changes may have driven the rise and fall of the Ediacara biota.

7.2.2 The Late Ordovician mass extinction

The Late Ordovician extinction was the first of five great extinction events of the Phanerozoic. In terms of the percentage of genera and families lost, it is the second largest, involving the extinction of almost half of marine invertebrate genera and an estimated approximately 85% of species (Harper et al., 2014). This extinction event occurred in two discrete pulses, one at the K-H (Katian and the Hirnantian) boundary and the other about 1.0 My later, near the end of the Hirnantian (Harper, 2006; Harper et al., 2014). Proposed mechanisms for the first phase have included glacially-induced cooling and falling sea level in the oceans, but a general consensus is lacking (Brenchley et al., 1994; Finnegan et al., 2012). The second phase is assumed to be linked to near-global marine anoxia associated with a marked transgression during the Late Hirnantian. Evidence for marine

anoxia during the Late Hirnantian Period are based on the occurrence of widespread organic-rich marine facies accumulating during this period and from geochemical redox proxy trends including pyrite sulfur isotopes, redox-sensitive trace elements, pyrite framboid-size distributions, and Fe speciation (Hammarlund et al., 2012; Jones and Fike, 2013; Yan et al., 2012; Zhang et al., 2009). However, the geochemical and lithologic redox proxies utilized for these prior interpretations evaluated only local or regional redox conditions, thus do not assess global-ocean redox trends. Redox chemistry changes in the global ocean are central to an examination of the links between global-ocean redox conditions and the end-Ordovician extinction event.

Bartlett et al. (2018) constructed a $\delta^{238}U$ record in carbonates from across the second pulse of the end-Ordovician extinction event (see figure 1 of Bartlett et al., 2018). The three middle Hirnantian samples gave an average $\delta^{238}U$ value of ~−0.1‰, followed by a rapid 0.3‰ negative shift, then continued with low, but fluctuating values (average = ~−0.45‰) in the late Hirnantian through early Silurian. Lithologic and geochemical criteria suggest this $\delta^{238}U$ signal represents global seawater redox conditions rather than trends related to local processes. This $\delta^{238}U$ signal suggests the late Hirnantian to the early Silurian experienced an episode of marine anoxia. The onset of this episode of marine anoxia is coincident with the second end-Ordovician mass extinction pulse, supporting the idea that marine anoxia influenced the extinction event.

Unfortunately, the Bartlett et al. data only covers the second pulse of the mass extinction (from the middle Hirnantian stage to the Rhuddanian), and cannot be used to evaluate whether there was a marine anoxic event during the first pulse of the extinction. Lu et al. (2017) analyzed $\delta^{238}U$ in organic-rich mudrock samples from the Late Ordovician

(Katian) Fjäcka Shale (see figure 4 of Lu et al., 2017); their study suggests late Katian seawater $\delta^{238}U$ was about −0.85‰ to −0.60‰. Indicative of marine anoxia during the late Katian that was likely coincident with the first pulse of mass extinction; although, a closer comparison of U isotope data and paleobiological data is required to confirm the exact temporal correlation between anoxia and the first pulse of the mass extinction. A longer $\delta^{238}U$ record that covers both extinction intervals (from the early Katian stage to the late Rhuddanian stage) from a successive carbonate section would significantly strengthen the implications from both Bartlett et al. (2018) and Lu et al. (2017).

7.2.3 The Late Devonian mass extinction

The Late Devonian mass extinction that occurred between 375 and 359 Ma, is one of the 'Big Five' mass extinctions in Earth history and the number of marine species decreased by 70–82% (McGhee et al., 2013; Sallan and Coates, 2010). The Late Devonian mass extinction was not a single event, but included a series of extinction pulses. The major crises occurred at the at the Frasnian-Famennian stage boundary (374 Ma) and the less well-documented Hangenberg event some 15 million years later at the Devonian-Carboniferous boundary (359 Ma; Alroy, 2010; Stearn, 1987). The cause of this mass extinction event remains under debate and has been proposed to involve one or more of the following factors: volcanism, climate change, sea-level changes, global cooling, submarine hydrothermal activity, or expanded marine anoxia (George et al., 2014; Joachimski et al., 2009; Joachimski and Buggisch, 1993, 2002; Joachimski et al., 2001; John et al., 2010; Liu et al., 2016; Racki et al., 2002; Tribovillard et al., 2004; Yudina et al., 2002).

While the proximate triggers for the Late Devonian extinction remain under debate, the expansion of ocean anoxia is commonly invoked as a key trigger of the Frasnian-Famennian mass extinction event due to the close stratigraphic association between the extinction event and the Kellwasser Anoxia Events. Although various approaches (e.g., carbon isotopes, oxygen isotopes, iron speciation, and trace metal geochemistry) have been conducted to evaluate the role of anoxia in triggering the Frasnian-Famennian extinction event anoxia (George et al., 2014; Joachimski and Buggisch, 1993; John et al., 2010; Racki et al., 2002; Tribovillard et al., 2004; Yudina et al., 2002), these techniques are better suited for inferring local or regional rather than global ocean redox conditions. Hence, no consensus has been reached because of the lack of geochemical data that enables more quantitative constraints to be placed on the extent of global ocean anoxia before, during, and after the Late Devonian extinction event.

There are two studies that have applied the U isotope proxy for the Frasnian-Famennian extinction interval. Wang et al. (2016) studied U isotopes from black shales of the Upper Devonian Kettle Point Formation (southwestern Ontario, Canada) (see figure 5 of Wang et al., 2016). The $\delta^{238}U$ values range from – 0.14‰ to 0.54‰, and exhibition an upward, increasing trend from –0.14‰ to 0.20‰ (average = –0.02‰) in the lower-middle portion of the record (Unit 1 to Unit 3, 137-65 m interval), and range from 0.11‰ to 0.54‰ (average = 0.34‰) in the upper part of the record (Unit 4, 65-25 m interval). Wang et al. conclude these data reflect that the Kettle Point black shales were deposited at a time of relatively widespread ocean oxygenation, with a slightly greater extent of ocean anoxia compared with today. Because the Kettle Point Formation contains the Frasnian-Famennian boundary, and the authors argue that marine anoxia was not the key driver of

the Late Devonian mass extinction event. A similar conclusion was reached by Song et al. (2017), who analyzed $\delta^{238}U$ in carbonates across the Frasnian-Famennian extinction boundary from the Baisha section in the Nanpanjiang Basin, South China (see figure 1 of Song et al., 2017). Their study argued that cooling, rather than oceanic anoxia, may have been the main killing mechanism.

However, there are a few issues regarding these studies. First, the recovery of seawater $\delta^{238}U$ values from marine black shale is not direct because of the poor constraints on the U isotopic fractionation factor between seawater and black shale deposition. Second, black shales can be deposited under a range of local redox conditions that is sufficiently wide to present complications for many paleoredox reconstructions. Third, the negative excursion reported by Song et al. (2017) is only represented by 1~3 data points, and the reliability of their interpretation calls for further study to confirm the result. Therefore, further $\delta^{238}U$ studies are essential to confirm the conclusion from these two studies.

At the Devonian-Carboniferous boundary, our recent $\delta^{238}U$ measurements from carbonates show rapid positive and negative shifts (Figure 7.1), suggesting that global ocean redox conditions at the Devonian-Carboniferous transition were likely characterized by rapid oscillation between oxic and anoxic condition. This finding may suggest that dynamic marine redox conditions may have played a role in the Devonian-Carboniferous boundary extinction.

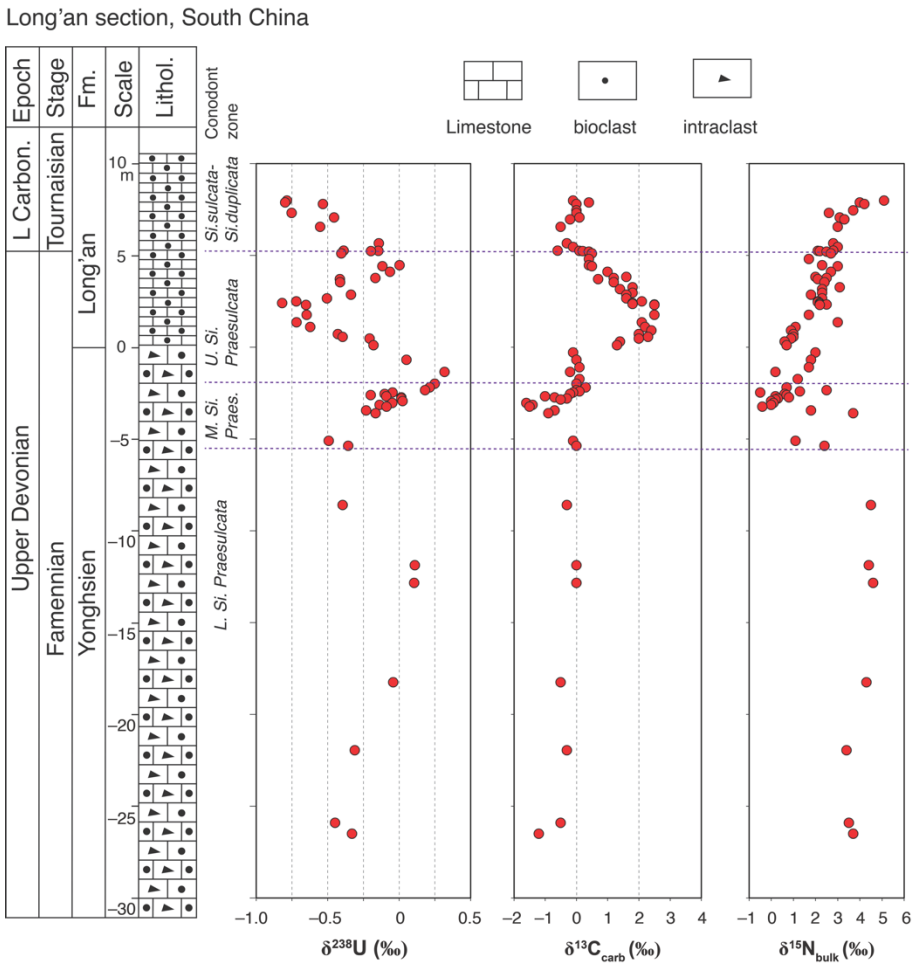

Figure 7.1 Litho- and biostratigraphy, and geochemical profiles of the Long'an section, South China. $\delta^{13}C_{carb}$ and $\delta^{15}N_{bulk}$ data are from Qie et al. (2015) and Liu et al. (2016). Fm.: Formation; Lithol.: Lithology; L Carbon.: Lower Carboniferous.

7.2.4 The end-Permian mass extinction

The end-Permian mass extinction is regarded as the "great dying" that led to the disappearance of some 95% of marine and 70% of terrestrial species (e.g., Erwin et al., 2002), the most dramatic loss of life in Earth's history. This extinction event is constrained to have occurred between 251.941 ± 0.037 and 251.880 ± 0.031 Ma, spanning an interval

of 60 ± 48 kyr, based on uranium-lead zircon ages from five ash beds from the highly condensed Global Stratotype Section and Point (GSSP) for the EPE at Meishan, South China (Burgess et al., 2014; Burgess and Bowring, 2015).

As discussed in chapter 2 and chapter 3, the PTB mass extinction has been attributed to various causes, including a bolide impact, major flood-basalt volcanism, climate change, methane release, and oceanic degassing of (see Erwin et al., 2002 and Wignall, 2007 for reviews). The eruption of the Siberian Traps flood basalts at 252-250 Ma is now known to have been effectively synchronous with the PTB mass extinction (Burgess et al., 2014; Burgess and Bowring, 2015). This event was the largest continental flood-basalt eruption of the Phanerozoic and is likely to have been the trigger for coeval changes in global climate and oceanic conditions that disrupted both marine and terrestrial ecosystems (Korte et al., 2010; Wignall, 2007; Wignall and Newton, 2003).

While the mechanism for the marine extinction event is still widely debated, marine anoxia is invoked in many models to explain the PTB mass extinction (e.g., Algeo and Twitchett, 2010; Grice et al., 2005; Isozaki, 1997; Shen et al., 2012b; Wignall and Twitchett, 1996; Winguth and Winguth, 2012). Alhough there is a broad consensus that enhanced ocean anoxia developed during the end-Permian mass extinction (EPME), connections between ocean anoxia and the EPME is greatly hampered by poor constraints on the timing of the onset, the extent, and the depth distribution of anoxia (e.g., Bond and Wignall, 2010; Payne and Clapham, 2012). Existing models vary from early onset anoxia to development of anoxia at the end Permian Mass Extinction (Grice et al., 2005; Isozaki, 1997) and from whole-ocean anoxia to anoxia only within oceanic oxygen-minimum zones

(Algeo et al., 2010; Bond and Wignall, 2010; Isozaki, 1997; Wignall and Twitchett, 1996; Winguth and Winguth, 2012).

The pilot $\delta^{238}U$ study in a carbonate sequence across the Permian-Triassic boundary by Brennecka et al. (2011a) revealed a negative excursion of $\delta^{238}U$ immediately predating the EPME horizon and argued that expanded ocean anoxia occurred immediately prior to the EPME horizon (Brennecka et al., 2011a). There have been a number of follow-up studies that confirmed this negative $\delta^{238}U$ shift is of global significance. These follow-up studies include the Dajiang (South China) and Taskent (Turkey) sections by Lau et al. (2016), and the Daxiakou section (South China) by Elrick et al. (2017) from the paleo-Tethys Ocean, and the Kamura section (Japan) by Zhang et al. (2018a) from the Panthalassic Ocean.

These Permian-Triassic $\delta^{238}U$ studies together suggest that the negative shift in $\delta^{238}U$ (0.4-0.5‰ in magnitude) was a global phenomenon and. A LOWESS smoothing of the combined $\delta^{238}U$ dataset suggests the negative shift in $\delta^{238}U$ began <70 kyr before the EPME (see *APPENDIX A*). The LOWESS curve also shows that the shift toward more negative $\delta^{238}U$ values was most rapid almost exactly at the EPME horizon (Zhang et al., 2018a). This temporal correspondence of rapid expansion of oceanic anoxia with the EPME strongly suggests that anoxia was a significant factor in mass mortality.

7.2.5 The end-Triassic mass extinction

The end of the Triassic has been generally accepted as one of the five big mass extinction events in the Phanerozoic marine fossil record. This extinction, occurred ~201.4

million years ago, is marked by a loss of up to 50% of marine biodiversity and major terrestrial ecosystem changes (e.g., Raup and Sepkoski, 1982).

There is a growing consensus that the end-Triassic extinction event was closely tied to the eruption of the Central Atlantic Magmatic Province and subsequent CO_2 release, global warming, ocean acidification, and marine anoxia. Although the basic architecture of events surrounding the Central Atlantic Magmatic Province is becoming clearer, the timing and relative importance of specific kill mechanisms remain a matter of debate (Blackburn et al., 2013; Hautmann et al., 2008; Kiessling and Simpson, 2011; Martindale et al., 2012).

During the end-Triassic mass extinction there is evidence for marine anoxia that is usually included among a host of other possible factors responsible for the mass extinction. However, similar to other extinction events, views on the timing, duration, and extent of ocean anoxia all vary widely, and thus opinions on the significance of anoxia as a kill mechanism range from primary driver to relatively unimportant. Existing evidence for marine anoxia is based largely on the increased prevalence of organic-rich black shales, increases in the abundance of biomarkers for photic-zone euxinia, globally observed positive excursions in the $\delta^{13}C$ composition of marine limestones and organic matter, and an overturn in phytoplankton assemblages (e.g., Hallam, 1990; van de Schootbrugge et al., 2013; van de Schootbrugge et al., 2008). Such proxies for local conditions are useful tools for recognizing the presence or absence of anoxic conditions at individual sections, but they cannot easily be extrapolated to quantify global changes in the extent of anoxic bottom waters.

Jost et al. (2017) quantified the increase in the extent of global anoxia across the end-Triassic extinction interval and through the Hettangian (early Jurassic) recovery phase

using $\delta^{238}U$ measured in shallow marine carbonates from two sections (the Val Adrara section and the Italcementi section) in northern Italy (see figure 2 of Jost et al., 2017). The $\delta^{238}U$ records from the two Italian sections are similar where they overlap stratigraphically. The $\delta^{238}U$ values for samples in the uppermost Triassic Zu Formation are variable but generally high (up to −0.01‰ at Val Adrara and up to −0.09‰ at Italcementi). Beginning at the Triassic/Jurassic boundary, $\delta^{238}U$ values from both sections begin to decrease rapidly, reaching a minimum at the base of the Albenza Formation (of –0.63‰ at Val Adrara and –0.69‰ at Italcementi). This nadir occurs at the same stratigraphic level in both sections based on correlation via bio-, litho-, and $\delta^{13}C$ chemo-stratigraphy.

Averaging the $\delta^{238}U$ before and after the end-Triassic extinction horizon, the $\delta^{238}U$ signals a 0.4‰ negative. Uranium isotope mass balance models demonstrate that the pattern of uranium isotope variation is best explained by an expansion in anoxic uranium deposition and thus expansion of marine anoxia in the earliest Jurassic (Jost et al., 2017). The negative shift in $\delta^{238}U$ appears to correspond with the start of the end-Triassic extinction, highlighting the role of marine anoxia in the end-Triassic mass extinction.

7.3 Summary

Mass extinctions reflect important interactions between biology, geology, geochemical cycles, and climate. The U isotopes in sedimentary marine carbonates provide an exciting new tool to evaluate the relationships between marine anoxia and marine biological crisis in geological history. However, the extinction events are not merely an interplay between marine biology and marine redox chemistry, they are a complex system that involves multiple Earth system processes. For instance, it is generally accepted at the

end-Permian and at the end-Triassic that the ultimate trigger of the marine anoxia was the eruption of the Siberia Trap Large Igneous Province and the Central Atlantic Magmatic Province, respectively. The volcanic eruptions released CO_2, caused global warming, enhanced continental weathering (silicate weathering), and affected the ocean thermalhaline circulation and marine primary productivity. A combination of these factors likely leads to the expansion of marine anoxia. Uranium isotopes in marine carbonates provide an important opportunity to bridge different components of Earth system together, and to decipher how different components of Earth system interact with each other is not precisely know. In future studies, it is essential to combine multiple proxy studies with Earth system models. For instance, we need proxy data for changes in silicate weathering, variations in marine productivity, and perturbations in marine redox chemistry. We then need to evaluate the leads and lags among these events using models such as the Genie model and General Circulation Model, or even the relative simple COPSE model (Lenton et al., 2018). This will eventually provide useful information on how modern climate changes affect the marine chemistry and marine biology.

REFERENCES

Algeo, T.J., Wilkinson, B.H., Lohmann, K.C., 1992. Meteoric-burial diagenesis of Middle Pennsylvanian limestones in the Orogrande Basin, New Mexico: water/rock interactions and basin geothermics. Journal of Sedimentary Petrology 62(4), 652-670.

Algeo, T., Shen, Y., Zhang, T., Lyons, T., Bates, S., Rowe, H., and Nguyen, T. K. T., 2008. Association of 34S-depleted pyrite layers with negative carbonate $\delta^{13}C$ excursions at the Permian-Triassic boundary: Evidence for upwelling of sulfidic deep-ocean water masses. Geochemistry, Geophysics, Geosystems 9(4), Q04025.

Algeo, T.J., Henderson, C.M., Tong, J.N., Feng, Q.L., Yin, H.F., Tyson, R.V., 2013. Plankton and productivity during the Permian-Triassic boundary crisis: an analysis of organic carbon fluxes. Global and Planetary Change 105, 52-67.

Algeo, T. J., Chen, Z.-Q., and Bottjer, D. J., 2015. Global review of the Permian–Triassic mass extinction and subsequent recovery: Part II. Earth-Science Reviews 149, 1-4.

Algeo, T. J., Hinnov, L., Moser, J., Maynard, J. B., Elswick, E., Kuwahara, K., and Sano, H., 2010. Changes in productivity and redox conditions in the Panthalassic Ocean during the latest Permian. Geology 38(2), 187-190.

Algeo, T. J., and Twitchett, R. J., 2010. Anomalous Early Triassic sediment fluxes due to elevated weathering rates and their biological consequences. Geology 38(11), 1023-1026.

Alroy, J., 2010. Geographical, environmental and intrinsic biotic controls on Phanerozoic marine diversification. Palaeontology 53(6), 1211-1235.

Amthor, J. E., Grotzinger, J. P., Schröder, S., Bowring, S. A., Ramezani, J., Martin, M. W., and Matter, A., 2003. Extinction of Cloudina and Namacalathus at the Precambrian-Cambrian boundary in Oman. Geology 31(5), 431-434.

Anbar, A. D., and Knoll, A. H., 2002. Proterozoic ocean chemistry and evolution: a bioinorganic bridge? Science 297(5584), 1137-1142.

Anbar, A. D., and Rouxel, O., 2007. Metal stable isotopes in paleoceanography. Annual Review of Earth and Planetary Sciences 35(1), 717-746.

Andersen, M. B., Romaniello, S., Vance, D., Little, S. H., Herdman, R., and Lyons, T. W., 2014. A modern framework for the interpretation of $^{238}U/^{235}U$ in studies of ancient ocean redox. Earth and Planetary Science Letters 400, 184-194.

Andersen, M. B., Stirling, C. H., and Weyer, S., 2017. Uranium isotope fractionation. Reviews in Mineralogy and Geochemistry 82(1), 799-850.

Andersen, M. B., Vance, D., Keech, A. R., Rickli, J., and Hudson, G., 2013. Estimating U fluxes in a high-latitude, boreal post-glacial setting using U-series isotopes in soils and rivers. Chemical Geology 354, 22-32.

Andersen, M. B., Vance, D., Morford, J. L., Bura-Nakić, E., Breitenbach, S. F. M., and Och, L., 2016. Closing in on the marine $^{238}U/^{235}U$ budget. Chemical Geology 420, 11-22.

Bambach, R. K., 2006. Phanerozoic biodiversity mass extinctions. Annual Review of Earth and Planetary Sciences 34(1), 127-155.

Banner, J. L., and Hanson, G. N., 1990. Calculation of simultaneous isotopic and trace element variations during water-rock interaction with applications to carbonate diagenesis. Geochimica et Cosmochimica Acta 54(11),3123-3137.

Barnes, C.E., and Cochran J.K, 1990. Uranium removal in oceanic sediments and the oceanic U balance. Earth and Planetary Science Letter 97, 94-101.

Barron, E.J., and Washington, W.M., 1982. Atmospheric circulation during warm geologic periods: Is the equator-to-pole surface-temperature gradient the controlling factor? Geology 10(12), 633-636.

Barnosky, A. D., Matzke, N., Tomiya, S., Wogan, G. O., Swartz, B., Quental, T. B., Marshall, C., McGuire, J. L., Lindsey, E. L., Maguire, K. C., Mersey, B., and Ferrer, E. A., 2011. Has the Earth's sixth mass extinction already arrived? Nature 471(7336), 51-57.

Bartlett, R., Elrick, M., Wheeley, J. R., Polyak, V., Desrochers, A., and Asmerom, Y., 2018. Abrupt global-ocean anoxia during the Late Ordovician-early Silurian detected using uranium isotopes of marine carbonates. Proceedings of the National Academy of Sciences U.S.A., in press.

Basu, A., Sanford, R. A., Johnson, T. M., Lundstrom, C. C., and Löffler, F. E., 2014. Uranium isotopic fractionation factors during U(VI) reduction by bacterial isolates. Geochimica et Cosmochimica Acta 136, 100-113.

Behrenfeld, M.J., and Kolber, Z.S., 1999. Widespread iron limitation of phytoplankton in the south Pacific Ocean. Science 283 (5403), 840-843.

Bergmann, K. D., Zentmyer, R. A., and Fischer, W. W., 2011. The stratigraphic expression of a large negative carbon isotope excursion from the Ediacaran Johnnie Formation, Death Valley. Precambrian Research 188(1-4), 45-56.

Bigeleisen, J., 1996. Nuclear size and shape effects in chemical reactions. Isotope chemistry of the heavy elements. Journal of the American Chemical Society 118 (15), 3676–3680.

Blackburn, T. J., Olsen, P. E., Bowring, S. A., McLean, N. M., Kent, D. V., Puffer, J., McHone, G., Rasbury, E. T., and Et-Touhami, M., 2013. Zircon U-Pb geochronology links

the end-Triassic extinction with the Central Atlantic Magmatic Province. Science 340(6135), 941-945.

Bluth, G.J.S., and Kump, L.R., 1991. Phanerozoic paleogeology. American Journal of Science 291(3), 284-308.

Bluth, G.J.S., and Kump, L.R., 1994. Lithologic and climatologic controls of river chemistry. Geochimica et Cosmochimica Acta 58(10), 2341-2359.

Bond, D. P. G., and Wignall, P. B., 2010. Pyrite framboid study of marine Permian–Triassic boundary sections: A complex anoxic event and its relationship to contemporaneous mass extinction. Geological Society of America Bulletin 122(7-8), 1265-1279.

Bond, D. P. G., and Wignall, P. B., 2014. Large igneous provinces and mass extinctions: an update. Geological Society of America Special Paper 505, 29–55.

Brayard, A., Escarguel, G., Bucher, H., Monnet, C., Bruhwiler, T., Goudemand, N., Galfetti, T., and Guex, J., 2009. Good genes and good luck: ammonoid diversity and the end-Permian mass extinction. Science 325(5944), 1118-1121.

Brenchley, P. J., Marshall, J. D., Carden, G. A. F., Robertson, D. B. R., Long, D. G. F., Meidla, T., Hints, L., and Anderson, T. F., 1994. Bathymetric and isotopic evidence for a short-lived Late Ordovician glaciation in a greenhouse period. Geology 22(4), 295-298.

Brennecka, G. A., Herrmann, A. D., Algeo, T. J., and Anbar, A. D., 2011a. Rapid expansion of oceanic anoxia immediately before the end-Permian mass extinction. Proceedings of the National Academy of Sciences U.S.A. 108(43), 17631-17634.

Brennecka, G. A., Wasylenki, L. E., Bargar, J. R., Weyer, S., and Anbar, A. D., 2011b. Uranium isotope fractionation during adsorption to Mn-oxyhydroxides. Environmental Science & Technology 45(4), 1370-1375.

Brocks, J. J., Jarrett, A. J. M., Sirantoine, E., Hallmann, C., Hoshino, Y., and Liyanage, T., 2017. The rise of algae in Cryogenian oceans and the emergence of animals. Nature 548(7669), 578-581.

Broecker, W. S., and Peng, T.-H., 1982. Tracers in the Sea. Eldigio Press, Lamont-Doherty Geological Observatory, New York, NY, 690 pp.

Burgess, S. D., Bowring, S., and Shen, S. Z., 2014. High-precision timeline for Earth's most severe extinction. Proceedings of the National Academy of Sciences U.S.A. 111(9), 3316-3321.

Burgess, S. D., and Bowring, S. A., 2015. High-precision geochronology confirms voluminous magmatism before, during, and after Earth's most severe extinction. Science Advances 1(7), e1500470.

Butterfield, N. J., 2007. Macroevolution and cacroecology through deep time. Palaeontology 50(1), 41-55.

Cai, J.X., and Zhang, K.J., 2009. A new model for the Indochina and South China collision during the Late Permian to the Middle Triassic. Tectonophysics 467(1-4), 35-43.

Cai, Y., Hua, H., Xiao, S., Schiffbauer, J. D., and Li, P., 2010. Biostratinomy of the late Ediacaran pyritized Gaojiashan Lagerstatte from Southern Shaanxi, South China: Importance of Event Deposits. Palaios 25(8), 487-506.

Canfield, D. E., Poulton, S. W., Knoll, A. H., Narbonne, G. M., Ross, G., Goldberg, T., and Strauss, H., 2008. Ferruginous conditions dominated later neoproterozoic deep-water chemistry. Science 321(5891), 949-952.

Canfield, D. E., Poulton, S. W., and Narbonne, G. M., 2007. Late-Neoproterozoic deep-ocean oxygenation and the rise of animal life. Science 315(5808), 92-95.

Catling, D. C., Glein, C. R., Zahnle, K. J., and McKay, C. P., 2005. Why O_2 is required by complex life on habitable planets and the concept of planetary "oxygenation time". Astrobiology 5(3), 415-438.

Chen, X., Romaniello, S., Herrmann, A. D., Hardisty, D. S., Gill, B. C., and Anbar, A. D., 2018. Diagenetic effects on uranium isotope fractionation in carbonate sediments from the Bahamas. Geochimica et Cosmochimica Acta, in press.

Chen, X., Romaniello, S. J., Herrmann, A. D., Wasylenki, L. E., and Anbar, A. D., 2016. Uranium isotope fractionation during coprecipitation with aragonite and calcite. Geochimica et Cosmochimica Acta 188, 189-207.

Chen, Y.L., Jiang, H.S., Lai, X.L., Yan, C.B., Richoz, S., Liu, X.D., Wang, L.N., 2015. Early Triassic conodonts of Jiarong, Nanpanjiang Basin, southern Guizhou Province, South China. Journal of Asian Earth Sciences 105, 104-121.

Chen, Y.L., Kolar-Jurkovšek, T., Jurkovšek, B., Aljinović, D., Richoz, S., 2016. Early Triassic conodonts and carbonate carbon isotope record of the Idrija-Žiri area, Slovenia. Palaeogeography Palaeoclimatology Palaeoecology 444, 84-100.

Chen, Z., Zhou, C., Xiao, S., Wang, W., Guan, C., Hua, H., and Yuan, X., 2014. New Ediacara fossils preserved in marine limestone and their ecological implications. Scientific Report 4, 4180.

Chen, Z.-Q., and Benton, M. J., 2012. The timing and pattern of biotic recovery following the end-Permian mass extinction. Nature Geoscience 5(6), 375-383.

Chen, Z.-Q., Tong, J., and Fraiser, M. L., 2011. Trace fossil evidence for restoration of marine ecosystems following the end-Permian mass extinction in the Lower Yangtze

region, South China. Palaeogeography, Palaeoclimatology, Palaeoecology 299(3-4), 449-474.

Chun, C. O. J., Delaneym, M. L., Zachos, J. C., 2010. Paleoredox changes across the Paleocene‐Eocene thermal maximum, Walvis Ridge (ODP Sites 1262, 1263, and 1266): Evidence from Mn and U enrichment factors. Paleoceanography 25, PA4202.

Clark, P.U., Pisias, N.G., Stocker, T.F., Weaver, A.J., 2002. The role of the thermohaline circulation in abrupt climate change. Nature 415, 863-869.

Clarkson, M. O., Poulton, S. W., Guilbaud, R., and Wood, R. A., 2014. Assessing the utility of Fe/Al and Fe-speciation to record water column redox conditions in carbonate-rich sediments. Chemical Geology 382, 111-122.

Clarkson, M. O., Stirling, C. H., Jenkyns, H. C., Dickson, A. J., Porcelli, D., Moy, C. M., Pogge von Strandmann, P. A. E., Cooke, I. R., and Lenton, T. M., 2018. Uranium isotope evidence for two episodes of deoxygenation during Oceanic Anoxic Event 2. Proceedings of the National Academy of Sciences U.S.A. 115(12), 2918-2923.

Clarkson, M. O., Wood, R. A., Poulton, S. W., Richoz, S., Newton, R. J., Kasemann, S. A., Bowyer, F., and Krystyn, L., 2016. Dynamic anoxic ferruginous conditions during the end-Permian mass extinction and recovery. Nature Communication 7, 12236.

Condon, D., Zhu, M., Bowring, S., Wang, W., Yang, A., and Jin, Y., 2005. U-Pb ages from the neoproterozoic Doushantuo Formation, China. Science 308(5718), 95-98.

Condon, D. J., McLean, N., Noble, S. R., and Bowring, S. A., 2010. Isotopic composition $^{238}U/^{235}U$ of some commonly used uranium reference materials. Geochimica et Cosmochimica Acta 74(24), 7127-7143.

Corsetti, F. A., and J. Kaufman, A., 2003. Stratigraphic investigations of carbon isotope anomalies and Neoproterozoic ice ages in Death Valley, California. Geological Society of America Bulletin 115(8), 916-932.

Cortijo, I., Cai, Y., Hua, H., Schiffbauer, J. D., and Xiao, S., 2015. Life history and autecology of an Ediacaran index fossil: Development and dispersal of Cloudina. Gondwana Research 28(1), 419-424.

Cui, H., Kaufman, A. J., Xiao, S., Peek, S., Cao, H., Min, X., Cai, Y., Siegel, Z., Liu, X. M., Peng, Y., Schiffbauer, J. D., and Martin, A. J., 2016a. Environmental context for the terminal Ediacaran biomineralization of animals. Geobiology 14(4), 344-363.

Cui, H., Kaufman, A. J., Xiao, S., Zhou, C., and Liu, X.-M., 2016b. Was the Ediacaran Shuram Excursion a globally synchronized early diagenetic event? Insights from methane-derived authigenic carbonates in the uppermost Doushantuo Formation, South China. Chemical Geology 450, 59-80.

Cui, H., Xiao, S., Zhou, C., Peng, Y., Kaufman, A. J., and Plummer, R. E., 2016c. Phosphogenesis associated with the Shuram Excursion: petrographic and geochemical observations from the Ediacaran Doushantuo formation of South China. Sedimentary Geology 341, 134-146.

Cui, Y., Kump, L.R. Ridgwell, A., 2013. Initial assessment on the carbon emission rate and climatic consequences during the end-Permian mass extinction. Palaeogeography, Palaeoclimatology, Palaeoecology 387, 176-184.

D'Arcy J., Gilleaudeau G. J., Peralta S., Gaucher C. and Frei R., 2017. Redox fluctuations in the Early Ordovician oceans: An insight from chromium stable isotopes. Chemical Geology 448, 1-12.

Dahl, T. W., Boyle, R. A., Canfield, D. E., Connelly, J. N., Gill, B. C., Lenton, T. M., and Bizzarro, M., 2014. Uranium isotopes distinguish two geochemically distinct stages during the later Cambrian SPICE event: Earth and Planetary Science Letter 401, 313-326.

Dahl, T. W., Connelly, J. N., Kouchinsky, A., Gill, B. C., Månsson, S. F., and Bizzarro, M., 2017. Reorganisation of Earth's biogeochemical cycles briefly oxygenated the oceans 520 Myr ago. Geochemical Perspectives Letters 3(2), 210-220.

Daines, S. J., Mills, B. J., and Lenton, T. M., 2017. Atmospheric oxygen regulation at low Proterozoic levels by incomplete oxidative weathering of sedimentary organic carbon. Nature Communication 8, 14379.

Danise, S., Twitchett, R.J., Little, C.T., Clemence, M.E., 2013. The impact of global warming and anoxia on marine benthic community dynamics: an example from the Toarcian (Early Jurassic). PLOS One 8(2), e56255.

Darroch, S. A., Sperling, E. A., Boag, T. H., Racicot, R. A., Mason, S. J., Morgan, A. S., Tweedt, S., Myrow, P., Johnston, D. T., Erwin, D. H., and Laflamme, M., 2015. Biotic replacement and mass extinction of the Ediacara biota. Proceedings. Biological Sciences 282, 1814.

Darroch, S. A. F., Rahman, I. A., Gibson, B., Racicot, R. A., and Laflamme, M., 2017. Inference of facultative mobility in the enigmatic Ediacaran organism Parvancorina. Biology Letters 13, 20170033.

Diaz, R. J., and Rosenberg, R., 2008. Spreading dead zones and consequences for marine ecosystems. Science 321(5891), 926-929.

Dunk, R. M., Mills, R. A., and Jenkins, W. J., 2002. A reevaluation of the oceanic uranium budget for the Holocene. Chemical Geology 190(1-4), 45-67.

Elrick, M., Polyak, V., Algeo, T. J., Romaniello, S., Asmerom, Y., Herrmann, A. D., Anbar, A. D., Zhao, L., and Chen, Z.-Q., 2017. Global-ocean redox variation during the middle-

late Permian through Early Triassic based on uranium isotope and Th/U trends of marine carbonates. Geology 45(2), 163-166.

Enos, P., Jiayong, W. E. I., and Yangji, Y. A. N., 1997. Facies distribution and retreat of Middle Triassic platform margin, Guizhou province, south China. Sedimentology 44(3), 563-584.

Erwin, D. H., 2009. Early origin of the bilaterian developmental toolkit. Philosophical Transactions of the Royal Society B: Biological Sciences 364(1527), 2253-2261.

Erwin, D. H., Bowring, S. A., and Yugan, J., 2002. End-Permian mass extinctions: A review. Geological Society of America Special Paper 356, 363-383.

Erwin, D. H., Laflamme, M., Tweedt, S. M., Sperling, E. A., Pisani, D., and Peterson, K. J., 2011, The Cambrian conundrum: early divergence and later ecological success in the early history of animals. Science 334(6059), 1091-1097.

Feng, Q., and Algeo, T. J., 2014. Evolution of oceanic redox conditions during the Permo-Triassic transition: Evidence from deepwater radiolarian facies. Earth-Science Reviews 137, 34-51.

Fike, D. A., Bradley, A. S., and Rose, C. V., 2015. Rethinking the Ancient Sulfur Cycle. Annual Review of Earth and Planetary Sciences 43(1), 593-622.

Fike, D. A., Grotzinger, J. P., Pratt, L. M., and Summons, R. E., 2006. Oxidation of the Ediacaran ocean. Nature 444(7120), 744-747.

Finnegan, S., Heim, N. A., Peters, S. E., and Fischer, W. W., 2012. Climate change and the selective signature of the Late Ordovician mass extinction. Proceedings of the National Academy of Sciences U.S.A. 109(18), 6829-6834.

Foster, W. J., Danise, S., Price, G. D., and Twitchett, R. J., 2017. Subsequent biotic crises delayed marine recovery following the late Permian mass extinction event in northern Italy. PLoS One 12(3), e0172321.

Frei R., Gaucher C., Stolper D. and Canfield D. E., 2013. Fluctuations in late Neoproterozoic atmospheric oxidation—Cr isotope chemostratigraphy and iron speciation of the late Ediacaran lower Arroyo del Soldado Group (Uruguay). Gondwana Research 23, 797-811.

Froelich, P.N., 1988. Kinetic control of dissolved phosphate in natural rivers and estuaries: A primer on the phosphate buffer mechanism. Limnology and Oceanography 33, 649-668.

Galfetti, T., Hochuli, P.A., Brayard, A., Bucher, H., Weissert, H., Vigran, J.O., 2007. Smithian-Spathian boundary event: evidence for global climatic change in the wake of the end-Permian biotic crisis. Geology 35(4), 291-294.

Galfetti, T., Bucher, H., Martini, R., Hochuli, P.A., Weissert, H., Crasquin-Soleau, S., Brayard, A., Goudemand, N., Brühwiler, T., Guodun, K., 2008. Evolution of Early Triassic outer platform paleoenvironments in the Nanpanjiang Basin (South China) and their significance for the biotic recovery. Sedimentary Geology 204, 36-60.

Gaschnig, R.M., Rudnick, R.L., McDonough, W.F., Kaufman, A.J., Valley, J., Hu, Z., Gao, S., Beck, M.L., 2016. Compositional evolution of the upper continental crust through time, as constrained by ancient glacial diamictites. Geochimica et Cosmochimica Acta 186, 316-343.

Gehling, J. G., Droser, M. L., Jensen, S. R., and Runnegar, B. N., 2005. Ediacara organisms: relating form to function, in Briggs, D. E. G., ed., Evolving Form and Function: Fossils and Development: New Haven, Yale Peabody Museum Publications, p. 43-66.

Gehling, J. G., Runnegar, B. N., and Droser, M. L., 2015. Scratch traces of large Ediacara bilaterian animals. Journal of Paleontology 88(02), 284-298.

George, A. D., Chow, N., and Trinajstic, K. M., 2014. Oxic facies and the Late Devonian mass extinction, Canning Basin, Australia. Geology 42(4), 327-330.

German, C. R., and Elderfield, H., 1990. Application of the Ce anomaly as a paleoredox indicator: The ground rules. Paleoproductivity and Paleochemistry of the Oceans 5(5), 823-833.

Gill, B. C., Lyons, T. W., Young, S. A., Kump, L. R., Knoll, A. H., and Saltzman, M. R., 2011. Geochemical evidence for widespread euxinia in the later Cambrian ocean. Nature 469(7328), 80-83.

Gilleaudeau, G.J., Kah, L.C., 2013. Carbon isotope records in a Mesoproterozoic epicratonic sea: Carbon cycling in a low-oxygen world. Precambrian Research 228, 85-101.

Gilleaudeau G. J., Frei R., Kaufman A. J., Kah L. C., Azmy K., Bartley J. K., Chernyavskiy P. and Knoll A. H., 2016. Oxygenation of the mid-Proterozoic atmosphere: Clues from chromium isotopes in carbonates. Geochemical Perspective Letter 2, 178-187.

Gilleaudeau, G. J., Sahoo, S. K., Kah, L. C., Henderson, M. A., and Kaufman, A. J., 2018. Proterozoic carbonates of the Vindhyan Basin, India: Chemostratigraphy and diagenesis. Gondwana Research, in press.

Glass, J.B., Axler, R.P., Chandra, S., Goldman, C.R., 2012. Molybdenum limitation of microbial nitrogen assimilation in aquatic ecosystems and pure cultures. Frontiers in Microbiology 3, 331.

Gong, S. C., and Swart, P. K., 1990. The concentration of uranium in freshwater vadose and phreatic cements in a Holocene ooid cay; a method of identifying ancient water tables. Journal of Sedimentary Research 60 (5), 735-746.

Gong, Z., Kodama, K. P., and Li, Y.-X., 2017. Rock magnetic cyclostratigraphy of the Doushantuo Formation, South China and its implications for the duration of the Shuram carbon isotope excursion. Precambrian Research 289, 62-74.

Goto, K. T., Anbar, A. D., Gordon, G. W., Romaniello, S. J., Shimoda, G., Takaya, Y., Tokumaru, A., Nozaki, T., Suzuki, K., Machida, S., Hanyu, T., and Usui, A., 2014. Uranium isotope systematics of ferromanganese crusts in the Pacific Ocean: Implications for the marine $^{238}U/^{235}U$ isotope system. Geochimica et Cosmochimica Acta 146, 43-58.

Grasby, S. E., Beauchamp, B., Embry, A., and Sanei, H., 2012. Recurrent Early Triassic ocean anoxia. Geology 41 (2), 175-178.

Grasby, S. E., Beauchamp, B., and Knies, J., 2016. Early Triassic productivity crises delayed recovery from world's worst mass extinction. Geology 44 (9), 779-782.

Grice, K., Cao, C., Love, G. D., Bottcher, M. E., Twitchett, R. J., Grosjean, E., Summons, R. E., Turgeon, S. C., Dunning, W., and Jin, Y., 2005. Photic zone euxinia during the Permian-triassic superanoxic event. Science 307(5710), 706-709.

Grotzinger, J. P., Fike, D. A., and Fischer, W. W., 2011. Enigmatic origin of the largest-known carbon isotope excursion in Earth's history. Nature Geoscience 4(5), 285-292.

Hallam, A., 1990. The end-Triassic mass extinction event. Geological Society of America Special Paper 247, 577–584.

Hammarlund, E. U., Dahl, T. W., Harper, D. A. T., Bond, D. P. G., Nielsen, A. T., Bjerrum, C. J., Schovsbo, N. H., Schönlaub, H. P., Zalasiewicz, J. A., and Canfield, D. E., 2012. A sulfidic driver for the end-Ordovician mass extinction. Earth and Planetary Science Letters 331-332, 128-139.

Hardisty, D. S., Lu, Z., Bekker, A., Diamond, C. W., Gill, B. C., Jiang, G., Kah, L. C., Knoll, A. H., Loyd, S. J., Osburn, M. R., Planavsky, N. J., Wang, C., Zhou, X., and Lyons, T. W., 2017. Perspectives on Proterozoic surface ocean redox from iodine contents in ancient and recent carbonate. Earth and Planetary Science Letters 463, 159–170.

Harper, D. A. T., 2006. The Ordovician biodiversification: Setting an agenda for marine life. Palaeogeography, Palaeoclimatology, Palaeoecology 232(2-4), 148-166.

Harper, D. A. T., Hammarlund, E. U., and Rasmussen, C. M. Ø., 2014. End Ordovician extinctions: A coincidence of causes. Gondwana Research 25(4), 1294-1307.

Hartmann, J., Moosdorf, N., Lauerwald, R., Hinderer, M., West, A.J., 2014. Global chemical weathering and associated P-release—The role of lithology, temperature and soil properties. Chemical Geology 363, 145-163.

Hautmann, M., Benton, M. J., and Tomašových, A., 2008. Catastrophic ocean acidification at the Triassic-Jurassic boundary. Neues Jahrbuch für Geologie und Paläontologie – Abhandlungen 249(1), 119-127.

Hawkesworth, C. J., and Kemp, A. I., 2006. Evolution of the continental crust. Nature 443(7113), 811-817.

Henderson, G. M., Slowey, N. C., and Haddad, G. A., 1999. Fluid flow through carbonate platforms: constraints from $^{234}U/^{238}U$ and Cl^- in Bahamas pore-waters. Earth and Planetary Science Letters 169(1-2), 99-111.

Henderson, G. M., Anderson, R.F., 2003. The U-series toolbox for paleoceanography. Reviews in Mineralogy and Geochemistry 52 (1), 493-531.

Hofmann, R., Hautmann, M., Brayard, A., Nützel, A., Bylund, K. G., Jenks, J. F., vennin, E., Olivier, N., and Bucher, H., 2014. Recovery of benthic marine communities from the end-Permian mass extinction at the low latitudes of eastern Panthalassa. Palaeontology 57, 547–589.

Holmden, C., Amini, M., and Francois, R., 2015. Uranium isotope fractionation in Saanich Inlet: A modern analog study of a paleoredox tracer. Geochimica et Cosmochimica Acta 153, 202-215.

Holmden C., Jacobson A. D., Sageman B. B. and Hurtgen M. T., 2016. Response of the Cr isotope proxy to Cretaceous Ocean Anoxic Event 2 in a pelagic carbonate succession from the Western Interior Seaway. Geochimica Cosmochimica Acta 186, 277-295.

Hood, A. v. S., Planavsky, N. J., Wallace, M. W., Wang, X., Bellefroid, E. J., Gueguen, B., and Cole, D. B., 2016. Integrated geochemical-petrographic insights from component-selective $\delta^{238}U$ of Cryogenian marine carbonates. Geology 44(11), 935-938.

Horacek, M., Richoz, S., Brandner, R., Krystyn, L., and Spötl, C., 2007, Evidence for recurrent changes in Lower Triassic oceanic circulation of the Tethys: The $\delta^{13}C$ record from marine sections in Iran. Palaeogeography, Palaeoclimatology, Palaeoecology 252(1-2), 355-369.

Huber, B.T., Hodell, D.A., Hamilton, C.P., 1995. Middle–Late Cretaceous climate of the southern high latitudes: stable isotopic evidence for minimal equator-to-pole thermal gradients. Geological Society of America Bulletin 107(10), 1164-1191.

Isozaki, Y., 1997. Permo-Triassic boundary superanoxia and stratified superocean: records from lost deep sea. Science 276(5310), 235-238.

Isozaki, Y., 2009. Integrated "plume winter" scenario for the double-phased extinction during the Paleozoic–Mesozoic transition: The G-LB and P-TB events from a Panthalassan perspective. Journal of Asian Earth Sciences 36(6), 459-480.

Ivantsov, A. Y., and Malakhovskaya, Y. E., 2002. Gigantskiye sledy vendskikh zhivotnykh. Doklady Akademii Nauk 385, 382-386.

Jablonski, D., and Chaloner, W. G., 1994. Extinctions in the fossil record [and discussion]. Philosophical Transactions of the Royal Society B: Biological Sciences 344(1307), 11-17.

Jacobsen, S. B., and Kaufman, A. J., 1999. The Sr, C and O isotopic evolution of Neoproterozoic seawater. Chemical Geology161(1-3), 37-57.

Joachimski, M. M., Breisig, S., Buggisch, W., Talent, J. A., Mawson, R., Gereke, M., Morrow, J. R., Day, J., and Weddige, K., 2009. Devonian climate and reef evolution: Insights from oxygen isotopes in apatite. Earth and Planetary Science Letters 284(3-4), 599-609.

Joachimski, M. M., and Buggisch, W., 1993. Anoxic events in the late Frasnian—Causes of the Frasnian-Famennian faunal crisis? Geology 21(8), 675.

Joachimski, M.M., Buggisch, W., 2002. Conodont apatite $\delta^{18}O$ signatures indicate climatic cooling as a trigger of the Late Devonian mass extinction. Geology 30(8), 711.

Joachimski, M. M., Lai, X., Shen, S., Jiang, H., Luo, G., Chen, B., Chen, J., and Sun, Y., 2012. Climate warming in the latest Permian and the Permian-Triassic mass extinction. Geology 40(3), 195-198.

Joachimski, M. M., Ostertag-Henning, C. P., R.D., Strauss, H., Freeman, K. H., Littke, R., and Sinninghe Damste, J. S. R., G., 2001. Water column anoxia, enhanced productivity and concomitant changes in $\delta^{13}C$ and $\delta^{34}S$ across the Frasnian–Famennian boundary (Kowala — Holy Cross Mountains/Poland). Chemical Geology 175, 109-131.

John, E. H., Wignall, P. B., Newton, R. J., and Bottrell, S. H., 2010. $\delta^{34}S_{CAS}$ and $\delta^{18}O_{CAS}$ records during the Frasnian–Famennian (Late Devonian) transition and their bearing on mass extinction models. Chemical Geology 275(3-4), 221-234.

Johnston, D. T., Poulton, S. W., Tosca, N. J., O'Brien, T., Halverson, G. P., Schrag, D. P., and Macdonald, F. A., 2013. Searching for an oxygenation event in the fossiliferous Ediacaran of northwestern Canada. Chemical Geology 362, 273-286.

Jones, D. S., and Fike, D. A., 2013. Dynamic sulfur and carbon cycling through the end-Ordovician extinction revealed by paired sulfate–pyrite $\delta^{34}S$. Earth and Planetary Science Letters 363, 144-155.

Jost, A. B., Bachan, A., van de Schootbrugge, B., Lau, K. V., Weaver, K. L., Maher, K., and Payne, J. L., 2017. Uranium isotope evidence for an expansion of marine anoxia during the end-Triassic extinction. Geochemistry, Geophysics, Geosystems 18(8), 3093-3108.

Kah, L. C., Bartley, J. K., and Teal, D. A., 2012. Chemostratigraphy of the Late Mesoproterozoic Atar Group, Taoudeni Basin, Mauritania: Muted isotopic variability, facies correlation, and global isotopic trends. Precambrian Research 200-203, 82-103.

Kah, L. C., Sherman, A. G., Narbonne, G. M., Knoll, A. H., and Kaufman, A. J., 1999. $\delta^{13}C$ stratigraphy of the Proterozoic Bylot Supergroup, Baffin Island, Canada: implications for regional lithostratigraphic correlations. Canadian Journal of Earth Sciences 36(3), 313-332.

Kakuwa, Y., and Matsumoto, R., 2006. Cerium negative anomaly just before the Permian and Triassic boundary event-The upward expansion of anoxia in the water column. Palaeogeography, Palaeoclimatology, Palaeoecology 229(4), 335-344.

Kaltenbach, A., 2013. Uranium isotopic analysis of terrestrial and extraterrestrial samples Thesis, Doctor of Philosophy, University of Otago.

Kaufman, A., and Knoll, A., 1995. Neoproterozoic variations in the C-isotopic composition of seawater: stratigraphic and biogeochemical implications. Precambrian Research 73(1-4), 27-49.

Kaufman, A. J., Corsetti, F. A., and Varni, M. A., 2007. The effect of rising atmospheric oxygen on carbon and sulfur isotope anomalies in the Neoproterozoic Johnnie Formation, Death Valley, USA. Chemical Geology 237(1-2), 47-63.

Keeling, R.E., Kortzinger, A., Gruber, N., 2010. Ocean deoxygenation in a warming world. Annual Review of Marine Science 2, 199-229.

Kelly, S. D., Newville, M. G., Cheng, L., Kemner, K. M., Sutton, S. R., Fenter, P., Sturchio, N. C., and Spötl, C., 2003. Uranyl incorporation in natural calcite: Environmental Science & Technology 37(7), 1284-1287.

Kelly, S. D., Rasbury, E. T., Chattopadhyay, S., Kropf, A. J., and Kemner, K. M., 2006. Evidence of a stable uranyl site in ancient organic-rich calcite. Environmental Science & Technology 40(7), 2262-2268.

Kendall, B., Komiya, T., Lyons, T. W., Bates, S. M., Gordon, G. W., Romaniello, S. J., Jiang, G., Creaser, R. A., Xiao, S., McFadden, K., Sawaki, Y., Tahata, M., Shu, D., Han, J., Li, Y., Chu, X., and Anbar, A. D., 2015. Uranium and molybdenum isotope evidence for an episode of widespread ocean oxygenation during the late Ediacaran Period. Geochimica et Cosmochimica Acta 156, 173-193.

Kiessling, W., and Simpson, C., 2011. On the potential for ocean acidification to be a general cause of ancient reef crises. Global Change Biology 17(1), 56-67.

Kimura, H., and Watanabe, Y., 2001. Oceanic anoxia at the Precambrian-Cambrian boundary. Geology 29(11), 995.

Knoll, A. H., Bambach, R. K., Payne, J. L., Pruss, S., and Fischer, W. W., 2007. Paleophysiology and end-Permian mass extinction. Earth and Planetary Science Letters 256(3-4), 295-313.

Korte, C., Pande, P., Kalia, P., Kozur, H. W., Joachimski, M. M., and Oberhänsli, H., 2010. Massive volcanism at the Permian–Triassic boundary and its impact on the isotopic composition of the ocean and atmosphere. Journal of Asian Earth Sciences 37(4), 293-311.

Kozur, H., 2003. Integrated ammonoid, conodont and radiolarian zonation of the Triassic. Hallesches Jahrbuch für Geowissenschaften 25, 49-79.

Ku, T.-L., Knauss, K. G., and Mathieu, G. G., 1977. Uranium in open ocean: concentration and isotopic composition. Deep Sea Research 24(11), 1005-1017.

Kump, L. R., and Arthur, M. A., 1999. Interpreting carbon-isotope excursions: carbonates and organic matter. Chemical Geology 161(1-3), 181-198.

Kump, L. R., Pavlov, A., and Arthur, M. A., 2005. Massive release of hydrogen sulfide to the surface ocean and atmosphere during intervals of oceanic anoxia. Geology 33(5), 397.

Laflamme, M., Darroch, S. A. F., Tweedt, S. M., Peterson, K. J., and Erwin, D. H., 2013. The end of the Ediacara biota: Extinction, biotic replacement, or Cheshire Cat? Gondwana Research 23(2), 558-573.

Laflamme, M., Xiao, S., and Kowalewski, M., 2009. From the Cover: Osmotrophy in modular Ediacara organisms. Proceedings of the National Academy of Sciences U.S.A. 106(34), 14438-14443.

Langmuir, D., 1978. Uranium solution-mineral equilibria at low temperatures with applications to sedimentary ore deposits. Geochimica et Cosmochimica Acta 42(6), 547-569.

Lau, K. V., Macdonald, F. A., Maher, K., and Payne, J. L., 2017. Uranium isotope evidence for temporary ocean oxygenation in the aftermath of the Sturtian Snowball Earth. Earth and Planetary Science Letters 458, 282-292.

Lau, K. V., Maher, K., Altiner, D., Kelley, B. M., Kump, L. R., Lehrmann, D. J., Silva-Tamayo, J. C., Weaver, K. L., Yu, M., and Payne, J. L., 2016. Marine anoxia and delayed Earth system recovery after the end-Permian extinction. Proceedings of the National Academy of Sciences U.S.A. 113(9), 2360–2365.

Lehrmann, D. J., Donghong, P., Enos, P., Minzoni, M., Ellwood, B. B., Orchard, M. J., Jiyan, Z., Jiayong, W., Dillett, P., Koenig, J., Steffen, K., Druke, D., Druke, J., Kessel, B., and Newkirk, T., 2007. Impact of differential tectonic subsidence on isolated carbonate-platform evolution: Triassic of the Nanpanjiang Basin, south China. AAPG Bulletin 91(3), 287-320.

Lenton, T. M., Boyle, R. A., Poulton, S. W., Shields-Zhou, G. A., and Butterfield, N. J., 2014. Co-evolution of eukaryotes and ocean oxygenation in the Neoproterozoic era. Nature Geoscience 7(4), 257-265.

Lenton, T. M., Daines, S. J., and Mills, B. J. W., 2018. COPSE reloaded: An improved model of biogeochemical cycling over Phanerozoic time. Earth-Science Reviews 178, 1-28.

Liu, C., Wang, Z., Raub, T.D., 2013. Geochemical constraints on the origin of Marinoan cap dolostones from Nuccaleena Formation, South Australia. Chemical Geology 351(2), 95-104.

Li, C., Hardisty, D. S., Luo, G., Huang, J., Algeo, T. J., Cheng, M., Shi, W., An, Z., Tong, J., Xie, S., Jiao, N., and Lyons, T. W., 2016. Uncovering the spatial heterogeneity of Ediacaran carbon cycling. Geobiology 15(2), 211-224.

Li, C., Love, G. D., Lyons, T. W., Fike, D. A., Sessions, A. L., and Chu, X., 2010. A stratified redox model for the Ediacaran ocean. Science 328(5974), 80-83.

Ling, H.-F., Chen, X., Li, D., Wang, D., Shields-Zhou, G. A., and Zhu, M., 2013. Cerium anomaly variations in Ediacaran–earliest Cambrian carbonates from the Yangtze Gorges area, South China: Implications for oxygenation of coeval shallow seawater. Precambrian Research 225, 110-127.

Liu, A. G., McLlroy, D., and Brasier, M. D., 2010. First evidence for locomotion in the Ediacara biota from the 565 Ma Mistaken Point Formation, Newfoundland. Geology 38(2), 123-126.

Liu, J., Qie, W., Algeo, T. J., Yao, L., Huang, J., and Luo, G., 2016. Changes in marine nitrogen fixation and denitrification rates during the end-Devonian mass extinction. Palaeogeography, Palaeoclimatology, Palaeoecology 448, 195-206.

Liu, W., Xie, S.-P., Liu, Z., Zhu, J., 2017. Overlooked possibility of a collapsed atlantic meridional overturning circulation in warming climate. Science Advances, 3(1).

Long, J.A., Large, R.R., Lee, M.S.Y., Benton, M.J., Danyushevsky, L.V., Chiappe, L.M., Halpin, J.A., Cantrill, D., Lottermoser, B., 2016a. Severe selenium depletion in the Phanerozoic oceans as a factor in three global mass extinction events. Gondwana Research 36, 209-218.

Long, M.C., Deutsch, C., Ito, T., 2016b. Finding forced trends in oceanic oxygen. Global Biogeochemical Cycles 30(2), 381-397.

Loope, G. R., Kump, L. R., and Arthur, M. A., 2013. Shallow water redox conditions from the Permian–Triassic boundary microbialite: The rare earth element and iodine geochemistry of carbonates from Turkey and South China. Chemical Geology 351, 195-208.

Love, G. D., Grosjean, E., Stalvies, C., Fike, D. A., Grotzinger, J. P., Bradley, A. S., Kelly, A. E., Bhatia, M., Meredith, W., Snape, C. E., Bowring, S. A., Condon, D. J., and Summons, R. E., 2009. Fossil steroids record the appearance of Demospongiae during the Cryogenian period. Nature 457(7230), 718-721.

Lu, X., Kendall, B., Stein, H. J., Li, C., Hannah, J. L., Gordon, G. W., and Ebbestad, J. O. R., 2017. Marine redox conditions during deposition of Late Ordovician and Early Silurian organic-rich mudrocks in the Siljan ring district, central Sweden. Chemical Geology 457, 75-94.

Lu, Z., Jenkyns, H.C., Rickaby, R.E., 2010. Iodine to calcium ratios in marine carbonate as a paleo-redox proxy during oceanic anoxic events. Geology 38, 1107-1110.

Lyons, T. W., Anbar, A. D., Severmann, S., Scott, C., and Gill, B. C., 2009. Tracking euxinia in the ancient ocean: a multiproxy perspective and proterozoic case study. Annual Review of Earth and Planetary Sciences 37(1), 507-534.

Lyons, T. W., Reinhard, C. T., and Planavsky, N. J., 2014. The rise of oxygen in Earth's early ocean and atmosphere. Nature 506(7488), 307-315.

Macdonald, F. A., Strauss, J. V., Sperling, E. A., Halverson, G. P., Narbonne, G. M., Johnston, D. T., Kunzmann, M., Schrag, D. P., and Higgins, J. A., 2013. The stratigraphic relationship between the Shuram carbon isotope excursion, the oxygenation of Neoproterozoic oceans, and the first appearance of the Ediacara biota and bilaterian trace fossils in northwestern Canada. Chemical Geology 362, 250-272.

Martin, P. A., Lea, D. W., Mashiotta, T. A., Papenfuss, T., and Sarnthein, M., 2000. Variation of foraminiferal Sr/Ca over Quaternary glacial-interglacial cycles: Evidence for changes in mean ocean Sr/Ca? Geochemistry, Geophysics, Geosystems 1, 1004.

Martindale, R. C., Berelson, W. M., Corsetti, F. A., Bottjer, D. J., and West, A. J., 2012. Constraining carbonate chemistry at a potential ocean acidification event (the Triassic–Jurassic boundary) using the presence of corals and coral reefs in the fossil record. Palaeogeography, Palaeoclimatology, Palaeoecology 350-352, 114-123.

Matear, R.J., Hirst, A.C., 2003. Long-term changes in dissolved oxygen concentrations in the ocean caused by protracted global warming. Global Biogeochemical Cycles 17(4), 1125.

McFadden, K. A., Huang, J., Chu, X., Jiang, G., Kaufman, A. J., Zhou, C., Yuan, X., and Xiao, S., 2008. Proceedings of the National Academy of Sciences U.S.A. 105(9), 3197-3202.

McGhee, G. R., Clapham, M. E., Sheehan, P. M., Bottjer, D. J., and Droser, M. L., 2013. A new ecological-severity ranking of major Phanerozoic biodiversity crises. Palaeogeography, Palaeoclimatology, Palaeoecology 370, 260-270.

McKee, B. A., and Todd, J. F., 1993. Uranium behavior in a permanently anoxic fjord: Microbial control? Limnology and Oceanography 38(2), 408-414.

Meece, D. E., and Benninger, L. K., 1993. The coprecipitation of Pu and other radionuclides with CaCO3. Geochimica et Cosmochimica Acta 57(7), 1447-1458.

Meert, J. G., and Lieberman, B. S., 2008. The Neoproterozoic assembly of Gondwana and its relationship to the Ediacaran–Cambrian radiation. Gondwana Research 14(1-2), 5-21.

Melezhik, V., Fallick, A., and Pokrovsky, B., 2005. Enigmatic nature of thick sedimentary carbonates depleted in C beyond the canonical mantle value: The challenges to our understanding of the terrestrial carbon cycle. Precambrian Research 137(3-4), 131-165.

Melezhik, V. A., Pokrovsky, B. G., Fallick, A. E., Kuznetsov, A. B., and Bujakaite, M. I., 2009. Constraints on $^{87}Sr/^{86}Sr$ of Late Ediacaran seawater: insight from Siberian high-Sr limestones. Journal of the Geological Society 166(1), 183-191.

Meyer, K. M., Kump, L. R., and Ridgwell, A., 2008. Biogeochemical controls on photic-zone euxinia during the end-Permian mass extinction. Geology 36(9), 747.

Meyer, K. M., Ridgwell, A., and Payne, J. L., 2016. The influence of the biological pump on ocean chemistry: implications for long-term trends in marine redox chemistry, the global carbon cycle, and marine animal ecosystems. Geobiology 14(3), 207-219.

Meyer, K. M., Yu, M., Jost, A. B., Kelley, B. M., and Payne, J. L., 2011. $\delta^{13}C$ evidence that high primary productivity delayed recovery from end-Permian mass extinction. Earth and Planetary Science Letters 302(3-4), 378-384.

Meyer, M., Xiao, S., Gill, B. C., Schiffbauer, J. D., Chen, Z., Zhou, C., and Yuan, X., 2014. Interactions between Ediacaran animals and microbial mats: Insights from Lamonte trevallis, a new trace fossil from the Dengying Formation of South China. Palaeogeography, Palaeoclimatology, Palaeoecology 396, 62-74.

Mills, B., Lenton, T. M., and Watson, A. J., 2014. Proterozoic oxygen rise linked to shifting balance between seafloor and terrestrial weathering. Proceedings of the National Academy of Sciences U.S.A. 111(25), 9073-9078.

Minguez, D., and Kodama, K. P., 2017, Rock magnetic chronostratigraphy of the Shuram carbon isotope excursion: Wonoka Formation, Australia. Geology 45(6), 567-570.

Minguez, D., Kodama, K. P., and Hillhouse, J. W., 2015. Paleomagnetic and cyclostratigraphic constraints on the synchroneity and duration of the Shuram carbon isotope excursion, Johnnie Formation, Death Valley Region, CA. Precambrian Research 266, 395-408.

Morford, J. L., and Emerson, S., 1999. The geochemistry of redox sensitive trace metals in sediments. Geochimica et Cosmochimica Acta 63(11-12), 1735-1750.

Montoya-Pino, C., Weyer, S., Anbar, A.D., Pross, J., Oschmann, W., van de Schootbrugge, B., Arz, H.W., 2010. Global enhancement of ocean anoxia during Oceanic Anoxic Event 2: A quantitative approach using U isotopes. Geology 38(4), 315-318.

Musashi, M., Isozaki, Y., Koike, T., and Kreulen, R., 2001. Stable carbon isotope signature in mid-Panthalassa shallow-water carbonates across the Permo–Triassic boundary: evidence for ^{13}C-depleted superocean. Earth and Planetary Science Letters 191(1-2), 9-20.

Noordmann, J., Weyer, S., Georg, R. B., Jons, S., and Sharma, M., 2016. $^{238}U/^{235}U$ isotope ratios of crustal material, rivers and products of hydrothermal alteration: new insights on the oceanic U isotope mass balance. Isotopes in Environmental and Health Studies 52(1-2), 141-163.

Noordmann, J., Weyer, S., Montoya-Pino, C., Dellwig, O., Neubert, N., Eckert, S., Paetzel, M., and Böttcher, M. E., 2015. Uranium and molybdenum isotope systematics in modern euxinic basins: Case studies from the central Baltic Sea and the Kyllaren fjord (Norway). Chemical Geology 396, 182-195.

Orchard, M. J., 2007. Conodont diversity and evolution through the latest Permian and Early Triassic upheavals. Palaeogeography, Palaeoclimatology, Palaeoecology 252(1-2), 93-117.

Payne, J., and Kump, L., 2007. Evidence for recurrent Early Triassic massive volcanism from quantitative interpretation of carbon isotope fluctuations. Earth and Planetary Science Letters 256(1-2), 264-277.

Payne, J. L., and Clapham, M. E., 2012. End-Permian mass extinction in the oceans: an ancient analog for the twenty-first century? Annual Review of Earth and Planetary Sciences 40(1), 89-111.

Payne, J. L., Lehrmann, D. J., Follett, D., Seibel, M., Kump, L. R., Riccardi, A., Altiner, D., Sano, H., and Wei, J., 2007. Erosional truncation of uppermost Permian shallow-marine carbonates and implications for Permian-Triassic boundary events. Geological Society of America Bulletin 119(7-8), 771-784.

Payne, J. L., Lehrmann, D. J., Wei, J., Orchard, M. J., Schrag, D. P., and Knoll, A. H., 2004. Large perturbations of the carbon cycle during recovery from the end-permian extinction. Science 305(5683), 506-509.

Payne, J. L., Summers, M., Rego, B. L., Altiner, D., Wei, J., Yu, M., and Lehrmann, D. J., 2011. Early and Middle Triassic trends in diversity, evenness, and size of foraminifers on a carbonate platform in south China: implications for tempo and mode of biotic recovery from the end-Permian mass extinction. Paleobiology 37(3), 409-425.

Paytan, A., McLaughlin, K., 2007. The oceanic phosphorus cycle. Chemical Reviews 107(2), 563-76.

Penny, A. M., Wood, R., Curtis, A., Bowyer, F., Tostevin, R., and Hoffman, K. H., 2014. Early animals. Ediacaran metazoan reefs from the Nama Group, Namibia. Science 344(6191), 1504-1506.

Peter S. Mozley, S. J. B., 1993. Oxygen and carbon isotopic composition of marine carbonate concretions; an overview. Journal of Sedimentary Research 63 (1): 73-83.

Planavsky, N. J., Reinhard, C. T., Wang, X., Thomson, D., McGoldrick, P., Rainbird, R. H., Johnson, T., Fischer, W. W., and Lyons, T. W., 2014. Low mid-Proterozoic atmospheric oxygen levels and the delayed rise of animals. Science 346(6209), 635-638.

Portner, H.O., Knust, R., 2007. Climate change affects marine fishes through the oxygen limitation of thermal tolerance. Science 315(5808), 95-97.

Pu, J. P., Bowring, S. A., Ramezani, J., Myrow, P., Raub, T. D., Landing, E., Mills, A., Hodgin, E., and Macdonald, F. A., 2016. Dodging snowballs: Geochronology of the Gaskiers glaciation and the first appearance of the Ediacaran biota. Geology 44(11), 955-958.

Qie, W., Liu, J., Chen, J., Wang, X., Mii, H.-s., Zhang, X., Huang, X., Yao, L., Algeo, T. J., and Luo, G., 2015. Local overprints on the global carbonate $\delta^{13}C$ signal in Devonian–Carboniferous boundary successions of South China. Palaeogeography, Palaeoclimatology, Palaeoecology 418, 290-303.

Rabalais, N. N., Turner, R. E., and Wiseman, W. J., 2002. Gulf of Mexico Hypoxia, A.K.A. "The Dead Zone". Annual Review of Ecology and Systematics 33(1), 235-263.

Racki, G., Racka, M., Matyja, H., and Devleeschouwer, X., 2002. The Frasnian/Famennian boundary interval in the South Polish–Moravian shelf basins: integrated event-stratigraphical approach. Palaeogeography, Palaeoclimatology, Palaeoecology 181(1-3), 251-297.

Raup, D. M., and Sepkoski, J. J., Jr., 1982. Mass extinctions in the marine fossil record. Science 215(4539), 1501-1503.

Reeder, R. J., Nugent, M., Lamble, G. M., Tait, C. D., and Morris, D. E., 2000. Uranyl incorporation into calcite and aragonit: XAFS and luminescence studies. Environmental Science & Technology 34(4), 638-644.

Retallack, G. J., Sheldon, N. D., Carr, P. F., Fanning, M., Thompson, C. A., Williams, M. L., Jones, B. G., and Hutton, A., 2011. Multiple Early Triassic greenhouse crises impeded recovery from Late Permian mass extinction. Palaeogeography, Palaeoclimatology, Palaeoecology 308(1-2), 233-251.

Reinhard, C.T., Planavsky, N.J., Gill, B.C., Ozaki, K., Robbins, L.J., Lyons, T.W., Fischer, W.W., Wang, C., Cole, D.B., Konhauser, K.O., 2017. Evolution of the global phosphorus cycle. Nature 541(7637), 386-389.

Reinhard, C.T., Planavsky, N.J., Robbins, L.J., Partin, C.A., Gill, B.C., Lalonde, S.V., Bekker, A., Konhauser, K.O., Lyons, T.W., 2013. Proterozoic ocean redox and biogeochemical stasis. Proceedings of the National Academy of Sciences U.S.A. 110(14), 5357-5362.

Richter, F.M., Turekian, K.K., 1993. Simple models for the geochemical response of the ocean to climatic and tectonic forcing. Earth and Planetary Science Letters 119, 121-131.

Ridgwell, A., 2005. A Mid Mesozoic Revolution in the regulation of ocean chemistry. Marine Geology 217(3-4), 339-357.

Richoz, S., Krystyn, L., Baud, A., Brandner, R., Horacek, M., and Mohtat-Aghai, P., 2010. Permian–Triassic boundary interval in the Middle East (Iran and N. Oman): Progressive environmental change from detailed carbonate carbon isotope marine curve and sedimentary evolution. Journal of Asian Earth Sciences 39(4), 236-253.

Rolison, J. M., Stirling, C. H., Middag, R., and Rijkenberg, M. J. A., 2017. Uranium stable isotope fractionation in the Black Sea: Modern calibration of the $^{238}U/^{235}U$ paleo-redox proxy. Geochimica et Cosmochimica Acta 203, 69-88.

Romaniello, S. J., Herrmann, A. D., and Anbar, A. D., 2013. Uranium concentrations and $^{238}U/^{235}U$ isotope ratios in modern carbonates from the Bahamas. Assessing a novel paleoredox proxy. Chemical Geology 362, 305-316.

Romaniello, S., Brennecka, G.A., Anbar, A.D., Colman, A., 2009. Natural isotopic fractionation of $^{238}U/^{235}U$ in the water column of the Black Sea. AGU Abstract, V54C-06.

Romano, C., Goudemand, N., Vennemann, T. W., Ware, D., Schneebeli-Hermann, E., Hochuli, P. A., Brühwiler, T., Brinkmann, W., and Bucher, H., 2012. Climatic and biotic upheavals following the end-Permian mass extinction. Nature Geoscience 6(1), 57-60.

Rudnick, R.L., Gao, S., 2003. Major elements of Earth crust. Treatise on Geochemistry 3, pp. 1-64.

Sahoo, S. K., Planavsky, N. J., Jiang, G., Kendall, B., Owens, J. D., Wang, X., Shi, X., Anbar, A. D., and Lyons, T. W., 2016. Oceanic oxygenation events in the anoxic Ediacaran ocean. Geobiology 14(5), 457-468.

Sallan, L. C., and Coates, M. I., 2010. End-Devonian extinction and a bottleneck in the early evolution of modern jawed vertebrates. Proceedings of the National Academy of Sciences of U.S.A. 107(22), 10131-10135.

Sano, H., Onoue, T., Orchard, M. J., and Martini, R., 2011. Early Triassic peritidal carbonate sedimentation on a Panthalassan seamount: the Jesmond succession, Cache Creek Terrane, British Columbia, Canada. Facies 58(1), 113-130.

Saito, R., Kaiho, K., Oba, M., Takahashi, S., Chen, Z.-Q., Tong, J., 2013. A terrestrial vegetation turnover in the middle of the Early Triassic. Global and Planetary Change 105, 152-159.

Sawaki, Y., Ohno, T., Tahata, M., Komiya, T., Hirata, T., Maruyama, S., Windley, B. F., Han, J., Shu, D., and Li, Y., 2010. The Ediacaran radiogenic Sr isotope excursion in the Doushantuo Formation in the Three Gorges area, South China. Precambrian Research 176(1-4), 46-64.

Sarmiento, J.Á., Gruber, N., Brzezinski, M.A., Dunne, J.P., 2004. High-latitude controls of thermocline nutrients and low latitude biological productivity. Nature 427, 56-60.

Schauble, E. A., 2007. Role of nuclear volume in driving equilibrium stable isotope fractionation of mercury, thallium, and other very heavy elements. Geochimica et Cosmochimica Acta 71(9), 2170-2189.

Scheyer, T. M., Romano, C., Jenks, J., and Bucher, H., 2014. Early Triassic marine biotic recovery: the predators' perspective. PLoS One 3, e88987.

Schobben, M., Stebbins, A., Ghaderi, A., Strauss, H., Korn, D., and Korte, C., 2015. Flourishing ocean drives the end-Permian marine mass extinction. Proceedings of the National Academy of Sciences of U.S.A. 112 (33), 10298-10303.

Schrag, D. P., Higgins, J. A., Macdonald, F. A., and Johnston, D. T., 2013. Authigenic carbonate and the history of the global carbon cycle. Science 339(6119), 540-543.

Schroder, S., and Grotzinger, J. P., 2007. Evidence for anoxia at the Ediacaran-Cambrian boundary: the record of redox-sensitive trace elements and rare earth elements in Oman. Journal of the Geological Society 164(1), 175-187.

Scott, C., Lyons, T. W., Bekker, A., Shen, Y., Poulton, S. W., Chu, X., and Anbar, A. D., 2008. Tracing the stepwise oxygenation of the Proterozoic ocean. Nature 452(7186), 456-459.

Sedlacek, A. R. C., Saltzman, M. R., Algeo, T. J., Horacek, M., Brandner, R., Foland, K., and Denniston, R. F., 2014. $^{87}Sr/^{86}Sr$ stratigraphy from the Early Triassic of Zal, Iran: Linking temperature to weathering rates and the tempo of ecosystem recovery. Geology 42(9), 779-782.

Sephton, M. A., Looy, C. V., Brinkhuis, H., Wignall, P. B., de Leeuw, J. W., and Visscher, H., 2005. Catastrophic soil erosion during the end-Permian biotic crisis. Geology 33(12), 941.

Shen, B., Dong, L., Xiao, S., and Kowalewski, M., 2008. The Avalon explosion: evolution of Ediacara morphospace. Science 319(5859), 81-84.

Shen, J., Algeo, T. J., Hu, Q., Zhang, N., Zhou, L., Xia, W., Xie, S., and Feng, Q., 2012a. Negative C-isotope excursions at the Permian-Triassic boundary linked to volcanism. Geology 40(11), 963-966.

Shen, J., Algeo, T. J., Zhou, L., Feng, Q., Yu, J., and Ellwood, B., 2012b. Volcanic perturbations of the marine environment in South China preceding the latest Permian mass extinction and their biotic effects. Geobiology 10(1), 82-103.

Shen, J., Schoepfer, S.D., Feng, Q.L., Zhou, L., Yu, J.X., Song, H.Y., Wei, H.Y., Algeo, T.J., 2015. Marine productivity changes during the end-Permian crisis and Early Triassic recovery. Earth-Science Reviews 149, 136-162.

Shen, J., Algeo, T.J., Yuan, S.L., Feng, Q.L., Yu, J.X., Zhou, L., O'Connell, B., and Planavsky, N.J., 2018. Using mercury (Hg) enrichments to track volcanic outgassing during the Smithian-Spathian transition. Earth-Science Reviews, under review.

Shen, Y., Farquhar, J., Zhang, H., Masterson, A., Zhang, T., and Wing, B. A., 2011. Multiple S-isotopic evidence for episodic shoaling of anoxic water during Late Permian mass extinction. Nature Communation 2, 210.

Shepherd, J.G., Brewer, P.G., Oschlies, A., Watson, A.J., 2017. Ocean ventilation and deoxygenation in a warming world: Introduction and overview. Philosophical Transactions of the Royal Society A, 375(2102).

Shields, G., and Veizer, J., 2002. Precambrian marine carbonate isotope database: Version 1.1. Geochemistry, Geophysics, Geosystems 3(6), 1-12.

Slomp, C. P., and Van Cappellen, P., 2007. The global marine phosphorus cycle: Sensitivity to oceanic circulation. Biogeosciences 4(2), 155-171.

Sole, R. V., Montoya, J. M., and Erwin, D. H., 2002. Recovery after mass extinction: evolutionary assembly in large-scale biosphere dynamics. Philosophical Transactions of the Royal Society B: Biological Sciences 357(1421), 697-707.

Solien, M. A., 1979. Conodont Biostratigraphy of the Lower Triassic Thaynes Formation, Utah. Journal of Paleontology 53(2), 276-306.

Song, H. Y., Song, H., Algeo, T. J., Tong, J., Romaniello, S. J., Zhu, Y., Chu, D., Gong, Y., and Anbar, A. D., 2017. Uranium and carbon isotopes document global-ocean redox-productivity relationships linked to cooling during the Frasnian-Famennian mass extinction. Geology 45(10), 887-890.

Song, H. Y., Tong, J., Algeo, T. J., Horacek, M., Qiu, H., Song, H., Tian, L., and Chen, Z.-Q., 2013. Large vertical $\delta^{13}C_{DIC}$ gradients in Early Triassic seas of the South China craton. Implications for oceanographic changes related to Siberian Traps volcanism. Global and Planetary Change 105, 7-20.

Song, H.Y., Wu, K., Algeo, T.J., Tong, J.N., Owens, J.D., Song, H.J., Tian, L., Qiu, H., Zhu, Y., Liang, L., and Lyons, T.W., 2018. Amelioration of Early Triassic hyper-greenhouse conditions by enhanced organic carbon burial at the Smithian-Spathian boundary. Earth-Science Reviews, under review.

Song, H. J., Wignall, P. B., Chen, Z. Q., Tong, J., Bond, D. P. G., Lai, X., Zhao, X., Jiang, H., Yan, C., Niu, Z., Chen, J., Yang, H., and Wang, Y., 2011. Recovery tempo and pattern of marine ecosystems after the end-Permian mass extinction. Geology 39(8), 739-742.

Song, H. J., Wignall, P. B., Tong, J., Bond, D. P. G., Song, H., Lai, X., Zhang, K., Wang, H., and Chen, Y., 2012. Geochemical evidence from bio-apatite for multiple oceanic anoxic events during Permian–Triassic transition and the link with end-Permian extinction and recovery. Earth and Planetary Science Letters 353-354, 12-21.

Song, H. J., Wignall, P. B., Tong, J., Song, H., Chen, J., Chu, D., Tian, L., Luo, M., Zong, K., Chen, Y., Lai, X., Zhang, K., and Wang, H., 2015. Integrated Sr isotope variations and global environmental changes through the Late Permian to early Late Triassic. Earth and Planetary Science Letters 424, 140-147.

Sperling, E. A., Frieder, C. A., Raman, A. V., Girguis, P. R., Levin, L. A., and Knoll, A. H., 2013. Oxygen, ecology, and the Cambrian radiation of animals. Proceedings of the National Academy of Sciences of U.S.A. 110(33), 13446-13451.

Sperling, E. A., Wolock, C. J., Morgan, A. S., Gill, B. C., Kunzmann, M., Halverson, G. P., Macdonald, F. A., Knoll, A. H., and Johnston, D. T., 2015. Statistical analysis of iron geochemical data suggests limited late Proterozoic oxygenation. Nature 523(7561), 451-454.

Stanley, S. M., 2009. Evidence from ammonoids and conodonts for multiple Early Triassic mass extinctions. Proceedings of the National Academy of Sciences of U.S.A. 106(36), 15264-15267.

Stebbins, A., Algeo, T.J., Olsen, C., Sano, H., Orchard, M., Rowe, H.D., and Hannigan, R., 2018. Sulfur isotope variation across the Smithian-Spathian boundary in the Panthalassic Ocean (Jesmond, Cache Creek Terrane, western Canada). Earth-Science Reviews, in revision.

Stearn, C. W., 1987. Effect of the Frasnian-Famennian extinction event on the stromatoporoids. Geology 15(7), 677.

Stirling, C. H., Andersen, M. B., Potter, E.-K., and Halliday, A. N., 2007. Low-temperature isotopic fractionation of uranium. Earth and Planetary Science Letters 264(1-2), 208-225.

Stirling, C. H., Andersen, M. B., Warthmann, R., and Halliday, A. N., 2015. Isotope fractionation of 238U and 235U during biologically-mediated uranium reduction. Geochimica et Cosmochimica Acta 163, 200-218.

Stouffer, R.J., Yin, J., Gregory, J.M., Dixon, K.W., Spelman, M.J., Hurlin, W., Weaver, A.J., Eby, M., Flato, G.M., Hasumi, H., Hu, A., Jungclaus, J.H., Kamenkovich, I.V., Levermann, A., Montoya, M., Murakami, S., Nawrath, S., Oka, A., Peltier, W.R., Robitaille, D.Y., Sokolov, A., Vettoretti, G., Weber, S.L., 2006. Investigating the causes of the response of the thermohaline circulation to past and future climate changes. Journal of Climate 19, 1365-1387.

Stüeken, E.E., Foriel, J., Buick, R., Schoepfer, S.D., 2015. Selenium isotope ratios, redox changes and biological productivity across the end-Permian mass extinction. Chemical Geology 410, 28-39.

Stylo, M., Neubert, N., Wang, Y., Monga, N., Romaniello, S. J., Weyer, S., and Bernier-Latmani, R., 2015. Uranium isotopes fingerprint biotic reduction. Proceedings of the National Academy of Sciences of U.S.A 112(18), 5619-5624.

Sun, Y., Joachimski, M. M., Wignall, P. B., Yan, C., Chen, Y., Jiang, H., Wang, L., and Lai, X., 2012. Lethally hot temperatures during the Early Triassic greenhouse. Science 338(6105), 366-370.

Sun, Y. D., Wignall, P. B., Joachimski, M. M., Bond, D. P. G., Grasby, S. E., Sun, S., Yan, C. B., Wang, L. N., Chen, Y. L., and Lai, X. L., 2015. High amplitude redox changes in the late Early Triassic of South China and the Smithian–Spathian extinction. Palaeogeography, Palaeoclimatology, Palaeoecology 427, 62-78.

Takahashi, S., Yamasaki, S.-i., Ogawa, Y., Kimura, K., Kaiho, K., Yoshida, T., Tsuchiya, N., 2014. Bioessential element-depleted ocean following the euxinic maximum of the end-Permian mass extinction. Earth and Planetary Science Letters 393, 94-104.

Tang, M., Chen, K., Rudnick, R.L., 2016. Archean upper crust transition from mafic to felsic marks the onset of plate tectonics. Science 351(6271), 372-375.

Tissot, F. L. H., and Dauphas, N., 2015. Uranium isotopic compositions of the crust and ocean: Age corrections, U budget and global extent of modern anoxia. Geochimica et Cosmochimica Acta 167, 113-143.

Thomazo, C., Vennin, E., Brayard, A., Bour, I., Mathieu, O., Elmeknassi, S., Olivier, N., Escarguel, G., Bylund, K.G., Jenks, J., Stephen, D.A., Fara, E., 2016. A diagenetic control on the Early Triassic Smithian-Spathian carbon isotopic excursions recorded in the marine settings of the Thaynes Group (Utah, USA). Geobiology 14(3), 220-236.

Tong, J., Zuo, J., and Chen, Z. Q., 2007. Early Triassic carbon isotope excursions from South China: proxies for devastation and restoration of marine ecosystems following the end-Permian mass extinction. Geological Journal 42(3-4), 371-389.

Tostevin, R., Wood, R. A., Shields, G. A., Poulton, S. W., Guilbaud, R., Bowyer, F., Penny, A. M., He, T., Curtis, A., Hoffmann, K. H., and Clarkson, M. O., 2016. Low-oxygen waters limited habitable space for early animals. Nature Communication 7, 12818.

Tribovillard, N., Averbuch, O., Devleeschouwer, X., Racki, G., and Riboulleau, A., 2004. Deep-water anoxia over the Frasnian-Famennian boundary (La Serre, France): a tectonically induced oceanic anoxic event? Terra Nova 16(5), 288-295.

Tütken, T., Eisenhauer, A., Wiegand, B., and Hansen, B. T., 2002. Glacial–interglacial cycles in Sr and Nd isotopic composition of Arctic marine sediments triggered by the Svalbard/Barents Sea ice sheet. Marine Geology 182 (3-4), 351-372.

Twining, B.S., Baines, S.B., 2013. The trace metal composition of marine phytoplankton. Annual Review of Marine Science 5,191-215.

Tyrrell, T., 1999. The relative influences of nitrogen and phosphorus on oceanic primary production. Nature 400(6744), 525-531.

Vahrenkamp, V.C., Swart, P.K., 1990. New distribution coefficient for the incorporation of strontium into dolomite and its implications for the formation of ancient dolomites. Geology 18 (5), 387-391.

Van Cappellen, P., and Ingall, E. D., 1994. Benthic phosphorus regeneration, net primary production, and ocean anoxia: A model of the coupled marine biogeochemical cycles of carbon and phosphorus. Paleoceanography 9(5), 677-692.

van de Schootbrugge, B., Bachan, A., Suan, G., Richoz, S., Payne, J. L., and Jagt, J., 2013. Microbes, mud and methane: cause and consequence of recurrent Early Jurassic anoxia following the end-Triassic mass extinction. Palaeontology 56(4), 685-709.

van de Schootbrugge, B., Payne, J. L., Tomasovych, A., Pross, J., Fiebig, J., Benbrahim, M., Föllmi, K. B., and Quan, T. M., 2008. Carbon cycle perturbation and stabilization in the wake of the Triassic-Jurassic boundary mass-extinction event. Geochemistry, Geophysics, Geosystems 9, Q04028.

Vaquer-Sunyer, R., and Duarte, C. M., 2008. Thresholds of hypoxia for marine biodiversity. Proceedings of the National Academy of Sciences of U.S.A. 105(40), 15452-15457.

Verdel, C., Wernicke, B. P., and Bowring, S. A., 2011. The Shuram and subsequent Ediacaran carbon isotope excursions from southwest Laurentia, and implications for environmental stability during the metazoan radiation. Geological Society of America Bulletin 123(7-8), 1539-1559.

Veizer, J., 1983. Chemical diagenesis of carbonates: theory and application of trace element technique. In: Arthur, M.A., Anderson, T.F., Kaplan, I.R., Veizer, J., Land, L.S. ŽEds., Stable Isotopes in Sedimentary Geology, Vol. 10, Society of Economic Paleontologists and Mineralogists Short Course Notes, pp. III-1–III-100.

Voegelin, A. R., Nägler, T. F., Samankassou, E., and Villa, I. M., 2009. Molybdenum isotopic composition of modern and Carboniferous carbonates. Chemical Geology 265(3-4), 488-498.

Wallace, M.W., Hood, A.v., Shuster, A., Greig, A., Planavsky, N.J., Reed, C.P., 2017. Oxygenation history of the Neoproterozoic to early Phanerozoic and the rise of land plants. Earth and Planetary Science Letters 466, 12-19.

Wang, X., Johnson, T. M., and Lundstrom, C. C., 2015. Isotope fractionation during oxidation of tetravalent uranium by dissolved oxygen. Geochimica et Cosmochimica Acta 150, 160-170.

Wang, X., Planavsky, N. J., Reinhard, C. T., Hein, J. R., and Johnson, T. M., 2016. A Cenozoic seawater redox record derived from $^{238}U/^{235}U$ in ferromanganese crusts. American Journal of Science 316(1), 64-83.

Wei, H., Shen, J., Schoepfer, S. D., Krystyn, L., Richoz, S., and Algeo, T. J., 2015. Environmental controls on marine ecosystem recovery following mass extinctions, with an example from the Early Triassic. Earth-Science Reviews 149, 108-135.

Wen, H., Carignan, J., Zhang, Y., Fan, H., Cloquet, C., and Liu, S., 2011. Molybdenum isotopic records across the Precambrian-Cambrian boundary. Geology 39(8), 775-778.

Weyer, S., Anbar, A. D., Gerdes, A., Gordon, G. W., Algeo, T. J., and Boyle, E. A., 2008. Natural fractionation of 238U/235U. Geochimica et Cosmochimica Acta 72(2), 345-359.

Whitney, F.A., Crawford, W.R., Harrison, P.J., 2005. Physical processes that enhance nutrient transport and primary productivity in the coastal and open ocean of the subarctic NE Pacific. Deep Sea Research Part II: Topical Studies in Oceanography 52, 681-706.

Wignall, P. B., 2007. The End-Permian mass extinction – how bad did it get? Geobiology 5(4), 303-309.

Wignall, P. B., and Newton, R. J., 2003. Contrasting deep-water records from the upper Permian and lower Triassic of south Tibet and British Columbia: Evidence for a diachronous mass extinction. Palaios 18, 153–167.

Wignall, P. B., and Twitchett, R. J., 1996. Oceanic anoxia and the end Permian mass extinction. Science 272(5265), 1155-1158.

Winguth, C., and Winguth, A. M. E., 2012. Simulating Permian-Triassic oceanic anoxia distribution: Implications for species extinction and recovery. Geology 40(2), 127-130.

Wood, R. A., Poulton, S. W., Prave, A. R., Hoffmann, K. H., Clarkson, M. O., Guilbaud, R., Lyne, J. W., Tostevin, R., Bowyer, F., Penny, A. M., Curtis, A., and Kasemann, S. A., 2015. Dynamic redox conditions control late Ediacaran metazoan ecosystems in the Nama Group, Namibia. Precambrian Research 261, 252-271.

Xiang, L., Schoepfer, S. D., Shen, S.-z., Cao, C.-q., and Zhang, H., 2017. Evolution of oceanic molybdenum and uranium reservoir size around the Ediacaran–Cambrian

transition: Evidence from western Zhejiang, South China. Earth and Planetary Science Letters 464, 84-94.

Xiao, S., and Laflamme, M., 2009. On the eve of animal radiation: phylogeny, ecology and evolution of the Ediacara biota. Trends in Ecology & Evolution 24(1), 31-40.

Xiao, S., Narbonne, G. M., Zhou, C., Laflamme, M., Grazhdankin, D. V., Moczydlowska-Vidal, M., and Cui, H., 2016. Towards an Ediacaran time scale: problems, protocols, and prospects. Episodes 39(4), 540-555.

Xie, S., Pancost, R. D., Wang, Y., Yang, H., Wignall, P. B., Luo, G., Jia, C., and Chen, L., 2010. Cyanobacterial blooms tied to volcanism during the 5 m.y. Permo-Triassic biotic crisis. Geology 38(5), 447-450.

Yan, D., Chen, D., Wang, Q., and Wang, J., 2012. Predominance of stratified anoxic Yangtze Sea interrupted by short-term oxygenation during the Ordo-Silurian transition. Chemical Geology 291, 69-78.

Yang, S., Kendall, B., Lu, X., Zhang, F., and Zheng, W., 2017. Uranium Isotope Compositions of Mid-Proterozoic Black Shales: Evidence for an Episode of Increased Ocean Oxygenation at 1.36 Ga and Evaluation of the Effect of Post-Depositional Hydrothermal Fluid Flow. Precambrian Research 298, 187–201.

Yudina, A. B., Racki, G., Savage, N. M., Racka, M., and Małkowski, K., 2002. The Frasnian–Famennian events in a deep−shelf succession, Subpolar Urals: biotic, depositional and geochemical records. Acta Palaeontologica Polonica 47(2), 355–372.

Zhang, F., Algeo, T. J., Romaniello, S., Cui, Y., Zhao, L., Chen, Z. Q., and Anbar, A. D., 2018a. Congruent Permian-Triassic δ238U records at Panthalassic and Tethyan sites: Confirmation of global oceanic anoxia and validation of the U-isotope paleoredox proxy. Geology 46(4), 327-330.

Zhang, F., Romaniello, S. J., Algeo, T. J., Lau, K. V., Clapham, M. E., Richoz, S., Herrmann, A. D., Smith, H., Horacek, M., and Anbar, A. D., 2018b. Multiple episodes of extensive oceanic anoxia linked to global warming and continental weathering following the latest Permian mass extinction. Science Advances 4(4), e1602921.

Zhang, F., Xiao, S., Kendall, B., Romaniello, S., Cui, H., Meyer, M., Gilleaudeau, G., Kaufman, A. J., and Anbar, A. D., 2018c. Extensive marine anoxia during the terminal Ediacaran Period. Science Advances 4, eaan8983.

Zhang, G., Zhang, X., Hu, D., Li, D., Algeo, T. J., Farquhar, J., Henderson, C. M., Qin, L., Shen, M., Shen, D., Schoepfer, S. D., Chen, K., and Shen, Y., 2017. Redox chemistry changes in the Panthalassic Ocean linked to the end-Permian mass extinction and delayed Early Triassic biotic recovery: Proceedings of the National Academy of Sciences of U.S.A. 114(8), 1806-1810.

Zhang, L., Zhao, L., Chen, Z. Q., Algeo, T. J., Li, Y., and Cao, L., 2015. Amelioration of marine environments at the Smithian–Spathian boundary, Early Triassic. Biogeosciences 12(5), 1597-1613.

Zhang, L., Orchard, M. J., Algeo, T. J., Chen, Z.-Q., Lyu, Z., Zhao, L., Kaiho, K., Ma, B., and Liu, S., 2017. An intercalibrated Triassic conodont succession and carbonate carbon isotope profile, Kamura, Japan. Palaeogeography, Palaeoclimatology, Palaeoecology, in press.

Zhang, L., Orchard, M.J., Brayard, A., Algeo, T.J., Zhao, L., Chen, Z.Q., 2018a. The Smithian-Spathian boundary (late Early Triassic): a review and proposed definition. Earth Science Reviews, under review.

Zhang, L., Orchard, M.J., Algeo, T.J., Zhao, L.S., Chen, Z.Q., Wang, H.X., and Liu, S.J., 2018b. Uppermost Permian to Upper Triassic conodont zonation and carbonate carbon isotopes from Kamura section, southwestern Japan. Palaeogeography Palaeoclimatology Palaeoecology, in press.

Zhang, L., Zhao, L.S., Algeo, T.J., Chen, Z.Q., Li, C., Ma, B., and Ye, F.H., 2018c. Global-ocean circulation changes during the Smithian–Spathian transition inferred from carbon-sulfur cycle records. Earth Science Reviews, under review.

Zhang, T., Shen, Y., Zhan, R., Shen, S., and Chen, X., 2009. Large perturbations of the carbon and sulfur cycle associated with the Late Ordovician mass extinction in South China. Geology, 37(4), 299-302.

Zhou, X., Thomas, E., Rickaby, R.E., Winguth, A.M., Lu, Z., 2014. I/Ca evidence for upper ocean deoxygenation during the PETM. Paleoceanography 29, 964-975.

Zhou, X., Jenkyns, H.C., Owens, J.D., Junium, C.K., Zheng, X.Y., Sageman, B.B., Hardisty, D.S., Lyons, T.W., Ridgwell, A., Lu, Z., 2015. Upper ocean oxygenation dynamics from I/Ca ratios during the Cenomanian–Turonian OAE 2. Paleoceanography 30 (5), 510-526

APPENDIX A

SUPPLEMENTARY INFORMATION FOR CONGRUENT PERMIAN-TRIASSIC $\delta^{238}U$ RECORDS AT PANTHALASSIC AND TETHYAN SITES: CONFIRMATION OF GLOBAL-OCEAN ANOXIA AND VALIDATION OF THE U-ISOTOPE PALEOREDOX PROXY

A. 1 Geological background of the Kamura section

The Kamura section (32.7552 °N, 131.3386 °E) is located close to Shioinouso village, 5.6 km northeast of Takachiho-cho in Miyazaki Prefecture, in the center of Kyushu Island, Japan (Isozaki et al., 2007; Zhang et al., 2017). The Kamura section is located within the Chichibu Belt, which is a Jurassic accretionary complex belt in southwestern Japan and comprises a structurally complicated aggregate of metamorphosed Upper Paleozoic and Mesozoic sedimentary rocks (Isozaki, 2009; Musashi et al., 2001; Sano and Nakashima, 1997). Although now located in central Japan, the sedimentary succession at Kamura originally accumulated in the middle of the Panthalassic Ocean at peri-equatorial latitudes, as indicated by a paleomagnetic study (Ando et al., 2001).

The study section is lithologically divided into two units (Sano and Nakashima, 1997; Zhang et al., 2017): the Mitai Formation and the Kamura Formation. The Mitai Formation is Late Permian in age, and is primarily composed of white to light gray limestone and dolomitic limestone. The Mitai Formation records a shallowing-upward succession from subtidal to intertidal facies (Sano and Nakashima, 1997). The Kamura Formation is latest Permian to Late Triassic in age, and is mainly composed of micritic,

microbial, and bioclastic limestones. The lack of terrigenous clastics, such as coarse quartzo-feldspathic grains, in the two formations suggests that their origin was in a mid-oceanic setting far from continental areas (Isozaki et al., 2007; Musashi et al., 2001).

Previous biostratigraphic studies using fusulinids, corals, bivalves, ammonoids, and conodonts (Kambe, 1963; Kanmera and Nakazawa, 1973; Koike, 1979; Watanabe et al., 1979; Kanmera and Nishi, 1983; Ota and Isozaki, 2000) indicate that the Kamura section spans the mid-Permian to Late Triassic. Koike (1996) first confirmed that the Kamura section contains the Griesbachian (the earliest Triassic) interval by recognizing the conodonts *Hindeodus parvus* and *Isarcicella isarcica* in the lowermost Kamura Formation. The conodont biostratigraphy at Kamura has recently been updated by Zhang et al. (2017). The fusulinid taxa at Kamura are mostly of Tethyan affinity, and the ubiquitous occurrence of calcareous algae in the Mitai Formation suggests a shallow, warm tropical depositional environment (Isozaki et al., 2007).

The end-Permian mass extinction (EPME) horizon at Kamura has been placed at the Mitai-Kamura formation boundary by Koike (1996) and Zhang et al. (2017), which is at ~−0.15 m in our section. The Permian-Triassic boundary (PTB) at Kamura has been placed in the lowermost Kamura Formation based on the first appearance of the conodont *Hindeodus parvus* (Koike, 1996; Zhang et al., 2017), which is at 0.20 m in our section. The biostratigraphically well-constrained EPME and PTB horizons as well as the high-resolution carbon isotope chemostratigraphic profile for the Kamura section (Horacek et al., 2009; Isozaki et al., 2007; Zhang et al., 2017) make it possible to precisely correlate it to other well-studied PTB sections globally. The samples used in this study are from the

same sample suite that was analyzed for carbon and oxygen isotopes as well as for conodonts by Zhang et al. (2017).

A. 2 Analytical methods for U isotopes

Fresh carbonate samples collected in the field were crushed to small pieces in the lab. The fragments were cleaned using deionized water (DI water) and dried, and fresh fragments without veins were carefully chosen and powdered to ~200 mesh using a ball mill and silicon nitride jars.

The protocols for powder dissolution are summarized in Table A.1. In the first six steps, ~1.0–1.5 g of each sample was dissolved in 1 M hydrochloric acid (HCl) at room temperature. This protocol employed a 1.5× excess of HCl in order to ensure complete dissolution of the carbonate, thus avoiding U isotope fractionation from selective leaching of various carbonate phases. The solution was allowed to sit at room temperature for 24 h before centrifuging to separate the supernatant and undissolved residue. We compared carbonate dissolution protocols using 1M HCl, 1M Acetic Acid, and 3M HNO_3, and found that all these methods yield indistinguishable $\delta^{238}U$ provided that excess acid is available to ensure complete carbonate dissolution (Table A.2.).

Digests were centrifuged and the supernatant was separated. Major, minor, and trace element concentrations were measured on a Thermo iCAP™ quadrupole inductively coupled plasma mass spectrometer (Q-ICP-MS) at the W. M. Keck Laboratory for Environmental Biogeochemistry at Arizona State University (ASU) on splits from each supernatant. Typical precision was better than 5% based on repeated analysis of in-run check standards.

Prior to column chemistry, appropriate amounts of the ^{236}U:^{233}U double spike were added to each sample based on measured uranium concentrations. The spike-sample mixtures were evaporated to dryness and re-dissolved in 3 N HNO_3. Uranium was purified for isotopic analysis using the UTEVA method (Brennecka et al., 2011; Romaniello et al., 2013; Weyer et al., 2008). Purified U was dissolved in 0.32 M HNO_3 and diluted to a U concentration of 50 ppb. Uranium isotopes were measured at ASU on a Themo-Finnigan Neptune multi-collector ICP-MS at low mass resolution. When using a 75 µl/min nebulizer, a 50 ppb sample solution yielded 24−32 V of ^{238}U signal on a 10^{11} Ω amplifier. The unprocessed standard solution CRM145 (50 ppb U) was analyzed after every two samples. A secondary standard CRM129a and an in-house Ricca ICP solution were measured after every fifteen analyses. Sample $\delta^{238}U$ values were normalized by the average of the bracketing standards.

The U isotopic composition of standards CRM145, CRM129a, and Ricca was −0.00±0.07 ‰ (2σ), −1.68±0.07 ‰ (2σ), and −0.23±0.06 ‰ (2σ), respectively. The results are given in the Table A.6.

A. 3 Evaluation of carbonate diagenesis, detrital contamination and dolomitization

Marine carbonate sediments can faithfully record chemical signatures of seawater provided that post-depositional processes have not caused significant alteration. To assess diagenesis, we used standard geochemical criteria based on trace element ratios to evaluate the influence of meteoric or burial fluids on measured U isotope signatures. The concentrations of trace elements (Sr, Mn, and Fe) that substitute into the lattice of carbonate minerals is governed by their distribution coefficients and their concentrations in the fluids

Table A.1. Sample dissolution procedure

Dissolution step	Solvent	Time gap between steps
S1–S6	5mL 1M hydrochloric acid	10 minutes
S7	1mL 10M hydrochloric acid	
S9–S11	5mL 1M hydrochloric acid	10 minutes
Final volume	46 mL	

S denotes step, for instance, S1–S6 denotes steps 1 to 6.

Table A.2. A summary of results from different carbonate dissolution protocols

Sample	digestion methods	$\delta^{238}U$ (‰)
DW330-345-1	1M acetic acid	-0.49 ± 0.03
DW330-345-2	1M hydrochloric acid	-0.50 ± 0.04
DW330-345-3	ash at 750°C then dissolve in 3M nitric acid	-0.48 ± 0.02
DW435+450-1	1M acetic acid	-0.73 ± 0.03
DW435+450-2	1M hydrochloric acid	-0.75 ± 0.05
DW435+450-3	ash at 750°C then dissolve in 3M nitric acid	-0.75 ± 0.06
DXK-11 base-1	1M acetic acid	-0.81 ± 0.08
DXK-11 base-2	1M hydrochloric acid	-0.84 ± 0.03
DXK-11 base-3	ash at 750°C then dissolve in 3M nitric acid	-0.74 ± 0.06
DXK-2-1	1M acetic acid	0.33 ± 0.05
DXK-2-2	1M hydrochloric acid	0.37 ± 0.02
DXK-2-3	ash at 750°C then dissolve in 3M nitric acid	0.35 ± 0.07
DXK-32-1	1M acetic acid	-0.28 ± 0.07
DXK-32-2	1M hydrochloric acid	-0.27 ± 0.04
DXK-32-3	ash at 750°C then dissolve in 3M nitric acid	--

Note: -- denotes data not available. DW330-345, DW435+450, DXK-11, DXK-2, and DXK-32 are samples numbers, these samples are of Permian-Triassic age.

from which carbonates precipitate. Modern, well-oxygenated seawater is high in Sr relative to Mn and Fe such that primary precipitates and early diagenetic phases formed in in the presence of seawater are generally enriched in Sr relative to Mn and Fe (Banner and Hanson, 1990). This is particularly true for aragonite because of the high distribution coefficient for Sr into aragonite compared to other carbonate minerals (Veizer, 1983). Early fabric-retentive dolostone can also be enriched in Sr relative to Mn and Fe, although dolomite generally has a lower preference for Sr (Vahrenkamp and Swart, 1990) and a higher preference for Mn and Fe (Mazzullo, 1992) compared to calcite.

In contrast, meteoric and burial fluids tend to be depleted in Sr relative to seawater (Banner and Hanson, 1990). The recrystallization process also acts to expel Sr from the lattice of carbonate minerals because of its relatively large ionic radius compared to Ca in calcite and dolomite, which are the most important secondary phases (Rimstidt et al., 1998). As a result, meteoric or burial diagenetic phases are often depleted in Sr relative to precursor marine phases. Burial fluids can also be substantially enriched in Mn and Fe, particularly under reducing conditions (Veizer, 1983), leading to Mn and Fe enrichment in burial diagenetic phases. Meteoric fluids are variable in their Mn and Fe content—depending largely on redox conditions—such that meteoric calcite phases can be characterized by enrichment or depletion of Mn and Fe.

These general relationships have led to the establishment of widely used proxies such as the Mn/Sr ratio to assess the fidelity of primary geochemical signatures in carbonate rocks. For example, Kaufman and Knoll (Kaufman and Knoll, 1995) suggested that both limestone and dolostone with Mn/Sr ratios < 10 can be expected to retain their primary carbon isotopic signatures. In this study, we used a more conservative Mn/Sr ratio of 1 for identifying unaltered primary marine carbonates (also used by Lau et al., (2016). In the Kamura section, all samples have Sr concentrations of >150 ppm with 9 out of 17 samples having Sr concentrations of >500 ppm (Figure A.1.). Most samples have low Mn contents (<102 ppm for 12 out of 17 samples) and low Mn/Sr ratios (15 out of 17 samples have Mn/Sr ratios of <0.6, and the remaining two samples have ratios of 2.1 and 6.8; Figure A.1.). These results indicate that the Kamura samples are generally well preserved and likely to retain primary marine geochemical signatures.

The Ce anomalies in our samples range between 0.27 and 0.54 with exception of only one sample gives a Ce anomaly of 0.74 (Figure A.1., Ce anomalies are calculated according to Ling et al. (2013)). These values suggest the local depositional condition at Kamura was persistently oxic (Ling et al., 2013). The lack statistically significant correlations between $\delta^{238}U$ and Ce anomalies (Table A.3.) further indicate that the $\delta^{238}U$ trend at Kamura is not related to local redox variations.

When evaluating detrital contamination, we used detrital indicators such as Rb/Sr ratios and Al concentrations (cf. Ling et al., 2013). Among samples with Mn/Sr < 1, only those samples with Rb/Sr < 0.02 and Al (wt.%) < 0.35% (all samples met this criterion) were used in our analysis of secular redox patterns. Finally, for samples meeting the Mn/Sr < 1, Rb/Sr < 0.02 and Al < 0.35% thresholds, we examined their U/Al ratios to determine the degree of authigenic U enrichment. Relative to the U/Al ratio of average upper continental crust (~0.331 ppm/wt.%; Rudnick and Gao, 2003), all samples are enriched in U by approximately two orders of magnitude (Figure A.1.). This demonstrates that the majority of U in our samples is authigenic rather than detrital in origin.

Romaniello et al. (2013) observed U-isotope changes associated with dolomitization in a modern Bahamian tidal pond, as reflected in a strong correlation of $\delta^{238}U$ with Mg/Ca (R^2 = 0.96), suggesting possible U-isotope fractionation linked to dolomitization. The reason for this strong correlation remain unclear. This seems to be a special, spatially restricted case, however. In the Kamura samples, $\delta^{238}U$ and Mg/Ca show only a moderate correlation (R^2 = 0.41), and positive sign of this relationship is opposite that of the Bahamian carbonates. This indicates that the dolomitization process probably

does not have a systematic effect on carbonate U-isotope compositions, although this issue requires further investigation.

A recent texture-specific $\delta^{238}U$ study reported high variability in $\delta^{238}U$ values between different carbonate components (Hood et al., 2016). To better understand the range and variability of $\delta^{238}U$ in bulk carbonate sediments, we have conducted a 16-step leaching experiment using acetic acid with different molarities to sequentially extract different carbonate components in carbonate sediments (Table A.5. and Figure A.2.; see discussions below). In agreement with Hood et al. (2016), our leaching results show large variability in $\delta^{238}U$ values (up to 0.5 ‰) among different leaching steps, indicating that $\delta^{238}U$ are highly inhomogeneous between different carbonate components. However, contrary to Hood et al. (2016) who argue that U isotopes in bulk carbonates are seriously reset by diagenesis, our study strongly suggests that the bulk U isotopes are not typically isotopically reset and that U isotopes in bulk carbonates are reliable recorders. Even though $\delta^{238}U$ values vary between different carbonate components, the weighted sums of $\delta^{238}U$ of all leaching steps are indistinguishable to $\delta^{238}U$ of the bulk analysis (Table A.5.). The possible reason for this is that typically U isotopes are locally redistributed and fractionated during recrystallization and this results in different isotopic compositions between different generations of carbonate phases. However, since this process may happen in a closed system, the bulk U isotopic composition of the carbonates remains the same.

A. 4 Detailed comparison of Permian-Triassic $\delta^{238}U$ records at Panthalassic and Tethyan sites

Here, we compare our new $\delta^{238}U$ record from Kamura (Japan) with published $\delta^{238}U$ records for three other PTB sections: the Dawen (China) section studied by Brennecka et al. (2011), and the Dajiang (China) and Taşkent (Turkey) sections studied by Lau et al. (2016) (Figure 2.2 of main text). These sections were widely distributed paleogeographically, as shown in Figure A.3. All four sections have been correlated in detail to the well-dated Meishan section using a combination of conodont biostratigraphy and $\delta^{13}C$ chemostratigraphy. According to Burgess et al. (2014), the ages of the EPME and PTB horizons are 251.941 ± 0.037 Ma and 251.902 ± 0.024 Ma, respectively. The EPME is recognized as the transition from the *Clarkina yini* Zone to the *Clarkina meishanensis* Zone, and the PTB is defined by the first appearance datum of *Hindeodus parvus*. According to Burgess et al. (2014), an extrapolated age of 251.323 Ma has been assigned to the first positive shift of the $\delta^{13}C$ in the Lower Triassic $\delta^{13}C$ records. With these ages, sedimentation rates can be calculated for two intervals at each section: (1) between the EPME and PTB, and (2) between the PTB and the first positive shift in $\delta^{13}C$. Based on these sedimentation rate data, we calculated the age for each individual sample in each section. Using this method, the $\delta^{13}C$ excursions in all four sections are well-aligned (Figure 2.2 A in main text).

We are aware that there is another $\delta^{238}U$ study from a South China section by Elrick et al. (2017), who also documented an abrupt negative $\delta^{238}U$ shift of 0.4–0.5 ‰ across the EPME. However, their primary focus was on the Middle to Upper Permian, and they

analyzed only a few samples through the PTB interval. Thus, this study has been excluded from the present compilation which focuses on high-resolution records across the EPME.

The compiled $\delta^{238}U$ records show 0.2–0.4 ‰ (with a mean of 0.3 ‰) scatter around the EPME (Figure 2.2 B), the source of which is not fully understood yet. It may reflect differential incorporation of ^{238}U-enriched U(IV) from anoxic porewaters during early diagenesis, similar to the Bahamian carbonate sediments (Romaniello et al., 2013) or variation in pore water aqueous U-speciation during syndepositional carbonate recrystallization (Chen et al., 2016). Porewater data from deep drill cores in the Bahamas suggest that the potential for alteration following burial may be limited because the pore waters are anoxic rendering U essentially immobile (Henderson et al., 1999). Our interpretation is that following syndepositional diagenesis which imparts a +0.3±0.1 ‰ offset in $\delta^{238}U$, later burial diagenesis has no measurable effect on the bulk sediment U-isotope compositions because the sediments are essentially closed to U exchange. On this basis, we have applied a +0.3±0.1 ‰ correction to measured PTB bulk carbonate $\delta^{238}U$ values prior to mass balance calculations (presented below).

The available compilation of PTB $\delta^{238}U$ records strongly supports the inference that all observed $\delta^{238}U$ variations are primary and represent secular changes in Permian-Triassic seawater $\delta^{238}U$. This inference is based on the observation that multiple PTB sections have recorded the same $\delta^{238}U$ signal despite their manifest differences. First, these sections are located in different ocean basins and thus unlikely to have similar diagenetic histories. Second, as discussed above, the Mn and Sr concentrations, $\delta^{18}O$ values, and Mn/Sr ratios are commonly used to evaluate the extent of carbonate diagenesis. Although this study and all prior studies have applied conservative cutoffs of these diagenetic proxies to screen for

potential alterations, the combined sections exhibit different Mn and Sr concentrations, $\delta^{18}O$ values, and Mn/Sr ratios, as well as different patterns of correlation of $\delta^{238}U$ with these proxies, thus indicating that these sections experienced different diagenetic histories (Table A.3., Figure A.5. and Figure A.6.). Third, the U/Al ratios is carbonates are typically used to evaluate levels of authigenic U enrichment, these sections yield different U concentrations and U/Al ratios, indicating that levels of authigenic U factors vary between the sections (Table A.3., Figure A.5. and Figure A.6.). Fourth, the Mg/Ca molar ratios can be used to indicate the extent of dolomitization, these sections have different Mg/Ca molar ratios and different patterns of $\delta^{238}U$-Mg/Ca covariation, indicating variations in degree of dolomitization between the sections (Table A.3., Figure A.5. and Figure A.6.). Despites all these differences, after screening for potential diagenetic influences using well-established carbonate diagenetic indictors (e.g., Mn and Sr contents, Mn/Sr ratios, and $\delta^{18}O$), all of the studied PTB sections record the same $\delta^{238}U$ trend through the PTB interval.

A. 5 The lumped oxic sinks and other sinks and their associated fractionation factors

A simplified schematic of the major sources and sinks of U in the modern ocean along with the isotopic compositions of sources and isotopic fractionations associated with sinks is presented in Figure 1.2. Following Wang et al. (2016), in order to simplify the mass balance calculations presented below, several types of sinks are lumped into a single oxic sink, including Fe-Mn crusts, pelagic clays, low-temperature and high-temperature oceanic crustal alteration, marine carbonates, and coastal retention. Additionally, the oxic sink and suboxic sink are lumped into a single sink ("other") in order to simplify calculations of anoxic/euxinic sink fluxes. The overall U isotope fractionation factors for lumped sinks are

calculated as the weighted average of fractionations associated with their constituent sinks. The fractionation factors between the lumped oxic sink and seawater and between the lumped other sink and seawater are 0.005‰ (Δ_{oxic}) and 0.043‰ (Δ_{other}).

Table A.3. Cross-correlation coefficients (R^2) and p-values calculated to test the influence of diagenetic indicators on $\delta^{238}U$. "--" denotes related data are not available the original publication.

Kamura section, Japan	R^2	*p*-value
$\delta^{238}U$ vs. $\delta^{13}C$	0.50	<0.01
$\delta^{238}U$ vs. Mg/Ca (mol:mol)	0.38	<0.01
$\delta^{238}U$ vs. $\delta^{18}O$	0.02	0.60
$\delta^{238}U$ vs. Sr concentration	0.70	<0.01
$\delta^{238}U$ vs. Mn concentration	0.16	0.12
$\delta^{238}U$ vs. Mn/Sr	0.27	0.03
$\delta^{238}U$ vs. U/Al (ppm/w.t.%)	0.60	<0.01
$\delta^{238}U$ vs. Ce anomalies	0.27	0.29

Dawen section, South China	R^2	*p*-value
$\delta^{238}U$ vs. $\delta^{13}C$	0.18	<0.01
$\delta^{238}U$ vs. Mg/Ca (mol:mol)	--	--
$\delta^{238}U$ vs. $\delta^{18}O$	--	--
$\delta^{238}U$ vs. Mn/Sr	--	--
$\delta^{238}U$ vs. U/Al (ppm/w.t.%)	0.24	<0.01

Dajiang, China	R^2	*p*-value
$\delta^{238}U$ vs. $\delta^{13}C$	0.38	0.02
$\delta^{238}U$ vs. Mg/Ca (mol:mol)	0.00	0.93
$\delta^{238}U$ vs. $\delta^{18}O$	0.00	0.94
$\delta^{238}U$ vs. Mn/Sr	0.01	0.78
$\delta^{238}U$ vs. U/Al (ppm/w.t.%)	0.37	0.03

Taşkent, Turkey	R^2	*p*-value
$\delta^{238}U$ vs. $\delta^{13}C$	0.62	<0.01
$\delta^{238}U$ vs. Mg/Ca (mol:mol)	0.00	0.96
$\delta^{238}U$ vs. $\delta^{18}O$	0.28	0.03
$\delta^{238}U$ vs. Mn/Sr	0.015	0.14
$\delta^{238}U$ vs. U/Al (ppm/w.t.%)	0.19	0.09

Note: when $p(\alpha) < 0.05$, then $\delta^{238}U$ shows a statistically significant correlation with the proxy; if $p(\alpha) > 0.05$, then $\delta^{238}U$ does not show a statistically correlation with the proxy.

A. 6 Uranium isotope mass balance constraints on U removal to anoxic/euxinic sinks

Changes in U removal to anoxic sediments, as summarized in the main text, can be quantified using a mass balance relationship based on the fractions of the anoxic/euxinic sinks and their isotopic compositions (following Montoya-Pino et al., 2010):

$$\delta^{238}U_{input} = (f_{anoxic} \times \delta^{238}U_{anoxic}) + (f_{other} \times \delta^{238}U_{other}) \quad (1)$$

$$\delta^{238}U_{anoxic} = \delta^{238}U_{seawater} + \Delta_{anoxic} \quad (2)$$

$$\delta^{238}U_{other} = \delta^{238}U_{seawater} + \Delta_{other} \quad (3)$$

$$f_{anoxic} + f_{other} = 1 \quad (4)$$

The subscripts *input*, *anoxic*, and *other* denote the riverine input, anoxic/euxinic sink, and other sedimentary sinks, respectively, and f_{anoxic} represents the fraction of the riverine U input that is deposited in anoxic/euxinic sediments. Following Montoya-Pino et al. (2010) and Brennecka et al. (2011), we assume: (1) isotopically constant U input from rivers ($\delta^{238}U_{river}$) over geologic time with an average value of −0.34 ‰ (Andersen et al., 2016; Noordmann et al., 2016); (2) a constant isotopic fractionation between seawater and the other sinks (Δ_{other}) of +0.043 ‰ (Figure 1.2); and (3) a constant isotopic fractionation between seawater and anoxic/euxinic sinks (Δ_{anoxic}) of +0.6 ‰. This last value is an average from modern anoxic environments and similar to Δ_{anoxic} values that have been used in

previous U isotope modeling investigations (Brennecka et al., 2011; Dahl et al., 2014; Dahl et al., 2017; Elrick et al., 2017; Lau et al., 2016). Solving equations 1–4, we have:

$$f_{\text{anoxic}} = (\delta^{238}U_{\text{river}} - \delta^{238}U_{\text{seawater}} - \Delta_{other}) / (\Delta_{anoxic} - \Delta_{other}) \quad (5)$$

Using the parameters above, we can solve for f_{anoxic} for each sample analyzed. The results are shown in Figure 2.2D of the main text. Prior to making these calculations, we adjusted measured $\delta^{238}U$ values by 0.1 ‰ to 0.3 ‰ to account for diagenetic offsets relative to contemporaneous seawater $\delta^{238}U$, as discussed above:

$$\delta^{238}U_{\text{seawater}} = \delta^{238}U_{\text{carbonate}} - \Delta_{diagenetic\ offset} \quad (6)$$

A. 7 Estimating the timing of onset of oceanic anoxia

We evaluated the timing of onset of oceanic anoxia based on the observed initial negative shift in $\delta^{238}U$ relative to stable Late Permian background values. To more accurately identify the timing of the initial negative shift, we applied a robust LOWESS (Locally Weighted Scatterplot Smoothing) smoothing function to smooth the compiled data in Figure 2.2B of the main text. A tapered integration window of 0.2 Myr was used in the smoothing function. The smoothed $\delta^{238}U$ curve is shown in Figure A.7. The initial negative shift in $\delta^{238}U$ occurred <70 kyr before the EPME, representing the lag between the onset of oceanic anoxia and the mass extinction event. Although this estimate is associated with some age-model uncertainties related to compiling data from multiple

sections, this analysis serves to show that the expansion of oceanic anoxia probably predated the mass extinction event, although only by a limited interval (<70 kyr).

A. 8 Sequential extraction experiments

To better understand the range and variability of $\delta^{238}U$ in bulk carbonate sediments, we conducted a leaching experiment using acetic acid with different molarities to sequentially extract carbonate components in Permian-Triassic sediments. In this experiment, we analyzed five samples, two from the Permian-Triassic Kamura section (KAMD-20 and KAMD-31) and three from the modern Bahamian carbonate platform (including one modern coral sample and two sediment core samples: core 1 40-42 cm, and core 4 24-28 cm, which were previously studied by Romaniello et al. (2013). We used a 16-step sequential extraction protocol following the methods of Liu et al. (2013), as summarized in Table A.4.

Table A.4. Extraction protocol

Leaching step	Label	Leaching agent	pH
S1-S2	1	30 mL 1 N ammonium acetate and a few drops of H_2O_2	7.5
S3-S9	2	30 mL 0.25% (v/v) acetic acid for each step	
S10-S12	3	30 mL 1% (v/v) acetic acid for each step	
S13-S14	4	30 mL 5% (v/v) acetic acid for each step	
S15-S16	5	50 mL 10% (v/v) acetic acid for each step	

Note that after each step the sample was rinsed and ultrasonicated in DI water for 10 minutes, and then centrifuged at 4000 rpm for 5 min to separate the supernatant and undissolved residue. Major, minor, and trace element concentrations were measured on a Thermo iCAP™ quadrupole inductively coupled plasma mass spectrometer (Q-ICP-MS) at the W. M. Keck Laboratory for Environmental Biogeochemistry at Arizona State University (ASU) on splits from each supernatant.

Owing to low U concentrations for some samples, we combined Steps S1 and S2 (= Label 1), Steps S3 to S9 (= Label 2), Steps S10 to S12 (= Label 3), Steps S13 and S14 (= Label 4), and Steps S14 to S16 (= Label 5) for the purpose of U isotope analysis. U

isotope analytical methods were identical to those of the main study (see methods description above), and the results are given in Table A.5.

One of the key questions that we investigated is whether the measured isotopic variations in each sample were actually generated as an artefact of isotopic fractionation during the sequential leaching experiments. The modern coral sample showed no isotopic fractionation during the sequential leaching experiments, since the results for Labels 1 to 5 are statistically indistinguishable (Figure A.2., Table A.5.). We therefore tentatively suggest that differences in $\delta^{238}U$ among leaching steps for the other samples reflect true isotopic inhomogeneities within these samples (Figure A.2.).

For the two Permian-Triassic samples and two modern Bahamian carbonate sediments, the leaching experiments yielded large differences in $\delta^{238}U$ (to ~0.5 ‰) among different fractions. We infer that different carbonate components of these samples have different $\delta^{238}U$ compositions, and that partial carbonate leaching leads to expression of these isotopic differences. Our leaching results thus agree with Hood et al. (2016) that $\delta^{238}U$ varies among different carbonate fractions. However, the weighted sums of $\delta^{238}U$ of all leaching steps are indistinguishable to those of the bulk analysis (Table A.5.), indicating that the bulk U isotopes are not typically isotopically reset.

Table A.5. A summary of leaching results

Label	Leaching agents	Sample number	$\delta^{238}U$ (‰)	Amount of U (ng)	percent of U
bulk analysis	1 M hydrochloric acid	Modern coral	–0.40	2553.00	
1	ammonium acetate	Coral-1	–0.39	16.52	1
2	0.25% acetic acid	Coral-2	–0.43	322.45	13
3	1% acetic acid	Coral-3	–0.41	1293.06	51
4	5% acetic acid	Coral-4	–0.41	766.91	30
5	10% acetic acid	Coral-5	–0.40	161.53	6
weighted sums			**–0.41**		
bulk analysis	1 M hydrochloric acid	Core 1 40-42cm	0.14	5435.66	
1	ammonium acetate	C1-1	0.40	655.22	13
2	0.25% acetic acid	C1-2	0.34	1416.65	29
3	1% acetic acid	C1-3	0.07	1343.63	27
4	5% acetic acid	C1-4	–0.09	1305.14	27
5	10% acetic acid	C1-5	0.06	186.55	4
weighted sums			**0.15**		
bulk analysis	1 M hydrochloric acid	Core 4 24-28cm	–0.51	--	
1	ammonium acetate	C4-1	–0.79	20.28	1
2	0.25% acetic acid	C4-2	–0.80	211.80	6
3	1% acetic acid	C4-3	–0.65	970.19	27
4	5% acetic acid	C4-4	–0.54	1925.58	53
5	10% acetic acid	C4-5	–0.62	494.52	14
weighted sums			**–0.59**		
bulk analysis	1 M hydrochloric acid	PT carbonates	0.03	184.86	
1	ammonium acetate	KAMD-20-1	–0.06	12.11	11
2	0.25% acetic acid	KAMD-20-2	0.02	27.75	25
3	1% acetic acid	KAMD-20-3	0.03	29.74	27
4	5% acetic acid	KAMD-20-4	0.14	31.46	28
5	10% acetic acid	KAMD-20-5	0.17	10.07	9
weighted sums			**0.06**		
bulk analysis	1 M hydrochloric acid	PT carbonates	–0.12	1021.59	
1	ammonium acetate	KAMD-31-1	–0.20	100.14	6
2	0.25% acetic acid	KAMD-31-2	–0.04	248.46	15
3	1% acetic acid	KAMD-31-3	–0.04	782.70	46
4	5% acetic acid	KAMD-31-4	–0.07	422.00	25
5	10% acetic acid	KAMD-31-5	–0.46	154.32	9
weighted sums			**–0.10**		

Note that the weighted sums come from the weighted sum of all the leaching steps (step 1 to step 5). The weighted sums are indistinguishable to the bulk analysis. Modern coral, Core 1 40-42cm, and Core 4 24-28cm are three recent carbonate precipitates from the modern Bahamian carbonate platform, see Romaniello et al. (2013) for sample details. KAMD-20 and KAMD-31 are two Permian-Triassic (PT) carbonates from the Kamura section in Japan.

Table A.6. A summary of analytical results of the Kamura section, Japan.

Samples	$\delta^{238}U$	2SD	Mg	Al	Ca	Mn	Sr	Mo	U
	‰	‰	ppm	ppm	ppm	ppm	ppm	ppm	ppm
KAMX-1	-0.32	0.05	99052.2	100.9	270054.5	30.4	183.9	0.2	0.17
KAMX-2	-0.41	0.05	54521.4	58.6	346195.4	102.3	161.6	0.3	0.09
KAMX-3	-0.59	0.05	7135.4	21.4	397558.5	6.8	549.5	0.2	0.31
KAMX-4	-0.65	0.04	3438.8	14.7	401082.2	4.9	595.9	0.1	0.37
KAMX-5			3063.1	19.9	379953.3	11.7	817.1	0.4	0.43
KAMX-6	-0.66	0.04	2517.1	50.5	418117.9	7.3	741.1	0.3	0.47
KAMX-7			100742.8	98.5	251021.9	16.0	177.0	0.2	0.04
KAMX-8	-0.77	0.04	2975.2	13.1	429542.6	5.9	1151.5	0.1	0.40
KAMX-9			2413.5	18.9	439089.5	23.0	1342.7	0.1	0.50
KAMX-10			2680.9	58.2	430027.7	79.3	977.7	0.1	0.44
KAMX-11	-0.69	0.05	1858.7	19.3	428252.4	181.9	977.7	0.1	0.32
KAMX-12	-0.68	0.04	1641.5	19.5	387909.1	174.4	1264.9	0.2	0.36
KAMX-13	-0.63	0.05	1929.7	58.2	409533.3	82.4	1015.5	0.2	0.46
KAMX-14	-0.50	0.05	2532.5	32.7	402037.4	56.7	266.3	0.1	0.27
KAMX-15			1808.9	24.7	398760.9	25.0	657.0	0.1	0.27
KAMX-16	-0.46	0.06	1758.7	46.0	418210.8	15.5	647.8	0.1	0.28
KAMX-17	-0.41	0.06	7064.0	30.0	387562.6	45.2	190.8	0.2	0.19
KAMX-18	-0.56	0.04	1762.3	25.6	389086.9	527.5	1253.6	0.4	0.41
KAMX-19			36435.6	49.7	337679.5	48.0	160.7	0.1	0.09
KAMX-20	-0.41	0.05	27078.9	43.7	372910.7	79.1	169.0	0.2	0.20
KAMX-21	-0.41	0.04	47801.3	167.8	321727.1	393.2	187.0	0.2	0.12
KAMX-22	-0.30	0.06	23366.2	96.5	330394.3	1036.7	151.5	0.3	0.29
KAMX-23			57442.2	105.9	282972.7	557.3	131.2	0.1	0.25

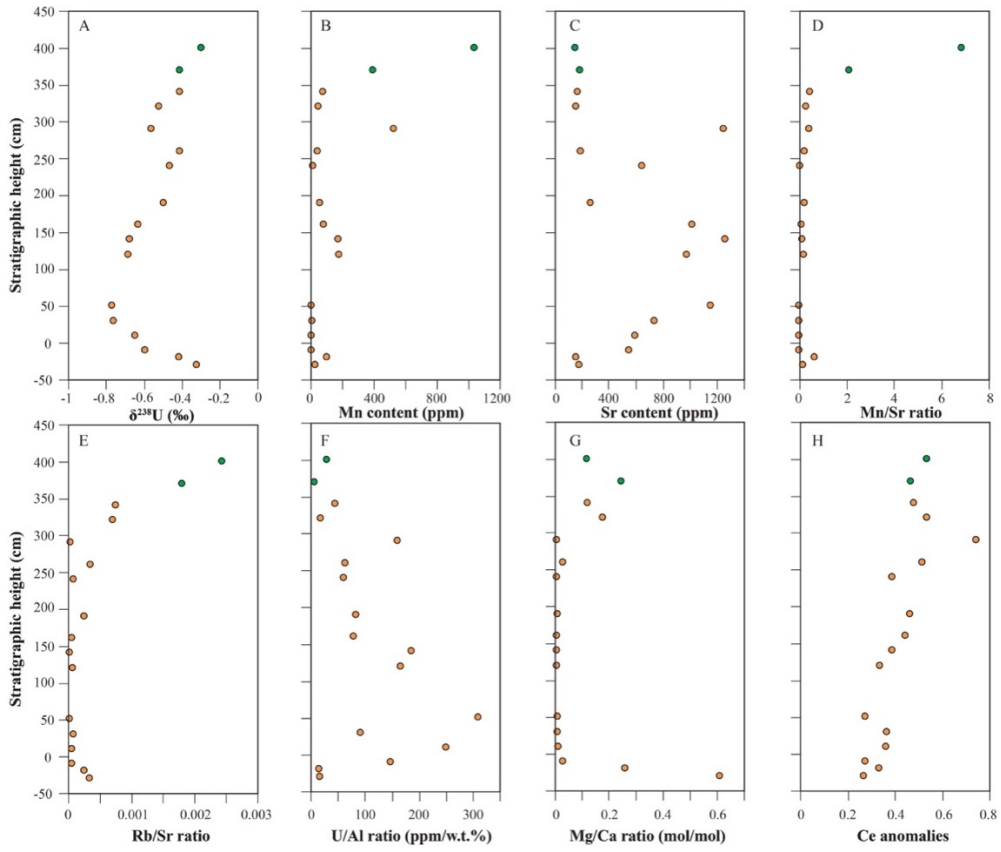

Figure A.1. Diagenetic plots. (A) $\delta^{238}U$ profile, (B) Mn content profile, (C) Sr content profile, (D) Mn/Sr ratio profile, (E) Rb/Sr ratio profile, (F) U/Al ratio profile, (G) Mg/Ca molar ratio profile, and (H) Ce anomalies profile. The two green circles at the top of each records denote two outliers with high Mn/Sr ratios, and have been excluded in the discussion presented in the main text.

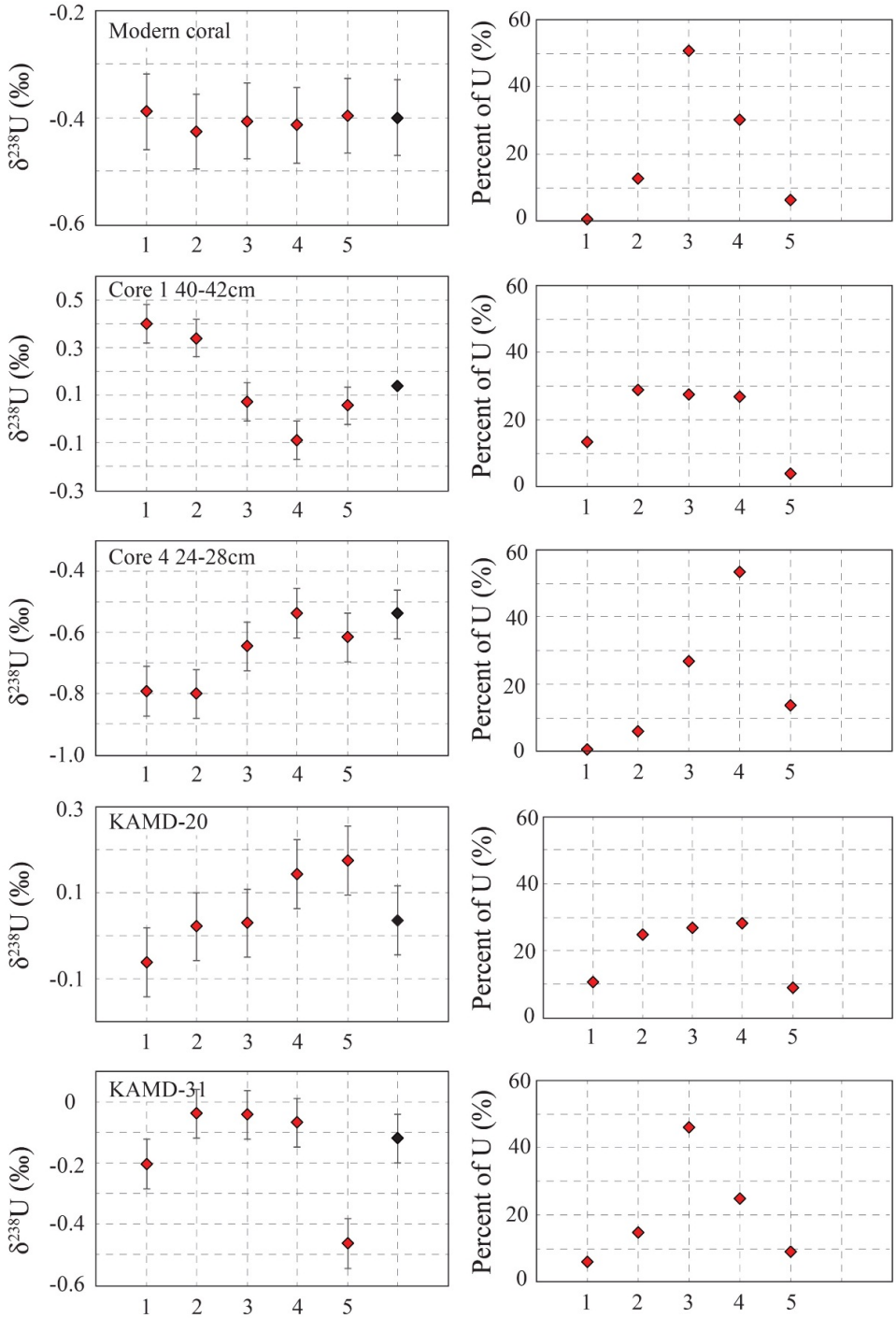

Figure A.2. Leaching results summary of $\delta^{238}U$ and percent of U dissolved during each leaching step. Modern coral, SC-1, and SC-4 are three recent carbonate sediments that collected from the Bahamian carbonate platform. KAMD-20 and KAMD-31 are two Permian-Triassic aged carbonate sediments that collected from Kamura, Japan.

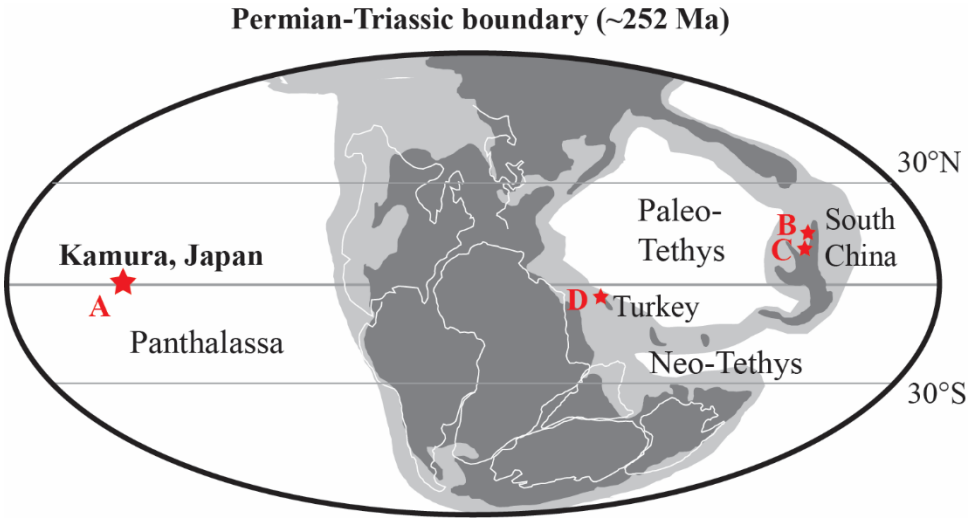

Figure A.3. Location of Japan, South China and Turkey at ~252 Ma, the time of the end-Permian extinction (modified after Payne et al. (2007)). (A): The Kamura section (Japan), this study. (B) The Dawen section (South China) studied by Brennecka et al. (2011). (C): The Dajiang section (South China) studied by Lau et al. (2016). (D): The Taşkent sections (Turkey) studied by Lau et al. (2016).

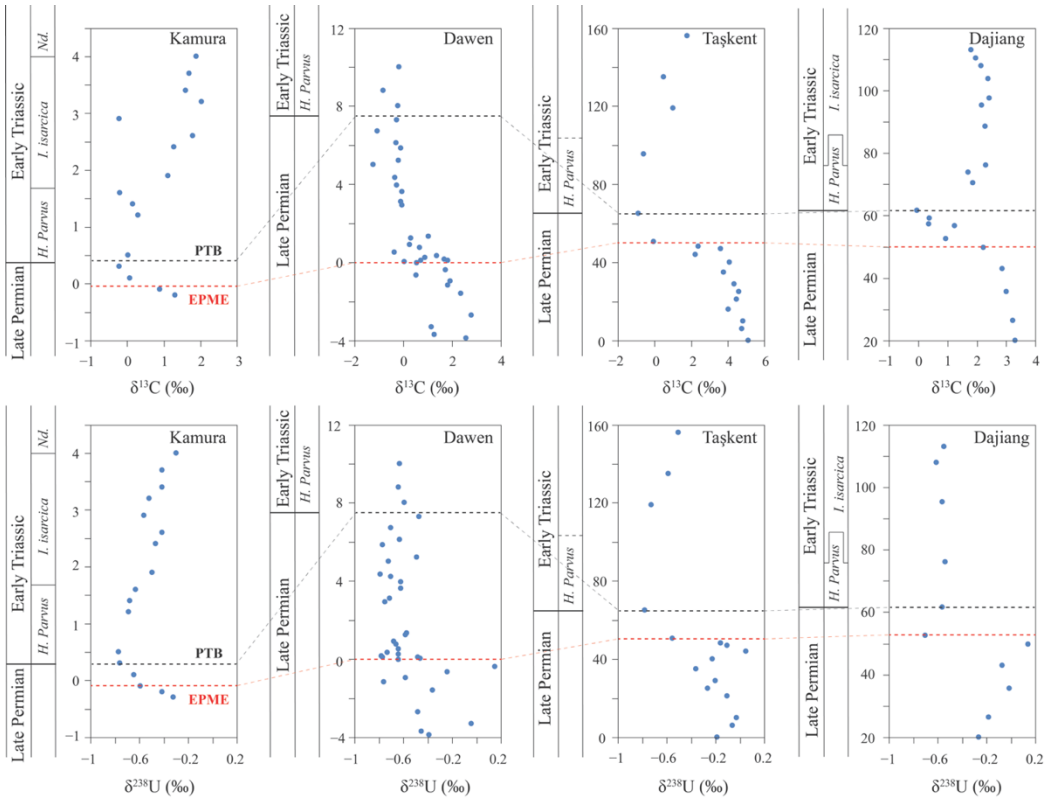

Figure A.4. A global compilation of $\delta^{13}C$ data across the Permian-Triassic boundary. $\delta^{13}C$ and conodont data of Kamura are from Zhang et al. (2017). $\delta^{238}U$, $\delta^{13}C$, and conodont data of the Dawen section are from Brennecka et al. (2011) and Chen et al. (2009). $\delta^{238}U$, $\delta^{13}C$, and conodont data of the Dajiang section and the Taşkent Section are from Lau et al. (2016). The well-characterized EMPE horizon and PTB horizon allow us to correlate these sections. The unit of the heights are in meters (m).

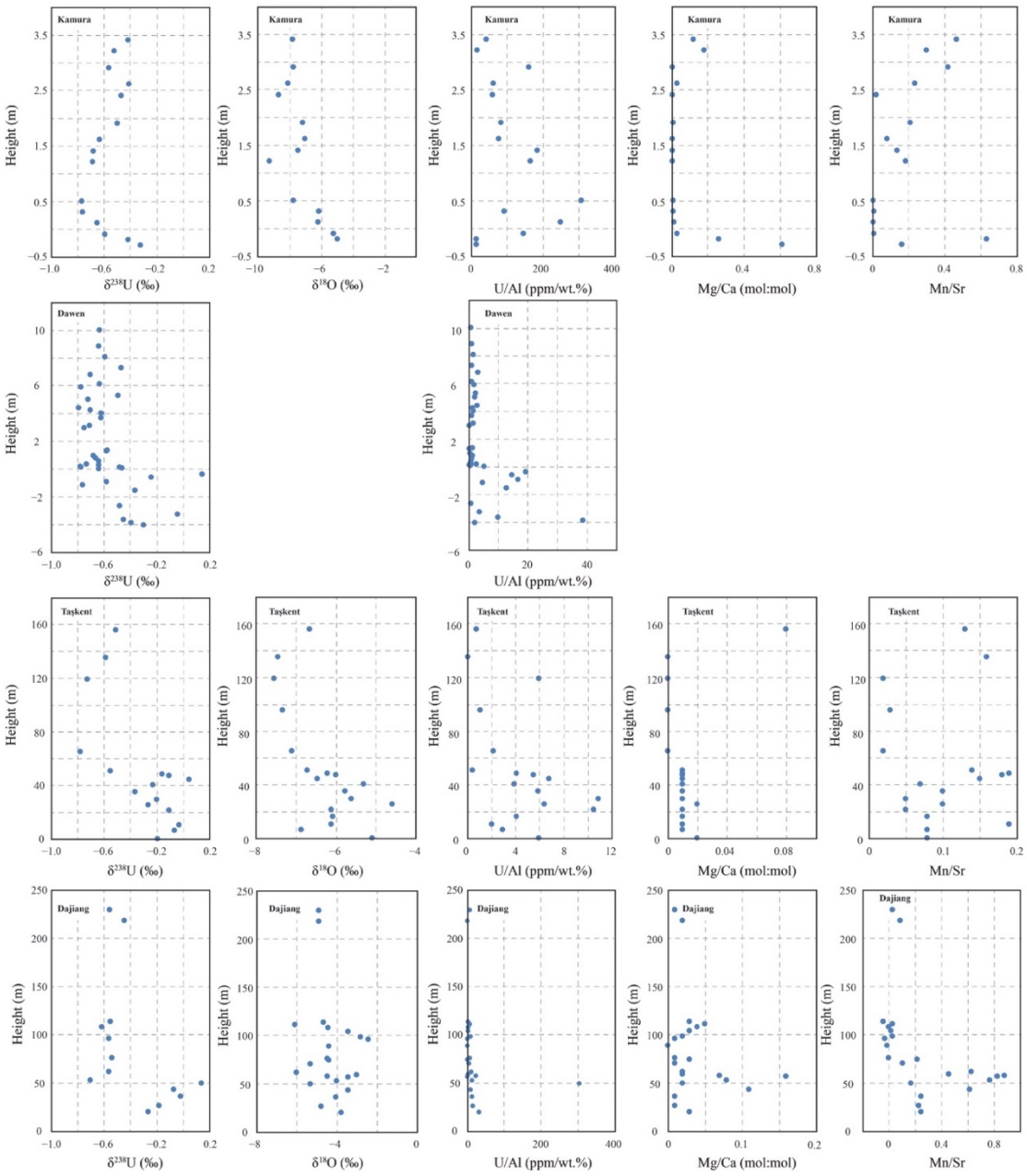

Figure A.5. Comparison of some common used diagenetic indictors among different Permian-Triassic sections. Data of the Kamura section are from this study. Data of the Dawen section are from Brennecka et al. (2011). Data of the Taşkent sections and the Dajiang section are from Lau et al.(2016). The empty spaces in the Dawen section deonate that we have not found the related data from original publication.

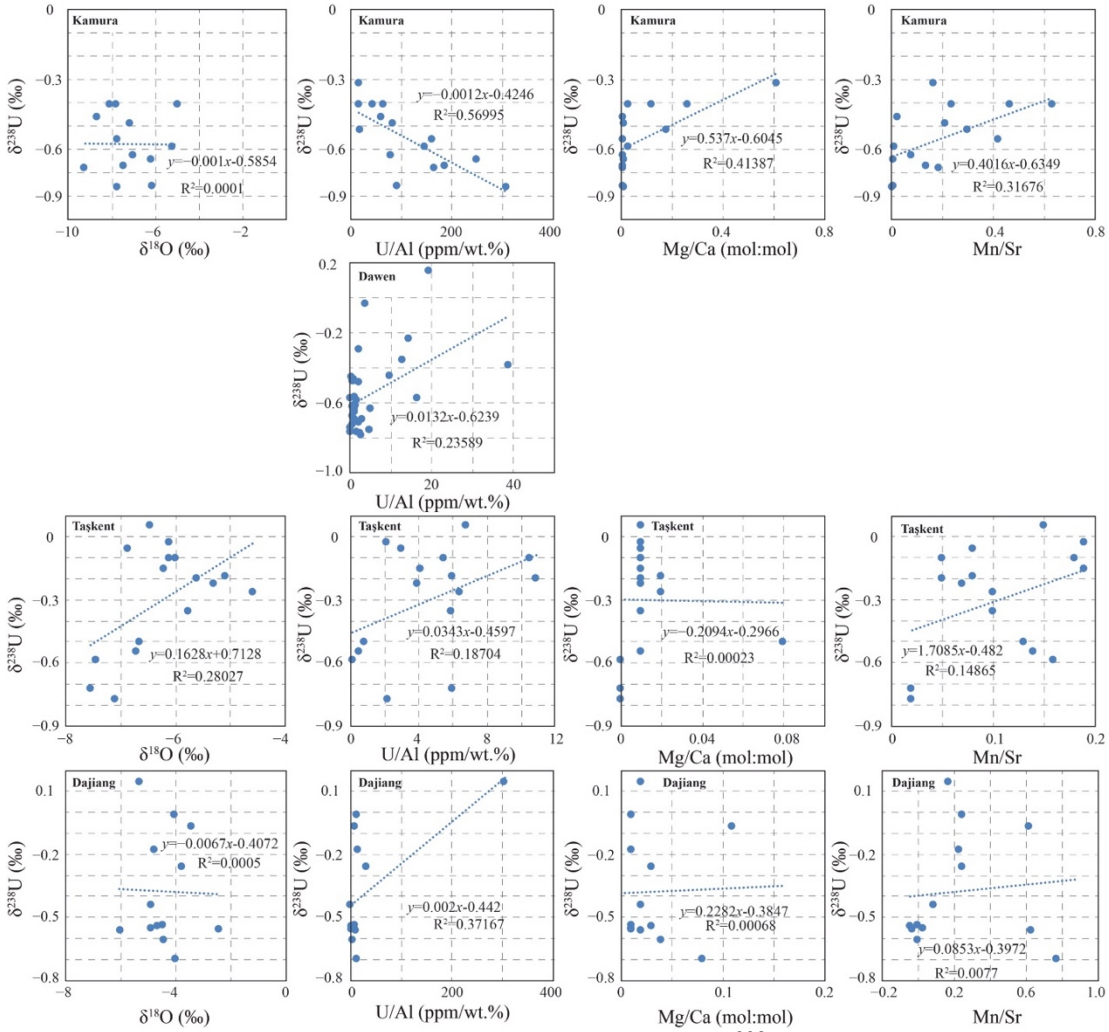

Figure A.6. Comparison of cross-correlation between $\delta^{238}U$ and some common used diagenetic indictors among different Permian-Triassic sections. Data of the Kamura section are from this study. Data of the Dawen section are from Brennecka et al. (2011). Data of the Taşkent sections and the Dajiang section are from Lau et al. (2016).

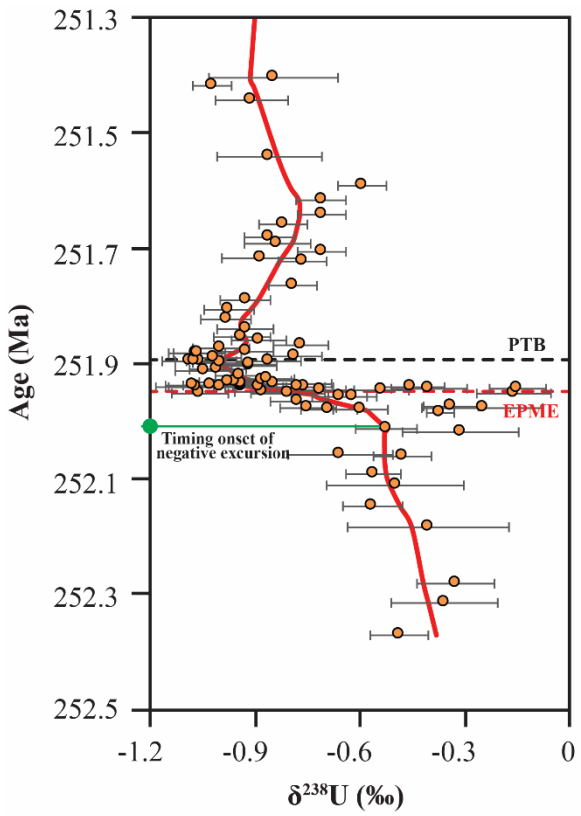

Figure A.7. A LOWESS smoothing method estimate the possible timing of onset of anoxia. The timing is estimated based on the timing of onset of negative excursion in $\delta^{238}U$ record. The red line denotes a LOWESS function smoothing of the combined data using a span of 0.2.

APPENDIX B

SUPPLEMENTARY INFORMATION FOR MULTIPLE EPISODES OF MARINE ANOXIA LINKED TO GLOBAL WARMING AND CONTINENTAL WEATHERING FOLLOWING THE LATEST PERMIAN MASS EXTINCTION

B. 1 The study section

The Zal section is an open-marine, mainly carbonate succession deposited on a microcontinent in the west-central Tethys Ocean during the Late Permian-Early Triassic (Figure 4.1). Its geological background has been described in detail by Horacek et al. (2007), Richoz et al. (2010), and Leda et al. (Leda et al., 2013). Samples used in this study are from the same sample suites that have been previously analyzed for C isotopes and Sr isotopes by Horacek et al. (2007), Richoz et al. (2010), and Sedlacek et al. (2014). The Zal section is important for several reasons: (1) the study site was isolated from siliciclastic influences and shows limited diagenetic alteration, resulting in preservation of original marine carbonate geochemical signals (Horacek et al., 2007; Richoz et al., 2010; Sedlacek et al., 2014); (2) sedimentation was nearly continuous from the Late Permian to the early Middle Triassic, providing a complete record for the Early Triassic; (3) the section was deposited at high sedimentation rates (estimated at ~400 m/Myr), resulting in excellent stratigraphic resolution.

The sampled section starts 37.45 m below the Permian-Triassic boundary (PTB) and extends through 752 m above the PTB. The Upper Permian primarily consists of gray and red nodular limestone. The Griesbachian to the Smithian (0 to 601 m above PTB) is mainly

comprised of well-preserved micritic limestone. The Upper Spathian contains mainly dolostone, which persists through the Lower/Middle Triassic boundary.

Horacek et al. (2007) identified four volcanic dikes in the study section, which are at 50–80 m, 180–190 m, 210–225 m, and 270–300 m above its base. These dikes appear to have had limited influence on geochemical records from Zal, because both the C and Sr isotope profiles at Zal mirror global Early Triassic C and Sr isotope records, even for samples located close to the dikes (Horacek et al., 2007; Payne et al., 2004; Sedlacek et al., 2014; Song et al., 2015). For a detailed description of lithostratigraphy and biostratigraphy, see refs. (2007; 2010).

B. 2 Evidence for primary seawater δ^{238}U values

Analytical results for the Zal section has been summarized in Table B.1. Trace elements (e.g., Sr and Mn) substituted into the lattice of carbonate minerals can be used as diagenetic indicators. The incorporation of trace elements into the carbonate lattice is governed by the distribution coefficient, and different types of diagenetic fluids have different trace element compositions. Modern, well-oxygenated seawater is high in Sr relative to Mn such that primary precipitates and early diagenetic phases formed in the presence of seawater are generally enriched in Sr relative to Mn (Banner and Hanson, 1990). This is particularly true for aragonite because of the high distribution coefficient for Sr into aragonite compared to other carbonate minerals (Veizer, 1983). Early fabric-retentive dolostone can also be enriched in Sr relative to Mn, although dolomite generally has a lower preference for Sr (Vahrenkamp and Swart, 1990) and a higher preference for Mn (Mazzullo, 1992) compared to calcite.

Meteoric and burial fluids, by contrast, tend to be depleted in Sr relative to seawater (Banner and Hanson, 1990). The recrystallization process also acts to expel Sr from the lattice of carbonate minerals because of its relatively large ionic radius compared to Ca (Rimstidt et al., 1998). As a result, meteoric or burial diagenetic phases are often depleted in Sr relative to precursor marine phases. Burial fluids can also be substantially enriched in Mn, particularly under reducing conditions (Veizer, 1983). This commonly leads to Mn enrichment in burial diagenetic phases. Meteoric fluids are variable in their Mn content—depending largely on redox conditions—such that meteoric calcite phases can be characterized by enrichment or depletion of Mn.

These general relationships have led to the establishment of traditional criteria such as the Mn/Sr ratio to assess the fidelity of primary geochemical signatures in carbonate rocks. For example, Kaufman and Knoll (Kaufman and Knoll, 1995) suggested that both limestone and dolostone with Mn/Sr ratios < 10 can be expected to retain their primary carbon isotopic signatures. In this study, we used a conservative Mn/Sr ratio of 2.5 as an initial benchmark for assessing diagenesis.

At Zal, the majority of samples below 500 m yielded Sr concentrations >400 ppm, and most Dienerian-age samples yielded >1000 ppm Sr (Figure B.1). These contents are consistent with those reported by Sedlacek et al. (2014) and in other studies of marine carbonates interpreted as primary carbonate precipitates. Samples above 500 m have Sr concentrations between 51 ppm and 1070 ppm. The decrease in Sr concentrations at the 500 m of the record corresponds to the appearance of dolomite in the study section.

The Mn/Sr ratios of most samples below 500 m are <0.5 with the exception of the samples below 3.5 m. Samples below 3.5 m have elevated Mn/Sr ratios ranging between

0.1 and 7.5. The majority of the samples above 500 m have Mn/Sr ratios ranging between 0.5 and 4. Because samples below 3.5 m and samples above 500 m have relative higher Mn/Sr ratios than samples between 3.5 and 500 m, samples have been divided into three stratigraphic intervals when evaluating crossplots. Samples with Mn/Sr ratios > 2.5 were not considered further in the analysis and discussion of the study section.

We further looked at crossplots of δ^{238}U–[Sr], δ^{238}U–Mn/Sr, and δ^{238}U–Mg/Ca for all samples as a group as well as samples from below 3.5 m, 3.5-500 m, and above 500 m. No statistically significantly correlations were observed in these crossplots (Figure B.2.), indicating our δ^{238}U record is unlikely to have been significantly altered by post-depositional processes including dolomitization.

All of the samples below 3.5 m have Rb/Sr ratios < 0.01, and most of the samples between 3.5 m and 500 m have Rb/Sr ratios < 0.01 (with only 3 outliers > 0.01), indicating minimal incorporation of clays into these carbonates. Samples above 500 m have elevated Rb/Sr ratios ranging between 0.01 and 0.03, indicating potentially larger proportions of clays. However, the lack of covariation between δ^{238}U and Rb/Sr ratios indicates that the δ^{238}U profile is unlikely to have been significantly affected by clay contamination (Figure B.3.).

Changes in the amount of detrital U inputs might also influence bulk carbonate δ^{238}U values. We examined this possibility by looking at U/Al ratios, which indicate that the U budget in our samples is dominated by authigenic U. The U/Al of most of samples is two to three order s of magnitude higher than the upper continental crust ratio of ~0.331 ppm/wt. % (Rudnick and Gao, 2003). Furthermore, there are no statistically significant

correlations between U/Al and $\delta^{238}U$ (Figure B.3.), indicating that observed $\delta^{238}U$ trends are unlikely related to detrital U inputs.

Because different processes might have altered sample $\delta^{238}U$ at different stratigraphic intervals, we therefore provide additional geochemical crossplots ($\delta^{238}U$ versus Mn/Sr, Mg/Ca, Rb/Sr, and U/Al) to test whether each of the negative $\delta^{238}U$ events were affected by the processes discussed above (Figs. S4, S5). No strong statistically significant correlations were observed between $\delta^{238}U$ and these proxies, thus further supporting our inference that the negative excursions in the Zal $\delta^{238}U$ record have recorded primary seawater events.

The carbon and oxygen isotope correlation for the Zal carbonates (the exact same sample set used for our U isotope study) have been investigated by Horacek et al. (Horacek et al., 2007). Briefly, in the Zal section as a whole, there is no correlation between carbon and oxygen isotope values ($R^2 = 0.095$; Figure B.6.). $\delta^{13}C$ and $\delta^{18}O$ tend to co-vary if both systems have been influenced by proportional mixing with an external (diagenetic) fluid, and in the case of the Zal section, the lack of co-variation between these parameters is another line of evidence supporting preservation of early, seawater-derived geochemical signatures.

We note that the C1 and C2 $\delta^{238}U$ excursions are relatively close to dikes in the Zal section. However, three independent lines of evidence suggest that these dikes had limited influence on our $\delta^{238}U$ records. First, samples IZ-13 to IZ-16 are within 10 m of the 50–80 m dike, yet their $\delta^{238}U$ values are nearly identical to samples higher and lower in the section. No samples were analyzed close to the 180–190 m dike. Only one sample was analyzed within 10 m of the 210–225 m dike, and that sample (IZ-33) yielded $\delta^{238}U$ of −0.31 ‰,

which is similar to the next sample above it (IZ-38; −0.34 ‰). Three samples (IZ40-42) were analyzed within 10 m of the 270–300 m sill, and their $\delta^{238}U$ values (−0.20 ‰ to −0.41 ‰) are similar to samples from the next 100 m upsection. Second, the C1 $\delta^{238}U$ excursion is similar to those observed from other coeval Permian-Triassic boundary sections from a wide range of localities, such as the Dawen, the Dajiang, and the Daxiakou sections in South China, and the Taskent section in Turkey (discussed further below). Third, the $\delta^{13}C$ and $\delta^{238}U$ excursions of the C1 and C2 cycles are strongly correlated, and since the C1 and C2 $\delta^{13}C$ excursions at Zal are known global $\delta^{13}C$ excursions of the Early Triassic (Horacek et al., 2007; Payne et al., 2004), it is logical to infer that the C1 and C2 $\delta^{238}U$ excursions were also of global significance.

Finally, we acknowledge the limitations of existing diagenetic proxies for evaluating the diagenesis of carbonate $\delta^{238}U$. The absence of a correlation between various diagenetic tracers and U isotope values does not mean that diagenesis did not occur. Existing indicators of carbonate diagenesis have been primarily developed for carbon, oxygen, and strontium isotopes studies, and further work is required to develop specific diagenetic indicators for uranium isotopes. However, given our present understanding, we argue that the analysis presented above strongly suggests that the Zal section likely recorded primary oceanographic U isotope trend. We further argue that the strongest evidence for the preservation of $\delta^{238}U$ in carbonates comes from the independent replications of secular trends in $\delta^{238}U$ in multiple, widely-spaced coeval sections (Zhang F. et al., 2018a), and therefore encourage future work to validate that the trends evident in the Zal section can be reproduced in other sections.

B. 3 Compilation of global carbonate $\delta^{238}U$ records for PTB interval

Here we compare our new PTB section (the Zal section in Iran) with four other published PTB sections, the Dawen section (South China) studied by Brennecka et al. (2011a), the Dajiang (South China) and the Taşkent (Turkey) sections studied by Lau et al. (2016), and the Kamura section (Japan) studied by Zhang et al. (Zhang et al., 2018a). The paleogeographic locations for these five sections during the latest Permian mass extinction (LPME) are shown in Figure B.7., and comparison of $\delta^{238}U$ and $\delta^{13}C$ records among those sections are shown in Figure B.8.

Our Zal record (Figure 4.1C and Figure B.8.) shows persistently high $\delta^{238}U$ values in the Upper Permian, with an average of –0.11±0.19 ‰ (2σ). At the PTB interval, a stepped decrease in $\delta^{238}U$ results in values as low as –0.69 ‰ by the lowermost Triassic. $\delta^{238}U$ values then remain low, varying around –0.50 ‰ through the Griesbachian. The $\delta^{238}U$ values of pre- and post-LPME samples are significantly different ($p<0.01$ for a *t*-test).

This observation is consistent with previous $\delta^{238}U$ studies (the Dawen section and the Dajiang section in South China, the Taşkent section in Turkey, and the Kamura section in Japan) that show a distinct decrease in $\delta^{238}U$ values across the LPME (Figure B.8.), suggesting that these $\delta^{238}U$ trends are primary and record widespread oceanic anoxia during the Permian-Triassic transition. The congruent Permian-Triassic $\delta^{238}U$ records at Panthalassic and Tethyan sites confirms that marine $\delta^{238}U$ records are globally identical (Zhang et al., 2018a), and thus supports the use of carbonate U isotopes as a paleoredox proxy for the Early Triassic global ocean.

An additional $\delta^{238}U$ study from a South China section by Elrick et al. (2017) also shows an abrupt negative shift in $\delta^{238}U$ of 0.4–0.5 ‰ across the LPME horizon. However,

their primary focus was the Middle to Late Permian, and there were only a few data points from the PTB interval, so we have excluded this study in Figures B.7. and B.8.

At a finer temporal scale, the compilation in Figure B.8. shows slight differences in the negative $\delta^{238}U$ peaks, i.e., in the peak values and the pattern of overlap among peaks, possibly due to differences in sample distribution and density and uncertainties in age models but perhaps also due to local watermass or diagenetic influences.

The 0.2–0.4 ‰ scatter of $\delta^{238}U$ values through the PTB interval may have been due to differential incorporation of ^{238}U-enriched U(IV) from anoxic porewaters during early diagenesis or variation in porewater U-speciation during carbonate recrystallization. Study of modern Bahamian bulk sediments indicates that bank-top carbonates record a normal-distribution of $\delta^{238}U$ values ranging from 0.2–0.4 ‰ (average 0.3 ‰) heavier than that of modern seawater (Romaniello et al., 2013). Measurements of $\delta^{238}U$ in deep Bahamian drillcores (Clino, Unda, and IODP Core 1006) extending to the upper Miocene has yielded a similar normal distribution with a mean and standard deviation of 0.27±0.15 ‰, which is close to the average for bank-top carbonates (Chen et al., in prep.). This offset may reflect differential incorporation of ^{238}U-enriched U(IV) from anoxic porewaters during early diagenesis or variation in porewater U-speciation during carbonate recrystallization (Chen et al., 2016; Romaniello et al., 2013). Porewater data from deep Bahamas drill cores suggests that the extent of burial diagenesis is likely self-limiting because porewater anoxia results in low dissolved U concentrations and renders U essentially immobile (Henderson et al., 1999). We therefore conclude that early diagenesis imparts a ~ +0.3 ‰ offset to bulk carbonate $\delta^{238}U$, and that subsequent burial diagenesis likely has no measurable effect. Because of we have found a similar distribution of variation among coeval Permo-Triassic

sediments from around the world (Fig S7), we assume that our Zal samples record $\delta^{238}U$ approximately 0.3 ‰ heavier than contemporaneous seawater, similar to modern Bahamian carbonate sediments (Romaniello et al., 2013). Considering the close agreement of $\delta^{238}U$ records from multiple, widely-spaced sections across the Permo-Triassic boundary, as well as the similar distribution of $\delta^{238}U$ values in modern and ancient carbonate sediments, we argue that the balance of available evidence points to a relatively constant diagenetic offset, both in time and space. Therefore, prior to U isotope mass balance calculations, we applied a diagenetic correction factor of 0.3 ‰ to all measured $\delta^{238}U$ values.

B. 4 Possible timing of onset of oceanic anoxia

We constrained the timing of the onset of oceanic anoxia in the latest Permian by evaluating when the Zal $\delta^{238}U$ record began to deviate significantly from pre-crisis background $\delta^{238}U$ values. We calculated a LOWESS (LOcally WEighted Scatterplot Smoothing) trend based on the compiled data in Figure B.9. A smoothing window of 0.2-Myr was applied, which was optimized based on cross-correlation analysis, to yield the LOWESS trend shown in Figure B.9. The negative shift in $\delta^{238}U$ began between 252.10 Ma (oldest) and 251.98 Ma (youngest), reflecting an onset that preceded the LPME by at least 40 kyr but not more than 160 kyr. Although there are some uncertainties in the age models for individual sections, this calculation demonstrates that expansion of oceanic anoxia predated the LPME by a measurable amount. This conclusion is consistent with the findings of several earlier studies that identified the onset of major environmental

perturbations up to ~100 kyr prior to the latest Permian extinction event (e.g.,(Algeo et al., 2012; Shen et al., 2012).

B. 5 Age-thickness model for Zal section

An age-thickness model was constructed for the Zal, Iran study section based on six geochronological tie-points, the stratigraphic positions of which in the Zal section were constrained by a combination of conodont biostratigraphic and C-isotope chemostratigraphic data (Horacek et al., 2007). The six tie-points include five stage/substage boundaries and one carbon-isotope feature: Latest Permian Mass Extinction (0 m), N2 carbon-isotope peak (30 m), Griesbachian-Dienerian boundary (125 m), Dienerian-Smithian boundary (499 m), Smithian-Spathian boundary (602 m), and Spathian-Anisian boundary (731 m). Due to insufficient biochronological control through conodont or ammonoids biozone and the lack of proper definition of some of these substages an incertitude exists on the high of these boundaries. The N2 carbon-isotope peak (terminology of Song et al. (Song et al., 2013)) is readily identifiable in the Zal carbonate carbon-isotope profile (Horacek et al., 2007).

The time scale used in the present study is that of Algeo et al. (Algeo et al., 2013), which is based on a combination of zircon U-Pb dating studies of the Lower Triassic (Burgess et al., 2014; Galfetti et al., 2007; Lehrmann et al., 2006; Ovtcharova et al., 2006) and an astrochronological study of the Induan that constrained the relative durations of the Griesbachian and Dienerian substages (Guo et al., 2008). The ages of the six tie-points in that time scale are: Latest Permian Mass Extinction (251.94 Ma), N2 carbon-isotope peak (251.45 Ma), Griesbachian-Dienerian boundary (251.3), Dienerian-Smithian boundary

(251.0 Ma), Smithian-Spathian boundary (250.6 Ma), and Spathian-Anisian boundary (247.2 Ma).

The age-thickness model for the Zal section is shown in Figure B.1. The model shows moderate sedimentation rates in the late Changhsingian to mid-Griesbachian (60-90 m Myr^{-1}), accelerating during the late Griesbachian (620 m Myr^{-1}) and Dienerian (1250 m Myr^{-1}), and then declining during the Smithian (260 m Myr^{-1}) and Spathian (70 m Myr^{-1}). Other age models (Ogg, 2012) lead to lower but still significantly elevated peak sedimentation rates (435 m Myr^{-1} in the Dienerian) and have the disadvantage of yielding erratic changes from one substage to the next, as opposed to the smooth pattern of acceleration and deceleration yielded by our age model (Figure B.10.). The exceedingly high sedimentation rates associated with the Dienerian in all age models must reflect a major episode of tectonic subsidence of the Iranian microcontinent during that substage of the Early Triassic.

B. 6 Cross-correlation analysis

The carbon, uranium, and strontium isotope profiles for the Zal, Iran study section (Figure 4.1) were compared using cross-correlation analysis (Davis and Sampson, 1986) for the purpose of establishing relative lead/lag relationships among these records. The underlying principle of cross-correlation analysis is that two records are offset relative to each other in successively larger increments, and the degree of correspondence is evaluated at each step. The metric that we used to evaluate the degree of correspondence between pair-wise records was Pearson's correlation coefficient (r).

Cross-correlation analysis requires that data series be spaced at equal intervals of length or time in order to be able to offset one record relative to another at equal increments. Thus, although all three of the Zal isotopic records were generated from the same suite of samples, it was nonetheless necessary to resample each record to produce data series at equal intervals. We chose to resample the Zal dataset at equal intervals of time (rather than length) based on the ages for individual samples calculated from our age-thickness model (see above). These ages were used to generate a LOWESS curve for each isotopic profile (Figure 4.1) with estimated values at 25-kyr nodes between about 252.25 Ma and 249.75 Ma (the exact interval depended on the age range of the specific isotopic record).

The LOWESS records were cross-correlated in a pairwise manner: δ^{238}U-vs- δ^{13}C and ^{87}Sr/^{86}Sr-vs- δ^{13}C. The C-isotope profile is longer, more complete (i.e., fewer gaps), and more coherent (i.e., less sample-to-sample variance) than the U- and Sr-isotope profiles, so it was chosen as the base record for cross-correlation analysis. For each pair of records, one was offset relative to the other in increments of 25 kyr, with a correlation coefficient calculated at each step. We conducted cross-correlation analysis based on (1) the full (~2.5-Myr-long) isotopic records, and (2) windowed intervals of each record (where correlation coefficients were calculated based on 200-kyr data windows). Analysis of the full records demonstrated that quantifiable lead/lag relationships existed, and analysis of shorter data windows demonstrated that the lead/lag relationships changed with time.

The correlations between δ^{238}U and δ^{13}C are strongly positive (mostly $r > +0.6$) throughout the Early Triassic study interval (Figure B.11.–top), demonstrating significant direct covariation among these two proxies. The δ^{238}U record lagged the δ^{13}C record mostly by 75-175 kyr (mean ~125 kyr) during the Griesbachian to Smithian, but this lag went to

zero during the Spathian, mainly because of lack of variation in the $\delta^{238}U$ and $\delta^{13}C$ records during that substage. The observation that the $\delta^{238}U$ record lagged the $\delta^{13}C$ record is a reflection of the longer residence time of U in seawater (~320-560 kyr; Dunk et al., 2002) than that of dissolved inorganic carbon (DIC) (~100 kyr; Zeebe and Wolf-Gladrow, 2001) and, hence, the slower response time of the U-isotope system to global perturbations.

The correlations between $^{87}Sr/^{86}Sr$ and $\delta^{13}C$ are strongly negative (mostly $r < -0.5$) throughout the Early Triassic study interval (Figure B.11.–bottom), demonstrating significant inverse covariation among these two proxies. The $^{87}Sr/^{86}Sr$ record led the $\delta^{13}C$ record by intervals mostly ranging from 0 to 225 kyr (mean ~100 kyr) during the Griesbachian to Smithian, but this lag reversed during the Spathian, when $\delta^{13}C$ led $^{87}Sr/^{86}Sr$ by ~75 kyr. Strontium has a longer residence time in modern seawater (~2 Myr; Davis et al., 2003) than dissolved inorganic carbon, and this is unlikely to have varied much in the Early Triassic given that the largest source of Sr to seawater is continental weathering. Thus, the observation that Sr-isotopic variation led C-isotopic variation is most easily interpreted as the result of continental weathering fluxes driving changes in the Early Triassic marine system. This is consonant with substantial evidence for major increases in terrestrial fluxes to marine systems during the Early Triassic (e.g., Algeo et al., 2011; Algeo and Twitchett, 2010). The observation of a reversal in lead/lag relationships close to the Smithian-Spathian boundary (i.e., a shift to $\delta^{13}C$ leading $^{87}Sr/^{86}Sr$) suggests that this continental driver of Early Triassic marine environmental changes tapered off or terminated around that time.

B. 7 High-resolution intercomparison of Zal $\delta^{13}C$, $^{87}Sr/^{86}Sr$, and $\delta^{238}U$ records

The relationship of the Zal $\delta^{238}U$ profile to previously published $\delta^{13}C$ and $^{87}Sr/^{86}Sr$ profiles for the same sample suite was investigated by generating a LOWESS curve for each record (Figure 4.2). Each of these records exhibits three cycles of variation through the Griesbachian-Smithian substages of the Early Triassic. The C-isotope minima and maxima were previously labeled N1-N3 ("negative" excursions) and P1-P3 ("positive" excursions), respectively, by Song et al. (2013, 2014). In this manuscript, we labeled the covariation in C-Sr-U isotope systems using C1 to C4, which donate four different cycles (Figure 4.2).

The first cycle (**C1**), which commenced at the LPME horizon and ended around the Griesbachian-Dienerian boundary, was characterized by (i) an initially rapid negative shift in $\delta^{238}U$ that slowed before reaching a minimum in the middle-to-late Griesbachian, (ii) an initially rapid negative shift in $\delta^{13}C$ that peaked in the early Griesbachian before a positive rebound in the late Griesbachian, and (iii) a sharp rise in $^{87}Sr/^{86}Sr$ in the early Griesbachian followed by little change.

The second cycle (**C2**), which commenced around the Griesbachian-Dienerian boundary and ended around the Dienerian-Smithian boundary, was characterized by (i) a large negative shift in $\delta^{238}U$ to a minimum in the mid-Dienerian, (ii) a relatively small negative C-isotope shift with a peak in the early Dienerian that was followed by a large positive shift culminating at the Dienerian-Smithian boundary, and (iii) a long, steady rise in $^{87}Sr/^{86}Sr$ through most of the Dienerian.

The third cycle (**C3**), which commenced around the Dienerian-Smithian boundary and ended in the earliest Spathian, was characterized by (i) a relatively small negative shift

in $\delta^{238}U$ with a minimum in the late Smithian, (ii) a large negative C-isotope shift with a minimum also in the late Smithian, and (iii) relatively uniform $^{87}Sr/^{86}Sr$ through most of the Smithian followed by a sharp rise in the late Smithian. The 3rd pair of negative excursions in $\delta^{238}U$ and $\delta^{13}C$ appears synchronous. However, there are several considerations here: (1) the U peak is effectively defined by a single point, so it is not very secure; and (2) there is either an unconformity or a highly condensed interval at the Smithian-Spathian boundary (SSB) in the Zal section. The unconformity/condensed interval may be reflected in the shape of the $\delta^{13}C$ curve—in most Lower Triassic sections, the $\delta^{13}C$ minimum is mid-Smithian (e.g., Song et al., 2013), but at Zal it appears at the very top of the Smithian interval, which suggests that the upper Smithian may be missing. The cause of this unconformity may have been strong cooling at the SSB, leading to renewed continental icesheet growth and a modest sea-level fall that affected shallow-water but not deep-water sections.

The Spathian may represent a fourth cycle (**C4**) similar to the preceding three cycles in that both the $\delta^{238}U$ and $\delta^{13}C$ profiles exhibit a long-term, gradual shift to another minimum in the latest Spathian ($\delta^{13}C$) or at the Spathian-Anisian boundary ($\delta^{238}U$), although the $^{87}Sr/^{86}Sr$ record lacks sufficient detail in the Spathian for comparison to the other records (Figure 4.2).

B. 8 Estimation of weathering rates and seawater PO_4^{3-} levels in the Early Triassic ocean

We constructed a simple box model to calculate seawater PO_4^{3-} concentrations in the Early Triassic ocean for the purpose of exploring possible connections between

seawater nutrient levels and expanded oceanic anoxia. The model was constructed in three parts, first using Sr isotopes to constrain Early Triassic weathering rates, then using these rates to estimate PO_4^{3-} fluxes to seawater, and finally combining this source estimate with estimated sinks to calculate the PO_4^{3-} concentration through time.

To determine Early Triassic weathering rates, which largely control riverine PO_4^{3-} fluxes, we first constructed a Sr isotope budget for the Early Triassic following Sedlacek et al. (2014). We constructed a smoothed Early Triassic $^{87}Sr/^{86}Sr$ record for this purpose by using a recently published Sr isotope data from Zal (Sedlacek et al., 2014) and using LOWESS smoothing and piecewise cubic interpolation to generate a continuous $^{87}Sr/^{86}Sr$ record (Figure B.12.A; green curve). We then developed a forward model to calculate seawater $^{87}Sr/^{86}Sr$ through time (Figure B.12.A; red curve), and varied the riverine Sr flux to match the smoothed $^{87}Sr/^{86}Sr$ record.

The three principal sources of Sr to seawater are rivers (i.e., continental crust), weathering of ocean crust/hydrothermal, and diagenesis of marine carbonates (Richter and Turekian, 1993; Sedlacek et al., 2014). Seawater $^{87}Sr/^{86}Sr$ is influenced most strongly by (1) the Sr isotopic composition of the riverine flux (~0.712 in the modern), and (2) the ratio of the riverine to hydrothermal fluxes (1.65, based on estimated baseline fluxes of ~3.3 and 2.0×10^{10} mol yr^{-1}, respectively) (Goddéris and François, 1995; Sedlacek et al., 2014).

Changes to seawater $^{87}Sr/^{86}Sr$ can be described by differential mass balance equations for the seawater Sr inventory and $^{87}Sr/^{86}Sr$ ratio, respectively

$$\frac{dSr}{dt} = J_{river}^{Sr} + J_H + J_{DC} - \frac{1}{\tau_{Sr}} \cdot Sr \qquad (1)$$

$$\frac{d(Sr\cdot\frac{^{87}Sr}{^{86}Sr})}{dt}=J_{river}^{Sr}\cdot(\frac{^{87}Sr}{^{86}Sr})_{river}+J_H\cdot(\frac{^{87}Sr}{^{86}Sr})_H+J_{DC}\cdot(\frac{^{87}Sr}{^{86}Sr})_{DC}-\frac{1}{\tau_{Sr}}\cdot Sr\cdot(\frac{^{87}Sr}{^{86}Sr}) \quad (2)$$

where Sr is the Sr inventory in the ocean, J_{river}^{Sr}, J_H, and J_{DC} are the total amount of Sr supplied by rivers, ocean crustal hydrothermal activity, and marine diagenetic carbonates, respectively. $(^{87}Sr/^{86}Sr)_{river}$, $(^{87}Sr/^{86}Sr)_H$, and $(^{87}Sr/^{86}Sr)_{DC}$ are the $^{87}Sr/^{86}Sr$ ratio for rivers, ocean crustal hydrothermal, and marine diagenetic carbonates, respectively, and τ_{Sr} is the residence time of Sr in the ocean. Model parameterization was based on studies of the modern and ancient marine Sr cycle and are summarized in Table B.2.

Equation (2) can be simplified by using the product rule to expand the left-hand side and substituting in equation (1) to get to an expression for the change in the isotope ratio itself:

$$\frac{d(\frac{^{87}Sr}{^{86}Sr})}{dt}=\frac{J_{river}^{Sr}\cdot(\frac{^{87}Sr}{^{86}Sr})_{river}+J_H\cdot(\frac{^{87}Sr}{^{86}Sr})_H+J_{DC}\cdot(\frac{^{87}Sr}{^{86}Sr})_{DC}}{Sr}-\frac{J_{river}^{Sr}+J_H+J_{DC}}{Sr}\cdot(\frac{^{87}Sr}{^{86}Sr}) \quad (3)$$

We further define a factor, R:

$$R=\frac{J_{river}^{Sr}}{J_{modern}} \quad (4)$$

which scales the Early Triassic riverine Sr flux, J_{river}^{Sr}, relative to the Sr flux in modern rivers, J_{modern}.

In our model, we make use of a simplified approach in which the fluxes and isotopic compositions for the hydrothermal and diagenetic carbonate sources are assumed to be invariant: (1) 2.0×10^{10} moles/yr and 0.7030 $^{87}Sr/^{86}Sr$ for the hydrothermal flux, and (2)

0.3×10^{10} moles/yr and 0.7084 $^{87}Sr/^{86}Sr$ for the diagenetic carbonate flux. Similar to Sedlacek et al. (2014), we also adopted a higher value for the hydrothermal flux (2.0×10^{10} moles/yr) than in the modern (1.0×10^{10} moles/yr) owing to generally higher eustatic sea level and, thus, inferred higher ocean-crustal spreading rates in the Late Paleozoic (see justification by Sedlacek et al. (2014).

We used a $(^{87}Sr/^{86}Sr)_{river}$ of 0.7090 for the first 0.5 Myr of the model simulation based on the assumption that the riverine flux likely contained large amounts of Sr derived from weathering of Siberian Traps basalts (Burgess and Bowring, 2015) for an interval up to ~0.5 Myr following the eruption events (Horton, 2015; Schaller et al., 2011). Thereafter, $(^{87}Sr/^{86}Sr)_{river}$ was set to 0.7120, which is an average value for modern rivers (Palmer and Edmond, 1989). The $(^{87}Sr/^{86}Sr)_{river}$ model input record is shown in Figure B.12.B.

Initial conditions for the model were calculated to assuming a steady state Sr cycle in the Late Permian, with a seawater $^{87}Sr/^{86}Sr = 0.7071$, corresponding to measured values in the Late Permian ocean (Sedlacek et al., 2014). Equations 1 and 3 were solved as a coupled system of differential equations using simple first-order Euler integration. We optimized the resulting model output by using non-linear fitting to adjust the river Sr flux, reflected in the R parameter, in order to achieve the best fit to the observed seawater $^{87}Sr/^{86}Sr$ isotope record (Figure B.12.A; red curve). The resulting estimates suggest the Early Triassic riverine Sr fluxes were general ~2-4 × higher than present day and briefly higher than 7 × (Figure B.12.C) in agreement with previously published results (Sedlacek et al., 2014).

The riverine PO_4^{3-} flux was estimated based on estimated riverine Sr flux by:

$$J_{river}^{P} = R \cdot J_{river}^{Sr} \cdot \left(P/Sr\right)_{river} \quad (5)$$

where $(P/Sr)_{river}$ is the P/Sr ratio of modern rivers. The major sources of P and Sr to the ocean is weathering release of P and Sr from the upper continental crust and transport of dissolved/particulate P and Sr to the oceans via rivers (Baturin, 2003; Paytan and McLaughlin, 2007; Van Cappellen and Ingall, 1994; Van Cappellen and Ingall, 1996). The modern reactive P flux to the oceans, sourced primarily by rivers, is estimated to be approximately (2–3) × 10^{11} mol yr^{-1} (Reinhard et al., 2017; Tyrrell, 1999). The vast majority of P in rivers is present as a solid phase; according to most estimates ~90% of the P delivered by rivers to the ocean is in particulate form (Froelich, 1988; Paytan and McLaughlin, 2007). About 99% of particulate P are removed from seawater at the coastal zones (Paytan and McLaughlin, 2007). Thus, the net riverine P flux (the total amount of P that can pass the coastal zone and dissolve in seawater) to the ocean is estimated to be 2–3×10^{10} mol yr^{-1}. The riverine Sr flux to the ocean is estimated to be 3.3×10^{10} mol yr^{-1} (Richter and Turekian, 1993). The estimated P/Sr ratio (moles/moles) therefore ranges from 0.61 to 0.91. In Figure 4.3C, we have presented modeling output using a P:Sr ratio of both 0.61 and 0.91, respectively, to test the modeling sensitivities associated with the P:Sr ratio.

Because the riverine flux represents the main phosphorus source to the ocean (Baturin, 2003; Paytan and McLaughlin, 2007; Van Cappellen and Ingall, 1994; Van Cappellen and Ingall, 1996), we can then model the seawater PO_4^{3-} concentration using a simple mass balance model:

$$\frac{d\left[PO_4^{3-}\right]}{dt} = \frac{J_{river}^{P}}{V_{Ocean}} - \frac{\left[PO_4^{3-}\right]}{\tau_{PO_4}} \qquad (6)$$

where [PO_4^{3-}] is the seawater phosphate concentration, J_{river}^{P} is the riverine PO_4^{3-} flux, V_{ocean} is the volume of the ocean, and τ_{PO4} is the residence time of PO_4^{3-} in the ocean.

The seawater residence time of PO_4^{3-} is thought to be depend significantly on average ocean redox conditions because the presence of iron oxides at the seawater-sediment interface inhibits diffusion of porewater PO_4^{3-} back to the water column, enhancing PO_4^{3-} burial efficiency (Handoh and Lenton, 2003; Ingall and Jahnke, 1997; Mort et al., 2007; Van Cappellen and Ingall, 1994; Van Cappellen and Ingall, 1996). To capture this behavior in our simplified model, we assume the residence time of PO_4^{3-} and the anoxic seafloor area follows a sigmoidal relationship in which τ_{PO4} increases when anoxic seafloor area expands, an assumption that has been applied in previous modeling studies (Ingall and Jahnke, 1997; Payne and Kump, 2007; Van Cappellen and Ingall, 1994). In the sigmoidal curve, the two endmembers are τ_{PO4} = 69 kyr when $\delta^{238}U = -0.4$ ‰, and $\tau_{PO4} = 4 \times 69$ kyr when $\delta^{238}U = -1.0$ ‰.

Equation 6 was integrated using first-order Euler integration with an initial [PO_4^{3-}] concentration of 0.610 uM (when P:Sr ratio = 0.61) and 0.736 (when P:Sr ratio = 0.91), calculated assuming the Late Permian ocean was at steady state. The resulting PO_4^{3-} concentrations are shown in Figure B.12.D. PO_4^{3-} concentrations peaked at ~251.6 Ma, ~251.2–250.9 Ma, 250.6 Ma, and 247.3 Ma, which generally correlate to peaks in anoxia seafloor areas calculated from the U isotope model (Figure 4.3).

B. 9 Box model estimates for f_{anox}

The implied changes to the extent of bottom water anoxia can be described by differential mass balance equations for the seawater uranium inventory and its isotopic composition, respectively (following Lau et al. (2016)):

$$\frac{dN_{sw}}{dt} = J_{riv}^{U} - J_{oxic} - J_{anox} \tag{7}$$

$$\frac{d(N_{sw} \cdot \delta^{238}U_{sw})}{dt} = J_{riv}^{U} \cdot \delta^{238}U_{sw} - J_{oxic} \cdot \delta^{238}U_{oxic} - J_{oxic} \cdot \delta^{238}U_{anox} \tag{8}$$

$$\delta^{238}U_{anox} = \delta^{238}U_{sw} + \Delta_{anox} \tag{9}$$

$$\delta^{238}U_{oxic} = \delta^{238}U_{sw} + \Delta_{oxic} \tag{10}$$

As with Eq. 2, Eq. 8 can be simplified to give an expression for the changing isotope composition:

$$\frac{d(\delta^{238}U_{sw})}{dt} = \frac{J_{riv}^{U} \cdot (\delta^{238}U_{riv} - \delta^{238}U_{sw}) - J_{oxic} \cdot \Delta_{oxic} - J_{anox} \cdot \Delta_{anox}}{N_{sw}} \tag{11}$$

where N_{sw} is the oceanic uranium inventory in moles, $\delta^{238}U_{sw}$ is the value of seawater, $\delta^{238}U_{riv}$ is the value of the riverine source, $\delta^{238}U_{anox}$ is the U isotope composition of anoxic sedimentary sinks, and $\delta^{238}U_{oxic}$ is average U isotope compositions of the remaining other sinks. Here, we simplify the inputs to J_{riv}^{U}, the riverine flux, whose modern value is ~4×10^{7} moles U/yr (Tissot and Dauphas, 2015). The outputs are assumed to consist of the anoxic sediment sink (J_{anox}) and the sum of the other sinks (J_{oxic}). In this model, we use the estimate of 0.6×10^{7} moles U/yr (Morford and Emerson, 1999) for J_{anox} and calculate J_{oxic} by mass balance to an initial steady-state value of 3.4×10^{7} moles U/yr. Δ_{anox} = +0.6 ‰ is the effective fractionation factor associated with anoxic sediment deposition (Andersen et al.,

2014), and Δ_{oxic} is the effective fractionation factor associated with the remaining other sinks (+0.005 ‰, calculated to maintain isotopic steady state in the modern ocean (e.g, Brennecka et al. (2011a), Montoya-Pino et al. (2010), and Wang et al. (Wang et al., 2016)).

We define the oxic and anoxic sinks in Eq. 7–11 assuming a first-order dependence on seawater U concentration:

$$J_{anox} = k_{anox} \cdot N_{sw} \cdot A_{anox} \quad (12)$$

$$J_{oxic} = k_{oxic} \cdot N_{sw} \cdot A_{oxic} \quad (13)$$

where A_{anox} and A_{oxic} are the total seafloor area overlain by anoxia waters and the total seafloor area overlain by non-anoxic waters, respectively, and k_{anox} and k_{other} are rate constants associated with anoxic sediment deposition and all other sediment deposition and are calculated for the moder n uranium system (e.g., Wang et al. (2016) and Lau et al. (2016)).

We further define the fraction of anoxic seafloor area overlain by anoxic water:

$$f_{anox} = \frac{A_{anox}}{A_{ocean}} \quad (14)$$

where f_{anox} is the total seafloor area overlain by anoxic waters, and A_{ocean} is the total seafloor area of modern ocean.

Equations 7 and 11 were solved using the same numerical method used for the Sr isotope model presented above. In order to drive the model, we adjusted the fraction of anoxic seafloor (f_{anox}) to optimize the fit between the model and measured U isotope composition. The modeling outputs of f_{anox} have been summarized in Figure 4.3B. In Figure 4.3B, we have presented modeling output without and with a diagenetic offset of 0.3 ‰, respectively, to consider uncertainties associated with the diagenetic offset between Early

Triassic carbonates and Early Triassic seawater. Model parameterization was based on studies of the modern U cycle and are summarized in Table B.3.

B. 10 Patterns of marine invertebrate clade recovery following the LPME

Patterns of recovery of marine invertebrate clades following the latest Permian mass extinction have been reviewed by Wei et al. (2015) and Chen and Benton (2012). Below is a brief summary:

Conodonts and ammonoids: these clades rebounded rapidly from the end-Permian mass extinction, but they suffered biodiversity losses at the ends of the Griesbachian, Smithian, and Spathian substages of the Early Triassic (Brayard et al., 2009; Orchard, 2007; Stanley, 2009).

Foraminifers, brachiopods, and ostracods: a sustained diversity increase began in the early Smithian (early Olenekian) (Song et al., 2011) and accelerated during the Anisian (early Middle Triassic) (Payne et al., 2011).

Gastropods: a sustained diversity increase began in the early Smithian (early Olenekian) (Song et al., 2011) and accelerated during the Anisian (early Middle Triassic) (Payne et al., 2011). The sizes of gastropod and bivalve shells were reduced across the P–Tr boundary and during the Griesbachian but returned to pre-extinction dimensions by the Anisian (Fraiser and Bottjer, 2004; Payne, 2005; Twitchett, 2007).

Trace-makers: they decreased during the LPME and recovered slowly in the Early Triassic (Chen et al., 2011; Pruss and Bottjer, 2004). Small trace-fossil burrow size, low tiering levels, and low ichnofabric indices (bioturbation) generally persisted until the end

of the Smithian substage. The early Spathian is marked by a strong increase in trace-fossil diversity and complexity (Chen et al., 2011; Pruss and Bottjer, 2004).

Reef-builders: they display a "reef gap", as represented by the absence of heavily calcified corals, that persisted through the Early Triassic (Payne et al., 2006; Wei et al., 2015).

B. 11 Ammonoid extinction rates

Data and methods

We evaluated ammonoid extinction rates at a high level of stratigraphic resolution (finer than substage) through the Early Triassic for the purpose of comparing biodiversity patterns with the detailed records of $\delta^{238}U$, $\delta^{13}C$, and $^{87}Sr/^{86}Sr$ from the Zal study section. We derived ammonoid range data from the Paleobiology Database (www.paleobiodb.org), which was accessed using the PaleoDB API. We supplemented those occurrences with Dienerian family ranges from the northern Indian margin from Ware et al. (2015), as the underlying occurrences for that dataset have not yet been published and cannot be included in the Paleobiology Database. We calculated extinction rates at the taxonomic family level because many genera are confined to a single biozone even with the high-resolution data available. Extinction rates were calculated using the boundary-crosser method (Alroy, 2016), and some time intervals had sparse occurrences, preventing us from using other methods such as the three-timer extinction rate (Brayard et al., 2013). We calculated extinction rates separately within three regions: the northern Indian margin, the western United States, and the Boreal realm (Canadian Arctic and Russian Arctic). Inter-regional correlations have been developed for some time intervals (such as the Smithian tropics;

Brayard et al., 2013) but are not available for the entire Early Triassic, so we were unable to produce a single multi-regional dataset. All extinction rates were calculated at a temporal resolution finer than substage; some intervals are formally defined biozones, whereas others are local/regional "horizons" or "beds." We also calculated a global extinction rate for ammonoid families at the Late Permian mass extinction horizon. This rate was calculated at the stage level, using Wuchiapingian, Changhsingian, and Early Triassic data from the Paleobiology Database.

Ammonoid zonal correlations

In the Griesbachian, the only published data with finer-than-substage resolution comes from the Boreal realm. We used the zonal correlations of Tozer (1994) and Ermakova (2002) and assumed equal durations for each of the three zones. The base of the lowest zone (*Otoceras concavum*) may overlap with the terminal Changhsingian in the paleoequatorial regions, but should be entirely post-extinction.

Dienerian data from the northern Indian margin were binned into the 12 Unitary Association zones of Ware et al. (2015), which we assumed to have equal duration. We also scaled the three Boreal zones to have equal duration, although we compressed the final interval (*Vavilovites sverdrupi/V. turgidus*/*Kingites korostelevi* Zone) to accommodate the observation that the overlying *hedenstroemi* Zone may be upper Dienerian at its base (Zakharov and Mousavi Abnavi, 2011). Implied correlations within the Dienerian in Figure B.13. are only approximate, although it seems plausible that the *Vavilovites meridialis* and *Kingites davidsonianus* beds of the northern Indian margin may be correlative to the *Vavilovites sverdrupi*, *V. turgidus*, and *Kingites korostelevi* zones in the Boreal region.

Brühwiler et al. (Brühwiler et al., 2010) defined 13 Unitary Association zones for the Smithian succession of the northern Indian margin. We scaled those intervals to be of equal duration and used the scheme of Brayard et al. (Brayard et al., 2013) to correlate ammonoid zones from the western USA (Brayard et al., 2013) and Boreal region (Ermakova, 2002; Tozer, 1994). Unlike in the Dienerian or Spathian, the inter-regional correlations are robust, particularly between the two paleoequatorial regions (Indian margin, western USA).

The Spathian timescale is based on the ammonoid zonation (including informal beds) developed for the western USA by Guex et al. We correlated the carbon isotope curve to Spathian ammonoid zonation by aligning the inflection point at the most negative Spathian carbon isotope values with the lower-middle Spathian boundary (above the *Procolumbites* beds) following Galfetti et al. (2007). The Zal carbon isotope curve implies that the middle and upper Spathian, as defined by ammonoids, may be very thin at this location. We scaled the three early Spathian intervals to have equal duration, and did the same for the four middle and late Spathian zones. We scaled the seven intervals to have equal duration. The Boreal region has been subdivided into four successive intervals (Ermakova, 2002), which we correlated tentatively to the more finely-resolved western USA scale. Implied correlations within the Spathian in Figure B.13. are only approximate.

We include data from the lower and part of the middle Anisian from the western USA and the Boreal realm. The western USA zonation is based on Bucher (1989) and is correlated approximately to Boreal zonations. Again, we scale the four western USA levels to have equal duration.

Extinction rate results

Boreal data may suggest a mid-Griesbachian extinction peak (*Otoceras boreale* Zone), although the boundary-crosser value is only slightly elevated. However, there are only a few boundary-crossing families in this interval, soon after the LPME, so it is mathematically impossible to obtain high absolute extinction rates. This turnover, which marks a transition from dominant Otoceratidae to dominant Ophiceratidae, is likely an important event.

Ammonoids suffered elevated family extinction rates around the middle-late Dienerian transition on the northern Indian margin (*Ambites bjerageri*/*Ambites lilangensis* beds and *Vavilovites meridialis* beds of Ware et al. (2015). In the Boreal region, the extinction in the *Vavilovites sverdrupi/V. turgidus*/*Kingites korostelevi* Zone is slightly later, within the late Dienerian, in our correlation scheme. However, correlations in this interval are tentative so it is possible that the two extinctions were synchronous. At this point, it is not possible to determine whether extinctions near the middle-late Dienerian transition were synchronous or slightly diachronous.

All three regions exhibit a pronounced and synchronous extinction peak at the end of the middle Smithian (*Nyalamites angustecostatus* beds along the northern Indian margin, Owenites beds/*Meekoceras gracilitatis* Zone in the western USA, and *Euflemingites romunderi*/*Lepiskites kolymensis* Zone in the Boreal region). On the northern Indian margin, extinction rates are also elevated in the preceding interval (*Pseudoceltites multiplicatus* beds); this either indicates that the extinction spanned both intervals in the late middle Smithian or that the earlier extinctions are biased by the Signor-Lipps effect.

Boreal ammonoids apparently underwent a major extinction in the latest Spathian (*Keyserlingites subrobustus*/*Olenikites spiniplicatus* Zone), although the western USA data do not show a comparable peak. Instead, extinction rates in the western USA were slightly elevated for several intervals leading up to the Spathian/Anisian boundary. Mid-late Spathian data are sparse in the western USA, so it seems reasonable to interpret the prolonged episode of slightly elevated rates as arising from the Signor-Lipps effect in the boundary-crosser data, which would be consistent with a larger extinction near the Spathian/Anisian boundary. It is also possible that the Boreal losses were a regional phenomenon that was more intense than extinctions elsewhere.

Table B.1. $\delta^{238}U$ data with selected geochemical data for the Zal section.

Sample	$\delta^{238}U$	elevation	Ca	Mg	Al	Mn	Sr	Th	U
	‰	m	ppm	ppm	ppm	ppm	ppm	ppm	pp
IZ 5	0.03	-37.45	383428.61	6217.78	984.74	983.60	402.79	0.44	0.18
IZ 6		-36.85							
IZ 7	-0.23	-34.35	337615.58	5478.71	1577.42	720.50	460.76	0.68	1.37
IZ 8	-0.17	-32.75	131791.99	10864.79	8714.27	402.38	492.01	2.54	1.24
IZ 9		-30.55							
IZ 11		-28.05							
IZ 12	-0.14	-25.85	341961.70	5711.62	1882.14	572.52	391.20	0.62	0.17
IZ 13		-25.15							
IZ 14	0.05	-23.65	342734.46	17344.24	1269.83	1142.94	391.53	0.64	0.16
IZ 15	-0.05	-22.95	78061.86	11499.00	9094.46	306.60	395.22	3.68	1.30
IZ 16	-0.21	-22.22	346947.02	5524.67	1661.68	1048.25	444.86	0.49	0.10
IZ 17		-20.95							
IZ 18	-0.16	-20.30	63997.82	6022.54	8538.49	184.66	1334.85	2.97	2.32
IZ 19		-19.2							
IZ 20	0.07	-17.45	946219.57	14606.60	1858.37	2157.80	858.43	0.40	0.61
IZ 21		-16.27							
IZ 22	-0.07	-14.60	54395.71	7083.45	12236.62	232.79	702.82	2.14	0.60
IZ 23	-0.12	-13.83	303719.80	4220.59	1828.76	810.70	538.62	0.77	0.28
IZ1	-0.13	-10.00	36785.68	7854.17	12931.80	142.43	356.78	0.37	0.12
IZ 26	-0.20	-8.95	369373.58	4896.88	816.82	1779.55	580.93	2.02	0.53
IZ 27	-0.19	-8.55	336849.21	5562.12	1577.76	1806.13	537.41	0.38	0.16
IZ 28									
IZ2	-0.32	-6.00	378434.55	6756.75	1166.07	735.15	330.11	0.57	0.09
IZ 33	-0.31	-4.35	366923.93	6211.15	1072.73	765.14	371.78	0.64	0.12
IZ 35		-3.78	350217.04	6002.70	1292.28	691.15	356.54	0.76	0.84
IZ3	0.05	-3.00	332172.13	6080.98	544.65	479.30	411.15	0.19	0.17
IZ 37		-2.98	365680.74	5926.56	841.52	593.85	352.71	0.55	0.08
IZ 38	-0.34	-2.82	351479.22	5590.69	843.00	612.00	342.97	0.53	0.09
IZ 40	-0.25	-2.25	324039.13	3808.22	1294.69	570.36	391.80	1.16	0.10
IZ 42	-0.20	-1.97	371817.40	5006.19	1979.68	673.93	362.55	0.93	0.10
IZ 44	-0.41	-1.60	365562.90	5998.35	1202.24	635.77	399.74	0.78	0.06
IZ 45	-0.37	-1.50	359059.12	5555.68	2365.82	554.76	352.41	0.96	0.08
IZ 46	-0.18	-1.27	356547.06	3931.09	1028.95	594.81	383.86	0.95	0.07

IZ 48	-0.24	-1.01	346229.83	3692.02	1003.23	667.98	429.38	0.89	0.08
IZ 49	-0.27	-0.93	365801.44	5492.86	1086.48	532.03	429.81	0.89	0.09
IZ 50	-0.39	-0.85	353957.75	3985.60	1684.38	649.35	392.97	0.98	0.07
IZ 52	-0.22	-0.65	374639.03	5448.40	897.31	644.06	440.86	0.69	0.09
IZ 56	-0.32	-0.30	340176.66	7035.45	2599.52	584.19	426.22	1.08	0.11
IZ 57	-0.30	-0.25	89715.10	2131.78	1165.36	183.19	93.51	0.58	0.03
IZ 59	-0.32	-0.17	318727.03	6832.66	3207.30	680.09	363.23	1.08	0.11
IZ 60	-0.28	-0.12	297198.37	6286.54	2527.21	575.90	379.55	1.24	0.11
IZ 61	-0.23	-0.10	337415.51	6259.47	1951.33	648.35	392.01	1.26	0.10
IZ 62	-0.10	-0.05	301802.07	6718.56	1375.91	629.08	374.19	1.32	0.10
IZ 63	-0.42	0.00	128716.17	30811.02	3613.17	1064.25	231.87	2.87	0.15
IZ 64	-0.27	0.10	359060.94	4144.21	1179.82	601.93	386.29	0.96	0.07
IZ 65	-0.30	0.15	113141.25	26265.79	2965.67	856.80	394.02	2.67	0.09
IZ 67	-0.34	0.22	96758.96	34774.87	2406.68	1014.24	323.05	2.41	0.09
IZ 68	-0.28	0.47	225194.38	20398.10	1743.31	881.46	250.08	1.88	0.16
IZ 69	-0.33	0.50	233953.01	14272.98	1395.01	680.87	248.74	1.58	0.12
IZ 70	-0.36	0.52	310753.69	10375.95	816.24	700.90	277.04	1.03	0.09
IZ 71	-0.27	0.55	269672.50	23994.26	1098.35	884.69	285.11	1.40	0.13
IZ 72	-0.20	0.57	298525.47	9783.45	675.62	782.30	318.97	1.14	0.08
IZ 73	-0.35	0.60	357580.96	11014.27	629.90	747.94	304.72	0.80	0.07
IZ 74	-0.29	0.64	313640.70	27155.63	782.89	1064.89	314.96	1.07	0.09
IZ 75	-0.36	0.68	320217.97	10811.29	988.80	743.40	301.18	1.24	0.09
IZ 77		0.83	259888.75	61101.88	875.66	3101.67	412.55	0.74	0.21
IZ 78		0.92	272612.36	25013.82	1301.21	1160.89	292.23	1.39	0.10
IZ 79	-0.51	1.02	411465.16	15068.12	156.60	227.54	409.05	0.06	0.27
IZ 80	-0.34	1.07	261408.79	38469.89	1206.60	1468.50	330.38	1.04	0.11
IZ 81	-0.29	1.17	279019.94	19635.90	1272.25	949.20	282.08	1.32	0.13
IZ 83	-0.26	1.37	335104.48	9479.91	731.35	887.04	450.44	0.91	0.83
IZ 84	-0.34	1.48	229014.98	41694.65	916.06	1241.53	422.20	1.13	0.07
IZ 85	-0.04	1.57	247553.79	59672.75	795.57	1749.05	410.59	0.96	0.14
IZ 86	-0.32	1.82	246635.93	58085.18	860.55	2400.89	468.42	1.11	0.14
IZ 87	-0.41	1.93	373713.95	3436.90	480.15	937.46	900.47	0.28	0.08
IZ 88	-0.24	1.98	345128.66	4649.04	886.32	1095.98	561.68	1.12	0.21
IZ 89	-0.33	2.15	323221.43	11733.59	957.14	676.69	533.68	0.71	0.21
IZ 90	-0.52	2.32	371105.67	10194.32	614.22	528.44	610.69	0.42	0.29
IZ 91	-0.38	2.60	365353.04	7078.00	819.22	387.56	645.87	0.56	0.24

IZ6	-0.32	3.00	315647.58	14884.47	1733.06	899.48	408.82	1.14	0.15
IZ 93	-0.15	3.12	348679.06	5785.74	1098.87	524.91	582.65	0.84	0.12
IZ 94	-0.54	3.40	403017.66	3134.76	617.77	350.09	2867.95	0.40	0.28
IZ 95	-0.54	3.65	364140.71	2866.19	660.74	251.24	1135.56	0.40	0.29
IZ 96	-0.59	4.03	436174.62	3028.24	808.18	261.76		0.38	0.29
IZ 97	-0.36	4.32	383684.10	4155.39	1009.18	324.81	980.90	0.56	0.28
IZ 100	-0.32	6.00	357308.24	9424.40	1407.00	336.07	663.50	0.61	0.26
IZ 101	-0.46	6.30	378350.32	4711.36	2358.69	350.82	831.93	0.91	0.29
IZ 102	-0.53	6.90	403220.43	4864.73	823.01	315.63	943.78	0.40	0.20
IZ 103	-0.58	7.57	389902.17	4756.00	1419.88	281.69	813.54	0.53	0.20
IZ8		10.00	400102.29	4857.57	1460.49	241.81	607.15	0.38	0.22
IZ 110	-0.59	11.63	438299.88	2648.29	84.13	145.91	883.05	0.11	0.20
IZ 113	-0.63	14.60	457635.45	1533.53	949.78	64.39	1164.69	0.14	0.27
IZ10	-0.69	15.00	439551.26	1566.45	227.40	70.27	1039.58	0.12	0.25
IZ 115	-0.51	17.00	449802.95	1503.00	281.84	86.20	2008.62	0.08	0.24
IZ 116	-0.64	18.20	441931.36	4401.67	254.29	121.91	479.46	0.10	1.60
IZ 117	-0.69	19.00	440175.69	1583.48	159.63	60.04	1595.43	0.05	0.23
IZ11	-0.72	19.00	274179.30	955.04	77.06	36.07	1073.23	0.06	0.15
IZ 120	-0.16	22.35	392484.09	6256.66	2237.79	243.88	844.93	0.31	0.13
IZ 122	-0.37	25.35	431391.86	3517.19	658.76	124.71	421.39	0.37	0.80
IZ 123	-0.45	26.85	394963.92	3312.18	1034.15	159.09	1141.30	0.26	0.22
IZ12		30.00	368382.17	10801.30	7682.03	189.73			
IZ 126	-0.51	33.30	428870.83	1714.33	1015.19	116.23	3505.77	0.19	0.12
IZ 127	-0.34	34.85	381935.80	7869.82	4512.15	170.68	449.95	0.48	0.12
IZ 128	-0.29	36.15	353430.60	9063.07	7846.68	158.05	449.00	1.16	0.23
IZ14	-0.46	50.00	336168.95	6145.40	6211.05	154.80	327.94	0.78	0.21
IZ20	-0.54	100.00	377297.26	3772.87	2441.33	229.69	352.04	0.37	0.11
IZ21	-0.69	125.00	390923.81	4824.31	1650.03	158.93	850.07	0.38	0.40
IZ23	-0.62	140.00	400046.99	2850.57	1735.26	96.03	1112.22	0.60	0.32
IZ24	-0.63	145.00	372794.34	3059.30	3106.42	101.43	1445.52	0.61	0.36
IZ25	-0.53	155.00	373761.27	3995.66	3128.69	141.25	1890.04	0.87	0.26
IZ26	-0.52	160.00	353956.44	3944.13	3627.61	123.09	1618.83	0.83	0.31
IZ29	-0.68	178.00	370526.44	4314.90	4071.07	99.60	1197.45	0.52	0.18
IZ30	-0.73	207.50	239211.28	24381.70	11547.85	152.38	894.27	1.30	0.35
IZ32a	-0.77	227.60	357989.86	3604.31	8049.46	87.86	1965.82	0.54	0.16
IZ35	-0.56	242.60	388254.35	5826.08	6389.57	77.37	3226.25	0.32	0.16

IZ39	-0.52	262.15	403834.20	2864.34	1523.55	89.15	1426.34	0.17	0.14
IZ43	-0.56	314.40	329824.25	6501.19	8218.21	118.25	1479.52	0.62	0.19
IZ60	-0.63	333.00	354273.95	4566.85	4260.36	73.88	990.78	0.70	0.26
IS61	-0.56	335.50	400452.06	2383.44	3258.72	53.88	1217.09	0.38	0.34
IS62	-0.56	343.00	355415.63	4147.73	7962.18	107.30	2386.59	0.64	0.30
IS63		345.50	406501.07	3100.15	2797.27	44.84	906.89	0.24	0.42
IS 64	-0.53	346.00	384852.40	3214.27	1275.82	79.89	899.24	0.30	0.38
IS 65	-0.56	348.00	307792.52	5477.24	3802.44	132.19	1383.24	0.47	0.28
IS 66	-0.46	357.10	398805.40	3614.15	1265.05	60.79	1162.94	0.34	0.45
IS 68	-0.47	369.20	412850.58	2266.57	700.61	31.15	1721.69	0.19	0.49
IS69		374.30	408918.15	2849.40	424.12	43.12	846.00	0.12	0.43
IS70a		378.50	429223.15	2435.55	393.41	115.40	1041.26	0.08	0.29
IS70	-0.68	379.80	412762.99	2895.86	321.50	48.92	972.41	0.09	0.31
IS71	-0.51	383.30	429623.91	2120.19	437.58	25.58	1437.89	0.24	0.53
IS72		389.80	429480.22	2613.88	565.86	38.99	1657.84	0.23	0.54
IS73	-0.47	391.00	427940.14	2184.03	375.79	33.85	1531.71	0.26	0.61
IS74	-0.51	393.00	434343.98	2018.70	301.86	35.57	2845.02	0.09	0.21
IS75	-0.39	394.40	361778.64	2392.91	376.80	43.48	2752.90	0.19	0.22
IS76	-0.52	406.50	389186.05	3048.17	534.68	104.32	1070.51	0.11	0.24
IS77	-0.46	413.50	399587.53	4054.94	617.52	160.08	1169.63	0.28	0.48
IS79	-0.44	429.50	400318.84	11638.79	372.97	165.98	395.05	0.06	0.26
IS80	-0.44	434.50	404322.78	1787.63	294.91	13.91	1322.13	0.13	0.40
IS81	-0.43	439.50	383532.84	18955.51	437.57	174.44	339.16	0.15	0.31
IS82	-0.51	443.50	422546.26	1797.40	289.80	12.30	814.23	0.05	0.51
IS83a	-0.58	446.50	416158.94	2568.82	278.40	29.38	512.85	0.06	0.32
IS83	-0.49	447.50	424475.96	2433.98	340.81	39.86	376.87	0.05	0.39
IS84	-0.53	452.50	416584.28	2982.96	238.56	54.41	565.05	0.09	0.34
IS85	-0.52	457.50	416846.27	1809.22	148.40	17.54	607.38	0.02	0.26
IS86	-0.68	462.50	427421.50	1737.60	299.08	24.91	952.19	0.09	0.41
IS90	-0.51	467.50	430041.16	2082.12	521.61	33.37	1499.35	0.06	0.27
IS92		474.50	368834.09	1584.62	475.79	68.36	1593.57	0.13	0.43
IZ93	-0.50	478.50	390258.30	2075.62	617.58	42.76	1711.78	0.12	0.30
IZ98	-0.59	504.30	410400.85	3329.11	253.90	118.33	601.69	0.09	0.37
IZ99		512.50							
IZ100	-0.50	513.60	380258.77	3794.44	1401.29	207.96	750.21	0.54	0.66
iz 104	-0.50	525.70	384288.56	3489.09	1194.76	248.03	1021.43	0.27	1.20

iz106	-0.43	540.60	377122.45	1809.26	841.58	170.69	495.22	0.17	0.33
IZ108	-0.36	544.35	372729.77	5275.71	1176.08	203.33	740.45	0.49	1.31
IZ109	-0.37	546.00	467147.33	9554.65	1952.28	207.30	871.27	0.43	1.01
IZ110	-0.42	548.80	396500.04	2775.03	812.57	89.86	1069.78	0.48	1.36
iz111		554.60							
iz113	-0.54	565.70	392501.99	3563.96	637.73	117.12	810.33	0.54	1.24
iz116		577.60	391858.89	3950.84	353.06	116.27	434.93	0.10	1.66
iz120	-0.70	594.00	381957.98	4220.78	869.19	164.55	516.22	0.42	1.12
iz122	-0.39	600.00	371117.48	3658.08	1015.11	124.53	387.84	0.39	0.86
iz124	-0.31	602.30	214530.27	123163.65	886.89	475.33	93.95	0.38	0.43
iz125	-0.38	609.30	252779.75	70452.52	4392.77	346.54	133.35	0.94	0.47
iz126	-0.31	614.30	216659.66	120571.49	729.47	479.95	93.39	0.37	0.43
iz128a	-0.34	626.50	220492.36	124955.35	576.46	105.30	118.09	0.16	1.39
iz130	-0.52	637.00	285175.98	8346.66	579.35	81.08	147.59	0.20	0.59
iz131	-0.36	639.20	362677.75	26366.91	979.46	246.78	235.28	0.35	0.69
iz132	-0.24	645.20	385635.83	4168.63	424.82	48.41	260.53	0.26	1.32
iz135a	-0.36	666.90	212706.99	123079.63	1371.21	105.55	64.83	0.36	0.98
iz137	-0.47	674.90	211457.62	121681.51	1596.00	270.72	58.37	0.40	0.25
iz140	-0.29	683.90	227309.86	110884.25	1778.38	181.92	107.91	0.32	0.59
iz141	-0.24	687.40	205025.42	125462.49	952.28	156.65	51.53	0.25	0.49
iz142	-0.46	690.50	190395.34	111479.00	1399.70	244.58	84.91	0.35	0.46
iz145	-0.43	703.20	212502.94	121742.82	676.45	216.52	71.67	0.21	0.99
IZ148	-0.39	712.70	194534.32	114766.61	916.74	192.15	57.96		0.29
IZ150	-0.43	718.50	208341.49	118686.72	2082.05	98.08	71.78	0.39	0.92
IZ151a	-0.66	721.50	191356.71	110514.92	2048.55	143.13	101.18	0.32	0.40
IZ152	-0.40	724.70	194405.27	118255.28	1385.07	142.84	91.99	0.36	0.38
IZ153a	-0.52	728.00	218534.06	125261.29	295.60	286.94	83.13	0.08	0.65
IZ154	-0.50	731.00	355905.36	5682.93	2142.78	400.17	326.70	0.51	0.76
IZ155	-0.62	734.00	212633.52	109344.17	4596.32	414.37	109.51	0.63	0.70
IZ156	-0.64	737.00	206994.25	120699.58	539.46	149.26	73.05	0.10	1.00
IZ157	-0.59	740.00	215635.11	124815.01	891.02	133.00	88.14	0.16	1.07
IZ158	-0.65	743.00	208849.01	121611.62	658.36	63.53	92.76	0.09	1.34
IZ160	-0.53	749.00	219331.86	124122.59	279.35	58.78	85.58	0.09	0.83

Table B.2. Strontium and phosphorus model parameterization

Parameter	Value	Reference
Sr	1.25×10^{17} moles	Richter and Turekian (1993)
J_{river}^{Sr}	3.3×10^{10} moles/yr	Richter and Turekian (1993)
J_H	2×10^{10} moles/yr	Richter and Turekian (1993); Sedlacek et al. (2014)
J_{DC}	0.3×10^{10} moles/yr	Richter and Turekian (1993)
$(^{87}Sr/^{86}Sr)_{river}$	0.7090, 0.7210	Palmer and Edmond (1989), and see adjusting above
$(^{87}Sr/^{86}Sr)_H$	0.7030	Albarède et al. (1981)
$(^{87}Sr/^{86}Sr)_{DC}$	0.7084	Richter and Liang (1993)
τ_{Sr}	3×10^6 yr	Hodell et al. (1990)
J_{river}^{P}	2×10^{11} moles/yr	Tyrrell (1999)
$(P/Sr)_{ratio}$	0.61–0.91 moles/moles	Calculated using modern riverine fluxes
τ_{PO4}	Follows a sigmoidal relationship with anoxic seafloor area	Payne an Kump (2007); Ingall and Jahnke (1997); Cappellen, E. D. Ingall (1994)
V_{ocean}	1.34×10^{21} L	

Table B.3. Uranium box model parameterization

Parameter	Value	Reference
$N_{sw,0}$	1.96×10^{13} mol U	Ku et al. (1977)
J_{riv}^{U}	4×10^{7} mol U yr^{-1}	Morford and Emerson (1999)
J_{anox}	0.6×10^{7} mol U yr^{-1}	Morford and Emerson (1999)
J_{oxic}	3.4×10^{7} mol U yr^{-1}	Calculated at steady state conditions
$\delta^{238}U_{river}$	–0.26 ‰	Andersen et al. (2017)
$\delta^{238}U_{seawater}$	–0.39 ‰	Tissot and Dauphas (2015)
Δ_{anox}	+0.6 ‰	Andersen et al. (2014)
Δ_{oxic}	+0.005 ‰	Calculated at steady state conditions
k_{anox}	1.41×10^{-19} yr^{-1} m^{-2}	Calculated using modern parameters with equation (*14*)
k_{oxic}	4.82×10^{-21} yr^{-1} m^{-2}	Calculated using modern parameters with equation (*13*)
A_{ocean}	3.62×10^{14} m^2	Lutgens, Frederick. Essentials of Geology. New York: MacMillan, 1992: 269.
V_{ocean}	1.34×10^{21} L	"The World Ocean." The Columbia Encyclopedia. CD-ROM. 2007, 6th Ed. New York: Columbia University Press.
Diag. corr. factor	0.3 ‰	Romaniello et al. (2013)

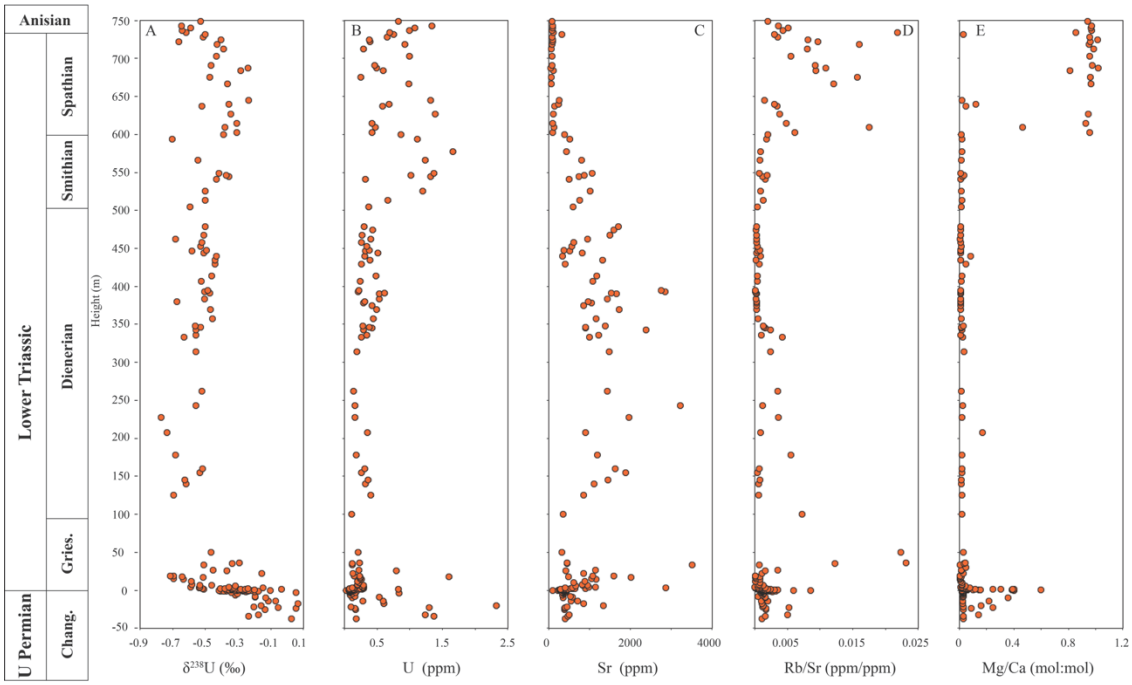

Figure B.1. Geochemical profile of Zal, Iran. (A) δ^{238}U profile, (B) U concentration profile, (C) Sr concentration profile, (D) Rb/Sr ratio profile, and (E) Mg/Ca (mol:mol) profile. Chang.: Changhsingian; Gries.: Griesbachian.

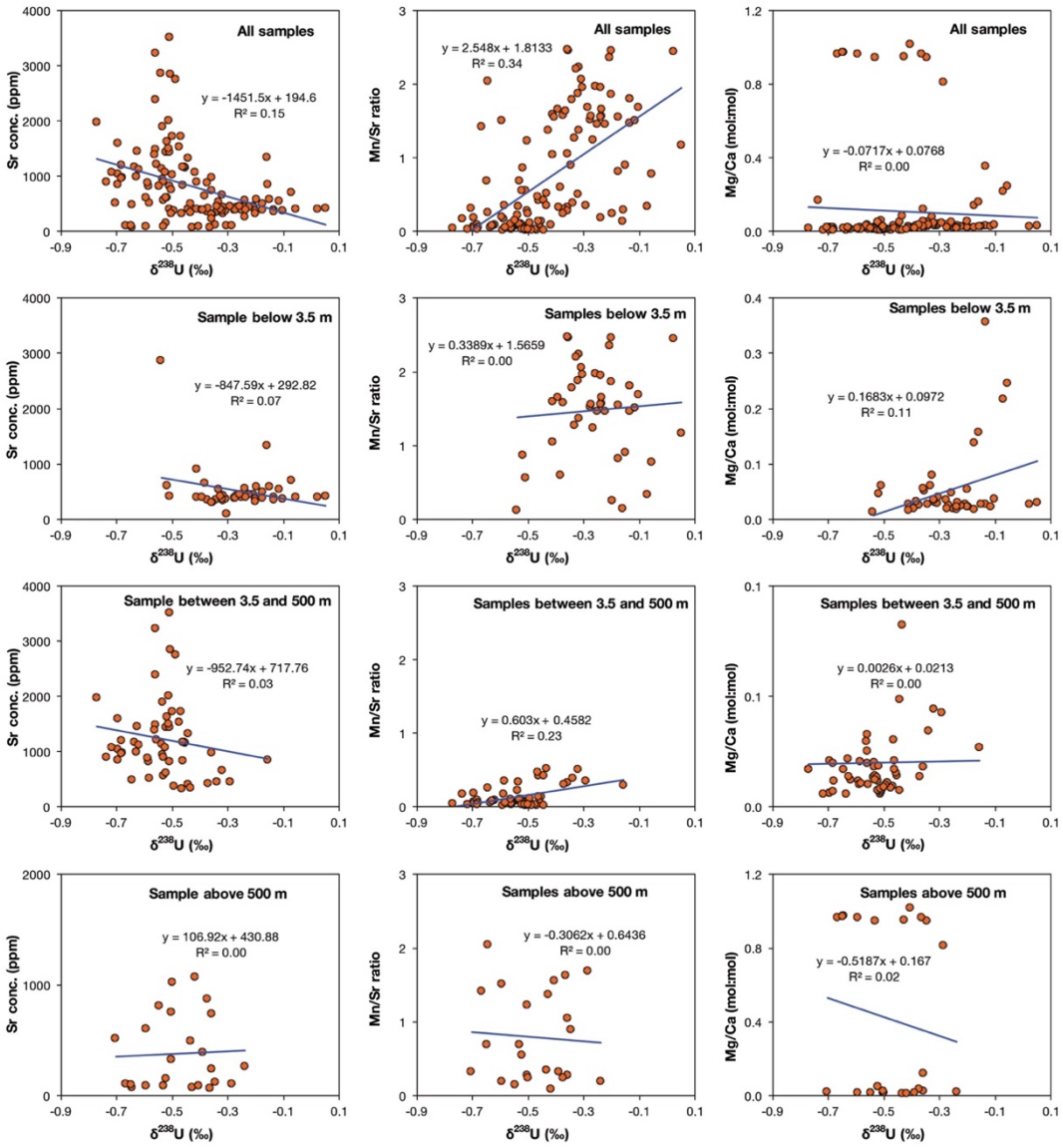

Figure B.2. Diagenetic evaluation crossplots of δ^{238}U–[Sr], δ^{238}U–Mn/Sr, and δ^{238}U–Mg/Ca (mol:mol) of all samples, samples below 3.5 m, samples between 3.5 m and 500 m, and samples above 500 m.

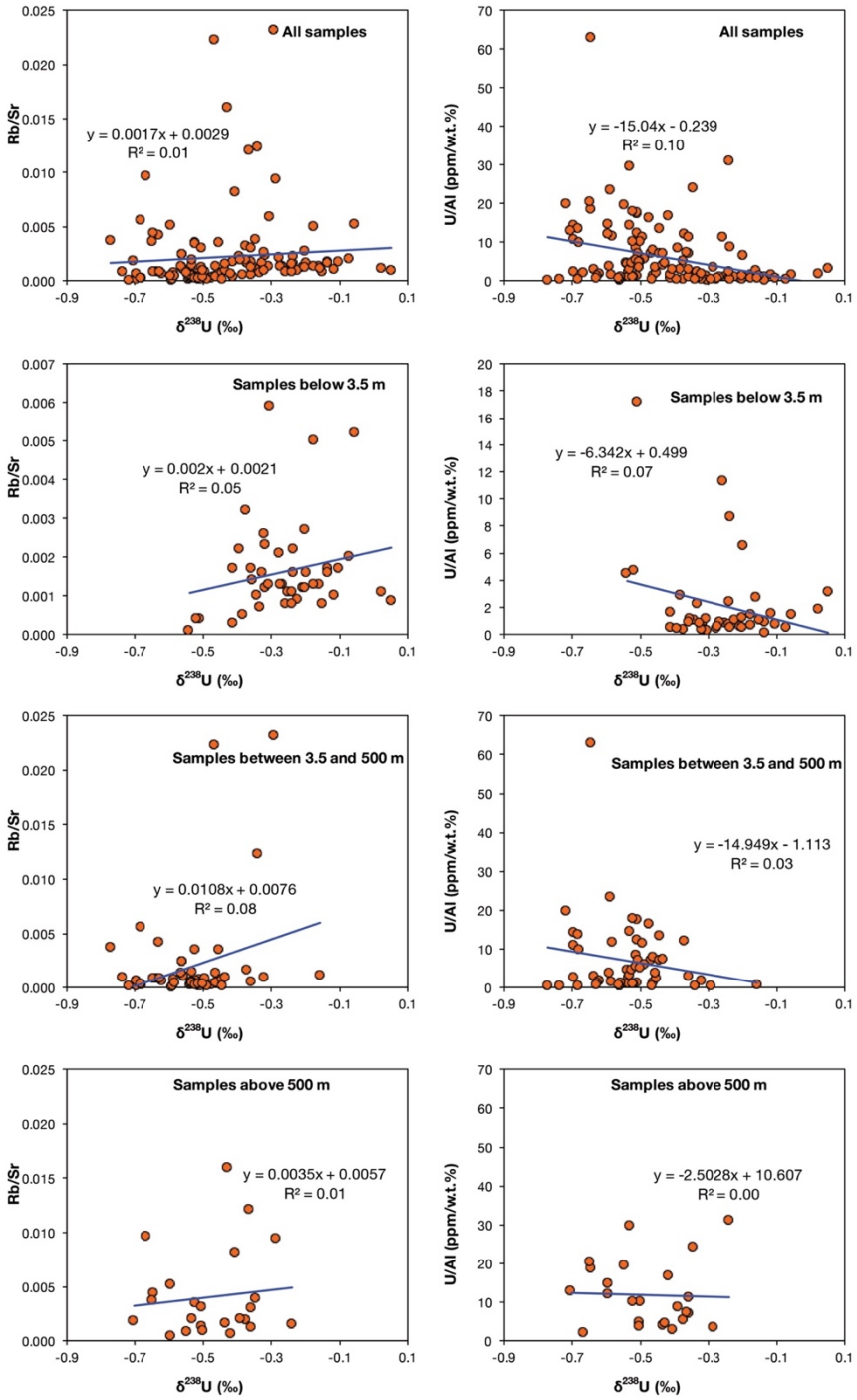

Figure B.3. Crossplots of δ^{238}U–Rb/Sr and δ^{238}U–U/Al ratio (ppm/w.t.%) for all samples, and samples below and above 500 m.

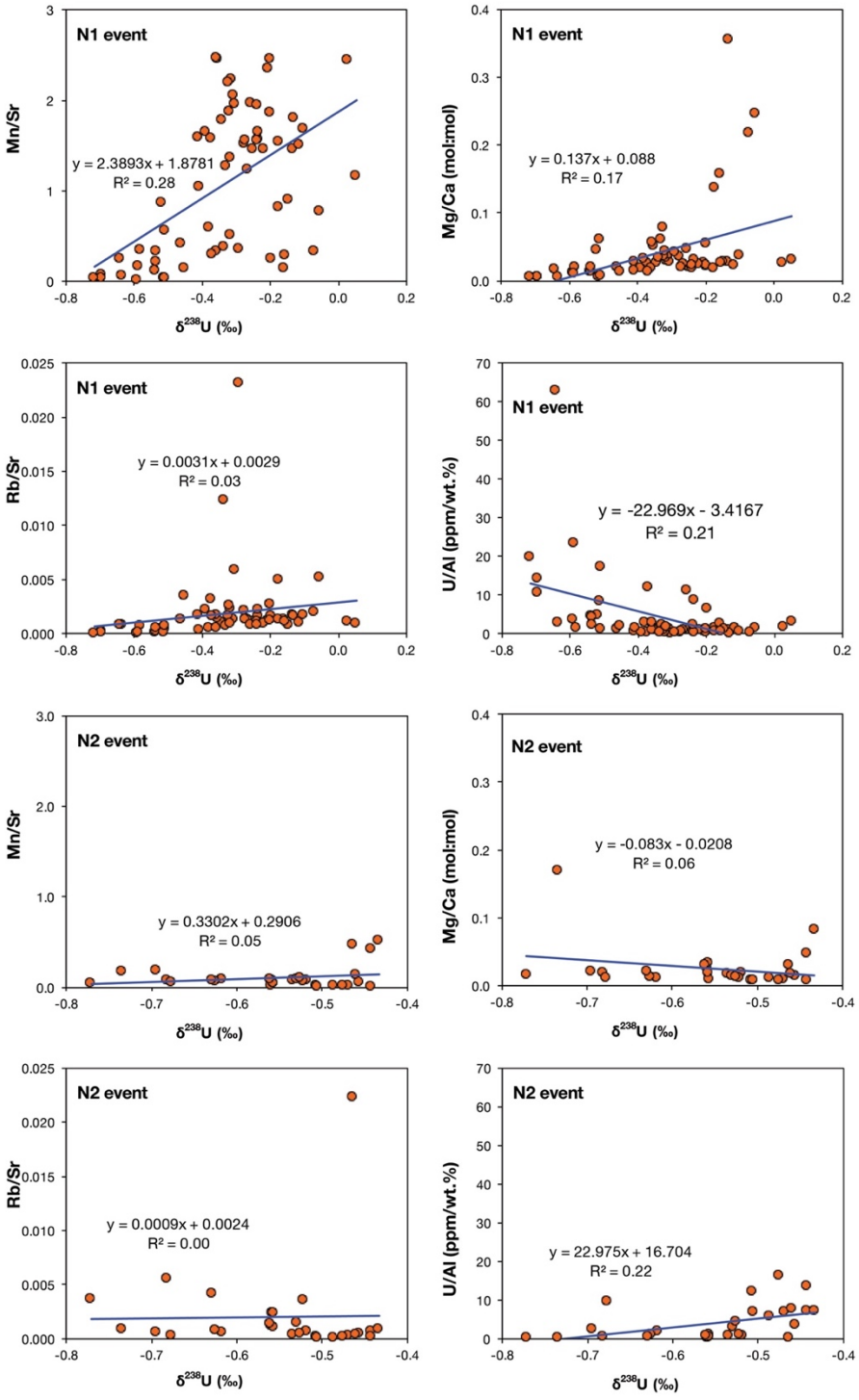

Figure B.4. Crossplots of δ^{238}U–Mn/Sr, δ^{238}U–Mg/Ca, δ^{238}U–Rb/Sr, and δ^{238}U–U/Al (wt./%) for anoxic events 1 and 2. The event numbers are marked in each panel.

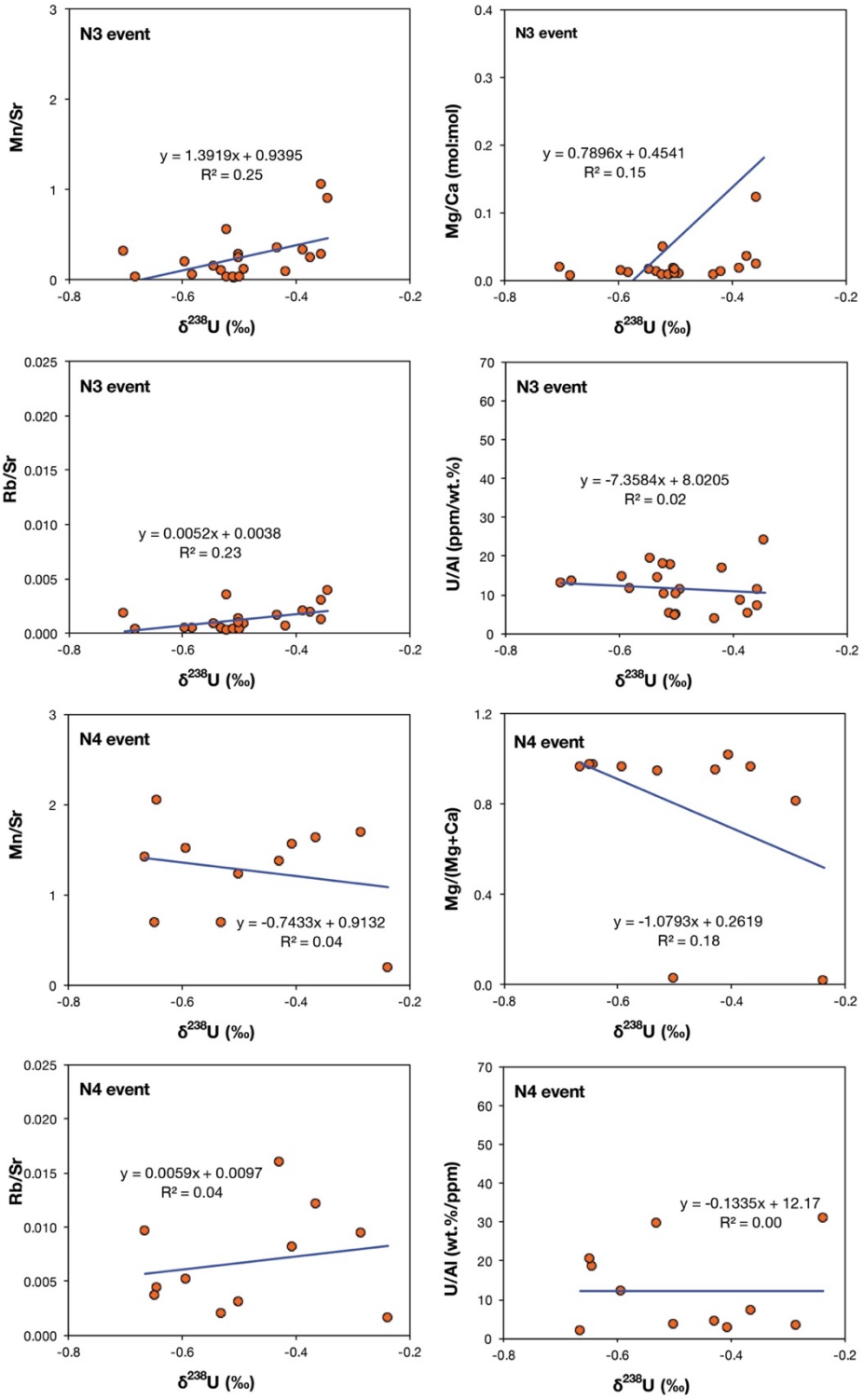

Figure B.5. Crossplots of δ^{238}U–Mn/Sr, δ^{238}U–Mg/Ca, δ^{238}U–Rb/Sr, and δ^{238}U–U/Al (wt./%) for anoxic events 3 and 4. The event numbers are marked in each panel.

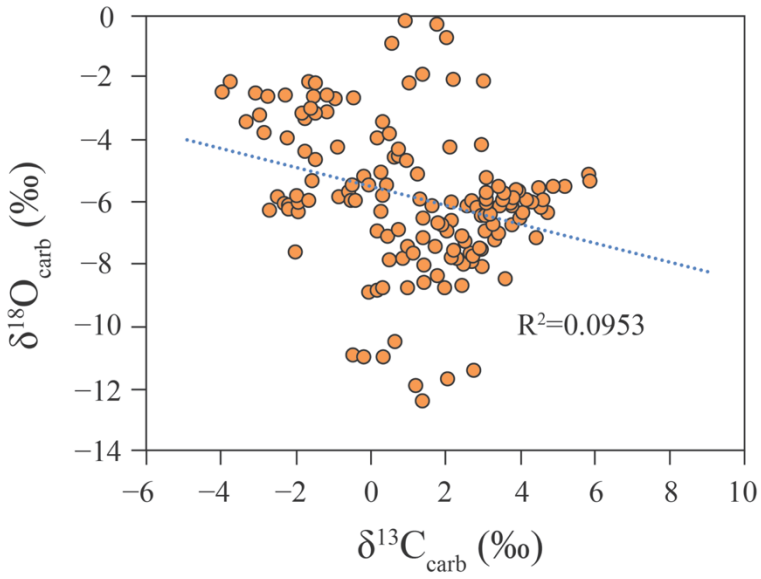

Figure B.6. Crossplots of $\delta^{13}C$– $\delta^{18}O$ for the Zal section. In the Zal section as a whole ($\delta^{18}O$ are data from Horacek et al. (2007)), there is no correlation between $\delta^{13}C$ and $\delta^{18}O$ (R^2 = 0.095).

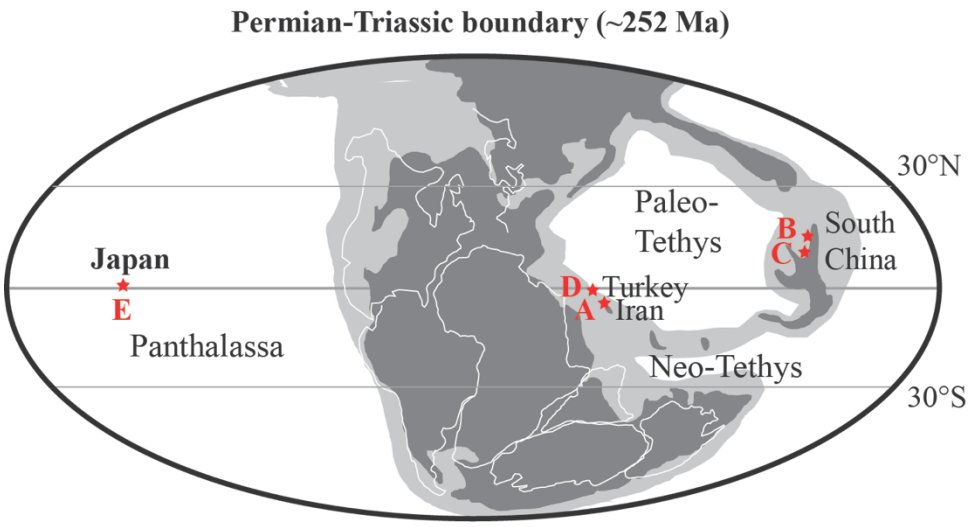

Figure B.7. Location of Iran, South China, and Turkey during the Permian-Triassic transition, ~252 Ma (modified after Payne et al. (60). (A): The Zal section (Iran). (B) The Dawen section (South China) studied by Brennecka et al. (22). (C): The Dajiang section (South China) studied by Lau et al. (18). (D): The Taşkent section (Turkey) studied by Lau et al. (18). (E): The Kamura section (Japan) studied by Zhang et al. (25).

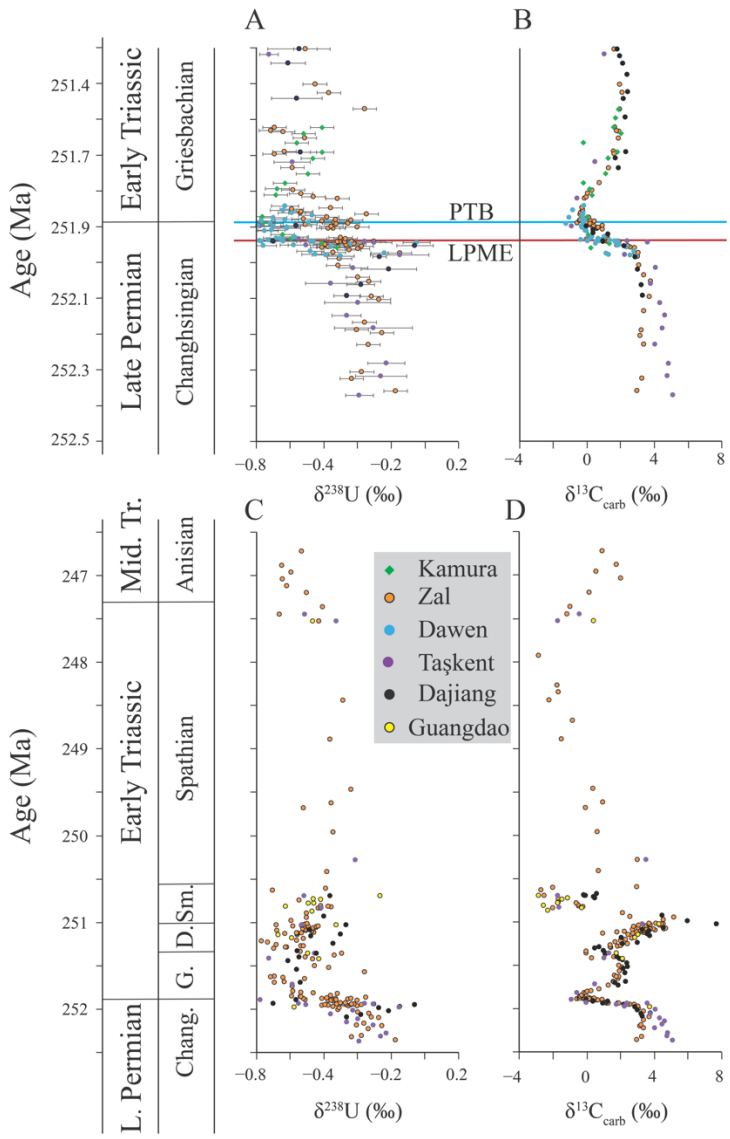

Figure B.8. Comparison of U and C isotope profiles for Zal, Dawen, Dajiang, Taşkent, and Kamura. $\delta^{13}C$ data for Dawen are from Chen et al. (2009), $\delta^{238}U$ data for Dawen are from Brennecka et al. (2011)), $\delta^{13}C$ and $\delta^{238}U$ data for Dajiang and Taşkent are from Lau et al. (2006), $\delta^{13}C$ data for Kamura are from Zhang et al. (2017), and $\delta^{238}U$ data for Kamura are from Zhang F. et al. (2018). The blue solid line denotes the Permian-Triassic boundary (PTB, 251.89 Ma), and the orange dash line denotes the latest Permian mass extinction horizon (LPME, ~251.94 Ma).

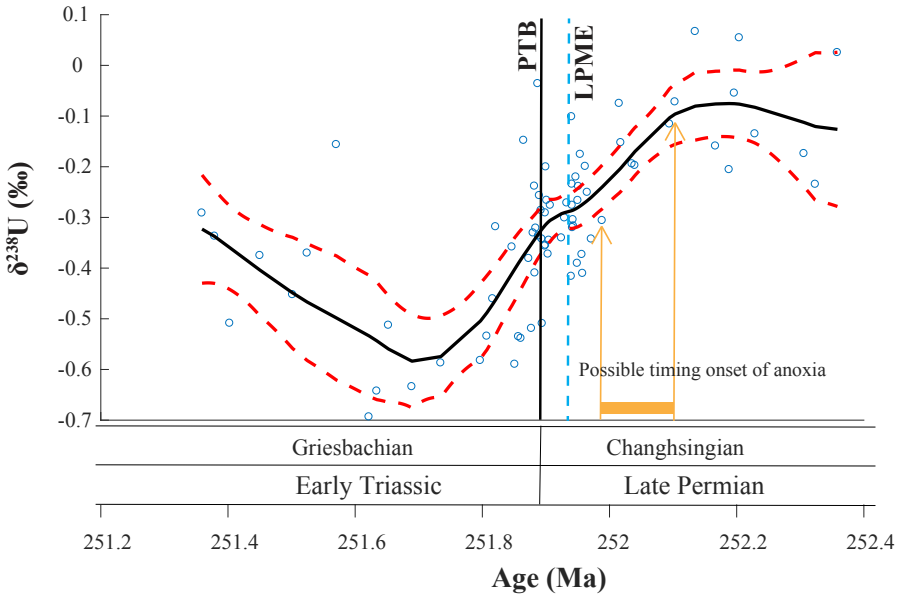

Figure B.9. A LOWESS trend showing inferred timing of onset of latest Permian oceanic anoxia. Included are all δ^{238}U data in Figure B.8.

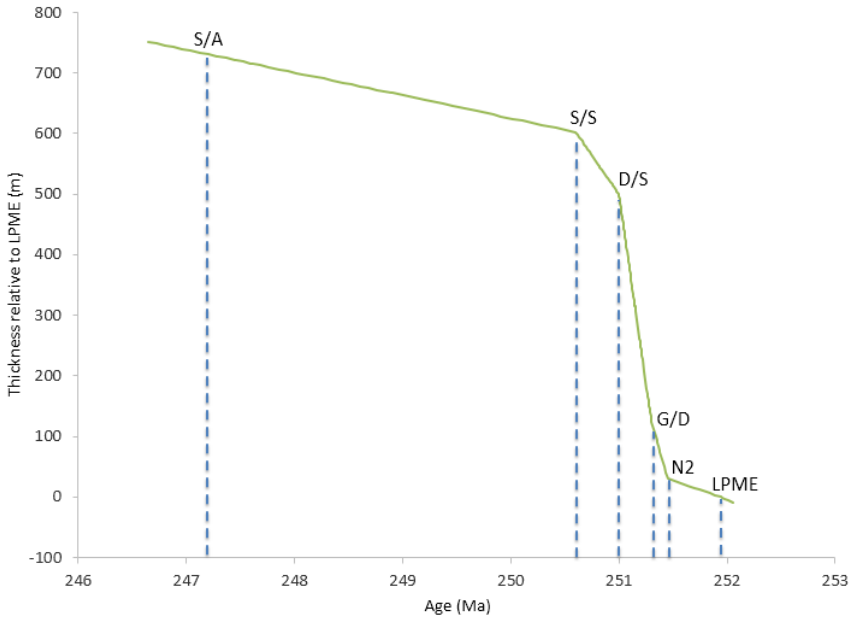

Figure B.10. Age-depth model for the Zal, Iran study section. Abbreviations: LPME = latest Permian mass extinction horizon; N2 = the N2 carbon-isotope excursion; G/D = Griesbachian-Dienerian boundary; D/S = Dienerian-Smithian boundary; S/S = Smithian-Spathian boundary; S/A = Spathian-Anisian boundary.

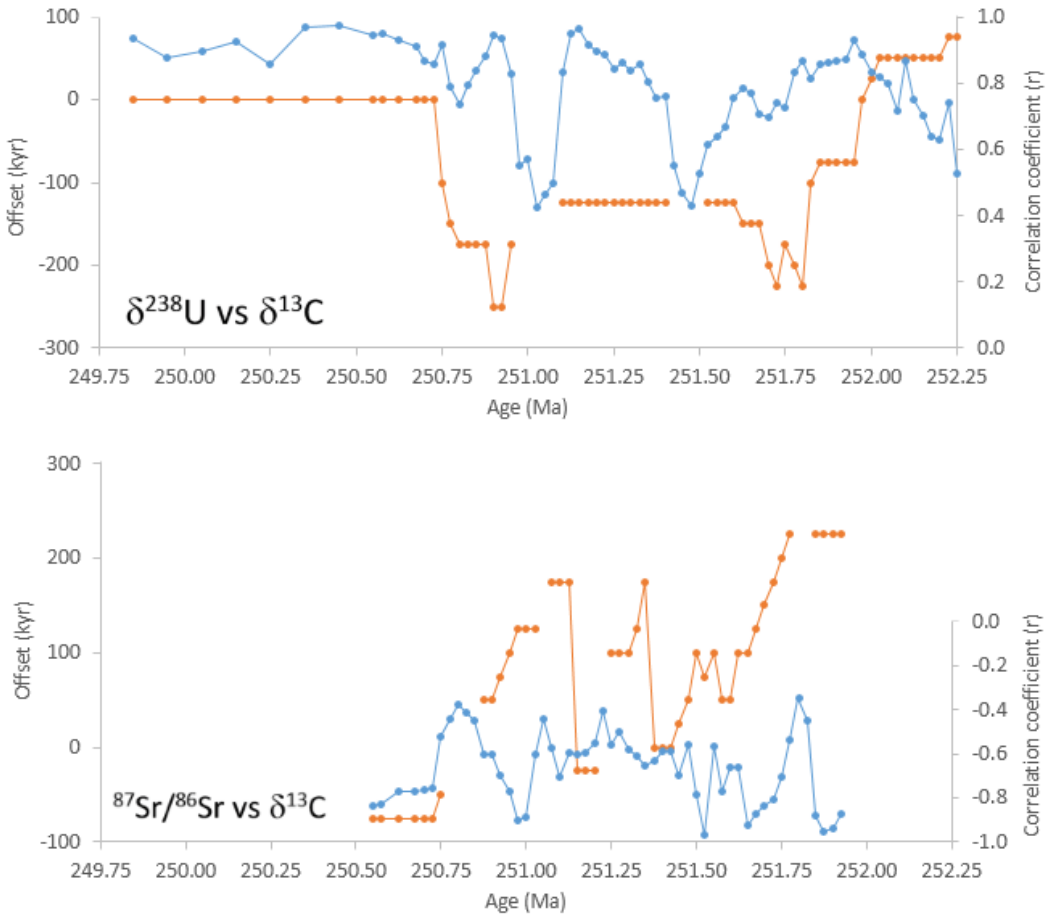

Figure B. 11. Cross-correlation analysis of LOWESS-smoothed curves for U-C-Sr records. Results of cross-correlation analysis for δ^{238}U-vs-δ^{13}C and ^{87}Sr/^{86}Sr-vs- δ^{13}C (bottom). The orange curves represent offsets in kyr (left y-axis), and the blue curves represent correlation coefficients (r; right y-axis). Gaps in the offset curves represent time windows with low correlation coefficients ($r < +0.6$ for U-C; $r > -0.5$ for Sr-C), which were characterized by less stable estimates of the offset magnitude.

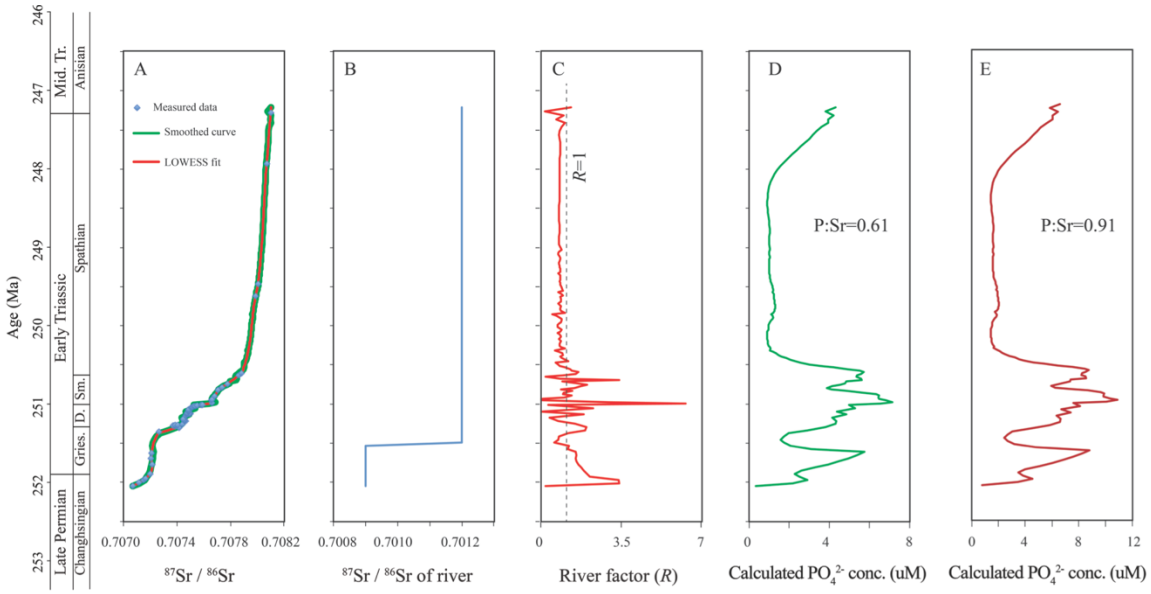

Figure B. 12. $^{87}Sr/^{86}Sr$-derived estimates of the continental weathering flux and calculated seawater PO_4^{3-} concentrations for the Early Triassic ocean. (A) Continental weathering fluxes, (B) riverine $^{87}Sr/^{86}Sr$, (C) "river factor" (F_R/F_M, = river flux / mantle flux), (D) calculated seawater PO_4^{3-} concentrations for the Early Triassic ocean assuming a P:Sr ratio of 0.61 mol:mol, and (E) calculated seawater PO_4^{3-} concentrations for the Early Triassic ocean assuming a P:Sr ratio of 0.91 mol:mol. In A, continental weathering fluxes were estimated based on the LOWESS trend of measured $^{87}Sr/^{86}Sr$ data (green line; from Sedlacek et al. (2014)) and a forward model fit (red line). In B, we set riverine $^{87}Sr/^{86}Sr$ ratios for the first 0.5 Myr lower than typical average seawater values of 0.7112 because the river flux at the PTB likely contained larger amounts of Sr from weathered Siberian Traps basalts. In D and E, seawater PO_4^{3-} concentrations were estimated based on calculated riverine phosphorus inputs assuming the oceanic residence time (T') of PO_4^{3-} and the anoxic seafloor area follows a sigmoidal relationship in which T' increases when anoxic seafloor area expands.

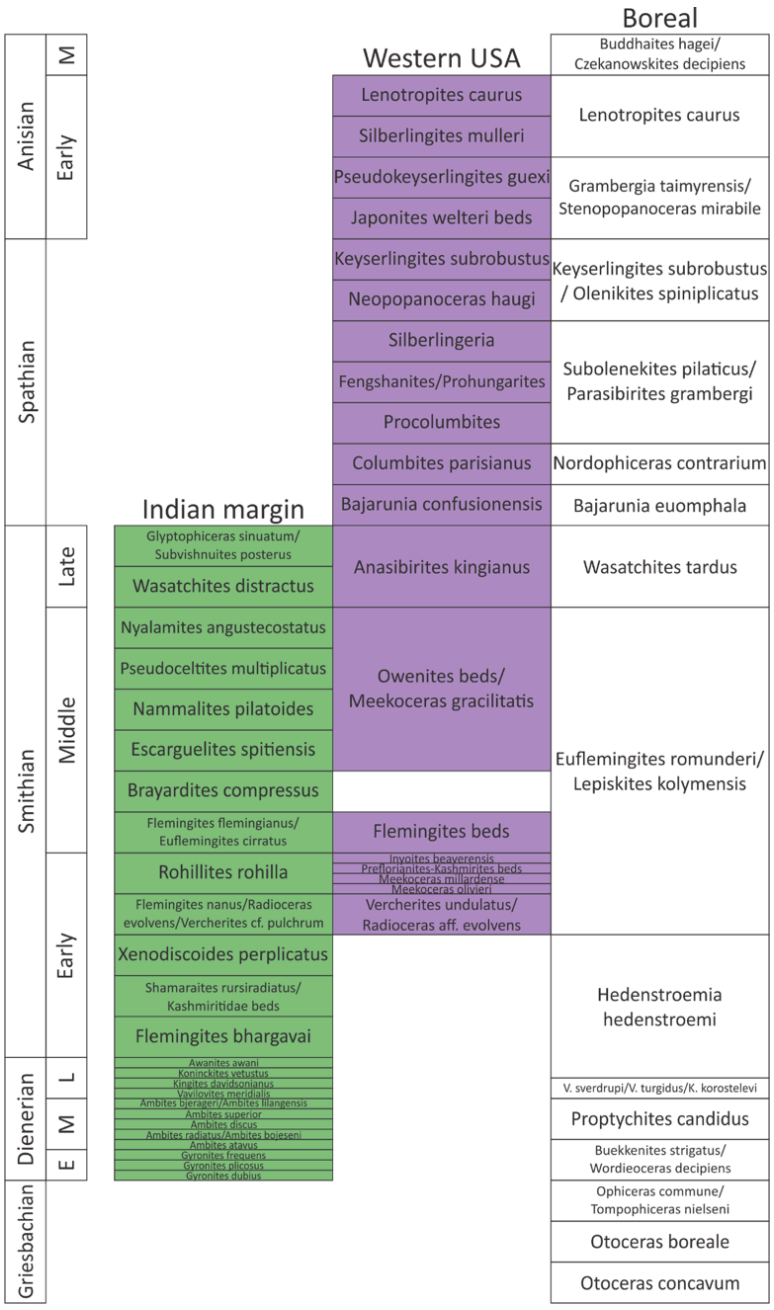

Figure B. 13. Interregional ammonoid zonation scheme. Note that some correlations are tentative. The sources on the data has been discussed in detail in section "Ammonoid extinction rates".

APPENDIX C

SUPPLEMENTARY INFORMATION FOR EXTENSIVE MARINE ANOXIA DURING THE TERMINAL EDIACARAN PERIOD

C. 1 Mass balance description of uranium isotope in the ocean

Uranium is a redox-sensitive trace metal with a residence time of ~500 kyr in the modern ocean (Dunk et al., 2002; Ku et al., 1977). Uranium occurs in two redox states in natural waters: soluble U(VI) under oxygenated conditions and insoluble U(IV) under anoxic conditions. Isotope fractionation between U(IV) and U(VI) is driven by the dominance of nuclear volume effects (Bigeleisen, 1996; Schauble, 2007). As a result, during reduction of U(VI) to U(IV), the reduced U(IV) is enriched in the heavier ^{238}U isotope, thus enriching the remaining dissolved U(VI) reservoir in the lighter ^{235}U isotope. This is observed in the Black Sea (Andersen et al., 2014; Rolison et al., 2017; Romaniello et al., 2009). Microbially-mediated reduction of U(VI) to U(IV) under anoxic conditions is associated with a large isotopic fractionation ranging between 0.68 ‰ and 0.99 ‰ (Basu et al., 2014; Stirling et al., 2015; Stylo et al., 2015).

The only major source of U to the ocean is oxidative mobilization of U from the upper continental crust and transport of dissolved U(VI) to the oceans via rivers. The $\delta^{238}U$ value of dissolved U in rivers is dominated by the U concentration and $\delta^{238}U$ of the source lithologies (Andersen et al., 2016). The estimated average $\delta^{238}U$ of the world's major rivers ranges between –0.26 ‰ and –0.34 ‰ (Andersen et al., 2017; Andersen et al., 2016; Noordmann et al., 2016), which reflects the estimated average $\delta^{238}U$ of the continental crust

[−0.30 ± 0.04 ‰ (2σ); Noordmann et al., 2016]; −0.31 ± 0.05 ‰ (2σ); Tissot and Dauphas, 2015]. In our U isotope modeling calculation below, we adopted a riverine δ^{238}U of –0.34 ‰.

There are multiple sinks for U in the ocean. The major sinks are sediments deposited beneath anoxic/euxinic bottom waters, sediments deposited beneath weakly oxygenated bottom waters, and marine carbonates (Dunk et al., 2002; Morford and Emerson, 1999; Tissot and Dauphas, 2015). Minor sinks include ferromanganese oxides and the hydrothermal alteration of oceanic crust (Dunk et al., 2002; Morford and Emerson, 1999; Tissot and Dauphas, 2015). The largest expression of U isotope fractionation (~0.4 ‰ to ~1.2 ‰) in the marine environment occurs during U burial in anoxic/euxinic sediments, like those of the Black Sea, the Saanich Inlet, and the Framvaren Fjord (Andersen et al., 2013; Holmden et al., 2015; Kaltenbach, 2013; Rolison et al., 2017; Weyer et al., 2008). By contrast, the fractionation of U isotopes during removal to suboxic sediments is only ~0.1 ‰ based on observations from the Peruvian continental margin and off the coast of Washington State, where sediments underlying weakly oxygenated waters have an average δ^{238}U of –0.28 ± 0.19 ‰ (Weyer et al., 2008) and –0.23 ± 0.19‰ (Andersen et al., 2016), respectively. Both natural and laboratory observations suggest at most a small offset between the δ^{238}U of primary carbonate precipitates and seawater (Andersen et al., 2014; Chen et al., 2016; Romaniello et al., 2013; Stirling et al., 2007; Weyer et al., 2008). Sedimentary carbonates may incorporate U(IV) from sulfidic pore waters, leading to values that are 0.2–0.4 ‰ higher compared with seawater, although this process can potentially be monitored by examining local depositional redox conditions where the carbonates precipitated (Romaniello et al., 2013). The fractionation of U isotopes during removal to

Mn nodules and metalliferous sediments is –0.24 ‰, and is well constrained by both natural samples (Goto et al., 2014; Wang et al., 2016) and adsorption experiments (Brennecka et al., 2011b). Seafloor alteration at high temperatures is assumed to have no isotope fractionation, and seafloor alteration at low temperatures is estimated to have a fractionation factor of 0.25 ‰ (Tissot and Dauphas, 2015).

C. 2 Non-anoxic sinks and the associated fractionation factors

A simplified schematic representation of the major source and sinks of U in the modern ocean along with their isotopic compositions (sources) or associated isotopic fractionations (sinks) is presented in Figure 1.2 (modified after Wang et al. (2016) and Tissot et al. (2015)). In order to simplify our mass balance calculations, several types of sinks are lumped into a single oxic sink, including Fe-Mn crusts, pelagic clays, low temperature and high temperature oceanic crust alteration, marine carbonates, and coastal retention. Additionally, the oxic sink and suboxic sink are lumped together into a single "other" sink to make the estimation of U removal associated with anoxic/euxinic sinks solvable. The overall U isotope fractionation factor for the oxic sink and the "other" sink are calculated as a weighted average of the fractionation factors for the individual components. The fractionation factors between the oxic sink and seawater and between the "other" sink and seawater are 0.01 ‰ (Δ_{oxic}) and 0.04 ‰ (Δ_{other}), respectively.

C. 3 Geological background of the studies sites

The geological and stratigraphic background of the Dengying Formation in the Yangtze Gorges area was detailed in Chen et al. (2013) and was summarized by Meyer et

al. (2014). To briefly summarize, the upper Ediacaran Dengying Formation overlies the lower–middle Ediacaran Doushantuo Formation and underlies the Yanjiahe Formation, which contains the Ediacaran–Cambrian boundary (Jiang et al., 2012). The Dengying Formation was deposited on a shallow marine carbonate platform in an inner shelf environment (Jiang et al., 2011), and its age is constrained between 551.1±0.7 Ma and ~541 Ma based on available radiometric dates and stratigraphic correlations (Amthor et al., 2003; Chen et al., 2015; Condon et al., 2005). The Dengying Formation is divided into three members. These are the Hamajing, Shibantan, and Baimatuo members from bottom to top (Figure C.1 and Figure 5.1). The Hamajing Member consists of peritidal dolostone. The Shibantan Member is composed of dark gray, thin-bedded, bituminous limestone interpreted to have been deposited in a subtidal environment (Zhou and Xiao, 2007). The Baimatuo Member is composed of light gray, massive peritidal dolostone (Chen et al., 2013; Zhou and Xiao, 2007).

The geological and stratigraphic background of the Dengying Formation in the Gaojiashan area was detailed in Cai et al. (2010) and Cui et al. (2016). To briefly summarize, the study area is located in the northwestern margin of the Yangtze Platform. Ediacaran successions in the Gaojiashan area consist of the Doushantuo and the Dengying formations, similar to classical Ediacaran successions in the southeastern margin of the Yangtze Platform. The Dengying Formation is divided into three members. These are the Algal Dolomite, Gaojiashan, and Beiwan members from bottom to top, which are typically correlated to the Hamajing, Shibantan, and Baimatuo members, respectively, in the Three Gorges area. The Algal Dolomite Member is characterized by light gray, peritidal dolostone. The overlying Gaojiashan Member is characterized by thin-bedded, subtidal,

fossiliferous calcisiltite-siltstone and mudstone with limestone interbeds. Microbial laminae and rip-up clasts are common in limestones of the upper Gaojiashan Member, which is capped by a thick sandstone bed. The overlying Beiwan Member consists of thick-bedded, peritidal dolostone with stromatactis-like structures and *Cloudina* fossils. The studied Gaojiashan Member is 55 m thick and can be divided into three units. The lower Gaojiashan Member is characterized by 19 m of greenish and brownish siltstone, greenish silicified tuffaceous siltstone, and silty shale. The middle Gaojiashan Member consists of 8 m of non-fossiliferous, interbedded calcisiltite-siltstone and calcilutite-mudstone, followed stratigraphically up-section by 12 m of fossiliferous calcisiltite-siltstone–calcilutite-mudstone interbeds that contain abundant pyritized fossils (*Conotubus and Gaojiashania*), calcareous microfossils (*Protolagena*), and horizontal trace fossils towards the upper part of this unit. In the succeeding 14 m of strata up-section, limestone becomes increasingly dominant over siltstone, fossils become increasingly scarce and are dominated by *Cloudina*, but wrinkled microbial sedimentary structures and rip-up clasts are common.

C. 4 Evaluation of carbonate diagenesis

Analytical results of the Wuhe section and the Gaojiashan section have been summarized in in Table C.1 and C.2. Sample dissolution protocol has been summarized in Table C.3.

Marine carbonate sediments can faithfully record chemical signatures of seawater provided that post-depositional processes have not caused significant alteration. To assess diagenesis, we used a combination of sedimentary petrography and standard geochemical criteria. Specifically, we compared our U isotope data to standard diagenetic indicators

such as Mn content, Sr content, Mn/Sr ratios, and O isotope composition to evaluate the influence of meteoric or burial fluids on preserved U isotope signatures.

To provide a framework for our interpretation, we briefly summarize the way in which petrography and geochemistry can be used to assess diagenesis (after Gilleaudeau et al., 2018). Broadly, grain size and the degree of preservation of primary textural features can be indicative of fluid composition during diagenesis. Fabric-retentive micritic to microsparitic fabrics that preserve original textural details indicate that recrystallization occurred in the presence of fluids similar in composition to seawater, leading to the inference that diagenesis was early—either synsedimentary or during shallow burial. Dolomitization may also occur during early diagenesis in the presence of seawater-buffered fluids, resulting in a high degree of fabric retention. By contrast, diagenesis in the presence of fluids very different in composition than seawater (meteoric or deep burial fluids) commonly results in crystal coarsening and destruction of primary textural details. Altered carbonate phases (both calcite and dolomite) are often sparry and characterized by planar grain boundaries.

The isotopic composition of oxygen can also be altered during diagenesis, and because of the high concentration of oxygen in diagenetic fluids, the oxygen isotopic composition of carbonate minerals will be reset at relatively low water/rock ratios (< 10; Banner and Hanson, 1990; Jacobsen and Kaufman, 1999). Diagenetic alteration tends to decrease $\delta^{18}O$ values, although the oxygen isotopic composition of meteoric fluids is highly variable depending on geographic location (Bowen and Wilkinson, 2002). Compilation of data for petrographically well-preserved Proterozoic carbonate phases indicates $\delta^{18}O$ values generally > −9 ‰ (Kah et al., 2012; Kah et al., 1999), although Kaufman and Knoll

(Kaufman and Knoll, 1995) suggested that values > −5 ‰ may be a more reliable indicator of relatively pristine oxygen isotope compositions in Neoproterozoic settings. These values can be used as an initial benchmark for assessing diagenesis.

Trace elements (Sr, Mn, and Fe) substituted into the lattice of carbonate minerals can also be used as diagenetic indicators. The incorporation of trace elements into the carbonate lattice is governed by the distribution coefficient, and different types of diagenetic fluids have different trace element compositions. Modern, well-oxygenated seawater is high in Sr relative to Mn and Fe such that primary precipitates and early diagenetic phases formed in the presence of seawater are generally enriched in Sr relative to Mn and Fe (Banner and Hanson, 1990). This is particularly true for aragonite because of the high distribution coefficient for Sr into aragonite compared to other carbonate minerals (Veizer, 1983). Early fabric-retentive dolostone can also be enriched in Sr relative to Mn and Fe, although dolomite generally has a lower preference for Sr (Vahrenkamp and Swart, 1990) and a higher preference for Mn and Fe (Mazzullo, 1992) compared to calcite.

Meteoric and burial fluids, by contrast, tend to be depleted in Sr relative to seawater (Banner and Hanson, 1990). The recrystallization process also acts to expel Sr from the lattice of carbonate minerals because of its relatively large ionic radius compared to Ca (Rimstidt et al., 1998). As a result, meteoric or burial diagenetic phases are often depleted in Sr relative to precursor marine phases. Burial fluids can also be substantially enriched in Mn and Fe, particularly under reducing conditions (Veizer, 1983). This commonly leads to Mn and Fe enrichment in burial diagenetic phases. Meteoric fluids are variable in their Mn and Fe content—depending largely on redox conditions—such that meteoric calcite phases can be characterized by enrichment or depletion of Mn and Fe.

These general relationships have led to the establishment of traditional criteria such as Mn/Sr ratio to assess the fidelity of primary geochemical signatures in carbonate rocks. For example, Kaufman and Knoll (1995) suggested that both limestone and dolostone with Mn/Sr ratios < 10 can be expected to retain their primary carbon isotopic signatures. In this study, we use a conservative Mn/Sr ratio of 2.5 as a benchmark for assessing diagenesis.

For the Hamajing Member at Wuhe, we examined four thin sections and we provide photomicrographs of samples HMJ-14 and HMJ-19 at various magnifications in Figure C.2. Overall, the Hamajing Member is comprised of relatively homogeneous micritic to microsparitic fabric-retentive dolomite with volumetrically insignificant veins and small voids filled with dolomite spar. For the overlying Shibantan Member, we examined ten thin sections and we provide photomicrographs of samples SBT-26, SBT-42, SBT-89, and SBT-107 at various magnifications in Figure C.3. The Shibantan Member is composed of micritic to microsparitic calcite that is fabric-retentive, preserving primary textural features such as thin, microbial laminations. Strata are generally organic-rich and preserve alternating organic-poor and organic-rich mm-scale laminations, as well as occasional intervals with small, dispersed mud clasts. For the Baimatuo Member, we examined four thin sections and we provide photomicrographs of samples BMT-172, BMT-186, and BMT-200 in Figure C.4A-C. In the Baimatuo Member, dolomite microspar is also fabric-retentive, preserving primary mm-scale laminations and small mud rip-up clasts. Lastly, for the Yanjiahe Formation that sits above the Dengying Formation, we examined five thin sections and we provide photomicrographs for samples YJH-2, YJH-21, and YJH-40 in Figure C.4D-F. Limestone of the Yanjiahe Formation is composed of micritic to microsparitic calcite that is generally fabric-retentive. Some intervals are organic-rich and

preserve thin, microbial laminations. Intraformational conglomerates composed of sub-mm-scale mud rip-up clasts are common.

In summary, none of the samples examined in this study show the degree of recrystallization observed by Hood et al. (Hood et al., 2016) in the Neoproterozoic Balcanoona reef complex, South Australia. The generally fabric-retentive nature of our samples is suggestive of primary marine precipitation or early stage diagenesis in the presence of seawater (*e.g.*, (Hood et al., 2011; Wood et al., 2017)).

With respect to geochemical characteristics, the Hamajing Member is characterized by relatively low Mn concentrations (< 100 ppm with the exception of two samples), as well as relatively low Sr concentrations (< 100 ppm). Mn/Sr ratios are < 2, with the exception of two samples that have been excluded from further consideration (Figure C.5). Relatively low Sr concentrations are not uncommon in early fabric-retentive dolostone, and therefore are not taken to indicate late-stage diagenetic alteration. Oxygen isotope values are > −6 ‰, which also argues against late-stage diagenesis. In summary, petrographic, trace element, and isotopic characteristics suggest that the Hamajing Member has the potential to record seawater geochemical signatures.

In the Shibantan Member, Mn concentrations are exceptionally low (< 15 ppm) and Sr concentrations are strongly elevated (up to ~2,700 ppm). As a result, Mn/Sr ratios are generally below 0.01 (Figure C.5). This is strong evidence for the preservation of seawater geochemical signatures. Oxygen isotope values are > −7 ‰, which also suggests the lack of substantial meteoric or deep burial diagenesis.

In the Baimatuo Member, dolostone is characterized by relatively low Mn contents (< 150 ppm with the exception of three samples) and relatively low Sr concentrations (<

65 ppm) (Figure C.5). Sr is easily expelled from the crystal lattice during recrystallization and dolomite has a generally lower preference for Sr than calcite, such that early fabric-retentive dolomite formed in the presence of seawater is often depleted in Sr. The low Mn contents and generally low Mn/Sr ratios of these samples (< 2.5 with the exception of six samples that have been excluded) indicate a high degree of preservation of seawater geochemistry, despite these low Sr contents. This hypothesis is also supported by oxygen isotope data ($\delta^{18}O$ values > −6 ‰). In summary, petrography and geochemistry both indicate that limestone and dolostone of the Shibantan and Baimatuo members are either primary precipitates or formed during early seafloor diagenesis.

In the Yanjiahe Formation, we excluded three samples based on high Mn contents, low Sr contents, and therefore, high Mn/Sr ratios (two samples with Mn/Sr > 15). The remaining samples are characterized by Mn contents < 100 ppm, Sr contents > 250 ppm, and oxygen isotope values > −7.5 ‰, suggesting preservation of seawater geochemistry (Figure C.5).

In addition to absolute Mn and Sr contents, we have also investigated Mn/(Mg+Ca) and Sr/(Mg+Ca) ratios (Figure C.6). Mn/(Mg+Ca) data strongly mirror the previously-discussed Mn contents, and suggest that no anomalous Mn enrichment occurred in the Wuhe section that can be attributed to late-stage diagenesis. In the Gaojiashan section, there is a trend of decreasing Mn/(Mg+Ca) upward in the section (Figure C.6D). If this were caused by late-stage burial diagenesis or pore water anoxia during early diagenesis, then we would also expect systematic differences in $\delta^{238}U$, with higher $\delta^{238}U$ in the lower interval compared to the upper interval. This is not observed, however, suggesting that $\delta^{238}U$ values were not systematically altered by early pore water anoxia or late-stage burial

diagenesis. We also note that $\delta^{238}U$ in the Gaojiashan section is identical to the well-preserved, coeval Shibantan Member at the Wuhe section, suggesting that both sections record primary values. Sr/(Mg+Ca) values also mirror the previously-discussed Sr contents, and show expected trends related to carbonate mineralogy.

In the Wuhe section as a whole, there is no correlation between carbon and oxygen isotope values ($R^2 = 0.009$; Figure C.7). $\delta^{13}C$ and $\delta^{18}O$ tend to co-vary if both systems have been influenced by proportional mixing with an external (diagenetic) fluid, and in the case of the Wuhe section, the lack of co-variation between these parameters is another line of evidence supporting preservation of early, seawater-derived geochemical signatures.

Lastly, in the Gaojiashan section, the lower 30 meters are characterized by Mn > 300 ppm (with the exception of one sample), Sr < 150 ppm (with the exception of two samples), and highly variable oxygen isotope values ranging from −1.78 to −8.39 ‰ (Figure C.5). Mn/Sr ratios are uniformly > 2.5, and we have therefore excluded eight samples from this interval. By contrast, the upper part of the section is characterized by low Mn contents (< 300 ppm with the exception of one sample), relatively high Sr contents (most samples > 400 ppm), low Mn/Sr ratios (< 1.5), and oxygen isotope values > −7.5 ‰ (with the exception of one sample). There is also no co-variation between carbon and oxygen isotopes for the entire Gaojiashan section ($R^2 = 0.017$; Figure C.7), which would be expected if both parameters were influenced by proportional mixing with an external fluid. These data, along with generally fabric-retentive petrographic characteristics, strongly indicate that the upper 20 meters of the Gaojiashan section have the potential to record seawater geochemistry.

Using these diagenetic criteria, 2, 0, 6, and 2 outliers have been identified from the Hamajing Member (total sample number #8), the Shibantan Member (total sample number #24), the Baimatuo Member (total sample number #23), and the Yanjiahe Formation (total sample number #7) at the Wuhe section. Eight outliers have been identified from the Gaojiashan Member (total sample number #27) at the Gaojiashan section.

Because the main conclusions of our study are based on the very light U isotope compositions recorded in the Shibantan and Gaojiashan members, we further investigated the extent of correlation between $\delta^{238}U$ and $\delta^{18}O$, Sr concentration, Mn concentration, and Mn/Sr for samples in these units with Mn/Sr ratios < 2.5 (Table C.4.). There is no systematic correlation between diagenetic indicators and $\delta^{238}U$ in the Shibantan and Gaojiashan members, suggesting that late-stage diagenesis did not progressively alter U isotope values. It is also important to note that these very light U isotope values are found in two geographically disparate, but coeval sections, which also argues against systematic alteration of U isotopes.

C. 5 Detrital contaminations

When evaluating detrital contamination, we used detrital indicators such as Rb/Sr ratios and Al contents (e.g., Ling et al., 2013). Among samples with Mn/Sr < 2.5, only those samples with Rb/Sr < 0.02 and Al (wt.%) < 0.35 % were used in our main text discussion. The Rb/Sr and Al content plots are shown in Figure C.8.

In addition, for samples with Mn/Sr < 2.5, Rb/Sr < 0.02 and Al < 0.35%, we further looked at U/Al ratios to confirm that our dissolution procedure primarily targets carbonate-bound (and not detrital) U. The U/Al ratio of the upper continental crust is ~0.331 ppm/wt.%

(Rudnick and Gao, 2003), and U/Al ratios in our samples are substantially enriched above crustal values by approximately two orders of magnitude (Figure C.8), indicating that the dissolution procedure is effective at isolating carbonate-bound U.

We have also used Al content (wt.%) data to estimate the possible amount of contribution of U from detrital sources. Specifically, assuming all the measured Al in our samples is from detrital minerals, and using the U/Al ratio of upper continental crust, we estimate that detrital U accounts for <2 % of total U for Wuhe samples, and < 10 % of total U for Gaojiashan samples. Thus, we conclude that detrital influence on our $\delta^{238}U$ signals are minimal. We also note that the estimated amount of U associated with detrital material is different between the Shibantan Member at Wuhe and its equivalent Gaojiashan Member. However, the δ238U signals of these two members are identical.

C. 6 Ce anomalies and dolomitization

Romaniello et al. (2013) point out that in the modern Bahamas, bulk carbonate sediments can incorporate U with a $\delta^{238}U$ value that is 0.2–0.4 ‰ heavier than seawater due to the incorporation of ^{238}U-enriched U(IV) under locally pore water euxinic conditions. If this were true in our Dengying carbonates, then we could have potentially underestimated the extent of U removal associated with anoxic sedimentary sinks.

First, we examined local water column redox conditions by looking at the Ce anomaly (Ce/Ce*) recorded in our carbonate samples. Unlike the other REEs, which are strictly trivalent in the oceans, cerium (Ce) can exist in either trivalent or tetravalent forms depending on redox conditions. The redox state of Ce is modulated by the presence of manganese oxides and/or bacteria, where Ce is oxidized by and adsorbed onto mineral

surfaces (Ling et al., 2013). Thus, the concentration of Ce relative to the other REEs is associated with dissolved oxygen concentrations, and can be used to infer redox conditions of the overlying water column (Lau et al., 2017; Ling et al., 2013).

Ce anomalies are calculated following Ling et al. (Ling et al., 2013). The Ce anomalies at Wuhe range between 0.29 and 0.79 with a mean of 0.5, and the Ce anomalies at Gaojiashan range between 0.70 and 0.98 with a mean of 0.76 (Figure C.9). The Ce anomalies indicate that the local water column at both Wuhe and Gaojiashan were likely dominated by oxic conditions (Ling et al., 2013; Tostevin et al., 2016). This confirms that our carbonates can be considered an oxic sink for U, and thus can passively capture the $\delta^{238}U$ signal of seawater.

Second, we examined the possibility of pore water euxinia using Mo and U concentrations, as well as correlations between $\delta^{238}U$ and U/(Mg+Ca) ratios and Mo/(Mg+Ca) ratios (Figure C.9). Under euxinic pore water conditions, U and Mo become authigenically enriched in carbonate (Romaniello et al., 2013, 2016), thus increasing [Mo], [U], U/(Mg+Ca), and Mo/(Mg+Ca) values. In our samples from both sections, Mo concentrations are <0.2 ppm, with the exception of two samples (BM-1 and YJH-40). This is in contrast to carbonate sediments from the modern Bahamas, most of which are characterized by Mo concentrations between 1.8 and 28 ppm (Romaniello et al., 2016). This indicates that pore water euxinia was less prevalent during deposition of our samples than on the modern Bahamian carbonate platform. In addition, U/(Mg+Ca) and Mo/(Mg+Ca) are extremely low (excluding two samples, BM-1 and YJH-40) and there is no systematic stratigraphic variation. Furthermore, there are no statistically significant correlations between $\delta^{238}U$ and U/(Mg+Ca) and Mo/(Mg+Ca) in our carbonates (Table

C.4.). We note that although the two "outliers", the BM-1 and the YJH-40, were likely affected by pore water anoxia during early diagenesis, their $\delta^{238}U$ did not depart from the surrounding samples with low U concentrations. If there were U addition (compared to the surrounding low U concentration samples) associated with pore water anoxia during early diagenesis, that would indicate 60–100% of U in these two samples are related to proewater anoxia, and thus these samples would show obvious high $\delta^{238}U$ values. However, this is in contrast to our observations that $\delta^{238}U$ of these three samples did not obviously depart from the surrounding low U concentration samples. And thus, these high concentrations might have been caused by other factors that did not affect $\delta^{238}U$.

Romaniello et al. (2013) also observed U-isotope change associated with dolomitization in one Bahamian tidal pond. There was a strong correlation with Mg/Ca ratio (R^2=0.96), suggesting that U-isotope change was possibly associated with dolomitization. This seems to be a special, spatially restricted case, however. In our samples from Wuhe, no statistically significant correlations are observed between $\delta^{238}U$ and Mg/Ca molar ratio (R^2=0.25), suggesting that dolomitization has not systematically altered the primary isotopic record. Further confidence that dolomitization may not have been an issue for paleo-$\delta^{238}U$ records comes from a global compilation of $\delta^{238}U$ studies across the Permian-Triassic boundary. Both the dolomitized section (the Dawen section in South China; Brennecka et al. (2011a)) and the non-dolomitized sections (the Kamura section in Japan, the Dajiang section and the Daxiakou section in South China, and the Taskent section in Turkey; Lau et al. (2016); Elrick et al. (2017); Zhang et al. (2018a)) show congruent $\delta^{238}U$ records. Despite potential uncertainty regarding dolomitization, the bulk of our conclusions hinge on the very light $\delta^{238}U$ values observed in limestone of the

Shibantan and Gaojiashan members. Both of our limestone sections (Wuhe and Gaojiashan) record these very light values, and we consider these results to be robust regardless of dolomitization in the underlying Hamajing Member and the overlying Baimatuo Member.

C. 7 Uranium isotope mass balance constraints on U removal to anoxic/euxinic sinks

The implied changes to the extent of U removal into anoxic sediments can be described by a mass balance equation for the fraction of anoxic/euxinic sinks and their isotopic composition (following Montoya-Pino et al., 2010):

$$\delta^{238}U_{input} = (f_{anoxic} \times \delta^{238}U_{anoxic}) + (f_{other} \times \delta^{238}U_{other}) \quad (1)$$

$$\delta^{238}U_{anoxic} = \delta^{238}U_{seawater} + \Delta_{anoxic} \quad (2)$$

$$\delta^{238}U_{other} = \delta^{238}U_{seawater} + \Delta_{other} \quad (3)$$

$$f_{anoxic} + f_{other} = 1 \quad (4)$$

Solving equations (1) to (4), we have

$$f_{anoxic} = (\delta^{238}U_{input} - \delta^{238}U_{seawater} - \Delta_{other})/(\Delta_{anoxic} - \Delta_{other}) \quad (5)$$

Here, the subscripts input, anoxic, and other denote the riverine input, anoxic/euxinic sink, and other sedimentary sinks, respectively, and f_{anoxic} represents the fraction of the riverine

U input that is deposited in anoxic/euxinic sediments. Following Montoya-Pino et al. (2010) and Brennecka et al. (2011a), we assume: (1) isotopically constant U input from rivers over geologic time with an average value of −0.34 ‰ ($\delta^{238}U_{input}$ = −0.34 ‰) (Andersen et al., 2016); (2) a constant isotope fractionation between seawater and the average isotopic composition of other sinks, including suboxic sinks, ferromanganese oxides, and hydrothermal alteration of oceanic crust (Δ_{other} = +0.043 ‰) (Figure 1.2); and (3) a fractionation factor of Δ_{anoxic} between seawater and anoxic/euxinic sinks between 0.4 ‰ and 1.2 ‰. Based on the assumptions above and our measured U isotope values from the Dengying Formation ($\delta^{238}U_{Ediacaran\ seawater}$ = −0.95 ‰, $\delta^{238}U_{input}$ = −0.34 ‰, $\delta^{238}U_{other\ sinks}$ = −0.907 ‰ (i.e., −0.95 + 0.043 ‰), and $\delta^{238}U_{anoxic\ sinks}$ = −0.95 ‰ + Δ_{anoxic}), we can derive a function for f_{anoxic} that depends on Δ_{anoxic}: $f_{anoxic} = 0.567 / (\Delta_{anoxic} - 0.043)$.

The estimated f_{anoxic} values can change with the $\delta^{238}U_{input}$ values used in the calculation. The present study used the global average riverine value reported by Andersen et al. (2016). Another study by Noordmann et al. (2016) have reported a slightly lighter average riverine value of −0.27 ‰ (all major rivers define a relatively narrow range between −0.31 and −0.13 ‰ with a weighted mean isotope composition of −0.27 ‰). However, the difference in average riverine values will only result in small differences in the estimated f_{anoxic} values. For instance, when applying a Δ_{anoxic} of 0.835 ‰ (discussed below), $f_{anoxic} = (0.907 + \delta^{238}U_{input}) / 0.792$, when using $\delta^{238}U_{input}$ of −0.34 ‰, −0.27 ‰, and −0.20 ‰, the estimated f_{anoxic} are 72%, 80%, and 89%, respectively.

C. 8 Anoxic seafloor area modeling calculation

The fraction of U removed into anoxic/euxinic sediments can be coupled to the extent of seafloor covered by anoxic/euxinic waters, as described by Wang et al. (2016), Lau et al. (2016), and Zhang et al. (2018b) and shown in Figure 5.3B and Figure C.10. Below is a summary of the modeling method:

The implied changes to the extent of bottom water anoxia can be described by differential mass balance equations for the seawater uranium inventory and its isotopic composition, respectively (following Wang et al. (2016), Lau et al. (2016), and Zhang et al. (2018b)):

$$\frac{dN_{sw}}{dt} = J_{riv} - J_{oxic} - J_{anoxic} - J_{suboxic} \quad (6)$$

$$\frac{d(N_{sw} \cdot \delta^{238}U)}{dt} = J_{riv} \cdot \delta^{238}U_{riv} - J_{oxic} \cdot \delta^{238}U_{oxic} - J_{anoxic} \cdot \delta^{238}U_{anoxic} - J_{suboxic} \cdot \delta^{238}U_{suboxic} \quad (7)$$

$$\delta^{238}U_{oxic} = \delta^{238}U_{sw} + \Delta_{oxic} \quad (8)$$

$$\delta^{238}U_{anoxic} = \delta^{238}U_{sw} + \Delta_{anoxic} \quad (9)$$

$$\delta^{238}U_{suboxic} = \delta^{238}U_{suboxic} + \Delta_{suboxic} \quad (10)$$

$\delta^{238}U_{sw}$ and $\delta^{238}U_{riv}$ are the U isotope composition of seawater and the riverine source, respectively. $\delta^{238}U_{anoxic}$, $\delta^{238}U_{suboxic}$, and $\delta^{238}U_{oxic}$ are the U isotope composition of anoxic sedimentary sink, suboxic sedimentary sink, and the sum of the other sinks, respectively. Here, we simplify the inputs to J_{riv}, the riverine flux, whose modern value is ~4×10^7 moles U/yr (Tissot and Dauphas, 2015). The outputs are assumed to consist of the anoxic sediment sink (J_{anoxic}), suboxic sediment sink ($J_{suboxic}$), and the sum of the other sinks (J_{oxic}). Δ_{anoxic} is the effective fractionation factor associated with anoxic sediment deposition, $\Delta_{suboxic}$ is the effective fractionation factor associated with suboxic sediment deposition,

and Δ_{oxic} is the effective fractionation factor associated with the remaining other sinks (+0.005‰, calculated to maintain isotopic steady state in the modern ocean (e.g, Brennecka et al. (2011a), Montoya-Pino et al. (2010), and Wang et al. (2016)).

At steady state, the left side of the equation (6) and (7) equal 0, yielding:

$$J_{riv} = J_{oxic} + J_{anoxic} + J_{suboxic} \tag{11}$$

$$J_{riv} \cdot \delta^{238}U_{riv} = J_{oxic} \cdot \delta^{238}U_{oxic} + J_{anoxic} \cdot \delta^{238}U_{anoxic} + J_{suboxic} \cdot \delta^{238}U_{suboxic} \tag{12}$$

We define the oxic, anoxic, and suboxic sinks in Eq. 6–12 assuming a first-order dependence on seawater U concentration (Lau et al., 2016; Partin et al., 2013; Reinhard et al., 2013):

$$J_{oxic} = k_{oxic} \cdot N_{sw} \cdot A_{oxic} \tag{13}$$

$$J_{anoxic} = k_{anoxic} \cdot N_{sw} \cdot A_{anoxic} \tag{14}$$

$$J_{suboxic} = k_{suboxic} \cdot N_{sw} \cdot A_{suboxic} \tag{15}$$

where A_{oxic}, A_{anoxic}, and $A_{suboxic}$ are the total seafloor area overlain by oxic waters, anoxic waters, and suboxic waters, respectively. k_{oxic} k_{anoxic}, and $k_{suboxic}$ are rate constants associated with oxic sediment deposition, anoxic sediment deposition, and suboxic sediment deposition and are calculated for the modern uranium system (e.g., Wang et al. (2016), Lau et al. (2016), and Zhang F. et al. (2018b)).

We further define the fraction of anoxic seafloor area overlain by anoxic water:

$$F_{anoxic} = \frac{A_{anoxic}}{A_{ocean}} \tag{16}$$

where F_{anox} is the total fraction of seafloor area overlain by anoxic waters, and A_{ocean} is the total seafloor area of modern ocean. Model parameterization was based on studies of the modern U cycle and are summarized in Table C.5. Modeling results are summarized in Figure 5.3B and Figure C.10.

Solving equations 6–15, we have

$$\delta^{238}U_{sw} = \delta^{238}U_{riv} - \frac{A_{anoxic} \cdot k_{anoxic} \cdot \Delta_{anoxic} + A_{suboxic} \cdot k_{suboxic} \cdot \Delta_{suboxic} + A_{oxic} \cdot k_{oxic} \cdot \Delta_{oxic}}{A_{anoxic} \cdot k_{anoxic} + A_{suboxic} \cdot k_{suboxic} + A_{oxic} \cdot k_{oxic}} \quad (17)$$

where $A_{anoxic} + A_{suboxic} + A_{oxic} = A_{ocean}$.

In this modeling, we adopted a value of –0.34‰ for rivers. As stated earlier, riverine input is the single major source of U into the ocean. The weighted average $\delta^{238}U$ of riverine input is −0.34 ‰ (Andersen et al., 2016). An exception not included in this average is the Yangtze River in China, where two reported measurements yield an average $\delta^{238}U$ value of ~–0.70 ‰. Although these data and their ability to represent the entire Yangtze catchment need to be confirmed, this "outlier" is interpreted to reflect local U contributions from evaporite minerals (halite) that are abundant near the source of the Yangtze River. If so, this is an unusual situation because evaporites are not major sources of U to the oceans overall. Previous global riverine estimates yielded values of −0.30 ‰ to −0.27 ‰ (Noordmann et al., 2016). It thus appears that the riverine composition is indistinguishable from average continental crust, which has been measured as −0.30 ± 0.04 ‰ and −0.31 ± 0.05 ‰ (Noordmann et al., 2016).

In this modeling exercise, we have simplified the ocean into oxic, suboxic, and anoxic states. Because of the fractionation factor of U isotopes under suboxic conditions are from $\delta^{238}U$ measurements from the Peruvian continental margin (Weyer et al., 2008)

and off the coast of Washington State (Andersen et al., 2016), and hence, by referring to suboxic conditions, we are discussing a situation that is similar to suboxic waters in Peruvian continental margin and off the coast of Washington State. Bottom water O_2 at both Peruvian continental margin and off the coast of Washington State are within the range of 0.2 to 2 ml L^{-1} that has previously been used to define suboxic depositional environments (Tribovillard et al., 2006). Similarly, the fractionation factor of U isotopes under anoxic conditions are primarily based on observations from the modern Black Sea and from the modern Saanich Inlet, and therefore, by referring to anoxic conditions, we are discussing a situation that is similar to these two modern anoxic environments. Here, bottom water O_2 concentrations are <0.2 ml L^{-1} and H_2S concentrations >400 μM (Rolison et al., 2017).

We first varied the areal extent of anoxic/euxinic and oxic seafloor area while keeping the areal extent of suboxic seafloor the same as the modern value [$f_{suboxic}$=6%, black curve in Figure C.10]. This modeling exercise suggests that essentially the entire seafloor was covered by anoxic/euxinic sediments (assuming a fractionation factor of 0.6 ‰ between seawater and anoxic/euxinic sediments) for terminal Ediacaran seawater $\delta^{238}U$ to approach values as low as −0.95 ‰. In reality, however, suboxic seafloor area is likely to co-vary with anoxic/euxinic seafloor area. We tested various suboxic areal extents [0 %, 6 %, 20 %, 30 %, 40 %, 50 %, and 75 %; Figure C.10], the results of which tell us that it is difficult or even impossible to generate seawater $\delta^{238}U$ of −0.95 ‰ with large suboxic seafloor areas (assuming anoxic/euxinic sink-seawater fractionation of 0.6 ‰). Thus, variations in suboxic seafloor area have a very small effect on our basic conclusion that

significantly expanded anoxic/euxinic seafloor area is likely the only major process that can cause terminal Ediacaran seawater $\delta^{238}U$ to reach values as low as −0.95 ‰.

Second, we varied the fractionation factor between seawater and anoxic/euxinic sediments and kept the suboxic seafloor area fixed at 0%. These results are summarized in Figure 5.3B. Our results suggest that the inferred extent of ocean anoxia largely depends on the assumed average fractionation factor between seawater and anoxic/euxinic sediments. If we use larger fractionation factors of 0.68 ‰ and 0.99 ‰—the two end member values observed for reduction of U(VI) to U(IV) by metal-reducing bacteria (Basu et al., 2014)—modeling results suggest that ~33 % and ~8.5 % of anoxic/euxinic seafloor area was required to drive terminal Ediacaran seawater $\delta^{238}U$ to values as low as −0.95 ‰.

We also ran our model with a Δ_{anoxic} of 0.835 ‰, which is an "average" fractionation factor that represents microbially-mediated U reduction (Basu et al., 2014), and is close to the maximum Δ_{anoxic} observed both in the modern Saanich Inlet (0.79 ‰) (Holmden et al., 2015) and in the Black Sea (0.83 ‰) (Weyer et al., 2008). Here, we calculate that f_{anoxic} = 0.7, meaning that a minimum of 70 % of global riverine U input was removed into anoxic/euxinic sediments when the Shibantan/Gaojiashan members were deposited. This fraction of U removal into anoxic/euxinic sediments is estimated to occur over an anoxic/euxinic seafloor area of ~14 %. In reality, suboxic seafloor area would not be 0 % and would co-vary with expanded anoxic/euxinic seafloor area. If we assume that $f_{suboxic}$ was greater than f_{anoxic} in the latest Ediacaran ocean, then a combination of $f_{suboxic}$ = 21% and f_{anoxic} = 21% will minimally be required in order to account for latest Ediacaran seawater average $\delta^{238}U$ of −0.95‰ (Figure C.11). In reality, 21% seafloor area overlain by anoxic waters will require an even larger seafloor area overlain by suboxic seafloor area.

For example, the f_{anoxic} = ~0.35% while $f_{suboxic}$ = 6% in the modern ocean. We therefore conclude that at least 42% of the seafloor was covered by oxygen-deficient (anoxic + suboxic) waters. However, in the abstract of the main text, we focus on emphasizing anoxic seafloor areas.

This simple modeling exercise thus gives us the lowest estimate of anoxic/euxinic seafloor area. Parameters used in the modeling exercise have been summarized in Table C.5.

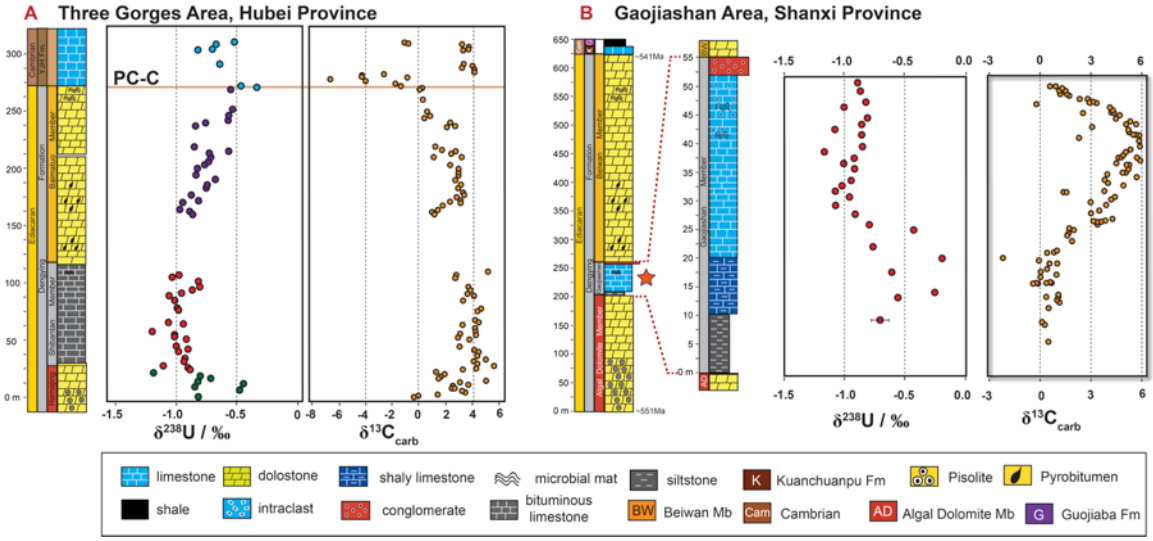

Figure C.1. Geochemical profiles of (A) the Dengying Formation and Yanjiahe Formation from the Wehe section, and (B) the Gaojiashan member from the Gaojiashan section. $\delta^{13}C$ data of the Gaojiashan member are from Cui et al. (2016).

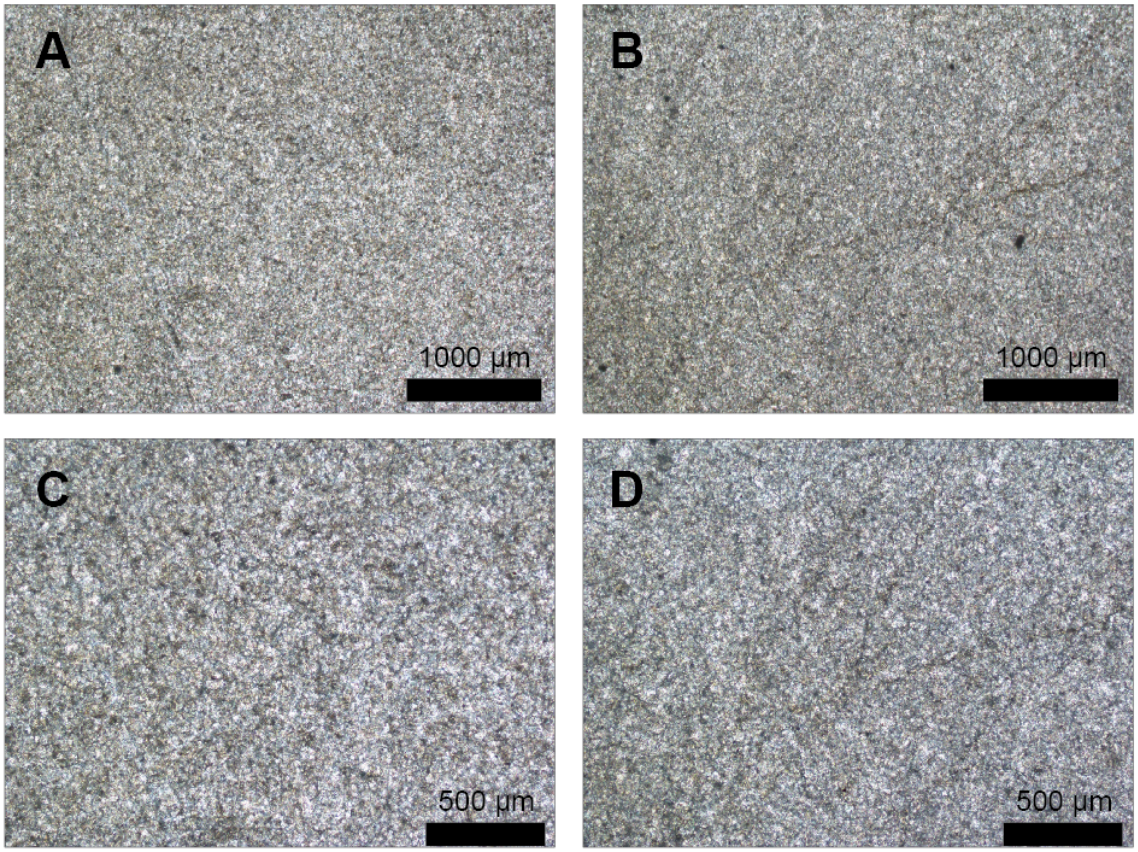

Figure C.2. Petrographic photos from the Hamajing dolomite (A-D) at the Wuhe section. Photos are of samples HMJ-14 (A, C) and HMJ-19 (B, D).

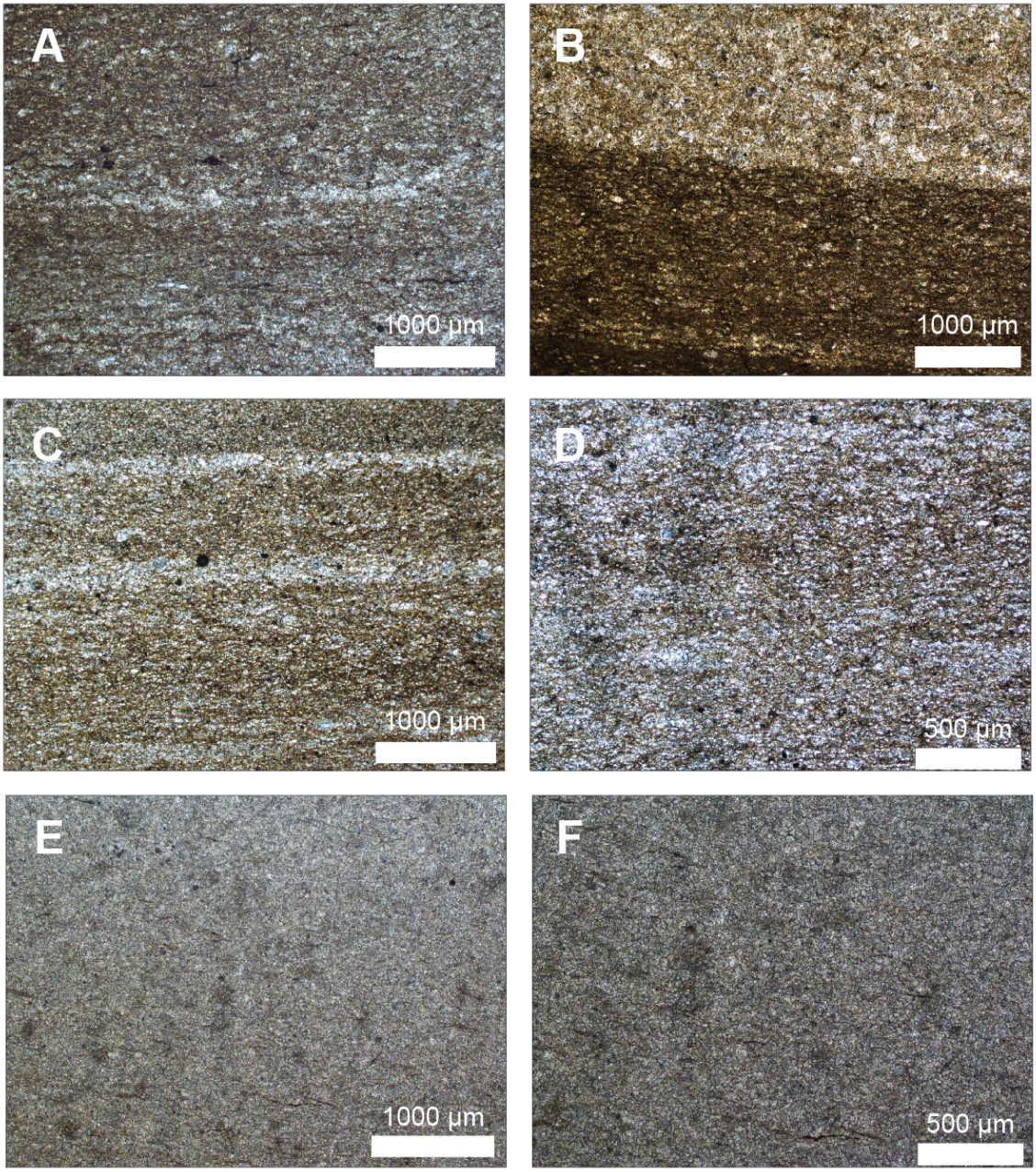

Figure C.3. Petrographic photos from the Shibantan limestone (A-F) at the Wuhe section. Photos are of sample SBT-89 (A), SBT-26 (B), SBT-42 (C, D), and SBT-107 (E, F).

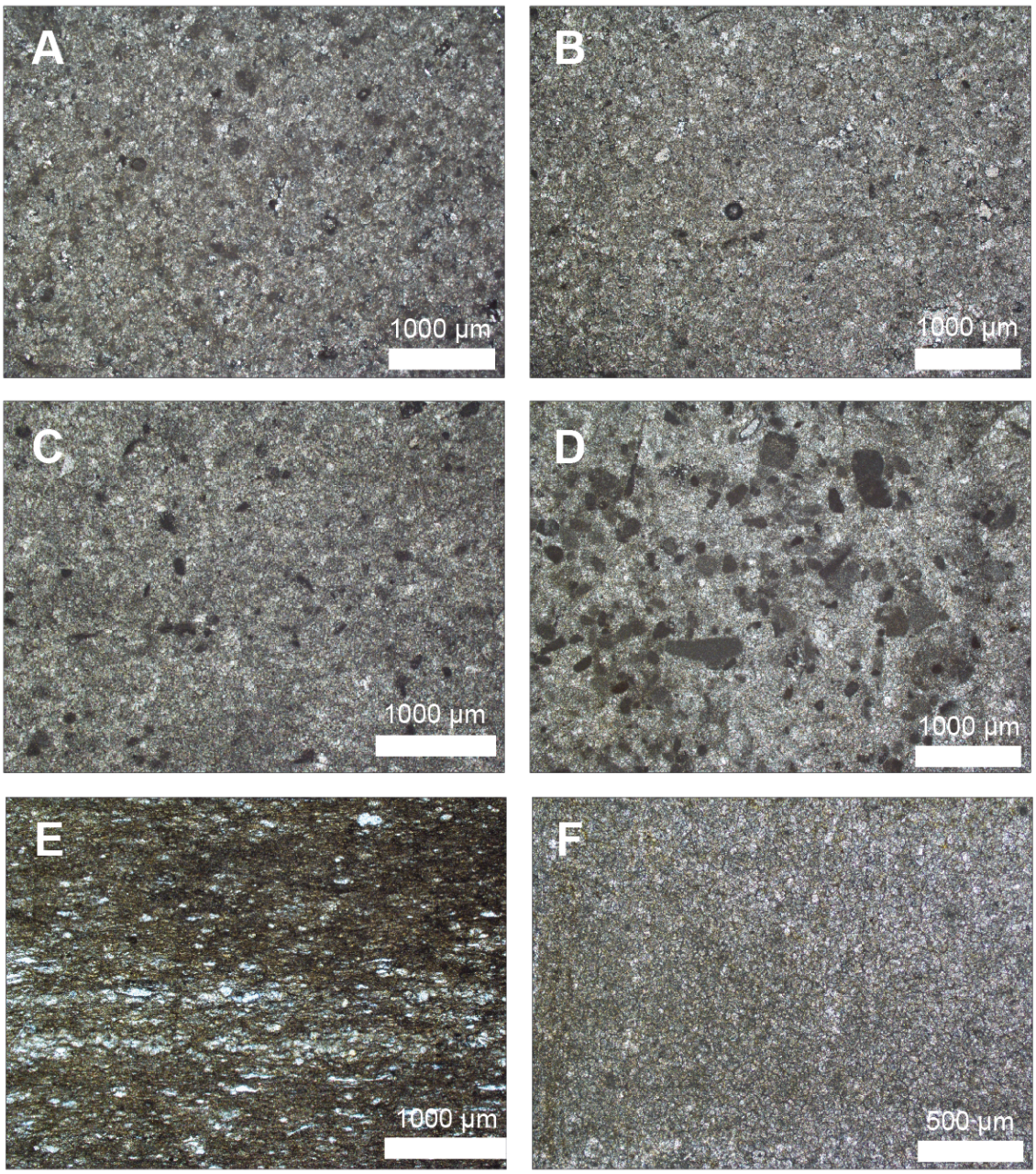

Figure C.4. Petrographic photos from the Baimatuo dolomite (A-C) and the Yanjiahe limestone (D-F) at the Wuhe section. Photos are of sample BMT-172 (A), BMT-186 (B), BMT-200 (C), YJH-2 (D), YJH-21 (E), and YJH-30 (F).

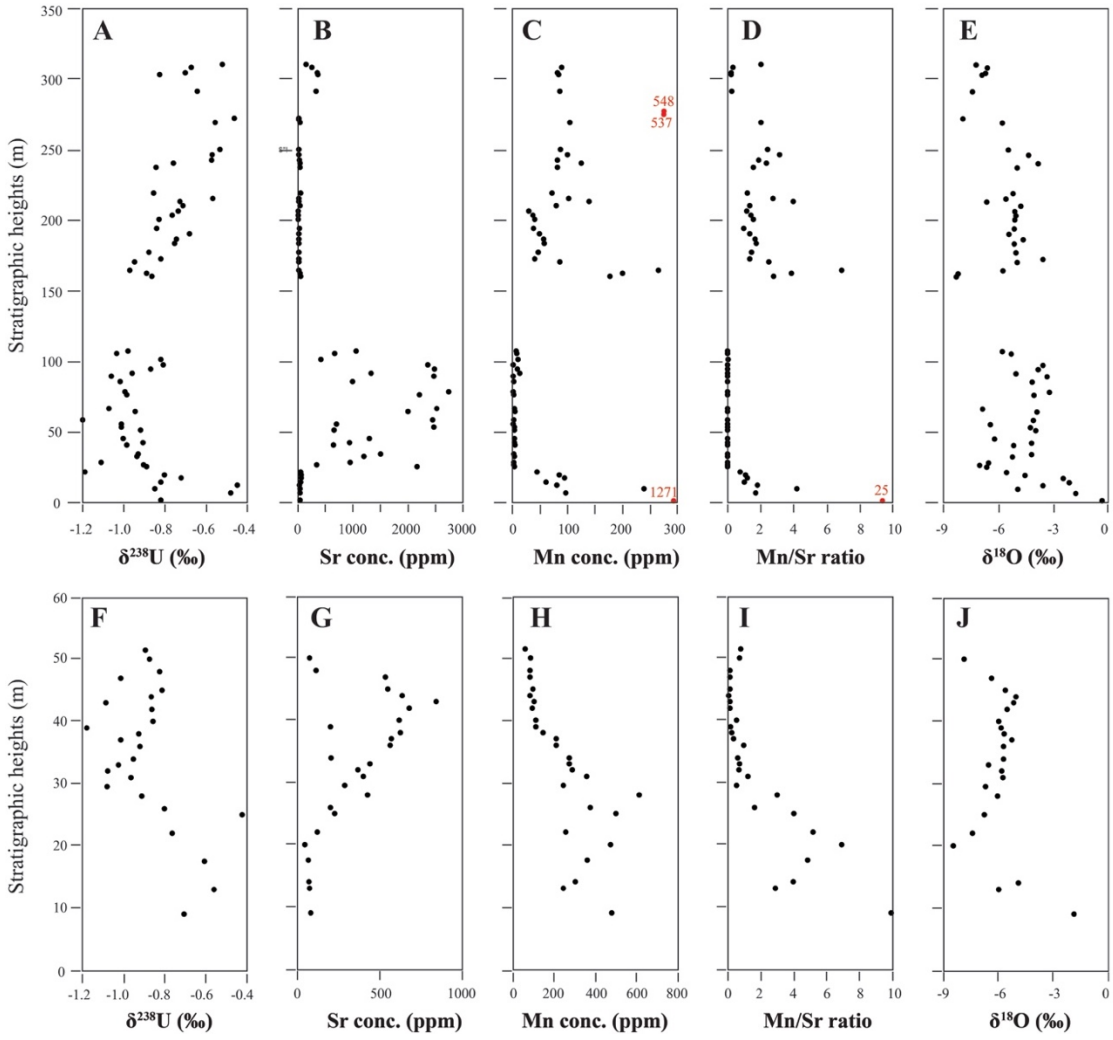

Figure C.5. δ^{238}U, Sr concentration, Mn concentrations, Mn/Sr ratios, and δ^{18}O profiles for samples from Wuhe (A– E) and Gaojiashan (F– J).

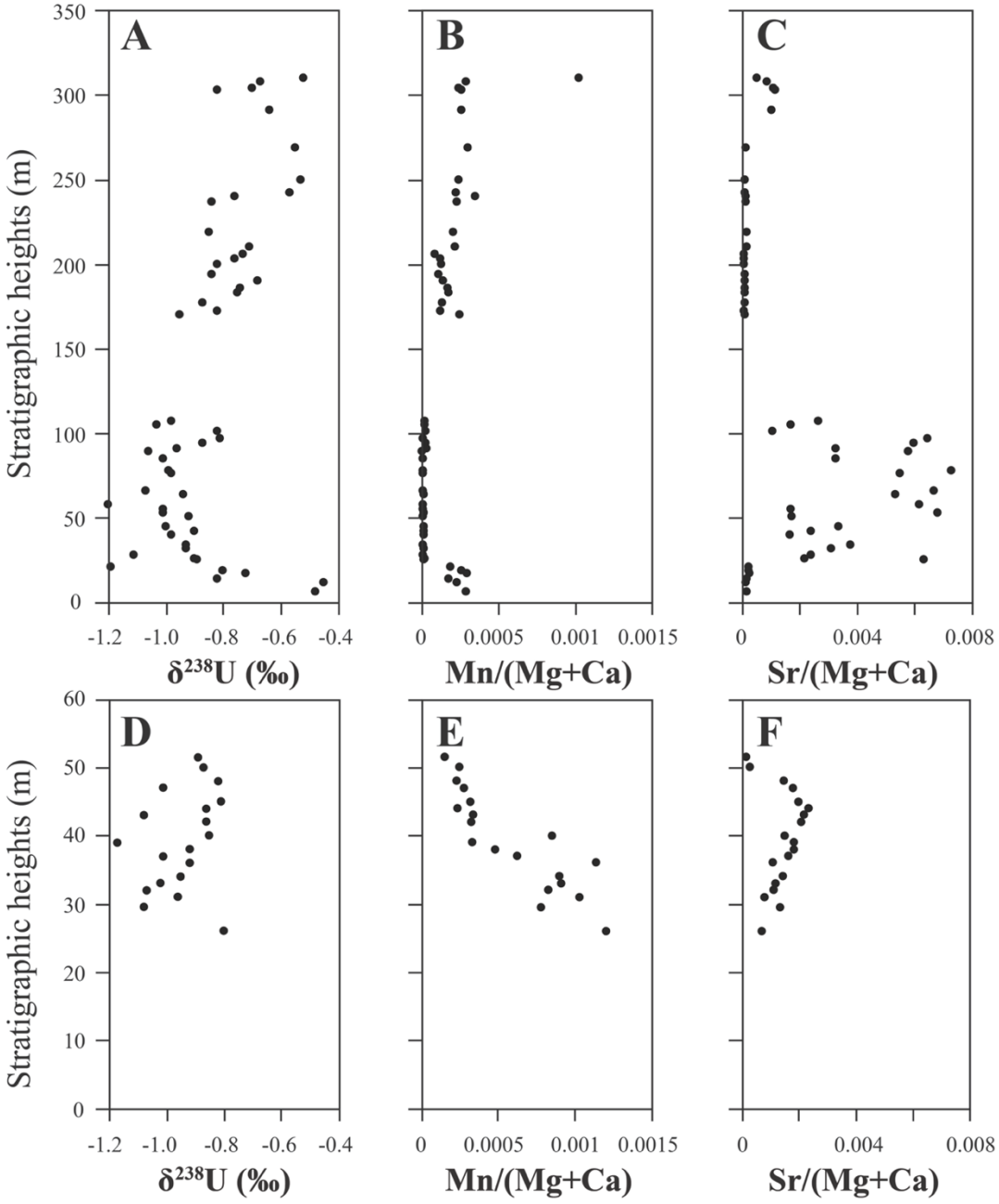

Figure C.6. δ^{238}U, Mn/(Mg+Ca) ratio, and Sr/(Mg+Ca) ratio profiles for samples from Wuhe (A–C) and Gaojiashan (D–F).

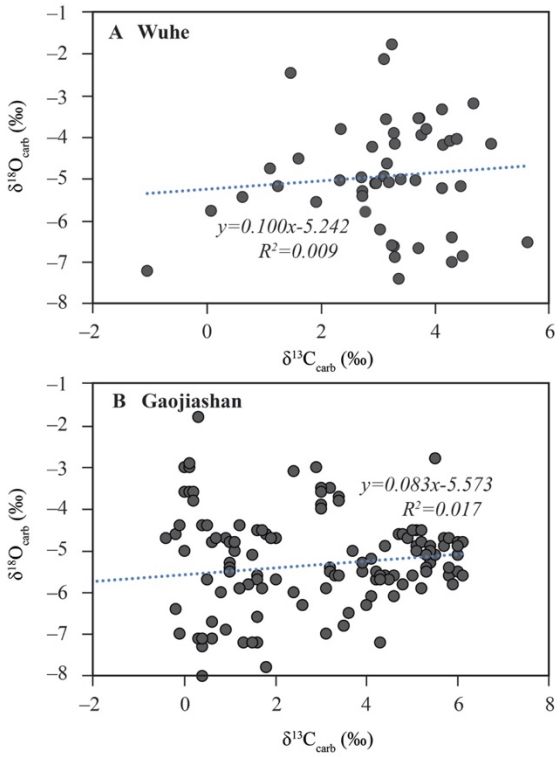

Figure C.7. $\delta^{13}C$ and $\delta^{18}O$ correlations of the Wuhe section (A) and the Gaojiashan section (B). No systematically significant correlations have been observed for both sections.

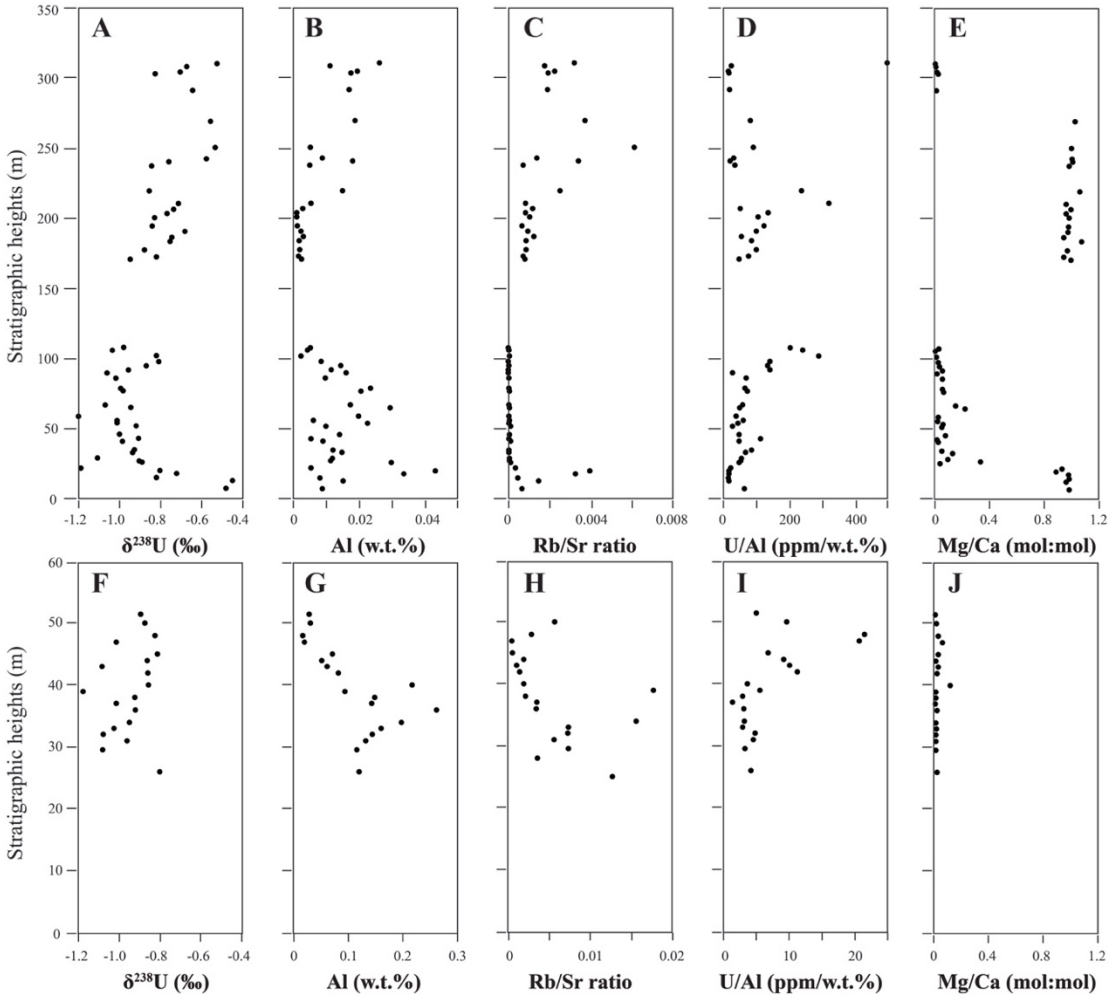

Figure C.8. δ^{238}U, Al content (w.t.%), Rb/Sr ratios, U/Al ratios (ppm/w.t.%), and Mg/Ca ratio (mol:mol) profiles for samples from Wuhe (A– E) and Gaojiashan (F– J). Samples with Mn/Sr>2.5 have been excluded from these plots.

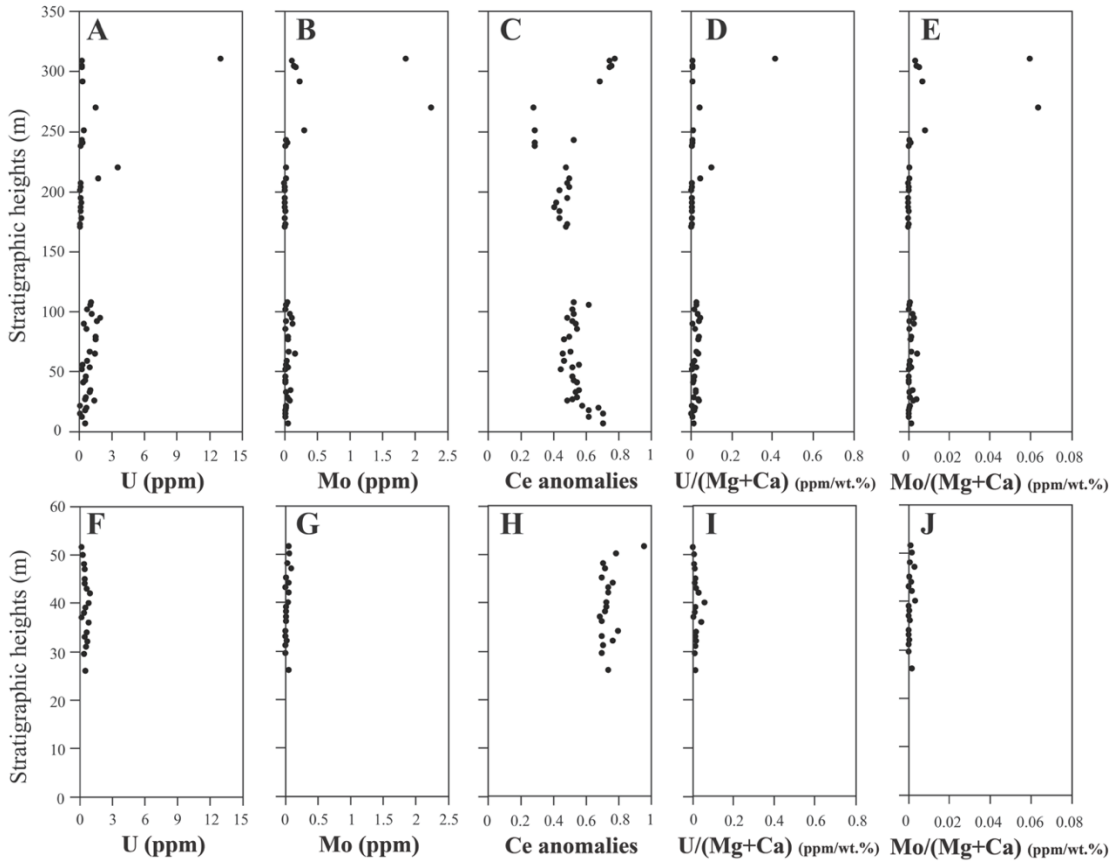

Figure C.9. U concentration, Mo concentrations, calculated Ce anomalies, U/(Mg+Ca) ratio, and Mo/(Mg+Ca) ratio profiles for samples from Wuhe (A–E) and Gaojiashan (F–J). Samples with Mn/Sr>2.5 have been excluded from these plots.

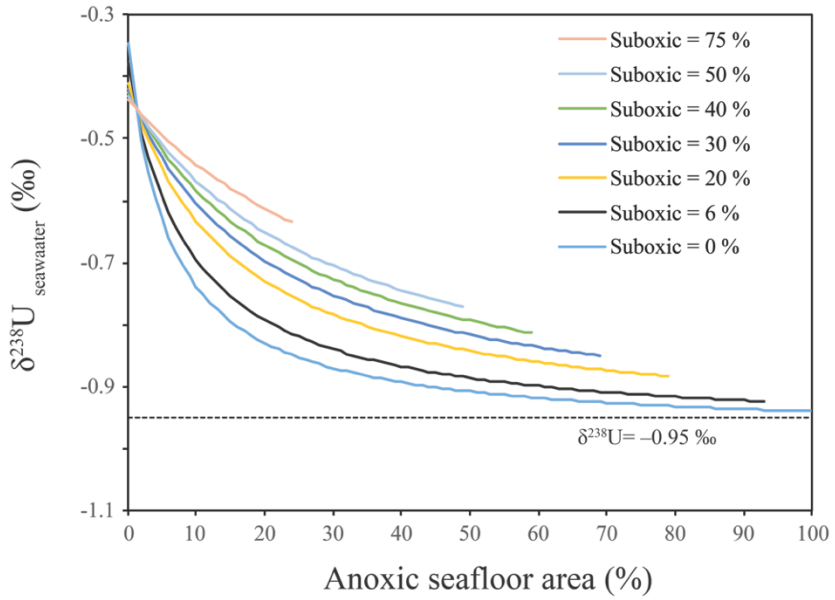

Figure C.10. Mass balance modeling calculations show variations of seawater $\delta^{238}U$ values as a function of anoxic/euxinic seafloor area while keeping Δ_{anoxic} constant (+0.6‰) and testing various suboxic areal extents.

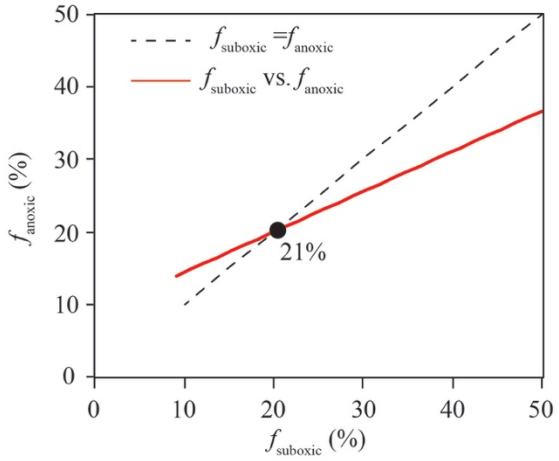

Figure C.11. Calculated combination f_{anoxic} and $f_{suboxic}$ in order to account for latest Ediacaran seawater average $\delta^{238}U$ of -0.95‰. The black dash line is a reference where equals f_{anoxic} to $f_{suboxic}$. The red solid line denotes a combination f_{anoxic} and $f_{suboxic}$ in order to account for latest Ediacaran seawater average $\delta^{238}U$ of -0.95‰.

Table C.1. $\delta^{238}U$ data with selected geochemical data at the Wuhe section.

Sample No.	height	$\delta^{238}U$	$\delta^{13}C$	Mg	Al	Ca	Mn	Sr	U
	m	‰	‰	ppm	ppm	ppm	ppm	ppm	ppm
HMJ-1	1	-0.82	-0.38	124742.55	343.45	208610.99	1271.42	50.35	1.26
HMJ-6.3	6.3	-0.48	3.24	126769.53	89.63	214530.78	98.05	57.72	0.57
HMJ-9.4	9.4	-0.85	2.68	127744.43	108.15	218258.08	239.74	57.11	0.64
HMJ-11.7	11.7	-0.72	3.72	129437.46	152.84	223746.03	80.98	44.30	0.28
HMJ-14	14	-0.82	3.11	130342.81	83.25	220314.61	61.54	61.05	0.13
HMJ-17	17	-0.72	1.46	118692.59	337.20	202098.40	95.37	80.50	0.60
HMJ-19	19	-0.80	1.61	114953.98	432.55	215868.77	86.25	78.60	0.72
HMJ-21	21	-1.19	1.92	88186.18	56.22	157580.97	46.12	61.32	0.13
SBT-25	25	-0.89	3.28	9119.43	299.30	334210.17	4.17	2181.87	1.43
SBT-26	26	-0.90	4.31	27354.59	116.06	134562.90	2.97	354.86	0.61
SBT-28	28	-1.11	5.63	23110.19	121.40	376989.17	3.39	965.90	0.67
SBT-32	32	-0.93	4.12	29695.72	150.01	360405.25	4.50	1221.78	1.01
SBT-34	34	-0.93	4.99	13703.84	123.09	390018.01	3.79	1524.86	1.05
SBT-40	40	-0.98	4.45	7530.18	91.45	386531.43	6.01	660.89	0.44
SBT-42	42	-0.90	4.14	5736.24	55.33	390120.79	4.61	954.59	0.62
SBT-45	45	-1.00	3.04	19200.80	142.91	369776.08	4.99	1317.59	0.68
SBT-51	51	-0.92	3.77	13109.18	100.90	369662.50	3.95	671.71	0.28
SBT-53	53	-1.01	2.90	14715.20	226.95	348907.45	4.35	2483.83	1.01
SBT-55	55	-1.01	4.29	7094.90	62.46	415818.34	2.83	718.30	0.38
SBT-58	58	-1.20	4.26	7781.06	199.89	390407.33	2.90	2461.90	0.78
SBT-64	64	-0.94	3.27	45458.44	294.90	332997.71	5.52	2024.92	1.47
SBT-66	66	-1.07	4.49	32721.48	174.80	346447.29	4.19	2538.55	1.03
SBT-76	76	-0.98	4.39	16968.90	207.70	385130.31	3.90	2225.22	1.53
SBT-78	78	-0.99	4.67	14129.95	236.52	362722.32	2.42	2761.75	1.56
SBT-85	85	-1.01	3.29	11641.42	100.02	297610.68	3.20	1015.59	0.70
SBT-89	89	-1.06	4.13	6581.00	162.92	421471.23	2.08	2484.67	0.45
SBT-91	91	-0.96	3.67	15104.18	117.84	396738.82	13.87	1344.91	1.67
SBT-94	94	-0.87	3.84	10114.64	146.98	405694.90	10.16	2498.31	1.97
SBT-97	97	-0.81	3.70	6924.18	86.07	359226.61	2.07	2373.03	1.22
SBT-101	101	-0.82		5432.11	26.30	398124.64	11.34	434.54	0.76
SBT-105	105	-1.03	2.73	3034.36	45.51	395084.98	8.34	681.75	1.09
SBT-107	107	-0.98	2.78	8771.38	54.93	395745.41	7.98	1080.23	1.11

BMT-160	160	-0.86	1.18	121494.21	133.46	218276.96	177.67	63.28	0.66
BMT-162	162	-0.89	0.98	130919.42	214.17	216525.14	200.80	51.71	0.79
BMT-164	164	-0.97	1.43	129097.97	169.98	219034.65	266.38	38.51	0.46
BMT-170	170	-0.95	3.11	130702.15	26.72	218416.66	86.80	34.80	0.13
BMT-172	172	-0.82	3.14	126029.28	18.81	221707.16	41.62	31.02	0.15
BMT-177	177	-0.87	3.39	129602.99	22.03	222184.71	47.79	32.69	0.22
BMT-183	183	-0.75	2.94	130385.88	20.40	201729.81	58.65	34.05	0.18
BMT-186	186	-0.74	3.16	125743.63	32.59	221564.27	58.06	35.07	0.18
BMT-190	190	-0.68	2.73	133485.49	25.07	227908.81	50.10	36.89	0.25
BMT-194	194	-0.84	2.96	132159.36	14.05	224705.19	38.93	40.08	0.17
BMT-200	200	-0.82	2.97	118591.36	12.06	201015.60	41.18	26.49	0.13
BMT-203	203	-0.76	2.33	112810.43	12.14	195586.97	37.80	26.63	0.16
BMT-206	206	-0.73	3.19	132233.07	31.54	220461.22	30.95	27.04	0.16
BM-60	210	-0.71	1.10	136311.33	56.21	235951.81	79.92	59.31	1.80
BM-57	213	-0.72	2.44	126001.35	22.62	221247.76	140.41	35.15	0.29
BM-55	215	-0.57	2.77	123565.25	23.10	195446.31	103.63	37.51	0.33
BM-51	219	-0.85	1.24	139339.33	151.41	218671.71	72.72	61.09	3.59
BM-33	237	-0.84	2.70	133090.71	52.05	225691.39	82.21	53.04	0.18
BM-30	240	-0.76	2.35	137578.13	181.93	226467.95	126.00	53.41	0.37
BM-28	242	-0.57		138765.02	91.14	229966.56	82.60	44.22	0.29
BM-24	246	-0.57	0.84	135748.59	43.00	221597.14	100.86	31.87	0.79
BM-20	250	-0.53	0.62	135928.29	54.05	225766.51	87.60	35.99	0.49
BM-1	269	-0.55	0.06	134527.43	188.56	217723.93	105.19	52.10	1.53
YJH-0.9	270.9	-0.34		63790.21	320.29	115408.90	537.01	30.24	0.53
YJH-2	272	-0.46	-1.35	72953.02		120191.92	548.44	33.02	0.65
YHJ-21	291	-0.64	3.36	4106.84	171.10	330739.84	86.45	351.38	0.34
YJH-33	303	-0.82	3.30	6388.73	177.14	320335.53	84.92	384.16	0.32
YJH-34	304	-0.70	3.72	4701.60	196.90	334323.01	82.75	375.20	0.30
YJH-38	308	-0.67	3.25	3461.46	113.97	310335.35	90.17	277.08	0.27
YJH-40	310	-0.52	-1.05	1924.99	262.61	310333.29	320.62	158.96	13.01

Table C.2. $\delta^{238}U$ data with selected geochemical data at the Gaojiashan section.

Sample No.	heights	$\delta^{238}U$	$\delta^{13}C$	Mg	Al	Ca	Mn	Sr	U
	m	‰	‰	ppm	ppm	ppm	ppm	ppm	ppm
14GJS-0.5	51.5	-0.89		4756.77	309.03	407021.26	62.95	78.27	0.16
14GJS-2	50.0	-0.87	1.76	5674.63	327.20	352607.35	88.80	116.73	0.32
14GJS-4	48.0	-0.82		8189.71	187.89	352411.85	84.69	541.18	0.41
14GJS-5	47.0	-1.01	2.59	11986.39	217.74	293320.63	85.37	554.70	0.45
14GJS-7	45.0	-0.81	5.81	7065.55	728.06	308820.44	101.58	643.61	0.50
14GJS-8	44.0	-0.86	5.37	4938.71	534.29	350468.91	84.35	849.99	0.49
14GJS-9	43.0	-1.08	5.99	7098.86	630.63	303184.88	105.22	683.76	0.64
14GJS-10	42.0	-0.86	5.99	5603.66	839.83	287952.66	96.73	622.13	0.95
14GJS-12	40.0	-0.85	5.20	9479.76	2189.48	123999.66	114.28	205.53	0.82
14GJS-13	39.0	-1.17	5.86	4489.66	964.00	335982.55	113.53	631.50	0.54
14GJS-14	38.0	-0.92	4.62	4307.39	1509.25	304499.01	149.85	574.86	0.44
14GJS-16	37.0	-1.01	4.06	3761.14	1445.78	336848.34	214.00	570.27	0.20
14GJS-18	36.0	-0.92	5.04	3632.43	2638.47	182162.53	212.46	210.74	0.83
14GJS-20	34.0	-0.95	4.53	4176.83	1993.97	300878.94	276.75	446.24	0.64
14GJS-22.5	33.0	-1.02	3.58	4481.54	1625.27	296767.11	276.80	372.18	0.48
14GJS-24	32.0	-1.07	4.34	4720.57	1461.53	347205.13	293.64	405.54	0.72
14GJS-26	31.0	-0.96	2.04	4302.25	1345.92	345115.42	363.14	291.18	0.62
14GJS-27	29.5	-1.08	1.63	4248.00	1174.33	311467.38	247.33	431.64	0.39
14GJS-30	28.0	-0.91	0.83	8335.17	1511.31	343278.34	617.12	204.00	0.84
14GJS-31	26.0	-0.80		5648.72	1217.80	308547.29	380.74	232.11	0.52
14GJS-32	25.0	-0.42	0.57	12012.81	2267.81	263215.02	506.12	125.16	0.44
14GJS-33	22.0	-0.76	0.41	4381.00	4480.03	116915.99	261.52	49.97	0.12
14GJS-34.5	20.0	-0.18	0.03	15871.96	2623.49	181901.81	479.12	68.95	0.21
14GJS-35	17.5	-0.60		18491.49	2738.18	192814.15	364.18	74.30	0.08
14GJS-38	14.0	-0.24	1.10	13855.59	1424.65	199004.22	307.99	76.39	0.08
14GJS-39	13.0	-0.55	1.16	10143.63	1900.73	181036.51	247.58	84.46	0.08
14GJS-43	9.0	-0.70	0.28	57816.74	1116.73	119446.46	483.39	48.49	0.98

Table C.3. The sample dissolving procedure.

Dissolving step	Dissolving agent	Time gap between steps
S1–S6	5mL 1M HCl	10 minutes
S7–S11	1mL 12M HCl	25 minutes
S11–S13	5mL 1M HCl	10 minutes
Final volume	45 mL	

S denotes steps, for instance, S1–S6 denote steps 1 to 6.

Table C.4. Cross-correlation coefficients (R^2) and p-values calculated to test the influence of diagenetic indicators on $\delta^{238}U$ (confidence interval = 95%).

Shibantan Member at Wuhe	R^2	*p*-value
$\delta^{238}U$ vs. $\delta^{13}C$	0.21	0.33
$\delta^{238}U$ vs. Mg/Ca (mol:mol)	0.00	0.78
$\delta^{238}U$ vs. $\delta^{18}O$	0.02	0.53
$\delta^{238}U$ vs. Sr concentration	0.03	0.37
$\delta^{238}U$ vs. Mn concentration	0.08	0.17
$\delta^{238}U$ vs. Mn/Sr	0.12	0.09
$\delta^{238}U$ vs. Mn/(Mg+Ca) (ppm/w.t.%)	0.35	0.09
$\delta^{238}U$ vs. Sr/(Mg+Ca) (ppm/w.t.%)	0.15	0.50
$\delta^{238}U$ vs. Ce anomalies	0.01	0.65
$\delta^{238}U$ vs. U/Al (ppm/w.t.%)	0.15	0.06
$\delta^{238}U$ vs. Al content	0.19	0.38
$\delta^{238}U$ vs. U/(Mg+Ca) (ppm/ wt.%)	0.33	0.12
$\delta^{238}U$ vs. Mo/(Mg+Ca) (ppm/ wt.%)	0.22	0.31
$\delta^{238}U$ vs. Mo/U	0.00	1.00
$\delta^{238}U$ vs. Fe/U (wt.%/ppm)	0.06	0.24

Gaojiashan Member at Gaojiashan	R^2	*p*-value
$\delta^{238}U$ vs. $\delta^{13}C$	0.02	0.61
$\delta^{238}U$ vs. Mg/Ca (mol:mol)	0.05	0.35
$\delta^{238}U$ vs. $\delta^{18}O$	0.00	0.96
$\delta^{238}U$ vs. Sr concentration	0.05	0.37
$\delta^{238}U$ vs. Mn concentration	0.02	0.60
$\delta^{238}U$ vs. Mn/Sr	0.03	0.46
$\delta^{238}U$ vs. Mn/(Mg+Ca) (ppm/w.t.%)	0.05	0.83
$\delta^{238}U$ vs. Sr/(Mg+Ca) (ppm/w.t.%)	0.15	0.53
$\delta^{238}U$ vs. Ce anomalies	0.03	0.51
$\delta^{238}U$ vs. U/Al (ppm/w.t.%)	0.03	0.46
$\delta^{238}U$ vs. Al content	0.11	0.67
$\delta^{238}U$ vs. U/(Mg+Ca) (ppm/ wt.%)	0.17	0.48
$\delta^{238}U$ vs. Mo/(Mg+Ca) (ppm/ wt.%)	0.43	0.07
$\delta^{238}U$ vs. Mo/U	0.29	0.23
$\delta^{238}U$ vs. Fe/U (w.t.%/ppm)	0.07	0.27

Dengying and Yanjiahe Formation at Wuhe	R^2	*p*-value
$\delta^{238}U$ vs. Mg/Ca (mol:mol)	0.22	0.00
$\delta^{238}U$ vs. Ce anomalies	0.01	0.47
$\delta^{238}U$ vs. U/Al (ppm/w.t.%)	0.02	0.28
$\delta^{238}U$ vs. Fe/U (wt.%/ppm)	0.07	0.06

Table C.5. A summary of the parameters used in the modeling excise.

Parameter	Description	Values	Unit	References
J_{riv}	Riverine U fluxes to oceans	4.2×10^{7}	Mol/yr	Barnes and Cochran, 1990; Dunk et al., 2002; Morford and Emerson, 1999; Tissot and Dauphas, 2015
J_{oxic}	Removal flux to oxic sinks	2.23×10^{7}	Mol/yr	Barnes and Cochran, 1990; Dunk et al., 2002; Morford and Emerson, 1999; Tissot and Dauphas, 2015
$J_{suboxic}$	Removal flux to suboxic sinks	1.53×10^{7}	Mol/yr	Barnes and Cochran, 1990; Dunk et al., 2002; Morford and Emerson, 1999; Tissot and Dauphas, 2015
J_{anoxic}	Removal flux to anoxic sinks	4.45×10^{7}	Mol/yr	Barnes and Cochran, 1990; Dunk et al., 2002; Morford and Emerson, 1999; Tissot and Dauphas, 2015
k_{oxic}	Effective burial rate constant for oxic sinks	0.0536	dm/yr	Dunk et al., 2002
$k_{suboxic}$	Effective burial rate constant for suboxic sinks	0.469	dm/yr	Dunk et al., 2002
k_{anoxic}	Effective burial rate constant for anoxic sinks	0.939	dm/yr	Zheng et al., 2002a, b; Zheng et al., 2000
$\delta^{238}U_{riv}$	$\delta^{238}U$ of river waters	−0.34	‰	Andersen et al., 2016
$[U]_{modern}$	Modern seawater U concentration	1.39×10^{-8}	mol/dm^3	Chen et al., 1986; Weyer et al., 2008
$\delta^{238}U_{sw}$	Modern seawater $\delta^{238}U$	−0.4	‰	Tissot and Dauphas, 2015; Weyer et al., 2008
Δ_{oxic}	Fractionation factor between oxic sink and seawater	0.005	‰	Weyer et al., 2008
$\Delta_{suboxic}$	Fractionation factor between suboxic sink and seawater	0.1	‰	Tissot and Dauphas, 2015
Δ_{anoxic}	Fractionation factor between anoxic sink and seawater	0.6	‰	Andersen et al., 2014; Holmden et al., 2015; Rolison et al., 2017; Weyer et al., 2008
V	Seawater volume	1.37×10^{21}	dm^3	Hastings et al., 1996
A	Total seafloor area	3.61×10^{16}	dm^2	Veeh, 1967
	Modern anoxic seafloor area	0.35	%	Dunk et al., 2002
	Modern suboxic seafloor aarea	6.00	%	Balance
	Modern oxic seafloor area	93.65	%	

APPENDIX D

SUPPLEMENTARY INFORMATION FOR NEAR-MODERN LEVELS OF OCEAN OXYGENATION CONTRIBUTED TO THE EDIACARAN EVOLUTION OF EARLY ANIMALS

D. 1 Study sections and their local redox information

We have studied three classical and paleogeographically widely-separated Shuram sections (Grotzinger et al., 2011): The Jiulongwan section from South China(Li et al., 2016), the Bol'shoy Patom section from Siberia(Melezhik et al., 2009), and the Death Valley section from western United States(Hardisty et al., 2017). The paleogeographic locations of the study sections have been summarized in Figure 6.1.

The SE at the Jiulongwan section (GPS: N 30°48'15.05", W 111°3'18.61") is represented by the Doushantuo Member III (Li et al., 2016; McFadden et al., 2008), which is ≈70 m thick and is composed of dolostone and bedded chert in the lower part that passes up-section into limestone and dolostone. Sedimentological evidence suggests that the entire Doushantuo Formation at Jiulongwan was deposited below or near wave base (McFadden et al., 2008). Though there are some debates about the detailed depositional environment (Jiang et al., 2011; McFadden et al., 2008; Zhu et al., 2007), the Doushantuo Formation at Jiulongwan was likely to have been accumulated in a basin that was connected to the open ocean, see McFadden et al. (2008) for a detailed description of the depositional environment at the Jiulongwan section. Fe-S-C systematics and Ce anomaly studies suggest the local depositional environmental at Jiulongwan was anoxic (Li et al., 2010; Ling et al., 2013).

The SE at the Bol'shoy Patom section is represented by the Kholychskaya Formation, the Alyanchskaya Formation, and the Nikol'skaya Formation, which are ≈200 m, ≈530 m, and ≈390 m thick, respectively, and are composed of well-preserved high Sr limestone (Melezhik et al., 2009). The sedimentary facies associations suggest deposition

on a shallow carbonate platform that was well connected to the open ocean with neither basin isolation nor chemical or physical stratification (Melezhik et al., 2009). Abundant red ooids and oncoids are indicative of oxidized and agitated depositional environments, see Melezhik et al. (2009) for a relative detailed description of the depositional environment at the Bol'shoy Patom section.

The SE in the Death Valley region, California comes from Saddle Peak Hills (GPS: N 35°45.439', W 116°20.936') and is represented by the Rainstorm Member of the Johnnie Formation, which is >100 m thick in the study section and is composed of interbedded siltstone, sandstone, and conglomerate, with locally abundant dolostone. Sedimentary features suggest deposition under distal-fluvial and shallow-marine (above storm wave base) conditions (Verdel et al., 2011). The Shuram $\delta^{13}C_{carb}$ excursion occurs primarily in dolomitic siltstone, but begins in an ~2 m thick dolomitic oolite member known as the Johnnie Oolite. The Johnnie Oolite is pervasive marker bed across the Death Valley region and has been characterized and discussed in many previous studies (Bergmann et al., 2011; Corsetti and J. Kaufman, 2003; Kaufman et al., 2007; Verdel et al., 2011). I/Ca studies suggests an oxic local depositional environment across the SE at the Johnnie Formation (Hardisty et al., 2017).

The precise stratigraphic/temporal correlation between different Shuram sections is difficult because of the lack of a radiometric date to constrain the beginning of the Shuram excursion. Recent paleomagnetic, rock magnetic, and cyclostratigraphic studies suggest that the Shuram Excursion from different locations occurred synchronously (Gong et al., 2017; Minguez and Kodama, 2017; Minguez et al., 2015). For example, rock magnetic studies from globally separated sites—the Doushantuo Member III (EN3) in South China, the Wonoka Formation from the Flinders Ranges in South Australia, and the Johnnie Formation from the Death Valley, California, USA— suggest that the Shuram Excursion at each location occurred synchronously (Gong et al., 2017; Minguez and Kodama, 2017; Minguez et al., 2015) over a duration of 8–10 Ma. In the absence of absolute age constraints and rock magnetic studies from the Bol'shoy Patom section in Siberia, the largest $\delta^{13}C_{carb}$ excursion found in Siberia is assumed and accepted to be correlated to the Shuram

Excursion found in other localities (Grotzinger et al., 2011; Melezhik et al., 2005; Melezhik et al., 2009).

D. 2 Analytical methods

Fresh rock samples were collected in the field. The rock samples have been crushed into small pieces in the core lab. We have carefully picked fresh pieces that without veins and cleaned using 18.2 MΩ Milli-Q water. The cleaned pieces were then dried and powdered to ~200 mesh using agate ball mill. Approximately 5 g of each sample was dissolved in 1 M hydrochloric acid (HCl) for 24 hours at room temperature. This method minimizes dissolution of non-carbonate minerals (e.g., silicates and sulfides) and organic matter. Digests were centrifuged and the supernatant was separated. Major, minor, and trace element concentrations were measured on a Thermo iCAP™ quadrupole inductively coupled plasma mass spectrometer (Q-ICP-MS) at the W. M. Keck Laboratory for Environmental Biogeochemistry at Arizona State University (ASU) on splits from each supernatant. Typical precision was better than 3 % and 5 % for major and trace elements, respectively, based on repeated analysis of in-run check standards.

Prior to U isotopes column chemistry, appropriate amounts of the ^{236}U:^{233}U double spike (Brennecka et al., 2011a; Romaniello et al., 2013; Weyer et al., 2008; Zhang et al., 2018a; Zhang et al., 2018b; Zhang et al., 2018c) were added to each sample to obtain molar spike/sample ratio of 0.0342. The spike-sample mixtures were evaporated to dryness and taken up in 3N HNO_3. Uranium was purified using the UTEVA method (Brennecka et al., 2011a; Romaniello et al., 2013; Weyer et al., 2008; Zhang F. et al., 2018a,b,c) for isotopic analysis. A volume of 1.0–1.2 mL UTEVA resin was loaded on a column. The resin was then washed with 5 × 2.5 mL 0.05 M HCl to remove impurities. The resin was then converted to the nitric form by loading 4 × 2.5 mL 3 M HNO_3. The double-spiked U sample (dissolved in 3 M HNO_3) was loaded on the column and rinsed with 10 × 2.5 mL 3 M HNO_3 to remove all matrix ions except U and Th. Then 10 M HCl (3 × 2 mL) was added to the column to convert the UTEVA resin to chloride form. Th was removed from the resin using a mixture of 5 M HCl and 0.05 M oxalic acid (3 × 2 mL). The oxalic acid left on the resin was rinsed with 3 × 2 mL 5 M HCl. The U adsorbed on the resin was eluted

with 13 mL (2+2+2+3+4) 0.05 M HCl. The U cuts were dried down and heated with concentrated HNO_3 + 30 % H_2O_2 (1.5 mL + 0.3 mL) to remove any organic residue eluted from the UTEVA resin. The last step was repeated for three times in order to remove all organic residue. All samples have been put through U isotopes column chemistry twice in order to completely remove matrix ions. The final purified U was dissolved in 0.32 M HNO_3 and diluted to a U concentration of 50 ppb.

Uranium isotopes were measured at ASU on a Themo-Finnigan Neptune multi-collector ICP-MS at low mass resolution and consisted of 50 cycles of 4.194 s integration time. Rinsing time was typically 210 s or more. When using a 100 μl nebulizer, a 50 ppb sample solution yielded 42−45 V of ^{238}U signal on a 10^{11} Ω amplifier. The standard solution CRM145 (50 ppb U) was analyzed every two samples. Two secondary standards CRM129a and Ricca ICP solution were measured after every fifteen measurements. Sample $\delta^{238}U$ values were normalized by the average of the bracketing standards. The isotopic compositions of standards CRM145, CRM129a, and Ricca are 0.00±0.07 ‰(2SD), −1.74±0.06 ‰(2SD), and −0.28±0.08 ‰(2SD), respectively. The $\delta^{238}U$ results are summarized in Figure 6.1 in the main text and in the Supplementary Database S1-S3.

D. 3 Evaluation of diagenetic alteration

We compared our U isotope data to standard diagenetic indicators such as Mn/Sr ratios and O isotope compositions to evaluate the influence of diagenesis. Mn/Sr ratios in carbonate precipitates have commonly been used as indicators of post-depositional alteration (Gilleaudeau et al., 2018; Jacobsen and Kaufman, 1999; Lau et al., 2017; Lau et al., 2016; Veizer, 1989), with a cutoff of 3 to 10 suggested for Precambrian carbonate sedimentary rocks (Jacobsen and Kaufman, 1999; Zhang et al., 2014). The Mn/Sr ratio of Jiulongwan carbonates range between 0.27 and 8.16 with 32 out of 49 samples with Mn/Sr ratios smaller than 3, indicating those carbonates are generally well preserved (Figure D.1A). The Mn/Sr ratio of Bol'shoy Patom carbonates range between 0 and 0.99, indicating those carbonates are exceptional well preserved (Fig. S2B). The Mn/Sr ratio of Johnnie sediments range between 2.79 and 35.46 (Figure D.1C), those higher Mn/Sr ratios might attribute to the lithology of the Johnnie sediment. The Johnnie Formation is comprised

mainly of dolomitic sandstone, which have a low capacity to reserve Sr while have a high capacity to reserve Mn, which may have led to relative high Mn/Sr ratio in those sediments (Gilleaudeau et al., 2018; Veizer, 1983). We further investigated the extent of correlation between Mn/Sr–δ^{238}U, Mn/Sr–U concentration, Sr concentration–δ^{238}U, Sr concentration–U concentration, Mn concentration–δ^{238}U, and Mn concentration–U concentration for all study samples; no statistically significant correlations between Mn/Sr, Sr concentration, Mn concentration and both δ^{238}U and U concentrations are observed (Table D.1).

Oxygen isotope ratios are widely cited to suggest that the Shuram carbonates may have undergone post-depositional alteration (Derry, 2010; Grotzinger et al., 2011; Knauth and Kennedy, 2009). Chen et al. (2018) recently observed that meteoritic diagenesis of Bahamian carbonate likely led to a ~ 0.2 ‰ enrichment of δ^{238}U in altered carbonates compared to samples that only experienced marine phreatic or marine burial diagenesis. To test whether a similar process could have impacted Shuram carbonates, we investigated the extent of correlation between δ^{18}O and both δ^{238}U and U concentrations for our samples (Table D.1). We did not observe any significant correlations between δ^{18}O vs. [U] for any of the three sections (Jiulongwan, $R^2 = 0.01$; Bol'shoy Patom, $R^2 = 0.14$; Death Valley, $R^2 = 0.03$). Likewise, we did not observe significant correlations between δ^{18}O and δ^{238}U for the Jiulongwan and the Bol'shoy Patom sections ($R^2 = 0.19$ and $R^2 = 0.11$, respectively). In contrast, we observed a weak-to-moderate correlation between δ^{18}O and δ^{238}U for the Death Valley section ($R^2 = 0.41$) possibly indicating meteoric alteration of δ^{238}U in this section. Although it is difficult to entirely preclude a meteoritic diagenetic influence, we argue that the relatively weak correlations between δ^{18}O and δ^{238}U, large magnitude of the δ^{238}U shift (0.5 ‰), and strong consistency of δ^{238}U between widely-spaced sections, argues against a meteoritic diagenetic origin for the observed uranium isotope trends, and instead strongly favors a primary seawater origin.

In carbonates that underwent extensive recrystallization, δ^{238}U may be offset from primary depositional values, and therefore petrographic studies and duplication in different sections are necessary when studying carbonate δ^{238}U (Hood et al., 2016). Prior studies suggest that the Bol'shoy Patom samples and the Jiulongwan limestones typically preserve pristine sedimentary fabrics such as microbially laminated micrites, while the Jiulongwan

and the Johnnie dolostones preserve relative fine-grained, planar structures (McFadden et al., 2008; Melezhik et al., 2009).These petrographic observations, together with the fact that we find the same $\delta^{238}U$ signatures in three paleogeographically widely separated sections that have experienced completely different diagenetic histories, strongly suggest that $\delta^{238}U$ was not significantly altered by diagenesis.

We note that some carbonates at the Jiulongwan section have comparatively heavy $\delta^{238}U$ values, which likely reflects incorporation of ^{238}U-enriched U(IV) from local anoxic porewaters during early diagenesis (Romaniello et al., 2013) (discussed further in the main text). Prior Fe-S-C systematic and Ce anomaly studies have suggested that the local depositional environments at the Jiulongwan section was anoxic (Li et al., 2010; Ling et al., 2013).Nevertheless, although minor diagenetic variability in the $\delta^{238}U$ of individual samples is unavoidable, the lack of statistical correlation between our $\delta^{238}U$ data and geochemical indicators of diagenesis suggests that the $\delta^{238}U$ recorded by Shuram carbonate sedimentary rocks was not pervasively nor systematically altered. Importantly, our bulk story is built on the average of the three study sections rather than the Jiulongwan section alone.

D. 4 Evaluation of detrital contamination

Changes in the extent of detrital input might also cause a $\delta^{238}U$ offset. Our samples were dissolved in 1 M hydrochloric acid (HCl) prior to extraction of U, which will minimize dissolution of any non-carbonate minerals (e.g., silicates) and organic matter. This expectation is supported by the high U/Al ratios in our analyses. The U/Al ratio is ~0.331 ppm/wt.% in upper continental crust (Rudnick and Gao, 2003), U/Al ratios in our samples are substantially enriched above crustal values by about 1~3 orders of magnitude (Figure D.2), indicating that our sequential dissolution protocol had efficiently extracted carbonate bounded U, and thus the majority of U in the samples is authigenic rather than detrital in origin. Furthermore, there are no statistically significant correlations between $\delta^{238}U$ and both U/Al ratio and U concentration (Table D.1), indicating that observed $\delta^{238}U$ trends are not related to detrital influence.

Evaluation of influence of lithology on $\delta^{238}U$

Two independent lines of evidence document that changes in lithology, such as due to dolomitization, are unlikely a significant contributor to the observed shift in $\delta^{238}U$ across the Shuram event. First, it appears that the shift towards heavier $\delta^{238}U$ values are coincident with lithology changes from dolostone to limestone at the Jiulongwan section, however, the onset of the positive $\delta^{238}U$ excursion in the Johnnie initially occurs within an oolitic dolomite unit and is then maintained above this unit in a dolomitic sandstone unit, and stratigraphic variations in Mg/Ca molar ratios document there were no lithology changes in the Bol'shoy Patom section (Figure D.3), which is mainly comprised of well-preserved high Sr limestone (Melezhik et al., 2009). Shift to heavier $\delta^{238}U$ values in both the Bol'shoy Patom section and the Johnnie section are not related to changes in lithology.

Second, Romaniello et al. (2013) observed $\delta^{238}U$ changes associated with dolomitization in a modern Bahamian tidal pond, as reflected in a strong correlation of $\delta^{238}U$ with Mg/Ca ($R^2 = 0.96$, $p<0.001$). On this basis, Romaniello et al. (2013) first raised concerns that extensive dolomitization (>30-50% dolomite) might have compromised the $\delta^{238}U$ record across the end-Permian mass extinction (EPME) horizon in the Dawen section studied by Brennecka et al. (2011a). However, there are now $\delta^{238}U$ data from seven carbonate sections spanning the EPME (the Dajiang, Lau et al., 2016; Guandao, Lau et al., 2016; Dawen, Brennecka et al., 2011a; Daxiakou, Elrick et al., 2017; Taşkent, Lau et al., 2016; Zal, Zhang et al., 2018b; Kamura, Zhang et al., 2018a) published by three independent research groups. All of these sections show strikingly similar trends in $\delta^{238}U$ across the EPME horizon, which is remarkable because they span 1000s of km—even different ocean basins—and have experienced very different diagenetic histories, including dolomitization. These $\delta^{238}U$ studies strongly suggest that dolomitization may not be an important factor to alter primary $\delta^{238}U$ record (Zhang et al., 2018a). Additionally, we also investigated the extent of correlation between Mg/Ca molar ratios and $\delta^{238}U$ for our Shuram samples, no statistically significant correlations are observed (Table D.1), suggesting that influence of lithology on $\delta^{238}U$ is not significant. Furthermore, as with these EPME work (Zhang et al., 2018a), we focus in this manuscript on the inter-comparison of multiple, widely-spaced Shuram sections, that come from different continents, different

water depths, and experienced different diagenetic histories. Similar to the EPME studies, the three widely separated sections with very different lithology that yielded identical $\delta^{238}U$ records, which strongly argues against anything but primary oceanographic trends.

D. 5 Stratigraphic variation of U concentrations

Several previous U isotope studies suggested that in unaltered rocks, changes to the extent of global seafloor oxygenation will affect the dissolved seawater reservoir of U, and in return the abundance of U incorporated into marine carbonates (Brennecka et al., 2011a; Elrick et al., 2017; Lau et al., 2016). Under ideal conditions, stratigraphic variation in U concentrations can record meaningful seawater redox variations, but this relationship can be easily masked by other sources of variation (Lau et al., 2017). Notably, prior studies have shown that the distribution coefficient of U into aragonite is significant larger than for calcite (DeCarlo et al., 2015; Meece and Benninger, 1993; Reeder et al., 2000). For instance, an experimental study indicated that the partition coefficients for U in aragonite range from 1.8 to 9.8, while the partition coefficient for U in calcite is less than 0.2 and may be as low as 0.046 (Meece and Benninger, 1993). Thus, environmental and ecological changes that drive variations in the abundance of primary aragonite and calcite will have a large effect on sediment U concentration. Even the primary carbonate precipitates in the modern Bahamian carbonate platform, their U concentrations from <0.1 ppm to > 4 ppm, while their $\delta^{238}U$ are the same (Romaniello et al., 2013).

In contrast, the effect of mineralogy and carbonate ion concentration on $\delta^{238}U$ is more limited. Uranium isotope measurements of aragonite and high-Mg calcite primary precipitates exhibit no offset from seawater (Romaniello et al., 2013). Laboratory-precipitated calcite and aragonite at pH ~ 8.5 showed only minor (<0.13‰) fractionation between the liquid medium and the solid (Chen et al., 2016; Stirling et al., 2015). At pH ~7.5 the precipitates of both polymorphs exhibit no fractionation (Chen et al., 2016). Therefore, changing carbonate mineralogy can result in large differences in uranium concentrations but only small changes in the isotopic composition (Lau et al., 2017).

There are obvious lithological and mineralogical changes in the studied sections. For example, the Jiulongwan section is comprised of interlayered limestone and dolostone,

the Death Valley section is comprised of dolomitic sandstone, sandy dolostone and dolostone, while the Siberia section is comprised of well-preserved high Sr limestone. Some of the limestone can originally be aragonite and/or high-Mg calcite (e.g., the high Sr carbonates from Siberia; Melezhik et al., 2009). The Jiulongwan section and the Siberia section have very different U concentrations while the U isotope trends are the same. Most of samples (44 out of 49 samples) from South China have U concentrations <0.5 ppm. In contract, 25 out of 44 samples from the Siberia have U concentration >3 ppm (with some samples have U >10 ppm) (Figure D.4). We hypothesize that the decoupling of U concentration from $\delta^{238}U$ in study sections can be attributed to mineralogical/lithological shifts that affect only the reliability of the carbonate U concentration paleoredox proxy and not $\delta^{238}U$. We therefore only focus on interpreting $\delta^{238}U$ data.

D. 6 Major sources and sinks of U in the ocean

The only major source of U to the ocean is oxidative mobilization of U from the upper continental crust and transport of dissolved U(VI) to the oceans via rivers. The $\delta^{238}U$ value of dissolved U in rivers is controlled by the U concentration and $\delta^{238}U$ of the source lithologies that dominate the upper continental crust. The estimated average $\delta^{238}U$ of the world's major rivers range between –0.24 ‰ and –0.34 ‰ (Andersen et al., 2017; Andersen et al., 2016; Noordmann et al., 2016; Tissot and Dauphas, 2015), which reflects the estimated average $\delta^{238}U$ of the continental crust [−0.30 ± 0.04 ‰ (2σ)] (Andersen et al., 2016; Tissot and Dauphas, 2015). An exception not included in this average is the Yangtze River in China, where two reported measurements average $\delta^{238}U$ of ∼−0.70 ‰ (Andersen et al., 2016). Although these data and their ability to represent the entire Yangtze catchment need to be confirmed, this "outlier" is interpreted to reflect local U contributions from evaporite minerals (halite) that are abundant near the source of the Yangtze River (Andersen et al., 2016). If so, this is an unusual situation because evaporites are not major sources of U to the oceans overall. Existing data suggests that the average composition of the continental crust has not changed significantly over the last 2.5 Ga (Gaschnig et al., 2016; Tang et al., 2016), so it is not likely that the $\delta^{238}U$ of global riverine input has changed significantly across the Shuram Excursion.

There are multiple sinks for U in the ocean. The major sinks are sediments deposited beneath anoxic/euxinic bottom waters, sediments deposited beneath weakly oxygenated bottom waters, and marine carbonates. Minor sinks include ferromanganese oxides and the hydrothermal alteration of oceanic crust (Dunk et al., 2002; Morford and Emerson, 1999; Tissot and Dauphas, 2015). The largest expression of U isotope fractionation (0.60–0.85 ‰, discussed further below) in the marine environment occurs during U burial in anoxic/euxinic sediments, like those of the Black Sea, the Saanich Inlet, and the Framvaren Fjord (Andersen et al., 2013; Holmden et al., 2015; Kaltenbach, 2013; Rolison et al., 2017; Weyer et al., 2008). By contrast, the fractionation of U isotopes during removal to suboxic sediments is only ~0.1 ‰ based on observations from the Peruvian continental margin and off the coast of Washington State, where sediments underlying weakly oxygenated waters have an average δ^{238}U of –0.28 ± 0.19 ‰ (Weyer et al., 2008) and –0.23 ± 0.19‰ (Andersen et al., 2016), respectively. Marine carbonate sediments record the δ^{238}U of seawater, subject to a 0.2–0.4 ‰ offset (Romaniello et al., 2013), which likely reflects incorporation of U(IV) into shallow sediments from anoxic porewaters (discussed further in the main text). The fractionation of U isotopes during removal to Mn nodules and metalliferous sediments is –0.24 ‰, and is well constrained by both natural samples (Goto et al., 2014; Wang et al., 2016) and laboratory adsorption experiments (Brennecka et al., 2011b). Seafloor alteration at high temperatures is assumed to have no isotope fractionation, and seafloor alteration at low temperatures is estimated to have a fractionation factor of 0.25 ‰ (Tissot and Dauphas, 2015).

D. 7 Other sinks and Δ_{other}

A simplified schematic representation of the major source and sinks of U in the modern ocean along with their isotopic compositions (sources) or associated isotopic fractionations (sinks) is presented in Figure 1.2(after Wang et al. (2016) and Tissot and Dauphas (2015)). In order to simplify our mass balance modeling calculations, several types of sinks are lumped into a single oxic sink, including Fe-Mn crusts, pelagic clays, low temperature and high temperature oceanic crust alteration, marine carbonates, and coastal retention (Figure 1.2). And the oxic sink and suboxic sink are lumped into a single

other sink in order to make the modeling estimation of U removal into anoxic/euxinic sediments solvable. The overall U isotope fractionation factor for the lumped oxic sink and the lumped other sink are calculated as the weighted average of individual ones. The fractionation factors between the lumped oxic sink and seawater and the lumped other sink and seawater are 0.005 ‰ (Δ_{oxic}) and 0.043 ‰ (Δ_{other}), respectively (Figure 1.2 and Table D.2).

D. 8 Uranium isotope mass balance constraints on U removal to anoxic sinks

The implied changes to the extent of U removal into anoxic sediments can be described by a mass balance equation for the fraction of anoxic sinks and its isotopic composition:

$$\delta^{238}U_{input} = (f_{anoxic} \cdot \delta^{238}U_{anoxic}) + (f_{other} \cdot \delta^{238}U_{other}) \quad (1)$$

$$\delta^{238}U_{anoxic} = \delta^{238}U_{seawater} + \Delta_{anoxic} \quad (2)$$

$$\delta^{238}U_{other} = \delta^{238}U_{seawater} + \Delta_{other} \quad (3)$$

$$f_{anoxic} + f_{other} = 1 \quad (4)$$

where the subscripts input, anoxic, other, and seawater denote the riverine input, anoxic sink, all other sedimentary sinks, and seawater, respectively, f_{anoxic} and f_{other} represent the fraction of total U removed to each sediment type, and Δ_{anoxic} and Δ_{other} represent the isotope fractionation factor between seawater and each sediment type. In this simplified modeling exercise, all types of sinks other than anoxic sinks are lumped into a single other.

Solving equations (*1*) to (*4*), we have

$$f_{anoxic} = \frac{\delta^{238}U_{input} - \delta^{238}U_{seawater} - \Delta_{other}}{\Delta_{anoxic} - \Delta_{other}} \quad (5)$$

Following Montoya-Pino et al.(2010), Brennecka et al.(2011), and Zhang F. et al. (2018a,b) we assume: (1) isotopically constant U input from rivers over geologic time with an average value of −0.34 ‰ (Andersen et al., 2016), $\delta^{238}U_{input} = -0.34$ ‰; (2) a constant (Δ_{other} = +0.043 ‰) isotope fractionation between seawater and the average isotopic composition of other sinks (Figure 1.2); and (3) a fractionation factor of Δ_{anoxic} (0.6 ‰ to

0.85 ‰) between seawater and anoxic/euxinic sinks. With any given seawater $\delta^{238}U$ values, we can calculate the U associated with anoxic sedimentary sinks.

Considering the range of diagenetic offset (0.2−0.4 ‰) discussed in the main text, our best estimate of $\delta^{238}U$ for the pre-SE seawater and the SE seawater are −0.94 ‰ to −1.14 ‰ and −0.46 ‰ to −0.66 ‰, respectively. When applying a of Δ_{anoxic} of 0.6 ‰, an average representative observed in some modern anoxic basins (the modern Saanich Inlet (Holmden et al., 2015) and the black sea (Andersen et al., 2014), we calculate that $f_{anoxic} \approx 1$ in the SE ocean, meaning that 100 % of the global U sink was removed into anoxic sediments in the pre-Shuram ocean. Assuming the same Δ_{anoxic} value, we calculate that f_{anoxic} =0.14 and 0.50 in the SE ocean, meaning that 14–50 % of the global U sink was removed into anoxic sediments in the SE ocean.

The estimated f_{anoxic} values can vary with the $\delta^{238}U_{input}$ values used in the calculation. The present study used the global average riverine value reported by Andersen et al. (2016). Another study by Noordmann et al. (2016) have reported a slightly heavier average riverine value of −0.27 ‰ (all major rivers in this study define a relatively narrow range between −0.31 and −0.13 ‰ with a weighted mean isotope composition of −0.27 ‰). However, the difference in average riverine values will only result in small differences in the estimated f_{anoxic} values. For instance, when applying a Δ_{anoxic} of 0.6 ‰, and using a SE seawater $\delta^{238}U$ of −0.46 ‰ as an example, $f_{anoxic} = (0.417 + \delta^{238}U_{input}) / 0.557$, when using $\delta^{238}U_{input}$ of −0.34 ‰ and −0.27 ‰, the estimated f_{anoxic} are 14% and 26%, respectively.

D. 9 Δ_{anoxic} variations in natural environments

The inferred extent of ocean anoxia calculated from the mass balance model depends on the assumed average fractionation factor (Δ_{anoxic}) between seawater and anoxic sediments, which is not tightly constrained because of the small dataset for modern anoxic environments. Large U isotope fractionations of 1.3 ‰ (Bigeleisen, 1996) and 1.1±0.2 ‰ (Wang et al., 2015) have been predicted by theoretical calculation and by a laboratory abiotic oxidation experiment, respectively. U isotope fractionations between 0.68 ‰ and 0.99 ‰ (average ~0.85 ‰) have been reported during reduction of U(VI) to U(IV) by

different species of metal-reducing bacteria (including iron- and sulfate-reducers) (Basu et al., 2014; Stylo et al., 2015).

Compared to these theoretical calculations (Bigeleisen, 1996) and laboratory experiments (Basu et al., 2014; Stylo et al., 2015; Wang et al., 2015), studies of U reduction in different natural modern anoxic marine basins have yielded smaller fractionation factors. For example, studies of the relatively open-ocean Saanich Inlet have determined a U isotope fractionation of 0.62 ± 0.17 ‰ between anoxic sediments and bottom waters (Holmden et al., 2015). The magnitude of the U isotope fractionation determined for the Black Sea water column ranges from 0.63 ± 0.09‰ to 0.84 ± 0.11‰ (Rolison et al., 2017). Similar U isotope fractionations of 0.6–0.8 ‰ have been reported from the Kyllaren fjord (Norway) (Noordmann et al., 2016). However, the strong basin restriction in the Black Sea and Kyllaren fjord has resulted in $\delta^{238}U_{auth}$ values for the euxinic sediments that are only about ~0.4 ‰ higher than global seawater, which reflects slow rates of deep-water recharge and partial U drawdown in the deep waters (Montoya-Pino et al., 2010; Noordmann et al., 2016; Rolison et al., 2017; Weyer et al., 2008). Restricted water exchange has also caused the deep waters of the Black Sea and Kyllaren fjord to have lower $\delta^{238}U$ than global seawater because of preferential ^{238}U removal to the euxinic sediments (Noordmann et al., 2016; Rolison et al., 2017).

Taken together, although larger isotopic fractionation factors of 1.0−1.3 ‰ have been predicted by laboratory experiments and theoretical calculations (Basu et al., 2014; Bigeleisen, 1996; Stylo et al., 2015; Wang et al., 2015), existing observations from modern anoxic basins imply that reductive removal of U from seawater could most likely result in U isotope fractionation between seawater and relatively open-ocean euxinic sediments ranging from 0.60–0.85 ‰. These relative smaller isotopic fractionation factors observed in modern anoxic basins are interpreted to reflect diffusion-limited U reduction below the sediment-water interface, which reduces the magnitude of the apparent isotopic fractionation factor by ~50 %(Andersen et al., 2014). Uranium removal in the water column or at the sediment-water interface can be associated with a larger U isotope fractionation (Andersen et al., 2017). However, studies of U reduction in most modern anoxic basins have shown that little, if any, U reduction occurs directly in the water column (Anderson

et al., 1989a; Anderson et al., 1989b; Holmden et al., 2015), a conclusion further supported by a recent $\delta^{238}U$ study in Black Sea sediments which found that the process of chemical reduction and subsequent removal of dissolved U from the Black Sea occurs primarily in pore waters close to the water-sediment interface (Rolison et al., 2017).

We therefore tested different Δ_{anoxic} values of 0.60–0.85 ‰ in our anoxic seafloor area modeling calculation below. This range of fractionation was also applied by a previous study (Yang et al., 2017). The range being used in the present study may also be consistent with observations from the Ediacaran geological record. For instance, our best estimate of $\delta^{238}U$ for SE seawater is −0.46 ‰ to −0.66 ‰, euxinic organic-rich mudrocks deposited near the end of the SE have an average $\delta^{238}U$ of +0.24 ‰ (Kendall et al., 2015), the difference between Ediacaran seawater and euxinic organic-rich mudrocks (euxinic sedimentary sinks) is 0.70–0.90 ‰.

D. 10 Anoxic seafloor area modeling calculation

To estimate the seafloor areas overlain by anoxic water, particularly before the Shuram Excursion, we use a simple U isotope mass balance model. Because prior studies by Goto et al. (2014) and Lau et al. (2017) suggested that Mn-oxide precipitation has limited leverage on seawater $\delta^{238}U$, thus, in this model, we discount the importance of enhanced precipitation of Mn-oxides. Instead, we fold the Mn-oxides into all "other oxic sedimentary sinks" (Figure 1.2 and Table D.2) to simplify the modeling calculation.

Transient global seawater uranium concentration, [U], and isotopic compositions, $\delta^{238}U$, can be written as:

$$\frac{dN_{sw}}{dt} = J_{riv} - J_{oxic} - J_{suboxic} - J_{anox} \quad (6)$$

$$\frac{d(N_{sw} \cdot \delta^{238}U_{sw})}{dt} = J_{riv} \cdot \delta^{238}U_{riv} - J_{oxic} \cdot \delta^{238}U_{oxic} - J_{suboxic} \cdot \delta^{238}U_{suboxic} - J_{anox} \cdot \delta^{238}U_{anox} \quad (7)$$

$$\delta^{238}U_{anox} = \delta^{238}U_{sw} + \Delta_{anox} \quad (8)$$

$$\delta^{238}U_{suboxic} = \delta^{238}U_{sw} + \Delta_{suboxic} \quad (9)$$

$$\delta^{238}U_{oxic} = \delta^{238}U_{sw} + \Delta_{oxic} \quad (10)$$

where N_{sw} is the oceanic U inventory in moles, $\delta^{238}U_{sw}$ is the value of seawater, $\delta^{238}U_{riv}$ is the value of the riverine source. $\delta^{238}U_{anox}$, $\delta^{238}U_{suboxic}$, and $\delta^{238}U_{oxic}$ are the U isotope

composition of anoxic sedimentary sink, *s*uboxic sedimentary sink, and the remaining other sinks, respectively. Here, we simplify the inputs to J_{riv}, the riverine flux, whose modern value is ~4×10^7 moles U/yr (Tissot and Dauphas, 2015). The outputs are assumed to consist of the anoxic sediment sink (J_{anox}), suboxic sediment sink ($J_{suboxic}$), and the sum of the other sinks (J_{oxic}). Δ_{anox} is the effective fractionation factor associated with anoxic sediment deposition, $\Delta_{suboxic}$ is the effective fractionation factor associated with suboxic sediment deposition, and Δ_{oxic} is the effective fractionation factor associated with the remaining other sinks. Model parameterization was based on studies of the modern U cycle and are summarized in Table D.3.

At steady state, the left side of the equation (*6*) and (*7*) equal 0, yielding:

$$J_{riv} = J_{oxic} + J_{suboxic} + J_{anox} \tag{11}$$

$$\delta^{238}U_{sw} = \delta^{238}U_{riv} - f_{oxic}\cdot\delta^{238}U_{oxic} + f_{suboxic}\cdot\delta^{238}U_{suboxic} + f_{anox}\cdot\delta^{238}U_{anox} \tag{12}$$

where f_i is the fraction of individual sink fluxes out of the total input flux: $f_{oxic} = J_{oxic}/J_{riv}$, $f_{suboxic} = J_{suboxic}/J_{riv}$, $f_{anox} = J_{anox}/J_{riv}$.

Assuming removal mechanisms are first order with respect to seawater U concentration (Partin et al., 2013; Reinhard et al., 2013), we have:

$$J_{anox} = k_{anox}\cdot A_{anox}\cdot[U] \tag{13}$$

$$J_{suboxic} = k_{suboxic}\cdot A_{suboxic}\cdot[U] \tag{14}$$

$$J_{oxic} = k_{oxic}\cdot A_{oxic}\cdot[U] \tag{15}$$

where A_{anox}, $A_{suboxic}$, and A_{oxic} represents the seafloor areas covered by anoxic sediment sink, suboxic sink, and all the other sedimentary sinks; [*U*] denotes seawater U concentration, and k_{anox}, $k_{suboxic}$, and k_{oxic} terms are effective burial rate constants associated with each sedimentary sinks, which are solved for by inverting modern areas and burial fluxes. Solving equations (8)–(15), we have

$$\delta^{238}U_{seawater} = \delta^{238}U_{input} - \frac{A_{anoxic}*k_{anoxic}*\Delta_{anoxic} + A_{suboxic}*k_{suboxic}*\Delta_{suboxic} + A_{oxic}*k_{oxic}*\Delta_{oxic}}{A_{anoxic}*k_{anoxic} + A_{suboxic}*\Delta_{suboxic} + A_{oxic}*k_{oxic}} \tag{16}$$

where $A_{anoxic} + A_{suboxic} + A_{oxic} = A_{ocean}$. This equation has been simplified into an expression of

$$\delta^{238}U_{seawater} = \delta^{238}U_{input} - \frac{A_{anoxic} * k_{anoxic} * \Delta_{anoxic} + (A_{ocean} - A_{anoxic}) * k_{other} * \Delta_{other}}{A_{anoxic} * k_{anoxic} + (A_{ocean} - A_{anoxic}) * k_{other}} \quad (17)$$

in the main text. Parameters used in these simple modeling exercises are summarized in Table D.3. Modeling results are summarized in Figure 6.3 and Figure D.5.

We first varied the areal extent of anoxic and oxic seafloor areas while keeping the areal extent of suboxic seafloor the same as the modern value [6 %; Figure D.5A]. When assuming a Δ_{anox} of fractionation factor of 0.6 ‰, this modeling exercise suggests that nearly the entire (~100 %) seafloor was covered by anoxic waters in order for pre-Shuram seawater δ^{238}U values to approach as low as −0.94 ‰ to −1.14 ‰.

Second, we varied the fractionation factor between seawater and anoxic sediments (Δ_{anox}) and kept the suboxic seafloor area fixed at modern ocean values (6 %). The results are summarized in Figure D.5A. The results indicate that the inferred extent of ocean anoxia largely depends on the assumed average fractionation factor between anoxic sediments and seawater**.** We further considered the range of plausible Δ_{anox} (0.60–0.85 ‰) discussed above, and the estimated anoxic seafloor areas have been summarized in Figure D.5A. When applying this upper limit (Δ_{anox}= 0.85 ‰), which is also an "average" fractionation factor that represents microbially mediated U reduction (Basu et al., 2014), and is close to the maximum Δ_{anox} observed both in the modern Saanich Inlet (0.79 ‰; Holmden et al., 2015) and in the Black Sea (0.83 ‰; Weyer et al., 2008), we estimate that 17–100 % of seafloor area needed to be covered by anoxic waters in order to account for pre-SE seawater δ^{238}U values of −0.94 ‰ to −1.14 ‰ (see Figure D.5). This estimation drops to 1.0 to 4.3 % when the SE seawater δ^{238}U value was −0.46 ‰ to −0.66 ‰ (see Figure D.5). We note that these estimations are conservative because we have kept the anoxic seafloor areas fixed at the modern ocean value (~6 %), however, in reality, suboxic seafloor areas would co-expand with expansion of anoxic seafloor area. Seawater U isotope composition is not very sensitive to increasing U flux into suboxic sedimentary sinks because the suboxic sedimentary sinks are only associated with a smaller U isotope

fractionation factor (~0.1 ‰). Therefore, larger suboxic seafloor areas in the middle Ediacaran ocean would require larger anoxic seafloor areas in order to explain the observed low seawater $\delta^{238}U$ values (see Figure D.6). For example, when assuming suboxic seafloor areas in the middle Ediacaran ocean were greater than anoxic seafloor areas (a situation that is similar to the modern ocean where $f_{suboxic} > f_{anoxic}$), and when using a U isotope fractionation factor of 0.85 ‰ between seawater and anoxic sedimentary sinks, the U isotope model predicts that 50 % of seafloor needed to be covered by anoxic waters in order to drive Pre-SE seawater $\delta^{238}U$ value to be −0.94 ‰ (Figure D.6).

In addition, the inferred extent of ocean anoxia calculated from the mass balance model may also be influence by the assumed removal rate constant in anoxic/euxinic sinks, which is not tightly constrained because of the small dataset for modern anoxic/euxinic environments. Zheng et al. (2000, 2002a,b) reported k_{anoxic} from the modern Framvaren Fjord, the modern Black Sea, the modern Cariaco Basin, and the modern Saanich Inlet. We tested the minimal (k_1 = 0.313), the mean (k_2 = 0.939), and the maximum (k_3 = 2.817) values from their reports. The results have been summarized in Figure D.5B.

Despite the large uncertainties discussed above, this U isotope modeling exercise indicates that the Ediacaran Shuram event represents a profound change in global ocean marine redox conditions, from a pre-Shuram state that was substantially more anoxic than what came later.

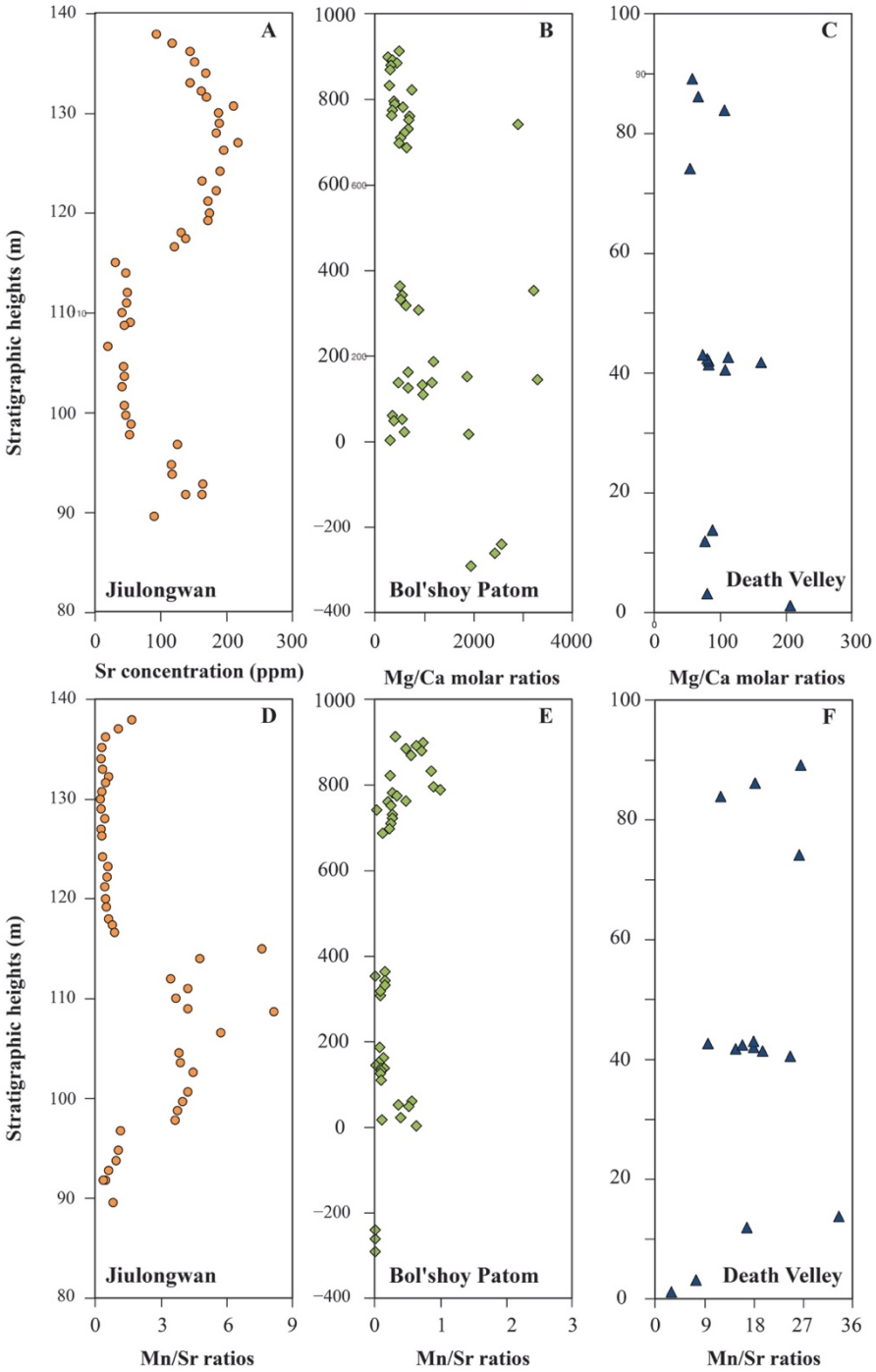

Figure D.1. Stratigraphic variation of Sr concentrations and Mn/Sr ratios from the Jiulongwan section (A and D), the Bol'shoy Patom section (B and E), and the Johnnie Formation (C and F).

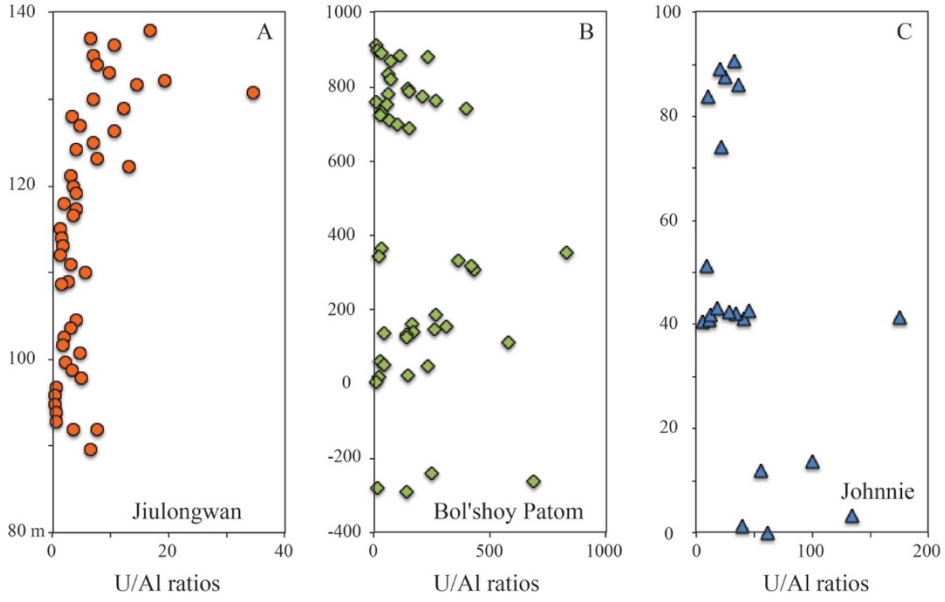

Figure D.2. Stratigraphic variation of U/Al ratios from the Jiulongwan section (A), the Bol'shoy Patom section (B), and the Johnnie Formation (C).

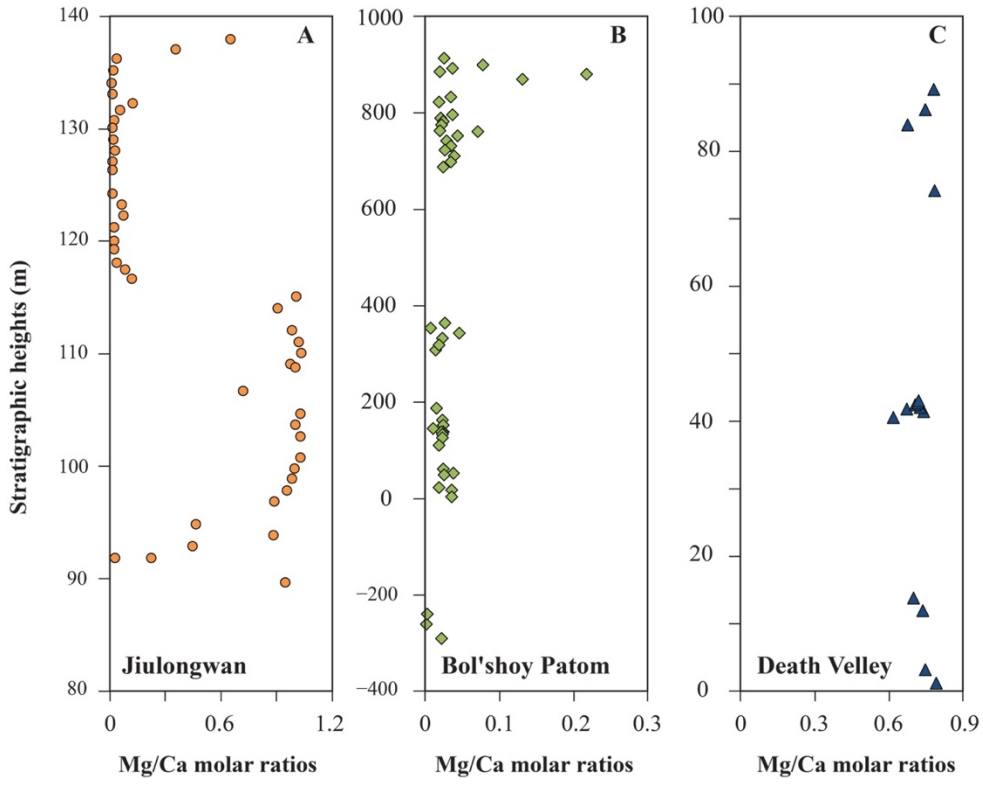

Figure D.3. Stratigraphic variation of Mg/(Mg+Ca) ratios and Mg/(Mg+Ca) ratios versus δ^{238}U plots. (A) and (D) are from the Jiulongwan section, (B) and (E) are from the Bol'shoy Patom section, and (C) and (F) are from the Johnnie Formation.

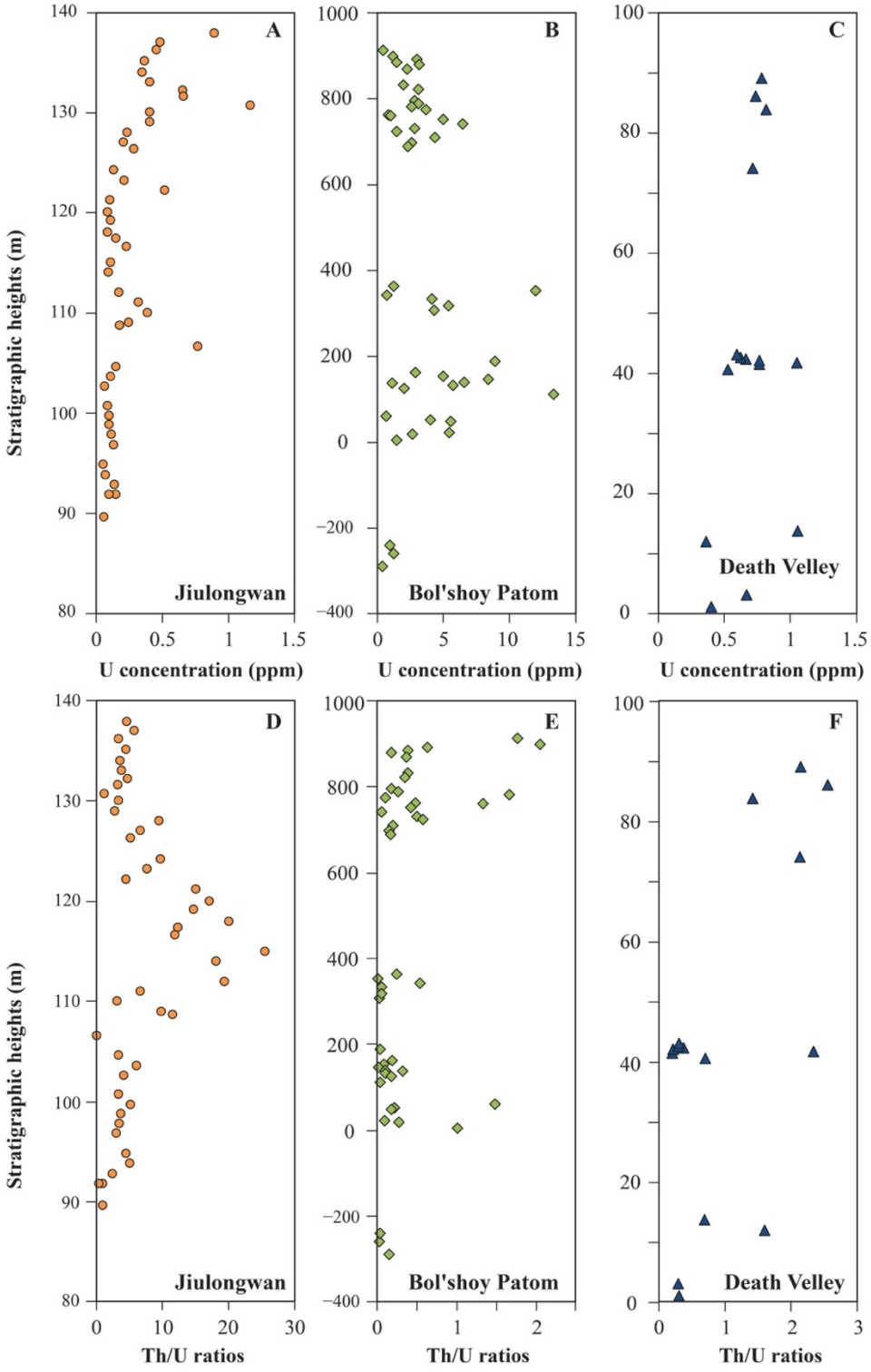

Figure D.4. Stratigraphic variation of U concentration and Th/U ratios. (A) and (D) are from the Jiulongwan section, (B) and (E) are from the Bol'shoy Patom section, and (C) and (F) are from the Johnnie Formation.

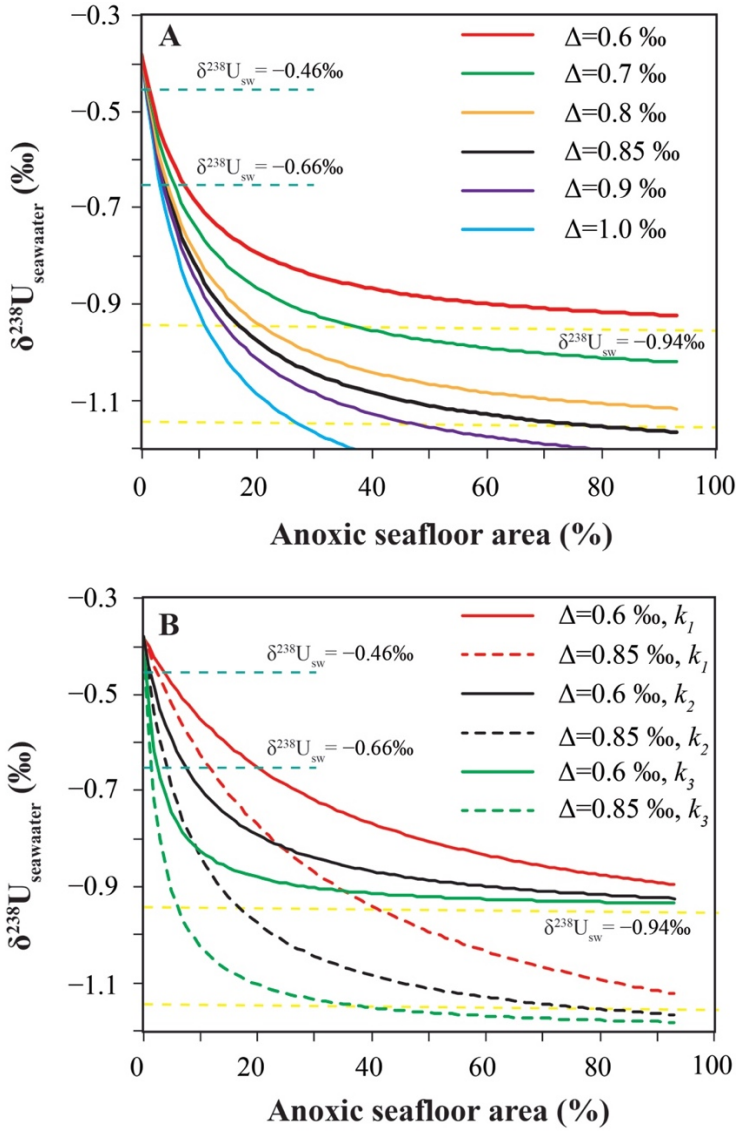

Figure D.5. Mass balance modeling calculations results. (A) Variations of seawater $\delta^{238}U$ values as a function of fractionation factor between anoxic/euxinic sinks and seawater (Δ_{anoxic}). All the other curves have kept suboxic seafloor area fixed at modern ocean values (6%). In this modeling exercise, an average rate constant (k_2) of U removal into anoxic/euxinic sediments has been used. (B) Testing of variations of seawater $\delta^{238}U$ values as a function of assumed removal rate constant and Δ_{anoxic} values. k_1 = 0.313, k_2 = 0.939, k_3 = 2.817, those k values are the minimal, mean, and maximum values reported by Zheng et al. (2000, 2002a,b) in the modern Framvaren Fjord, the modern Black Sea, the modern Cariaco Basin, and the modern Saanich Inlet. All the other curves have kept suboxic seafloor area fixed at modern ocean values (6%).

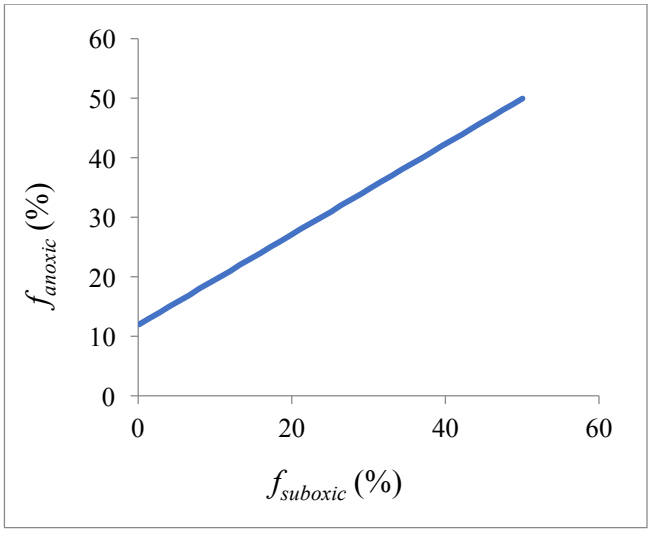

Figure D.6. Calculated combination f_{anoxic} and $f_{suboxic}$ in order to account for pre-SE seawater average $\delta^{238}U$ of −0.94 ‰. The red solid line denotes a combination f_{anoxic} and $f_{suboxic}$ in order to account for pre-SE seawater average $\delta^{238}U$ of −0.94 ‰.

Table D.1. Cross-correlation coefficients (R^2) and *p*-values calculated to test the influence of diagenetic indicators on $\delta^{238}U$.

South China section	R^2	*p*-value
$\delta^{238}U$ vs. $\delta^{13}C$	**0.623**	0.000
$\delta^{238}U$ vs. Mg/Ca (mol:mol)	0.258	0.000
$\delta^{238}U$ vs. Sr/Ca (ppm/w.t.%)	0.084	0.053
$\delta^{238}U$ vs. $\delta^{18}O$	0.191	0.003
U concentration vs. $\delta^{18}O$	0.005	0.636
$\delta^{238}U$ vs. Sr concentration	0.244	0.001
$\delta^{238}U$ vs. Mn concentration	0.041	0.182
$\delta^{238}U$ vs. Mn/Sr	0.076	0.066
$\delta^{238}U$ vs. Fe concentration	0.433	0.000
$\delta^{238}U$ vs. Rb/Sr	0.003	0.740
$\delta^{238}U$ vs. U concentration	0.138	0.012
$\delta^{238}U$ vs. Th/U	0.095	0.039
$\delta^{238}U$ vs. U/Al (ppm/w.t.%)	0.006	0.620
$\delta^{238}U$ vs. Mo/U ratios	0.000	0.951
Siberia section	R^2	*p*-value
$\delta^{238}U$ vs. $\delta^{13}C$	**0.572**	0.000
$\delta^{238}U$ vs. Mg/Ca (mol:mol)	0.055	0.122
$\delta^{238}U$ vs. Sr/Ca (ppm/w.t.%)	0.146	0.009
$\delta^{238}U$ vs. $\delta^{18}O$	0.108	0.028
U concentration vs. $\delta^{18}O$	0.136	0.013
$\delta^{238}U$ vs. Sr concentration	0.191	0.003
$\delta^{238}U$ vs. Mn concentration	0.196	0.002
$\delta^{238}U$ vs. Mn/Sr	0.161	0.006
$\delta^{238}U$ vs. Fe concentration	0.193	0.003
$\delta^{238}U$ vs. Rb/Sr	0.071	0.076
$\delta^{238}U$ vs. U concentration	0.043	0.170
$\delta^{238}U$ vs. Th/U	0.013	0.423
$\delta^{238}U$ vs. U/Al (ppm/w.t.%)	0.032	0.236
$\delta^{238}U$ vs. Mo/U ratios	0.014	0.440
$\delta^{238}U$ vs. Pr-based Ce/Ce*	0.049	0.145
$\delta^{238}U$ vs. Nd-based Ce/Ce*	0.007	0.590
Death Valley section	R^2	*p*-value
$\delta^{238}U$ vs. $\delta^{13}C$	**0.799**	0.000
$\delta^{238}U$ vs. Mg/Ca (mol:mol)	0.008	0.747
$\delta^{238}U$ vs. Sr/Ca (ppm/w.t.%)	0.010	0.726
$\delta^{238}U$ vs. $\delta^{18}O$	0.410	0.018
U concentration vs. $\delta^{18}O$	0.029	0.575
$\delta^{238}U$ vs. Sr concentration	0.030	0.535
$\delta^{238}U$ vs. Mn concentration	0.000	0.957
$\delta^{238}U$ vs. Mn/Sr	0.012	0.694
$\delta^{238}U$ vs. Fe concentration	0.839	0.000
$\delta^{238}U$ vs. Rb/Sr	0.369	0.016

$\delta^{238}U$ vs. U concentration	0.058	0.388
$\delta^{238}U$ vs. Th/U	0.243	0.062
$\delta^{238}U$ vs. U/Al (ppm/w.t.%)	0.393	0.012
$\delta^{238}U$ vs. Mo/U ratios	0.019	0.625

Note: when $p(\alpha) < 0.05$, then $\delta^{238}U$ shows a statistically significant correlation with the proxy; if $p(\alpha) > 0.05$, then $\delta^{238}U$ does not show a statistically correlation with the proxy.

Table D.2. Break down of the oxic sink into individual sinks, together with their isotope fractionation factors from seawater (Δ_i).

	Flux (10^6 mol/yr)	Fractionation factor Δ_i (‰)
Pelagic clay	3	0.04
carbonates	5.6	0.2
Mn-oxides	1	-0.24
High T oceanic crustal alteration	2	0
Low T oceanic crustal alteration	3.8	0.25
Coastal zone retention	7.6	-0.24
Weighted average Δ_{other}		0.005 ‰

Table D.3. A summary of the parameters used in the modeling excises.

Parameter	Description	Values	Unit	References
F_r	Riverine U fluxes to oceans	4.2×10^7	Mol/yr	Barnes and Cochran, 1990; Dunk et al., 2002; Morford and Emerson, 1999; Tissot and Dauphas, 2015
F_{ox}	Removal flux to oxic sinks	2.23×10^7	Mol/yr	Barnes and Cochran, 1990; Dunk et al., 2002; Morford and Emerson, 1999; Tissot and Dauphas, 2015
$F_{suboxic}$	Removal flux to suboxic sinks	1.53×10^7	Mol/yr	Barnes and Cochran, 1990; Dunk et al., 2002; Morford and Emerson, 1999; Tissot and Dauphas, 2015
F_{anoxic}	Removal flux to anoxic sinks	4.45×10^7	Mol/yr	Barnes and Cochran, 1990; Dunk et al., 2002; Morford and Emerson, 1999; Tissot and Dauphas, 2015
k_{ox}	Effective burial rate constant for oxic sinks	0.0536	dm/yr	Dunk et al., 2002
$k_{suboxic}$	Effective burial rate constant for suboxic sinks	0.469	dm/yr	Dunk et al., 2002
k_2 (k_{anoxic})	Effective burial rate constant for anoxic sinks	0.939	dm/yr	Zheng et al., 2002a, b; Zheng et al., 2000
δ_r	$\delta^{238}U$ of river waters	-0.34	‰	Andersen et al., 2016
$[U]_{modern}$	Modern seawater U concentration	1.39×10^{-8}	mol/dm^3	Chen et al., 1986; Weyer et al., 2008
δ_{modern}	Modern seawater $\delta^{238}U$	-0.4	‰	Tissot and Dauphas, 2015; Weyer et al., 2008
Δ_{ox}	Fractionation factor between oxic sink and seawater	0.005	‰	Weyer et al., 2008
$\Delta_{suboxic}$	Fractionation factor between suboxic sink and seawater	0.1	‰	Tissot and Dauphas, 2015
Δ_{anox}	Fractionation factor between anoxic sink and seawater	0.6	‰	Holmden et al., 2015; Weyer et al., 2008
V	Seawater volume	1.37×10^{21}	dm^3	Hastings et al., 1996
A	Total seafloor area	3.61×10^{16}	dm^3	Barnes and Cochran, 1990; Veeh, 1967;
	Modern anoxic seafloor area	6.00	%	
	Modern suboxic seafloor aarea	0.35	%	Dunk et al., 2002
	Modern oxic seafloor area	93.65	%	Balance